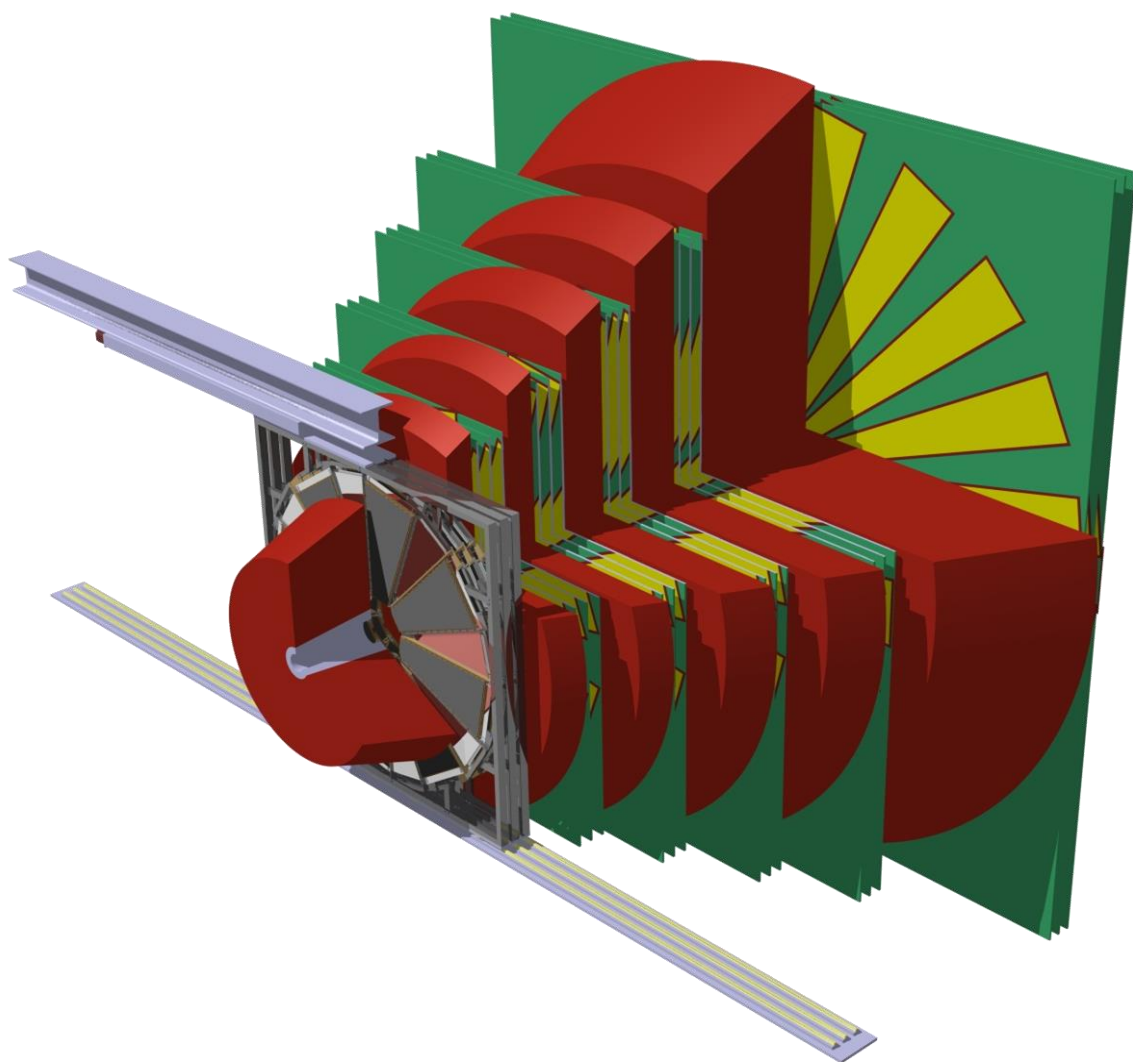Compressed Baryonic Matter Experiment

Technical Design Report for the CBM

Muon Chambers (MuCh)

The CBM Collaboration

November 2014

The MUCH TDR Workgroup and the CBM Collaboration[*]

Aligarh, Aligarh Muslim University
H. Jahan

Darmstadt, Germanny,GSI Helmholtzzentrum fur Schwerionenforschung GmbH
A. Abuhoza, U. Frankenfeld, V. Friese, J. Hehneri, V. Kleipa, W. Mueller, T. Morhardt, A. Senger, P. Senger, C.J. Schmidt, R. Schmidt, D. J. Schmidt

Dubna, Russia, Joint Institute for Nuclear Research (JINR)
I.V. Boguslavskiy, N. Grigalashvili, G.D. Kekelidze, V.M. Lysan, V.V. Myalkovskiy, V.D. Peshekhonov, S.V. Rabtsun, N.M. Shumeiko, A.B. Solin, A.I. Zinchenko

Frankfurt, Germany, Institute für Kernphysik, Goethe Universität Frankfurt
A. Lebedev

Gatchina, Russia, Petersburg Nuclear Physics Institute (PNPI) NRC *Kurchatov Institute*
V. Ivanov, A. Khanzadeev, L. Kochenda, B. Komkov, P. Kravtsov, L. Kudin, E. Kryshen, V. Nikulin, E. Roshchin, V. Samsonov,O. Tarasenkova, S. Volkov

Guahati, Gauhati University
K. Dey

Jammu, Jammu University
A.Gupta

Kolkata, Bose Institute
R.P. Adak, S. Das, S. Samanta

Kolkata, India, Variable Energy Cyclotron Centre
Z. Ahammed, T. Bandyopadhyay, S. BajiRao, P.P. Bhaduri, S. Biswas, S. Chattopadhyay,E. Nandy, M.S. Dey, A.K. Dubey, T. Ghosh, V. Jain, S.A. Khan, S.K. Pal, R. Raman, J. Saini, R.N. Singaraju, V. Singhal, Y.P. Viyogi[1]

Moscow, Russia, NRNU MEPhi
E.V. Atkin, E. Malankin, V. Shumikhin, A. Voronin

Srinagar, Kashmir University
S. Ahmad, F. Mir

Tübingen, Germany, Physikalisches Institut - Eberhard Karls Universitat Tubingen, D-72076, Tübingen, Germany
A. Lymanets, H.R. Schmidt, J Wiechula

Varanasi, India, Banaras Hindu University
A. Prakash

[*] The current list of CBM members is provided in Appendix A.
[1] Raja Ramanna Fellow under the Department of Atomic Energy, Government of India

CBM web page

`http://www.fair-center.eu/en/for-users/experiments/cbm.html`

Editors

S. Chattopadhyay, Y. P. Viyogi, P. Senger, W.F.J. Müller, C.J. Schmidt

Acknowledgements

4

Executive Summary

This document describes the technical layout and the performance of the Muon Chamber (MuCh) System of the Compressed Baryonic Matter (CBM) experiment at FAIR. The MuCh system is designed to identify muon pairs which are produced in high-energy heavy-ion collisions in the beam energy range from 4 to 40 AGeV. The measurement of lepton pairs is a central part of the CBM research program, as they are very sensitive diagnostic probes of the conditions inside the fireball. At low invariant masses, dileptons provide information on the in-medium modification of vector mesons which is a promising observable for the restoration of chiral symmetry. At intermediate invariant masses, the dilepton spectrum is dominated by thermal radiation from the fireball reflecting its temperature. At invariant masses around 3 GeV/c^2, dileptons are the appropriate tool to study the anomalous charmonium suppression in the deconfined phase. In the CBM experiment both electrons and muons will be measured in order to obtain a consistent and comprehensive picture of the dilepton physics.

The experimental challenge for muon measurements in heavy-ion collisions at FAIR energies is to identify low-momentum muons in an environment of high particle densities. The CBM strategy is to track the particles through a hadron absorber system, and to perform a momentum-dependent muon identification. This concept is realized by an instrumented hadron absorber, consisting of staggered absorber plates and tracking stations. The hadron absorbers vary in material and thickness, and the tracking stations consist of detector triplets based on different technologies. The MuCh system is placed downstream of the dipole magnet hosting the Silicon Tracking System (STS) which determines the particle momentum. In order to reduce the number of muons from pion and kaon weak decays, the absorber/detector system has to be as compact as possible.

Detailed simulations have been performed to optimize the detector system with respect to efficiency, signal-to-background ratio, and phase-space coverage. The event generator UrQMD and the transport code GEANT3 have been used within the CBMroot framework to simulate for example the worst-case background scenario, i.e. central Au+Au collisions at 25 AGeV.

The MuCh system will be built in stages which are adapted to the beam energies available. Within the FAIR modularized start version the SIS100 ring will provide heavy ion beams with energies up to 14 AGeV, and proton beams up to 29 GeV. The first two versions of MuCh (SIS100-A and SIS100-B) will comprise of 3 and 4 stations suitable for the measurement of low-mass vector mesons in A + A collisions at 4-6 AGeV and 8-14 AGeV, respectively. The third version of the MuCh system (SIS100-C) will be equipped with an additional iron absorber of 1 m thickness in order to be able to identify charmonium at the highest SIS100 energies. The absorber slices will be built only once so that they could be rearranged properly to obtain required absorber thicknesses. Once SIS300 is operational, we will upgrade the MuCh system further by inserting additional absorbers and detector stations for the measurement of low-mass vector mesons and charmonium at beam energies above 14 AGeV (MuCh versions SIS300-A and SIS300-B).

Calculations with the FLUKA code have been performed in order to optimize the absorber system under realistic beam conditions. As a result, the actual design of the full version of MuCh system

consists of 6 hadron absorber layers (60 cm carbon and iron plates of 2 x 20 cm, 30 cm, 35 cm, and 100 cm thickness) and 6 gaseous tracking chamber triplets behind each absorber slice. For the SIS100 versions, a reduced number of stations and absorber slices will be used. The tracking chambers are based on different technologies depending on the hit density and rate. The first two stations will consist of triple Gas Electron Multiplier (GEM) detectors, and the next one or two stations will be made of straw tube detectors. As the last tracking station behind the thick 1m absorber we use four layers of the Transition Radiation Detector (TRD) which is built for electron identification at CBM. For the full MuCh version at SIS300, the 5th station will be made of hybrid GEM+Micromegas technology, and as station number six after the 1 m iron absorber we will use again the 4 TRD layers. In total, the full version of muon chambers cover an active area of about 70 m^2 subdivided into about half a million channels. Simulations have been performed for different beam energy regions which show that, depending on the observables and on the beam energy, measurements can be performed successfully with varying number of absorber layers and detector stations.

The physics performance studies of the MuCh system are based on a realistic detector segmentation and response. Digitization and clustering algorithms have been developed in order to define the hits which then were used to reconstruct the trajectories. The trajectories in the MuCh are reconstructed by a track following method using the reconstructed tracks in the STS as seeds. The track reconstruction in the STS is based on the Cellular Automaton method. For track following from the STS into the MuCh the Kalman filter technique is used. Trajectories which do not point to the primary vertex or do not fit well to a certain number of hits are rejected in order to suppress weak decays and mismatches of tracks in the STS with tracks in the MuCh. The tracks which survive the quality cuts are used to calculate the combinatorial background. For the feasibility studies, the background is calculated for central Au+Au collisions using the UrQMD code. The signal muon pairs from decays of vector mesons are embedded in UrQMD events, and then reconstructed. The signal multiplicity is taken from the HSD event generator. For central Au+Au collisions at 25 AGeV the signal-to-background ratio for the ω meson is S/B=0.5, and for the J/ψ a value of S/B=1.7 is found. At SIS100 energies, low-mass vector mesons can be identified with a MuCh system consisting of 4 absorber layers and 4 tracking stations only. With this configuration, a value of S/B=0.5 for ω mesons is found for central Au+Au collisions at 8 AGeV. A setup has also been optimized for 4 AGeV Au + Au collisions. J/ψ mesons even can be already identified with 3 absorber layers and 3 tracking stations, resulting in a value of S/B=0.06 for central Au+Au collisions at 10 AGeV which is already below the threshold for charmonium production in p+p collisions.

The challenge for the first stations of muon chambers and for the track reconstruction algorithms is the very high particle density of up to 0.04 hits/cm^2 per event in the first detector layers after 60 cm of carbon. This value is calculated with the FLUKA transport code for minimum bias Au+Au collisions at an energy of 35 AGeV. For a reaction rate of 10 MHz this hit density translates into a hit rate of 0.4 MHz/cm^2. At VECC Kolkata and at GSI triple-GEM detectors of size 10 cm x 10 cm with a segmentation of 3 mm x 3 mm have been developed. The detectors have been tested successfully using X-rays and particle beams for efficiency, rate capability, and long-term stability. Prototype GEM detectors were operated at rates of about 1.4 MHz/cm^2 as measured by the anode currents using X-rays, and detection efficiencies of more than 95% have been achieved. Most of the tests have been performed with a self-triggered readout electronics as it will be used later in the experiment. Subsequently, a triple GEM detector of size 31 cm x 31 cm has been built and tested with X-rays and proton beams. This intermediate size chamber has exactly same pad segmentation as will be used for the full size chamber. The performance of the intermediate size chamber is very similar to the one of the small chamber of 10 cm x 10

cm size. A real size chamber has also been assembled and tested successfully with X-rays and proton beams. It showed $> 95\%$ efficiecny upto a beam rate of 2.5 MHz/cm^2.

The group at JINR-Dubna has rich experience in building and operating straw tube detectors for various experiments. For the MuCh system, a full size prototype module has been built and tested at JINR Dubna.The module has an active area of 366 cm in width varying in height between 84 and 190 cm. A full octagonal detector layer will be composed of two such modules with overlapping frames. The module consists of two layers of straws, each layer comprising 592 straws with 6 mm diameter. The straw layers are shifted with respect to each other by half a straw diameter to resolve left-right ambiguities, and to achieve a detection efficiency of better than 98% with a gas mixture of Ar/CO$_2$ (80/20) and a gain of 7x10^4. With such a two layer chamber an averaged spatial resolution of 90 to 120 μm can be obtained. The production technology has been developed for the straw detector of the COMPASS experiment at CERN-SPS, and further improved for the ATLAS TRT at LHC. Each of the straw tube chambers for the MuCh detector stations will consist of 3 double straw-tube layers which are rotated with respect to each other by 10 degrees.

At PNPI Gatchina, different types of detectors considered as muon chamber candidates have been developed. Among them there are combinations of a Micromegas detector with a GEM (MG), Double GEM (GG), Double Thick GEM (DTG), combinations of a Micromegas with a Thick GEM (TMG), and a thick GEM detector with 4 amplification stages, called Monolithic Thick GEM (MTG). The detector sizes were 10x10 cm^2 or 5x5 cm^2 and were successfully tested. A promising candidate for the muon chambers is the hybrid MG detector with a Helium based gas mixture which has an efficiency of 95-100% up to a rate of 3 MHz.

For GEM detectors of the MuCh system, the ASIC developed for the CBM Silicon Tracking System (STS-xyter) will be used with a provision of dual-gain to take care of difference n dynamic range difference. As a paralel development, at MePhi, Moscow, a first version of the MuCh ASIC frontend, comprising preamplifier and shaper circuits, has been built and tested. The backplane of the MuCh ASIC will be the same as for the STS-xyter.The MuCh read-out chain up to the high performance computer farm will be adopted from the other CBM detector systems.

For the Straw tube detector, we have taken the self-triggered readout system being developed for the TOF system of CBM as the baseline. The system will make use of PADI-chip for amplification and discrimination and GET4-chip as TDC. The TOF readout will handle MRPC readout that requires very good time resolution (tens of pico-seconds) which will be more than what will be required for the straw tube time readout (nano-seconds). The system for TOF is a result of detailed R&D is fully compatible for CBM. This readout will be used for the startup version of the CBM-MuCh straw tube detectors. For the later stage during SIS300 operations, R&D is ongoing to build a dedicated readout system for the straw tube detectors. A straw tube chamber coupled to such a readout ASIC has been tested successfully.

The MuCh system has to be very compact and to be located close to the magnet in order to reduce the background of muons from weak decays of pions or kaons. Therefore, the first muon absorber made of carbon will be integrated inside the magnet, the other absorbers positioned downstream the magnet will be built of iron blocks. The blocks and appropriate tooling are specially designed to guarantee relatively simple assembling, reliable fixation, proper positioning and sufficient wall planarity. The tracking chambers will be mounted on a superstructure which will be made of iron profiles stiff enough to withstand the magnetic forces. This structure is designed in such way that the chambers could be pulled from the running position (around the beam pipe) to service position (outside the absorbers), enabling access to the elements of the chamber. The

compactness requirement implies minimal gap for tracking chambers between the absorbers. A special system provides safe chamber mounting, position adjustment and translation from service to running positions and back. Most of the components of the MuCh start version will be used also at SIS300. A particular challenge for the mechanical integration of the MuCh system into the CBM setup arises from the requirement that the MuCh has to be removed for hadron or electron measurements.

The CBM MuCh system will be realized by the Indian Muon consortium (Aligarh Univ, Banaras Univ., Calcutta Univ., IIT Kharagpur, IOP Bhubaneshwar, Jammu Univ., Kashmir Univ., North Bengal Univ., Panjab Univ., Bose Institute and VECC) led by VECC Kolkata, JINR Dubna, PNPI St. Petersburg, and MEPhI Moscow.

Contents

Chapter 1

The Compressed Baryonic Matter Experiment

1.1   Exploring the phase diagram of nuclear matter

Substantial experimental and theoretical efforts worldwide are devoted to the exploration of the phase diagram of nuclear matter. Figure 1.1 illustrates the possible phases of nuclear matter and their boundaries in a diagram of temperature versus the baryon chemical potential. Cold nuclear matter - as found in normal nuclei with a net baryon density normalised to one - consists of protons and neutrons (i.e. nucleons) only. At moderate temperatures and densities, nucleons are excited to short-lived states (baryonic resonances) which decay by the emission of mesons. At higher temperatures, additionally baryon-antibaryon pairs are created. This mixture of baryons, antibaryons and mesons, all strongly interacting particles, is generally called hadronic matter, or baryonic matter if baryons prevail. At very high temperatures or densities the hadrons melt, and the constituents, the quarks and gluons, form a new phase: the Quark-Gluon-Plasma. For very low net baryon densities where the numbers of particles and anti-particles are approximately equal, theory predicts that hadrons dissolve into quarks and gluons above a temperature of about 160 MeV [1, 2]. The inverse process happened in the universe during the first few microseconds after the big bang: the quarks and gluons were confined into hadrons. In this region of the phase diagram the transition is expected to be a smooth crossover from partonic to hadronic matter [3]. Calculations suggest a critical endpoint at relatively large values of the baryon chemical potential [4]. Beyond this critical endpoint, for larger values of net baryon densities (and for lower temperatures), one expects a phase transition from hadronic to partonic matter with a phase coexistence region in between. A new phase of so called quarkyonic matter has also been proposed to exist beyond the first order phase transition at large baryon chemical potentials and moderate temperatures [5]. High-density but cold nuclear matter is expected to exist in the core of neutron stars, and at very high densities correlated quark-quark pairs are predicted to form a color superconductor.

As illustrated in Fig. 1.1, it is expected that the QCD phase diagram exhibits a rich structure at finite values of baryon chemical potentials, such as the critical point, the predicted first order phase transition between hadronic and partonic or quarkyonic matter, and the chiral phase transition. The experimental discovery of these prominent landmarks of the QCD phase diagram would be a major breakthrough in our understanding of the properties of nuclear matter. Equally important is quantitative experimental information on the properties of hadrons in dense matter
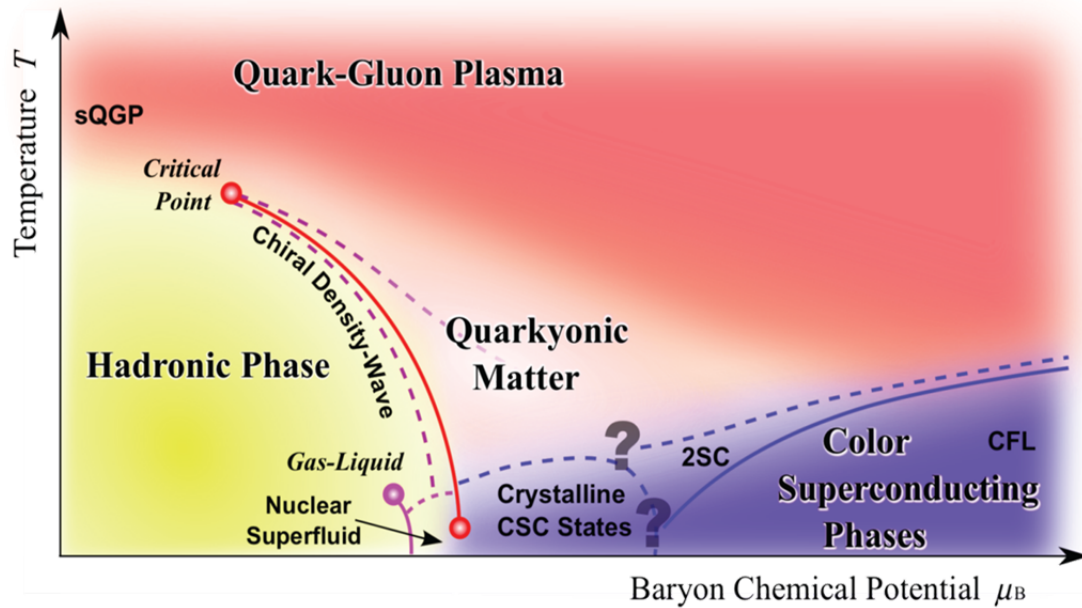
Figure 1.1: Sketch of the phase diagram for strongly-interacting matter (taken from [6]).

which may shed light on chiral symmetry restoration and the origin of hadron masses.

In the laboratory hot and dense nuclear matter is generated in a wide range of temperatures and densities by colliding atomic nuclei at high energies. The goal of the experiments at RHIC and LHC is to investigate the properties of deconfined QCD matter at very high temperatures and almost zero net-baryon densities. Several experimental programs are devoted to the exploration of the QCD phase diagram at high net-baryon densities. The STAR collaboration at RHIC scanned the beam energies in order to search for the QCD critical endpoint [7]. For the same reason, measurements are performed at the CERN-SPS with the upgraded NA49 detector (NA61) using light and medium size ion beams [8]. At the Joint Institute for Nuclear Research (JINR) in Dubna, a heavy-ion collider project (NICA) is planned with the goal to search for the coexistence phase of nuclear matter [9]. However, due to luminosity or detector limitations these experiments are constrained to the investigation of particles which are abundantly produced. In contrast, the Compressed Baryonic Matter (CBM) experiment at the Facility for Antiproton and Ion Research (FAIR) in Darmstadt is designed for precision measurements of multidimensional observables including particles with very low production cross sections using the high-intensity heavy-ion beams provided by the FAIR accelerators.

The SIS100/300 accelerators at FAIR are very well suited to create high net-baryon densities. This is illustrated in Fig. 1.2 which depicts results of transport code calculations for central Au+Au collisions. According to these calculations, densities of up to 7 times saturation density can be produced already at beam energies of 10 AGeV. Under these conditions the nucleons overlap, and theory predicts a transition to a mixed phase of baryons and quarks.
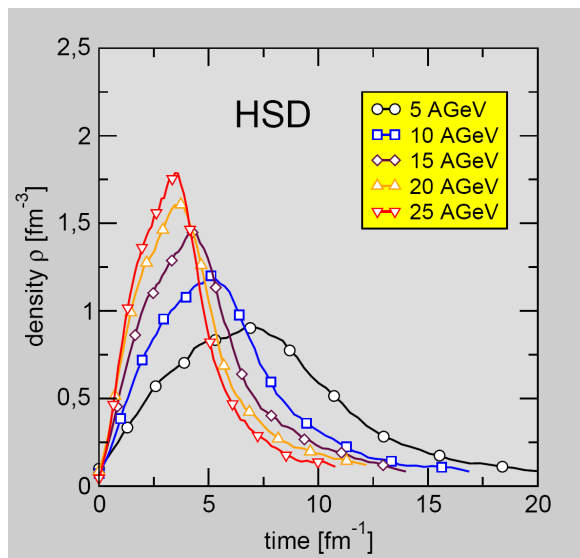
Figure 1.2: Baryon density as function of elapsed time for central Au+Au collisions at different energies as calculated with the HSD transport code [10].

1.2 Diagnostic probes of the high-density fireball

Figure 1.3 depicts three snapshots of the evolution of a heavy-ion collision at FAIR energies as calculated with the UrQMD transport code [2], and illustrates the time of production and eventual emission of various particle species. Particles containing charm quarks are expected to be created in the very first stage of the reaction. Then, D mesons and J/ψ mesons may serve as probes for the dense fireball and its degrees of freedom. Vector mesons like ω, ρ and ϕ mesons are produced continuously via $\pi\pi$ annihilation during the course of the reaction, and decay either again into mesons, or into a pair of leptons. However, as leptons are not affected by final-state interactions, the dileptonic decay offers the possibility to look directly into the fireball. In particular, the short-lived ρ meson is a promising diagnostic probe of hot and dense nuclear matter. Due to their small hadronic cross sections, also multi-strange hyperons and ϕ mesons carry information on the dense phase of the collision, in particular via their collective flow. Finally, the bulk of the particles freezes out at densities below saturation density. Up to date, essentially these freeze-out particles have been measured in heavy-ion collisions at beam energies between 2 and 40 AGeV (on stationary target). Diagnostic probes of the dense stage of the fireball such as multi-strange baryons, dilepton pairs and charmed particles will be measured for the first time by the CBM experiment in this beam energy range. Therefore, the CBM experiment has a unique discovery potential both at SIS100 and SIS300 energies.

The experimental challenge is to measure multi-differential observables and particles with very low production cross sections such as multi-strange (anti-) hyperons, particles with charm and lepton pairs with unprecedented precision. The situation is illustrated in Fig. 1.4 which depicts the product of multiplicity times branching ratio for various particle species produced in central Au+Au collisions at 25 AGeV. The data points are calculated using either the HSD transport code [12] or the thermal model based on the corresponding temperature and baryon-chemical potential [14]. Mesons containing charm quarks are about 9 orders of magnitude less abundant than pions (except for the ψ' meson which is even more suppressed). The dilepton decay of vector mesons is suppressed by the square of the electromagnetic coupling constant $(1/137)^2$, resulting in a dilepton yield which is 6 orders of magnitude below the pion yield, similar to the
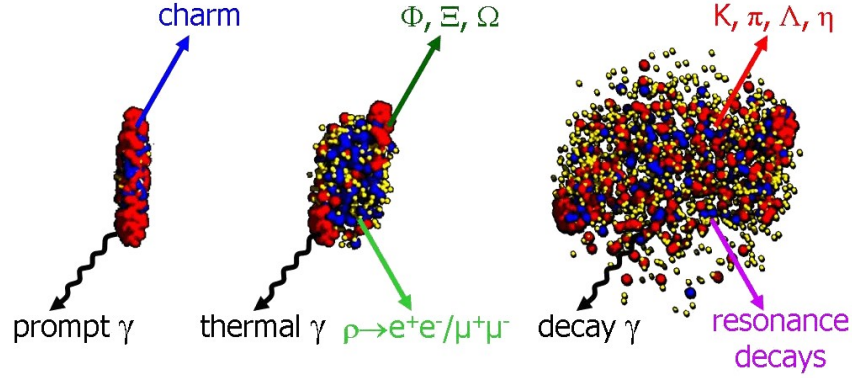
Figure 1.3: Three stages of a U+U collision at a laboratory beam energy of 23 AGeV as calculated with the UrQMD model [2]: the initial stage where the two Lorentz-contracted nuclei overlap (left), the high density phase (middle), and the final stage ("freeze-out") when all hadrons have been formed (right). Different particles are created in different stages of the collisions or escape from the interaction region at different times (see text). Almost 1000 charged particles are created in such a collision, most of them are pions.

multiplicity of multi-strange anti-hyperons.

In order to produce high statistics data even for the particles with the lowest production cross sections, the CBM experiment is designed to run at reaction rates of 100 kHz up to 1 MHz. For charmonium measurements - where a trigger on high-energy lepton pairs can be generated - reaction rates up to 10 MHz are envisaged.

1.3   CBM physics cases and observables

The CBM research program is focused on the following physics cases:

The equation-of-state of baryonic matter at neutron star densities.
The relevant measurements are:

- The excitation function of the collective flow of hadrons which is driven by the pressure created in the early fireball (SIS100);

- The excitation functions of multi-strange hyperon yields in Au+Au and C+C collisions at energies from 2 to 11 AGeV (SIS100). At subthreshold energies, Ξ and Ω hyperons are produced in sequential collisions involving kaons and Λ's, and, therefore, are sensitive to the density in the fireball.

In-medium properties of hadrons.
The restoration of chiral symmetry in dense baryonic matter will modify the properties of hadrons. The relevant measurements are:

- The in-medium mass distribution of vector mesons decaying in lepton pairs in heavy-ion collisions at different energies (2 - 45 AGeV), and for different collision systems. Leptons are penetrating probes carrying the information out of the dense fireball (SIS100/300);
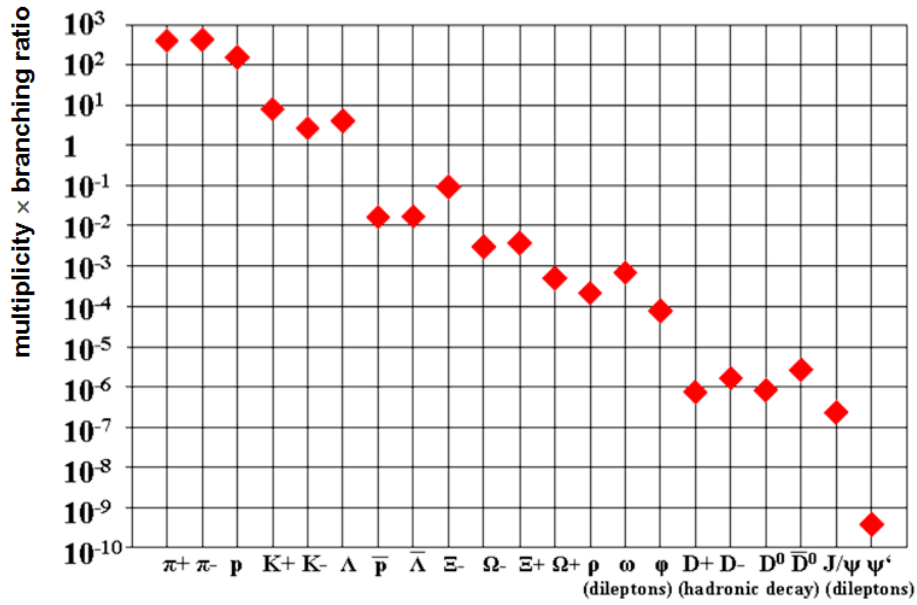
Figure 1.4: Particle multiplicities times branching ratio for central Au+Au collisions at 25 AGeV as calculated with the HSD transport code [12] and the statistical model [14]. For the vector mesons (ρ, ω, ϕ, J/ψ, ψ') the decay into lepton pairs was assumed, for D mesons the hadronic decay into kaons and pions.

- Yields and transverse mass distributions of charmed mesons in heavy-ion as a function of collision energy (SIS100/300).

Phase transitions from hadronic matter to quarkyonic or partonic matter at high net-baryon densities.
Already at SIS100 energies densities of up to 7 times ρ_0 are reached in central collisions between heavy-ions. A discontinuity or sudden variation in the excitation functions of sensitive observables would be indicative of a transition. The relevant measurements are:

- The excitation function of yields, spectra, and collective flow of strange particles in heavy-ion collisions from 6 - 45 AGeV (SIS100/300);

- The excitation function of yields, spectra, and collective flow of charmed particles in heavy-ion collisions from 6 - 45 AGeV (SIS100/300);

- The excitation function of yields and spectra of lepton pairs in heavy-ion collisions from 6 - 45 AGeV (SIS100/300);

- Event-by-event fluctuations of conserved quantities like baryons, strangeness , net-charge among others. in heavy-ion collisions with high precision as function of beam energy from 6 - 45 AGeV (SIS100/300).

Hypernuclei, strange dibaryons and massive strange objects.
Theoretical models predict that single and double hypernuclei, strange dibaryons and heavy multi-strange short-lived objects are produced via coalescence in heavy-ion collisions with the maximum yield in the region of SIS100 energies. The planned measurements include:

- The decay chains of single and double hypernuclei in heavy ion collisions at SIS100 energies;

- Search for strange matter in the form of strange dibaryons and heavy multi-strange short-lived objects. If these multi-strange particles decay into charged hadrons including hyperons they can be identified via their decay products.

Charm production mechanisms, charm propagation, and in-medium properties of charmed particles in (dense) nuclear matter.
The relevant measurements are:

- Cross sections and momentum spectra of open charm (D-mesons) in proton-nucleus collisions at SIS100/300 energies. In-medium properties of D mesons can be derived from the transparency ratio $T_A = (\sigma_{pA} \to DX)/(A \times \sigma_{pN} \to DX)$ measured for different size target nuclei;

- Cross sections, momentum spectra, and collective flow of open charm (D-mesons) in nucleus-nucleus collisions at SIS300 energies;

- Cross sections, momentum spectra, and collective flow of charmonium (J/ψ) in proton-nucleus and nucleus-nucleus collisions at SIS100/300 energies.

As discussed above, a substantial part of the CBM physics cases can be addressed already with beams from the SIS100 synchrotron. The intended measurements at SIS100 including the results of simulations and count rate estimates are described in [15]. A general review of the physics of compressed baryonic matter, the theoretical concepts, the available experimental results, and predictions for relevant observables in future heavy-ion collision experiments can be found in the CBM Physics Book [13].

1.4   The Facility for Antiproton and Ion Research (FAIR)

The international Facility for Antiproton and Ion Research (FAIR) in Darmstadt will provide unique research opportunities in the fields of nuclear, hadron, atomic and plasma physics [16]. The research program devoted to the exploration of compressed baryonic matter will start with primary beams from the SIS100 synchrotron (protons up to 29 GeV, Au up to 11 AGeV, nuclei with Z/A = 0.5 up to 14 AGeV), and will be continued with beams from the SIS300 synchrotron (protons up to 90 GeV, Au up to 35 AGeV, nuclei with Z/A = 0.5 up to 45 AGeV). The layout of FAIR is presented in Fig. 1.5. The beam extracted to the CBM cave reaches intensities up to 10^9 Au ions per second.

1.5   The Compressed Baryonic Matter (CBM) experiment

The CBM experimental strategy is to perform systematically both integral and differential measurements of almost all the particles produced in nuclear collisions (i.e. yields, phase-space distributions, correlations and fluctuations) with unprecedented precision and statistics. These measurements will be performed in nucleus-nucleus, proton-nucleus, and - for baseline determination - proton-proton collisions at different beam energies. The identification of multi-strange
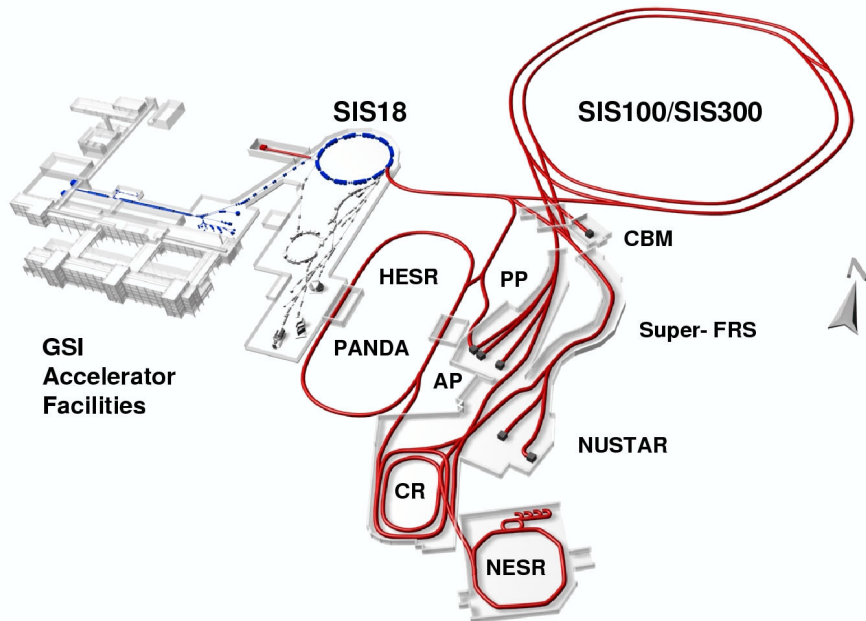
Figure 1.5: Layout of the Facility for Antiproton and Ion Research (FAIR) [16].

hyperons, hypernuclei, particles with charm quarks and vector mesons decaying into lepton pairs requires efficient background suppression and very high interaction rates. In order to select events containing those rare observables, the tracks of each collision have to be reconstructed and filtered online with respect to physical signatures. This concept represents a paradigm shift for data taking in high-energy physics experiments: CBM will run without hierarchical trigger system. Self-triggered read-out electronics, a high-speed data processing and acquisition system, fast algorithms, and, last but not least, radiation hard detectors are indispensable prerequisites for a successful operation of the experiment. Figures 1.6 and 1.7 depict the CBM experimental setup with electron detectors and the muon detection system, respectively. The CBM experiment comprises the following components:

Dipole magnet
The dipole magnet will be superconducting in order to reduce the operation costs. It has a large aperture of $\pm 25°$ polar angle, and provides a magnetic field integral of 1 Tm.

Micro-Vertex Detector (MVD)
The determination of the decay vertices of open charm particles ($c\tau = 123$ μm for D^0 mesons and $c\tau = 314$ μm for $D^\pm$ mesons) requires detectors with excellent position resolution and a very low material budget in order to reduce multiple scattering. These requirements are met by Monolithic Active Pixel Sensors (MAPS). The pixel size will be between 18×18 μm^2 and 20×40 μm^2. A position resolution of $\sigma = 3.5$ - 6 μm can be achieved depending on the pixel size. The goal of the detector development is to construct a vacuum compatible MAPS detector stations with a total thickness of about 300 - 500 μm silicon equivalent for sensors and support structures, depending on the size of the stations. The MVD consists of 3 MAPS layers located at

5, 10, and 15 cm downstream of the target in the vacuum. This detector arrangement permits to determine the secondary decay vertex of a D-meson with a resolution of about 50-100 μm along the beam axis.

Silicon Tracking System (STS)

The task of the STS is to provide track reconstruction and momentum determination of charged particles. The multiplicity of charged particles is up to 700 per event within the detector acceptance. The STS consists of 8 tracking layers of silicon detectors. They are located downstream of the target at distances between 30 cm and 100 cm inside the magnetic dipole field. The required momentum resolution is of the order of $\Delta p/p = 1\%$. This performance can only be achieved with an ultra-low material budget of the stations, imposing particular restrictions on the location of power-dissipating front-end electronics in the fiducial volume. The concept of the STS tracking is based on silicon microstrip sensors mounted onto lightweight mechanical support ladders. The sensors will be read out through multi-line micro-cables with fast electronics at the periphery of the stations where cooling lines and other infrastructure can be placed. The micro-strip sensors will be double-sided with a stereo angle of 7.5°, a strip pitch of 58 μm, strip lengths between 20 and 60 mm, and a thickness of 300 μm of silicon. The micro-cables will be built from sandwiched polyimide-Aluminum layers of several 10 μm thickness.

Ring Imaging Cherenkov Detector (RICH)

The RICH detector is designed to provide identification of electrons and suppression of pions in the momentum range below 10 GeV/c. This will be achieved using a gaseous RICH detector build in a standard projective geometry with focusing mirror elements and a photo detector. CO_2 with a pion threshold for Cherenkov radiation of 4.65 GeV/c will be used as radiator gas. The detector will be positioned behind the dipole magnet about 1.6 m downstream of the target. It will consist of a 1.7 m long gas radiator (overall length approximately 2 m) and two arrays of mirrors and photo detector planes. The mirror plane is split horizontally into two arrays of spherical glass mirrors, (4×1.5) m^2 each. The 72 mirror tiles have a curvature of 3 m radius, a thickness of 6 mm and a reflective AL+MgF$_2$ coating. Rings of Cherenkov radiation will be projected onto two photo detector planes (2×0.6) m^2 each located behind the CBM dipole magnet and shielded by the magnet yokes. The design of the photo detector plane is based on MAPMTs (e.g. H8500 from Hamamatsu) in order to provide high granularity, high geometrical acceptance, high detection efficiency of photons also in the near UV region and a reliable operation. In-beam tests with a prototype RICH of real size length showed that 22 photons are measured per electron ring. On the order of 100 rings are seen in central Au+Au collisions at 25 AGeV beam energy due to the large material budget in front of the RICH detector. Still, due to the high granularity (approx. 55 000 channels) and high number of photons per ring, a pion suppression on the order of 500 is expected to be achieved according to simulations.

Muon Chamber System (MUCH)

The experimental challenge for muon measurements in heavy-ion collisions at FAIR energies is to identify low-momentum muons in an environment of high particle densities. The CBM concept is to track the particles through a hadron absorber system, and to perform a momentum-dependent muon identification. This concept is realized by segmenting the hadron absorber in several layers, and placing triplets of tracking detector planes in the gaps between the absorber layers. The absorber/detector system is placed downstream of the Silicon Tracking System (STS) which determines the particle momentum. In order to reduce meson decays into muons the absorber/detector system has to be as compact as possible. The final design of the muon

detector system consists of 6 hadron absorber layers (60cm carbon and iron plates of 2×20 cm, 30 cm, 35 cm and 100 cm thickness) and 18 gaseous tracking chambers located in triplets behind each absorber slab. The identification of a muon depends on its momentum which varies with the mass of the vector mesons and with beam energy. The challenge for the muon chambers and for the track reconstruction algorithms is the very high particle density up to a maximum of 0.3 hits/cm^2 per central event in the first detector layers after the first absorber. For a reaction rate of 10 MHz this hit density translates into a hit rate of 3 MHz/cm^2. Prototype chambers based on GEM technology were operated successfully at rates of about 1.4 MHz/cm^2 as measured by anode currents using X-rays. In total, the muon chambers cover an active area of about 70 m^2 subdivided into about half a million channels. The low particle multiplicities behind the last muon absorber favors the implementation of a trigger on muon pairs. The trigger concept is based on the measurement of short track segments in the last tracking station triplet, and extrapolation of these tracks to the target. After selection of tracks with good vertices the event rate can be reduced already by a factor of about 600 for J/ψ measurements in minimum bias Au+Au collisions. For J/ψ measurements at SIS100 a MUCH start version with 3 chamber triplets has been found to be sufficient.

Transition Radiation Detector (TRD)
Three Transition Radiation Detector stations each consisting of 3 detector layers will serve for particle tracking and for the identification of electrons and positrons with p > 1.5 GeV/c ($\gamma \geq 1000$). The detector stations are located at approximately 5 m, 7.2 m and 9.5 m downstream the target, the total active detector area amounts to about 600 m^2. For example, at small forward angles and at a distance of 5 m from the target, we expect particle rates on the order of 100 kHz/cm^2 for 10 MHz minimum bias Au+Au collisions at 25 AGeV. In a central collision, particle densities of about 0.05/cm^2 are reached. In order to keep the occupancy below 5% the minimum size of a single cell should be about 1 cm^2. The TRD detector readout will be realized in rectangular pads giving a resolution of 300-500 μm across and 3 - 30 mm along the pad. Every second TR layer is rotated by 90 degree. Prototype gas detectors based on MWPC and GEM technology have been built and tested with particle rates of up to 400 kHz/cm^2 without deterioration of their performance. The pion suppression factor obtained with 9 TRD layers is estimated to be well above 100 at an electron efficiency of 90%. For measurements at SIS100 only one station with 3 detector layers will be used as an intermediate tracker between the STS and the TOF wall.

Timing Multi-gap Resistive Plate Chambers (MRPC)
An array of Resistive Plate Chambers will be used for hadron identification via TOF measurements. The TOF wall covers an active area of about 120 m^2 and is located about 6 m downstream of the target for measurements at SIS100, and at 10 m at SIS300. The required time resolution is on the order of 80 ps. For 10 MHz minimum bias Au+Au collisions the innermost part of the detector has to work at rates up to 20 kHz/cm^2. Prototype MRPCs built with low-resistivity glass have been tested with a time resolution of about 40 ps at 20 kHz/cm^2. At small deflection angles the pad size is about 5 cm^2 corresponding to an occupancy of below 5% for central Au+Au collisions at 25 AGeV.

Electromagnetic Calorimeter (ECAL)
A "shashlik" type calorimeter as installed in the HERA-B, PHENIX and LHCb experiments will be used to measure direct photons and neutral mesons (π^0, η) decaying into photons. The ECAL will be composed of modules which consist of 140 layers of 1mm lead and 1mm scintillator, with

cell sizes of 3×3 cm^2, 6×6 cm^2, and 12×12 cm^2. The shashlik modules can be arranged either as a wall or in a tower geometry with variable distance from the target.

Projectile Spectator Detector (PSD)
The PSD will be used to determine the collision centrality and the orientation of the reaction plane. A precise characterization of the event is of crucial importance for the analysis of event-by-event observables. The study of collective flow requires a well-defined reaction plane which has to be determined by a method not involving particles participating in the collision. The detector is designed to measure the number of non-interacting nucleons from a projectile nucleus in nucleus-nucleus collisions. The PSD is a full compensating modular lead-scintillator calorimeter which provides very good and uniform energy resolution. The calorimeter comprises 44 individual modules, each consisting of 60 lead/scintillator layers with a surface of 20×20 cm^2. The scintillation light is read out via wavelength shifting (WLS) fibers by Multi-Avalanche Photo-Diodes (MAPD) with an active area of 3×3 mm^2 and a pixel density of $10^4/$mm^2.

Online event selection and data acquisition
High statistics measurements of particles with very small production cross sections require high reaction rates. The CBM detectors, the online event selection systems, and the data acquisition will be designed for event rates of 10 MHz, corresponding to a beam intensity of 10^9 ions/s and a 1% interaction target, for example. Assuming an archiving rate of 1 GByte/s and an event volume of about 10 kByte for minimum bias Au+Au collisions, an event rate of 100 kHz can be accepted by the data acquisition. Therefore, measurements with event rates of 10 MHz require online event selection algorithms (and hardware) which reject the background events (which contain no signal) by a factor of 100 or more. The event selection system will be based on a fast on-line event reconstruction running on a high-performance computer farm equipped with many-core CPUs and graphics cards (GSI GreenIT cube). Track reconstruction, which is the most time consuming combinatorial stage of the event reconstruction, will be based on parallel track finding and fitting algorithms, implementing the Cellular Automaton and Kalman Filter methods. For open charm production the trigger will be based on an online search for secondary vertices, which requires high speed tracking and event reconstruction in the STS and MVD. The highest suppression factor has to be achieved for J/ψ mesons where a high-energetic pair of electrons or muons is required in the TRD or in the MUCH. For low-mass electron pairs no online selection is possible due to the large number of rings/event in the RICH caused by the material budget of the STS. In the case of low-mass muon pairs some background rejection might be feasible.
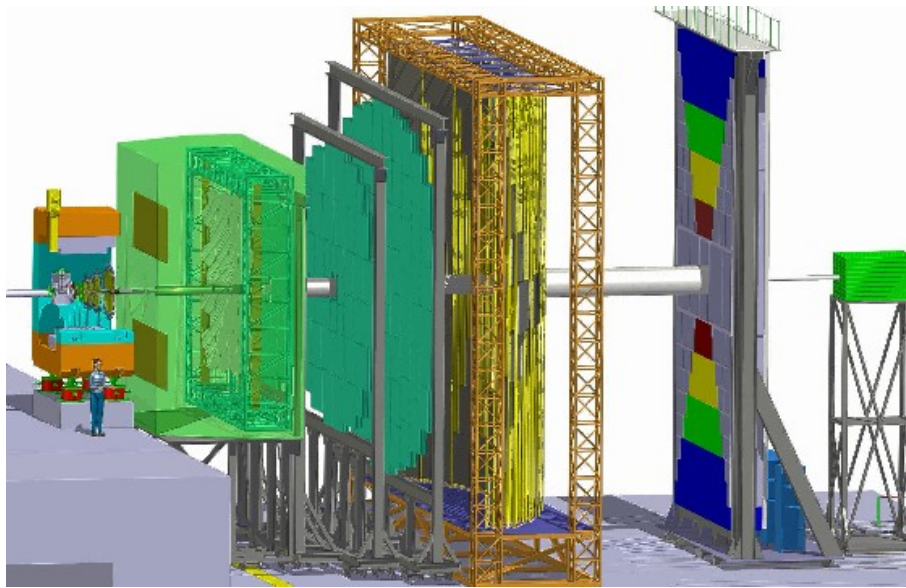
Figure 1.6: The CBM experimental facility with the electron detectors RICH and TRD.
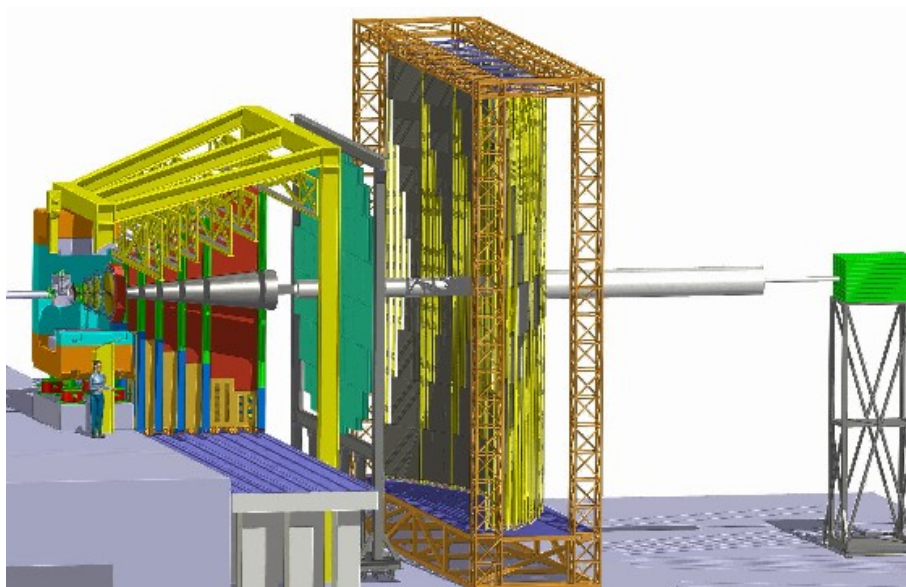

Figure 1.7: The CBM experimental facility with the muon detection system.

1.6   Dimuon measurements at FAIR

Lepton pairs emitted in heavy-ion collisions are very sensitive diagnostic probe of the conditions inside the fireball because they are not affected by final-state interactions. The most interesting sources of lepton pairs are:

- Low-mass vector mesons, in particular the ρ^0 meson which has a short lifetime and decays inside the fireball, change their properties in the hot and dense medium. Such in-medium modifications are expected when chiral symmetry is (partly) restored.

- Thermal electromagnetic radiation - converted into lepton pairs - reflects the temperature of the fireball. Thermal lepton pairs are emitted all over the course of the collision, and, hence, provide integrated information on the temperature evolution.

- Charmonium dissociation due to color screening in a deconfined medium was predicted as a signature of the Quark-Gluon Plasma [17].

Up to date, no dilepton data have been measured in heavy-ion collisions in the FAIR energy range, i.e. between about 2 AGeV (with DLS at LBL [18] and HADES at GSI [19]), and 40 A GeV (with CERES at CERN-SPS [20]). The experimental challenge in dilepton measurements is to suppress the huge combinatorial background of lepton pairs. In the case of muon measurements, the muon background is generated by weak decays of pions and kaons, by mismatches of hadrons upstream and muons downstream the hadron absorber, and by hadrons punching through the absorber. In the following, we will briefly review our present knowledge on dilepton physics based on the results of the NA60 experiment which represent the most precise dilepton data measured so far in heavy-ion collisions.

1.6.1   Low mass vector mesons

In fig. 1.8 (left panel) the dimuon invariant mass distributions for In+In collisions at 158 A GeV measured by the NA60 collaboration are shown [21, 22]. The black histogram represents the mass spectra of the opposite-sign muon pairs including the combinatorial background which has been determined by analyzing like-sign muon pairs (blue histogram). After subtraction of the combinatorial background and of the fake matches (blue dashed-dotted histogram) one obtains the signal pairs (red histogram). The signal pairs are also shown in the right panel of fig. 1.8 (red dots) together with a cocktail of known dimuon sources. After subtracting the ϕ, ω and η resonances together with the muon pairs from the corresponding Dalitz decays, one is left with an unknown "excess yield" which still contains the ρ meson contribution (black triangles).
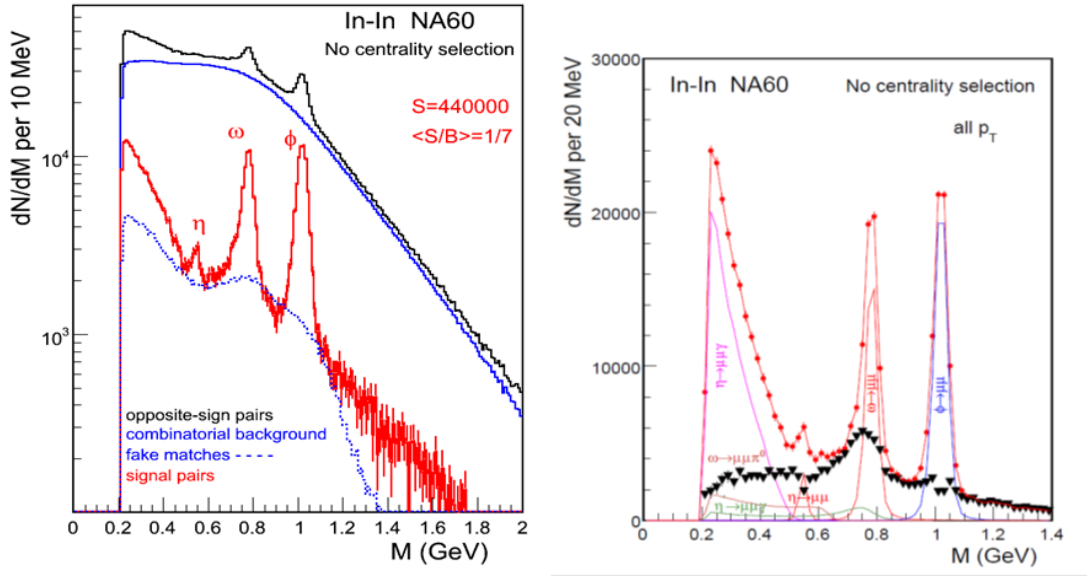
Figure 1.8: NA60 dimuon invariant mass distributions measured in In+In collisions at 158 A GeV. Left: mass spectra of the opposite-sign dimuons (upper black histogram), combinatorial background (blue histogram), signal pairs (red histogram), and fake matches (blue dotted histogram). Right: Signal pairs (red dots), excess yield (black triangles, see text) [21].
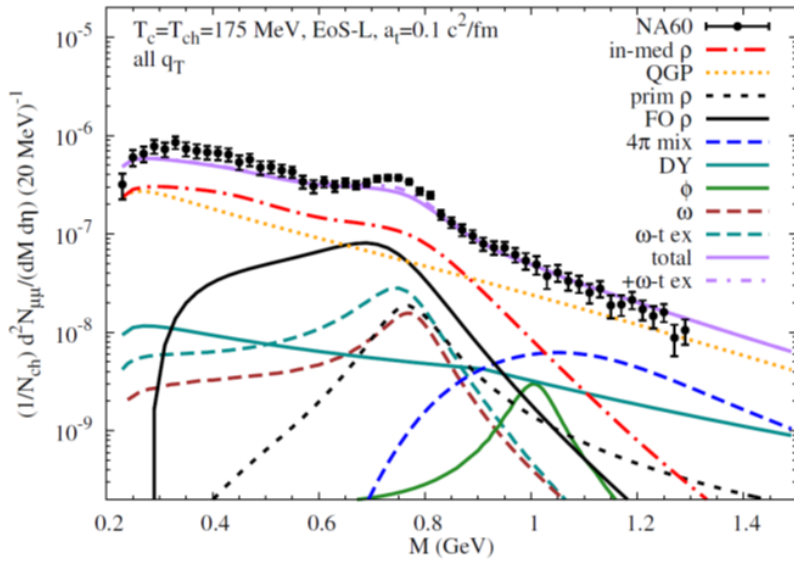

Figure 1.9: Acceptance corrected dimuon excess spectra measured in In+In collisions at 158 A GeV by NA60 [21, 22] compared to theoretical calculations with in-medium vector spectral functions [24].

Fig. 1.9 depicts the acceptance corrected excess yield (black dots with error bars) [21]. Moreover, a cocktail of various contributions to the excess yield is shown as calculated with an expanding fireball model including a phase transition by R. Rapp et al. [24]. According to the calculations, the low-mass range (M < 0.8 GeV/c^2) is dominated by the broadened in-medium ρ^0 meson red dashed-dotted line), the radiation from the QGP (orange dotted line), and by the freeze-

out ρ^0 (black solid line). R. Rapp argues that the melting of the ρ^0 resonance is theoretically compatible with chiral symmetry restoration and suggestive for a gradual change in the effective degrees of freedom in the system. It is worthwhile to note that the coupling of the vector mesons to the baryons is essential to explain the data in the low mass range. In the intermediate mass range (M > 1.0 GeV/c^2) the major contributions are radiation from the QGP, from multi-hadron annihilation (blue dashed line), and from quark-antiquark annihilation (Drell-Yan, solid turquois line). The calculation assumes a lattice EoS, a critical emperature which coincides with the chemical freeze-out temperature of 175 MeV, and an initial temperature of 245 MeV which is reflected in the slope of the invariant mass spectra.

1.6.2   Thermal radiation

According to the calculation of R. Rapp et al. the intermediate mass range of the dimuon excess spectrum shown in fig. 1.9 is dominated by thermal radiation from the QGP. The slope of the invariant mass spectrum directly allows the extraction of the initial temperature of the QGP. More information can be obtained from the slope of the transverse momentum spectra of dimuons with different masses. This effective temperature of the dimuon excess yield (Drell-Yan contribution subtracted) is shown in the left panel of fig. 1.10 [25]. In the low-mass range, the effective temperature increases with invariant mass. The same observation is made for the hadrons. This effect is attributed to the increase of collective flow in the late phase of the collision. In the intermediate mass range, the effective temperature drops. This observation suggests that the intermediate mass dimuons are emitted in the early (partonic?) phase of the collision where the collective flow is not yet developed. A very similar pattern of the effective temperature (or slope parameter) was observed for hadrons with masses up to charmonium (see right panel of fig. 1.10) [26]. In summary, the temperatures extracted both from the invariant mass spectrum of the dimuon excess yield and from the transverse momentum spectra exceed the critical temperature, and thus provide evidence for radiation from the QCD transition region.
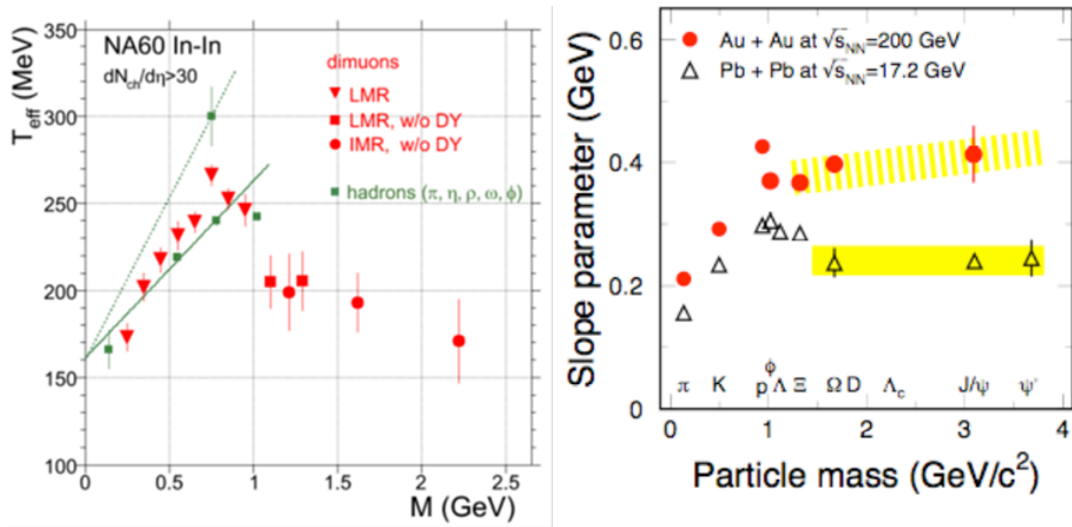

Figure 1.10: Left panel: Inverse slope parameter T_{eff} versus dimuon mass M for the low and intermediate mass range measured in In+In collisions at 158 A GeV [25]. Right panel: Inverse slope parameter versus particle mass for hadrons measured in Pb+Pb collisions at 158 A GeV and for A+Au collisions at $\sqrt{s_{NN}} = 200$ GeV [26].

1.6.3 Charmonium

Heavy quarks are unique probes to study the properties of the Quark-Gluon Plasma produced in heavy ion collisions. Due to their large masses, they are produced predominantly in hard scatterings, during the initial phase of the collision. D mesons and charmonium are exposed to the highest temperatures and densities. Therefore, it was suggested to study the dissociation of charmonium which was predicted to occur due to color screening in a deconfined medium [17]. The NA50/NA60 collaborations investigated charmonium suppression in Pb+Pb and In+In collisions at 158 A GeV. They plotted the ratio of the measured J/ψ yield over the expected yield as function of participating nucleons N_{part} (see fig. 1.11) [23]. The expected yield was calculated from the J/ψ production cross section measured in p+A collisions at the same beam energy. The data in fig. 1.11 demonstrate that no deviation from expectation is observed up to N_{part} of 200 both for In+In and Pb+Pb collisions, whereas for central Pb+Pb collisions an anomalous J/ψ suppression of the order of 20-30% is visible.
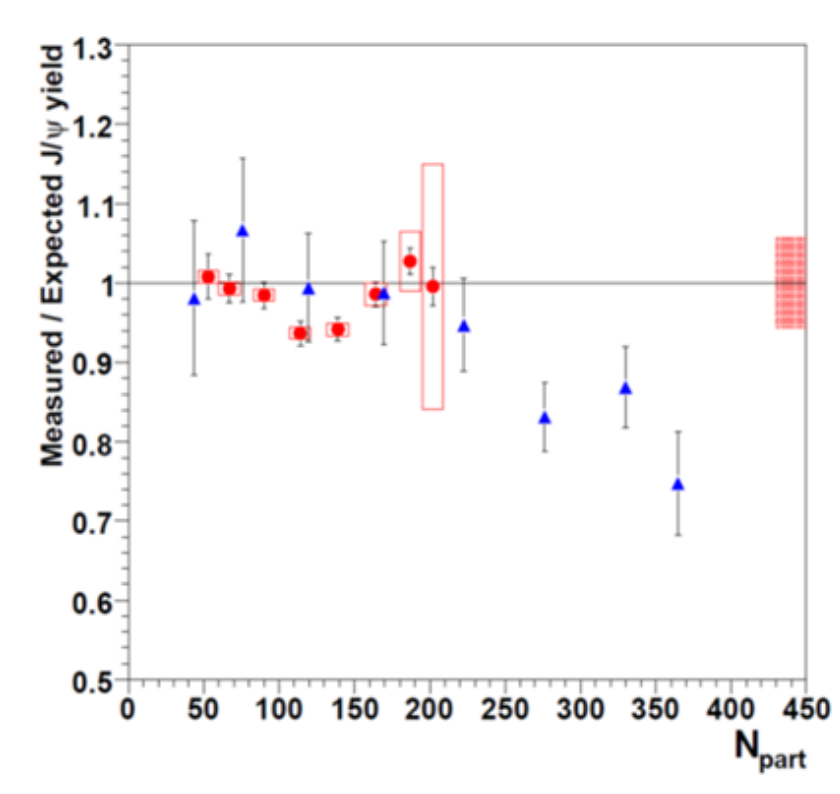

Figure 1.11: J/ψ suppression pattern in In+In collisions (red circles) and Pb+Pb collisions (blue triangles) at 158 A GeV [23].

Charmonium measurements at FAIR energies are particularly challenging due to the very low production charm production cross section. This is illustrated in fig. 1.12 which depicts a compilation of experimental results on the total charm production cross section as function of particle energy, together with a NLO pQCD calculation and its uncertainty [27]. No data are existing at FAIR heavy-ion beam energies ($\sqrt{s_{NN}} < 8$ GeV). New precision data on charm production at FAIR energies are needed to clarify the production mechanism of charm close to threshold.
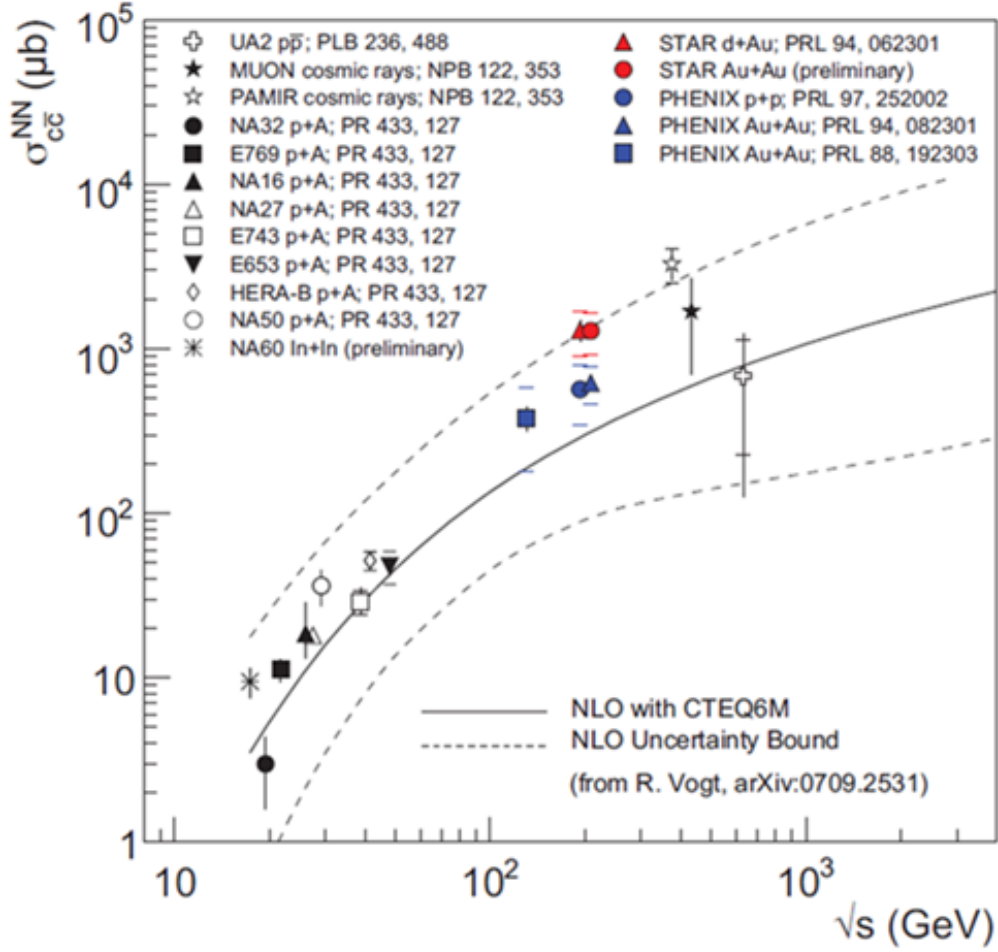
Figure 1.12: Compilation of total charm production cross-section measurements compared to pQCD NLO calculations (solid line). The dashed lines represent the uncertainty bands of the calculations [27].

1.6.4 Conclusion

The comparison of high precision data with theoretical models has demonstrated that dilepton pairs emitted in energetic heavy-ion collisions provide valuable information on the evolution and on the properties of the hot and dense fireball. It was shown, that the in-medium mass distribution of short-lived vector mesons decaying in lepton pairs is modified both due to their coupling to baryon resonances, and by their interaction with the chiral condensate. A careful analysis of the measured dilepton excess yield - i.e. the dilepton mass distribution with the contribution from vector mesons subtracted - allows to extract the thermal radiation, and, hence, the temperature evolution of the fireball. At top SPS energies, the dilepton mass distribution in the intermediate mass range is dominated by radiation from a deconfined phase. The comparison of charmonium yields measured in proton-nucleus and nucleus-nucleus collisions has led to the observation of an anomalous dissociation of charmonium in central collisions of heavy nuclei which was explained by color screening in the quark-gluon phase. Till today, this observation

still has remained one of the most convincing experimental facts hinting towards the existence of partonic degrees of freedom in the fireball at top SPS energies.

The dilepton measurements at the CERN-SPS have been performed mainly at 158 A GeV, except for one spectrum taken in Pb+ Au at 40 A GeV by the CERES collaboration where even an increased excess yield has been observed [20]. A systematic beam energy scan in order to search for the onset of in-medium mass modifications of vector mesons or for partonic contributions to the dilepton yield has not been performed yet.

With the dilepton measurements in heavy-ion collisions at FAIR energies the CBM collaboration will open a new era of dilepton experiments. Moreover, CBM will enter terra incognita: in the beam energy range between 2 and 40 A GeV where the highest net- baryon densities can be created in the laboratory, no dileptons have been measured in heavy ion collisions. The CBM collaboration will systematically measure both dielectrons and dimuons in p+p, p+A and A+A collisions as function of beam energy and size of the collision system. The dielectron and dimuon high-precision data will complement each other, and will provide a complete picture on dilepton radiation off dense baryonic matter. Therefore, the CBM experiment has a large discovery potential both at SIS100 and SIS300.

In this report, the performance of the planned muon measurements and the technical layout of the CBM muon detection system will be described.

Bibliography

[1] S. Borsanyi et al., JHEP 1009 (2010) 073

[2] A. Basavov et al., arXiv:1111.1710v1

[3] Y. Aoki et al., Nature 443 (2006) 675

[4] Z. Fodor and S.D. Katz, JHEP 0404 (2004) 050

[5] A. Andronic et al., Nucl. Phys. A837 (2010) 65

[6] K. Fukushima and T. Hatsuda, Rept. Prog. Phys. 74 (2011) 014001

[7] A.Schmah , Cent. Eur. J. Phys.,10 (2012) 1238

[8] A. Aduszkiewicz et al., Acta Physica Polonica B43 (2012) 635

[9] NICA White Paper, `http://nica.jinr.ru/files/WhitePaper.pdf`

[10] W. Ehehalt and W. Cassing, Nucl. Phys. A602 (1996) 449

[11] S.A. Bass et al, Prog. Part. Nucl. Phys. 41 (1998) 225

[12] W. Cassing, E.L. Bratkovskaya, and A. Sibirtsev, Nucl. Phys. A691 (2001) 753, and E.L. Bratkovskaya, priv. comm.

[13] B. Friman et al. (Eds.), The CBM Physics Book, Lect. Notes Phys. 814, Springer-Verlag Berlin Heidelberg 2011

[14] A. Andronic, P. Braun-Munzinger, J. Stachel, Nucl. Phys. A772 (2006) 167

[15] CBM Report 2012-01, `http://www.gsi.de/documents/DOC-2011-Aug-29-1.pdf`

[16] FAIR Baseline Technical Report 2006, `http://www.gsi.de/fair/reports/btr.html`

[17] T. Matsui and H. Satz, Phys. Lett. 178B (1986) 416

[18] R.J. Porter et al. [DLS Collaboration], Phys. Rev. Lett. 79 (1997) 1229

[19] G. Agakichiev et al. [Hades Coll.], Phys.Rev.C84 (2011) 014902

[20] G. Agakichiev et al. [CERES/NA45 Coll.], Eur. Phys. J. C41, 475 (2005);

[21] R. Arnaldi et al. [NA60 Coll.], Phys. Rev. Lett. 96, (2006) 162302

[22] R. Arnaldi et al. [NA60 Coll.], Eur. Phys. J. C 61, (2009) 711

[23] R. Arnaldi [NA60 Coll.], Nucl.Phys.A830 (2009) 345c

[24] R. Rapp, J. Wambach and H. van Hees, in Relativistic Heavy-Ion Physics, edited by R. Stock and Landolt Brnstein (Springer), New Series I/23A (2010), arXiv:0901.3289 hep-ph

[25] R. Arnaldi et al., (NA60), Phy. Rev. Lett. 100 (2008) 022302

[26] N. Xu, Int. J. Mod. Phys. E16 (2007) 715

[27] A. Frawley, T. Ulrich, R. Vogt, Phys.Rept.462 (2008) 125

Chapter 2

The CBM muon detector system

2.1   Conceptual layout of the CBM muon detection system

One of the major experimental challenges of muon measurements in heavy-ion collisions in the FAIR energy regime is the identification of low momentum muons, originating from the decay of low-mass vector mesons, in a very high particle density environment. The novel feature of the muon detection system for the CBM [1] experiment, as compared to the muon detectors in other HEP experiments, is that the total absorber is sliced and chambers are placed in between absorbers to facilitate momentum dependent track identification. This is to improve the capturing of low momentum muons, which would have been otherwise stopped by a single thick absorber. The high efficiency for detection of low momentum muons is a prerequisite to reconstruct the low mass vector mesons in the muon chambers (MUCH). The layout of the MUCH system, i.e. the number, thickness and material of the absorber slices, and the number and granularity of the tracking detectors, has been optimized by simulating the response of the Au+Au collisions in a range of energies spanning from 4 AGeV to 25 AGeV beam energy having input particles generated by the UrQMD [2] event generator. The GEANT3 [3] code was used to transport particles through the absorbers and tracking chambers.

The required thicknesses of the hadron absorbers for the measurement of low-mass vector mesons and charmonia can be estimated from Fig. 2.1 where the absorptions of various particles are shown as function of thickness of the iron absorber thickness. Whereas the muons from J/ψ traverse a distance up to 250 cm in iron without considerable suppression, most of the low momentum muons from ω mesons get absorbed by a factor of 10 in such a thick absorber. Moreover, it can be seen that beyond an iron thickness of 1.5 m, muons from ω mesons get as strongly absorbed as pions and protons which means that the signal-to-background ratio (S/B) will not improve further by adding absorbers beyond 1.5 m. In conclusion, for the efficient detection of low mass vector mesons the iron absorber thickness should not exceed 1.5 m, whereas for the measurement of muons from the J/ψ decays, one should add an additional iron absorber of about 1 m thickness together with a number of detector layers. Apart from the total absorber thickness, one has to optimize the thicknesses of the individual absorber layers in the MUCH system. Particularly important is the thickness and material of the first absorber slice where one has to find a compromise between hadron absorption and multiple scattering. The absorber should be sufficiently thick to reduce the hadron multiplicity to a level such that the tracking chambers will be able to operate. On the other hand, a thick absorber enhances multiple scattering and for a given thickness, the scattering increases with Z, hence, the number of mismatched tracks. In
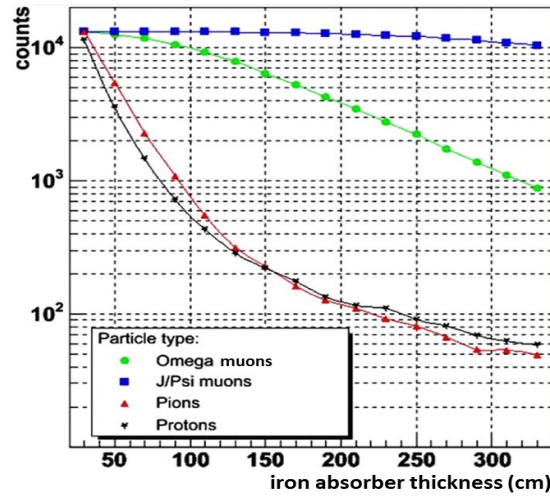
Figure 2.1: Total number of particles as a function of the traversed length in iron. The particle momenta have been taken from the simulation of central Au+Au collisions at 25 AGeV, their numbers have been normalized.

Fig. 2.2 and Fig. 2.3 we have shown the variation of particle multiplicity as a function of thickness of the first absorber for central Au+Au collisions at 10 and 25 AGeV beam energies, respectively. Simulations have been performed for two absorber materials, i.e. iron (left) and carbon (right). The simulations indicate that for both absorber materials the particle multiplicity is dominated by the yield of secondary electrons that rises initially and then drops with increasing material thickness. It can be seen that the multiplicity of particles, which survive after 60 cm carbon or 20 cm iron are somewhat different. However carbon has been chosen as the first absorber material in the MUCH setup mainly from the practical considerations as discussed later.
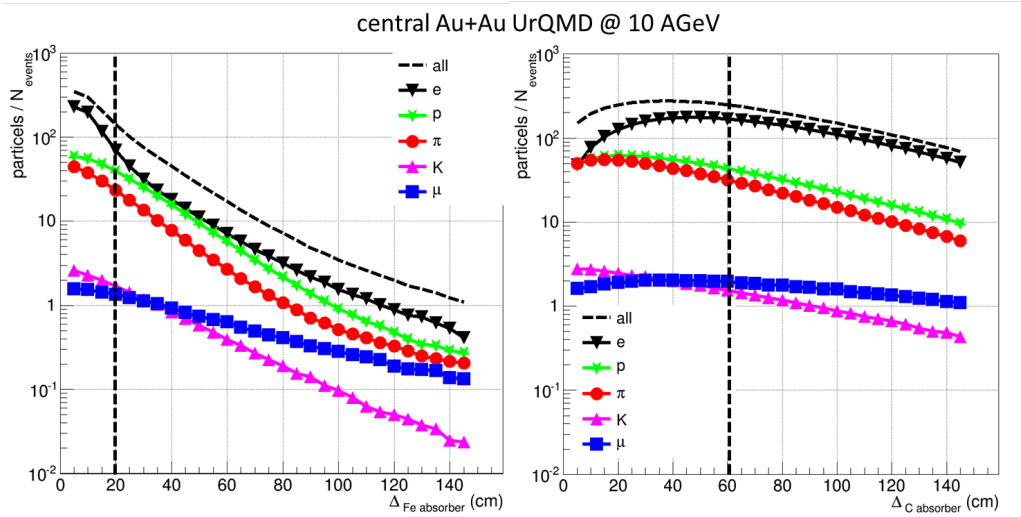
Figure 2.2: Variation of particle multiplicity (primary + secondary) per central Au+Au collision at 10 AGeV as a function of the thickness of an iron absorber (left) and a carbon absorber (right).

As mentioned above, an important criterion for the optimization of the hadron absorber is the small-angle multiple scattering, which increases with the absorber thickness, and decreases the
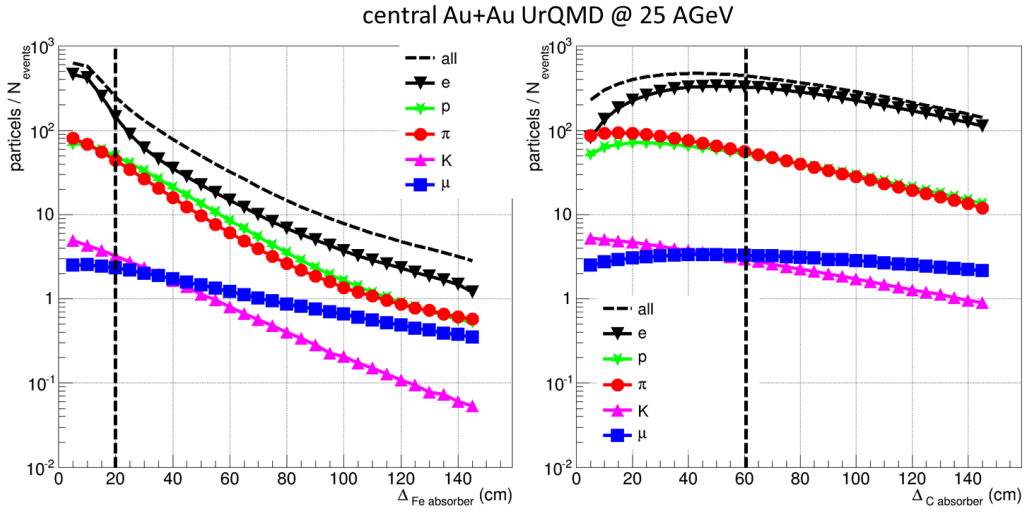
Figure 2.3: Variation of particle multiplicity (primary + secondary) per central Au+Au collision at 25 AGeV as a function of the thickness of an iron absorber (left) and a carbon absorber (right).

matching efficiency between the incoming and outgoing tracks. This reduction in matching efficiency results in an increased number of mismatches, and, finally, in a larger number of falsely reconstructed background tracks. This effect is illustrated in Fig. 2.4 where the ratio of the number of reconstructed tracks to that of the accepted tracks is shown as a function of the thickness of the first absorber. The simulation, which was performed for iron, clearly shows a strong increase of reconstructed background tracks with increasing absorber thickness. The resulting invariant mass spectrum from the reconstructed tracks, which represents combinatorial background for the di-muon measurement shows that the background increases by almost a factor of 10 when the thickness of the first iron absorber is increased from 10 cm to 40 cm. Thus, a first iron absorber of 20 - 30 cm thickness or equivalently 60 cm carbon absorber seems to be an optimum choice based on hit density and background tracks. Even though iron was taken to be the only absorber material in early days of simulation studies, subsequently, taking into consideration the mechanical integration of the first absorber inside the high magnetic field of the CBM dipole magnet, carbon absorber of 60 cm thickness is found to be preferable.
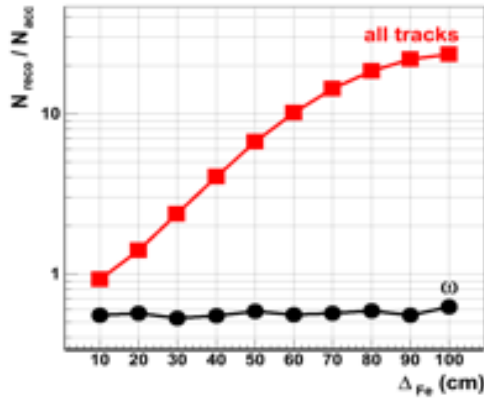

Figure 2.4: Variation of the ratio of the reconstructed tracks to the accepted tracks in the muon detection system as a function of the thickness of the first absorber station. The simulation was performed for iron as absorber material.

We have performed simulations using the FLUKA transport code to estimate the hit density in the first tracking chamber behind a 60 cm thick carbon absorber. The results are shown in Fig. 2.5 as counts per cm^2 per event as a function of the distance from the beam axis for minimum bias Au+Au collisions at 10 AGeV (left panel) and 35 AGeV (right panel). The maximum hit density at 25 AGeV for the innermost part of the first detector (i.e. for small polar emission angles) reaches $0.04/cm^2$/event corresponding to a rate of 0.4 MHz/cm^2 for a total reaction rate of 10 MHz. For central events the hit density is expected to be higher by a factor of 4. In Fig. 2.6, the hit densities behind the iron and carbon absorbers are studied for different absorber thicknesses. This has been calculated with the UrQMD event generator and the GEANT3 transport code for central Au+Au collisions at 25 AGeV. In this case, for 60 cm thick carbon absorber, the hit density reaches $\approx 0.1/cm^2$/event. This study suggests that we need pads of smaller area of the order of 15-20 mm^2, at least for the inner part of the first detector station, in order to keep the occupancy at a reasonably low level (5%).
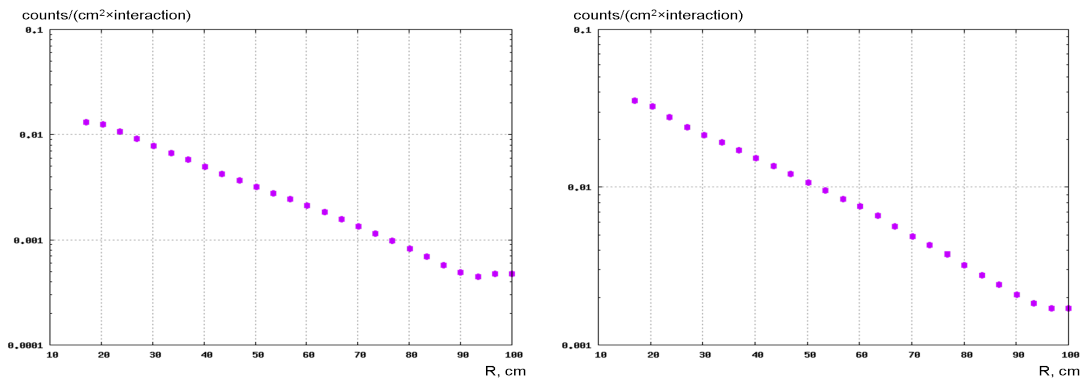
Figure 2.5: Hit densities in the first tracking chamber behind a carbon absorber of 60 cm thickness as function of distance from the beam axis for minimum bias Au+Au collisions at 10 AGeV (left panel) and 35 AGeV (right panel). The simulations have been performed with the FLUKA transport code.
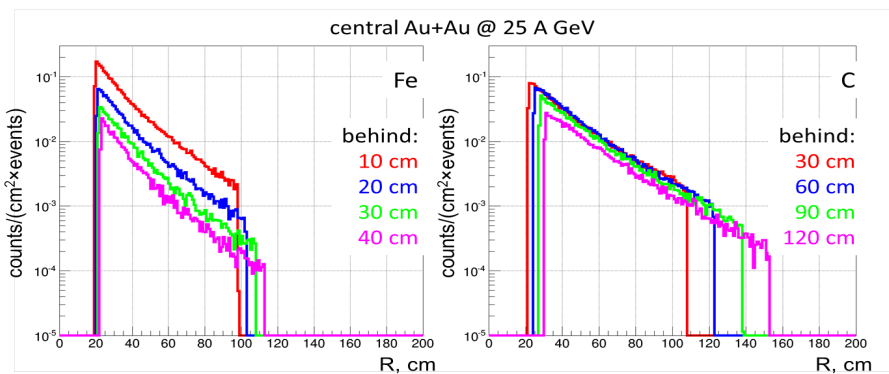

Figure 2.6: Hit densities behind iron (left) and carbon (right) absorbers of different thicknesses. The Geant simulation was performed for central Au + Au collisions at 25 AGeV using the UrQMD event generator as input.

2.2   MUCH configurations

FAIR will be built in phases, in the first phase beams will be available only from SIS100. As discussed in chapter-1, densities of up to 7 times saturation density can be produced in central Au+Au collisions at a beam energy of 10 AGeV as it will be delivered by SIS100. In order to investigate the conditions inside such a dense fireball with dimuons, we develop a MUCH system which is able to identify muon pairs in a wide range of beam energies, from low energies at SIS100 up to top SIS300 energies. To this end, we plan to build a modular MUCH which can be easily upgraded according to the beam energies under investigation. The design of the different MUCH configurations is guided by the following considerations: (a) the absorber slices will be built only once and will be placed suitably to obtain the required absorber thickness at a particular configuration. In all the configurations, first absorber will be made of 60 cm carbon (b) the number of tracking stations will be strictly decided based on physics requirements, for example, for low mass vector mesons, the number of stations to be installed will be such that the tracks will have a good number of space points for reconstruction. This depends on the momentum of the tracks. For charmonium detection, an additional absorber of 1 m thickness will be employed,(c) the technology to be used for different tracking chambers will be optimised as per the rate handling capability, the size limitations and the cost. In the following, we describe the evolution of the MUCH configurations. In Table 2.1 the main parameters of the various configurations are listed. In all the setups, TOF of CBM will be used during analysis.

MUCH version	Carbon absorber	No. of iron absorber slices	total thickness of iron absorber	No. of tracking chamber triplets	Type of Chambers	Physics case
SIS100-A	60 cm	2	40 cm	3	2 GEM, 1 Straw tube	LMVM A + A 4-6 AGeV
SIS100-B	60 cm	3	70 cm	4	2 GEM, 2 Straw tubes	LMVM A + A 8-10 AGeV
SIS100-C	60 cm	4	170 cm	5	2 GEM 2 Straw tubes 1 TRD	p + A (J/ψ) 29 GeV
SIS300-A	60 cm	5	105 cm	5	2 GEM, 2 Straw tubes, 1 TRD	LMVM (A + A) 15-25 AGeV
SIS300-B	60 cm	6	205 cm	6	2 GEM, 2 Straw tubes 1 Hybrid GEM, 1 TRD	J/ψ (A + A) 10-35 AGeV

Table 2.1: Various MUCH configurations in SIS100 and SIS300

As shown in Fig. 2.7, the SIS100-A setup aiming to study the Au + Au collisions in the energy range of 4 to 6 AGeV will consist of 3 tracking stations each consisting of 3 layers of chambers. Like other configurations, the first absorber will be made of carbon of 60 cm thickness, the iron

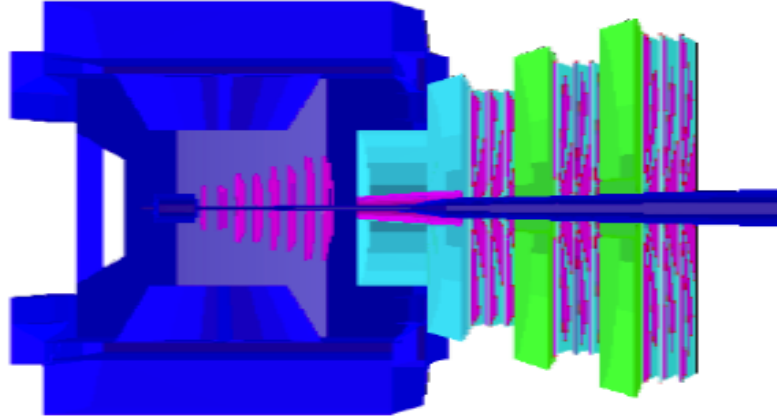absorber consisting of two slices will have total thickness of 40 cm. The SIS100-A setup will be

Figure 2.7: A schematic view of MUCH SIS100-A layout. It consists of 9 detector layers and 3 absorbers including the first absorber of 60 cm carbon. The TOF wall is not shown at the end of the setup. This setup is suitable for LMVM measurement at 4-6 AGeV Au + Au collisions.

subsequently extended to accommodate more tracking stations and more iron absorber slices so as to make it suitable for measurement of low mass vector mesons at higher energy collisions (E_{lab} = 8 - 11.5 AGeV). The first extension, called SIS100-B, consists of 4 absorbers and 12 detector layers (Fig. 2.8). For charmonium measurements, a 1-m thick iron absorber will be added to
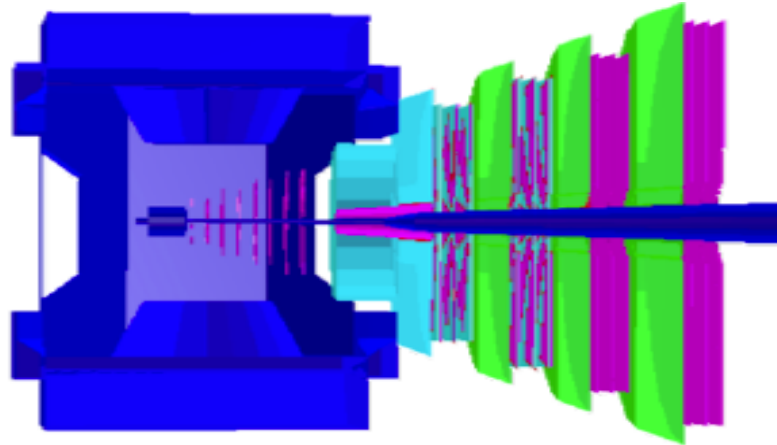
Figure 2.8: Schematic view of the MUCH SIS100-B configuration. It consists of 12 detector layers and 4 absorbers including the first absorber of 60cm carbon. The TOF wall is not shown at the end of the setup. This setup is suitable for LMVM measurement at 8 - 10 AGeV Au + Au collisions.

the version SIS100-B at the end of the setup. This configuration, called SIS100-C, consists of 5 absorbers and 15 detector layers and is shown in Fig. 2.9.

The sketch of the muon detection system designed for the heavy-ion collisions at top SIS300 energies is shown in Fig. 2.10. It comprises of 6 absorbers, first one made of carbon and the rest of iron, and 18 detector layers. The configuration with the first five layers after STS is designated as SIS300-A for the LMVM measurement at the SIS-300 energy and the full setup including the last thick absorber and last tracking station is called SIS300-B for charmonium measurement at
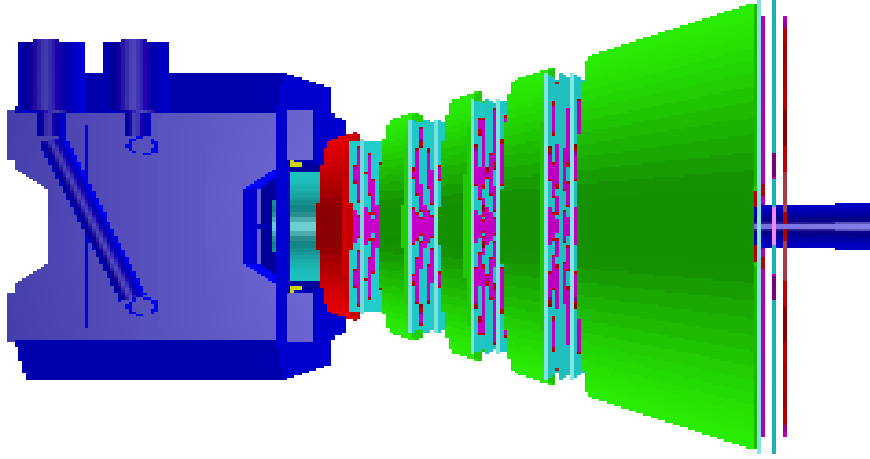
Figure 2.9: A schematic view of the extended version of MUCH SIS100 layout called SIS100-C. It consists of 15 detector layers and 5 absorbers. The last 3 layers are used for charmonium trigger and hence the effective number of layers for the measurement of low-mass vector mesons is 12. The TOF wall is not shown at the end of the setup.

top FAIR energy.

Each tracking station consists of three layers of chambers located in the gap between the absorber segments. The total absorber thickness in the full setup is 265 cm divided into 60 cm carbon and $(20 + 20 + 30 + 35 + 100)$ cm of iron which is equivalent to 13.5 times the hadronic interaction length λ. In all the setups, additional lead shieldings are used around the beam pipe to reduce the background of secondary electrons produced in the beam pipe. As mentioned earlier, these setups are flexible enough for the identification of both the charmonium and the low mass vector mesons. Only hits upstream of the last 100 cm absorber are relevant only for the latter study, i.e the effective number of detector layers for low-mass vector meson measurements are 9, 12 an 15 for SIS100-A, SIS100-B and SIS300-A respectively. The angular acceptance of the detector spans from $\approx 5°$ to $25°$.

The technologies to be used in different stations have been given in Table.2.1. The detector chambers on a particular station will use one particular type of technology. The covered active area of each layer has been divided into trapezoidal sector-shaped modules. Each module is arranged on a support structure, of around 2 cm thickness. Detector modules are attached at the front and the back sides of the support structure and filled with Argon based gas mixture as the active medium. Even though the technologies differ from one station to the other, all stations will however have gaseous detectors of different technologies. This allows us to use gas as sensitive medium in the simulation throughout. The Argon gas used as active medium has thickness of 3 mm. Cables, gas tubes, PCBs and front-end-electronics are not included in the present version of simulation. The distance between the chamber centers is 10 cm to provide enough space for accommodating the detector profile that includes electronics boards, mechanics, cooling arrangement among others. A 2 cm overlap of the sensitive volume is kept along the radial direction to avoid the dead zone. The number of sectors in a particular detector plane depends on the radii of the station. In Fig. 2.11, the layout of the muon chambers on the 1st station consisting of trapezoidal-shaped sectors is shown. Half of the total set of sectors are arranged in the front face and rest half in the back face. The number of sectors that can be
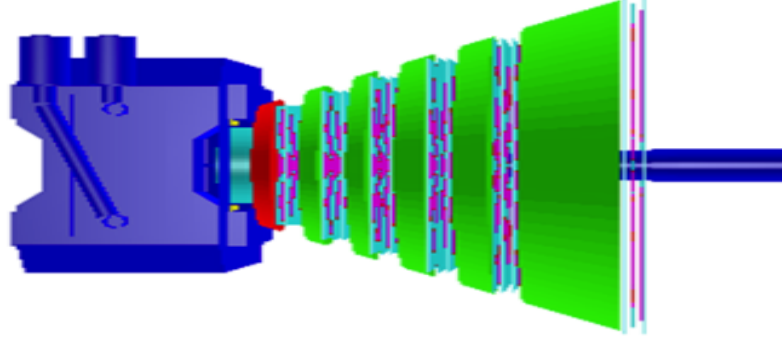
Figure 2.10: A schematic view of MUCH SIS300 layout. It consists of 18 detector layers and 6 absorbers with total absorber thickness of 265 cm. The effective number of layers for the measurement of low-mass vector mesons is 15 (SIS300-A) and the setup including the last 3 layers are used for charmonium trigger (SIS300-B). The TOF wall is not shown in the setup.

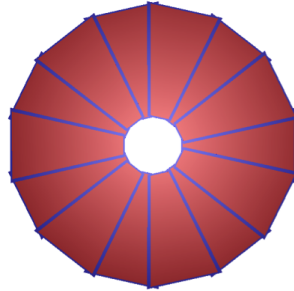accommodated in a detector layer is a tunable parameter. It should be mentioned that for the

Figure 2.11: Schematic view of the layout of the muon chambers with trapezoidal overlapping sectors

simulation results presented here, the chambers in all the detector stations have been taken to be made of GEM for ease of implementation in simulation geometry. Even though in actual setup, other technological options like straw tubes or an existing Transition Radiation Detector will be used. However, given the realistic segmentation, gas detector response of those chambers will be similar as obtained in the present implementation.

2.3 Simulation procedure of MUCH

The simulation chain performed using the UrQMD event generator for input and the GEANT3 transport engine can be summarized by the block diagram given in Fig. 2.12. As discussed briefly below and detailed later, it consists of the following fundamental blocks: (a) geometry implementation and transport (b) segmentation and digitization (c) hit formation (d) track propagation in MUCH chambers and (e) selection of tracks as muon candidates. The final identification of muon tracks is part of the di-muon analysis.
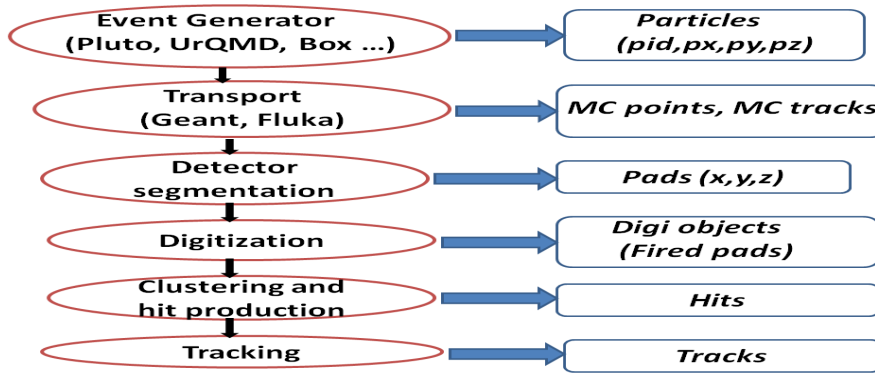
Figure 2.12: Schematic layout of the simulation chain in MUCH. The output from a particular step is used as input to the next step

- **Geometry implementation and transport:** MUCH aims to study the propagation of tracks inside the segmented absorbers. The study of geometry therefore involves the implementation of conical absorbers of varying sizes placed around the conical beam pipe. Conical absorbers are used to accept the forward focused particles. The detector modules are of trapezoidal profiles that are placed behind each absorber block. For effective tracking, each tracking station consists of 3 layers of tracking chambers. Each tracking layer consists of a thin support structure and an equal number of sector-shaped modules are placed on two faces of the support structure. For reducing the dead-space, modules on two faces are placed in such a way that a border of the module on one side has overlap with an active zone of the module on the opposite side. The number of stations, their shape, size and number of modules are varied for optimization of efficiency and signal to background ratio (S/B) for detecting low-mass vector mesons and charmonia.

- **Digitization:** GEANT3 provides the position of energy deposition inside the detector module. These locations along with the energy depositions taken together are called MUCH points. To account for realistic detector geometry, the readout planes of the modules are segmented in pads for obtaining final detectable response. The procedure of distributing the MUCH points to pads, known as digitization involves the detailed procedure of implementing the response of the gas detector to the energy deposition inside the chamber as described in detail later. The projective segmentation scheme has been implemented as per the optimization requirements of the modules. The pad dimensions are varied to reduce the pad occupancy and the multi-hit probability in a pad. In the *simple* digitization scheme, points falling inside a given pad area are added together to obtain a *digit*, and in the *advanced* digitization scheme, MUCH points are subjected to create primary ionization, multiplication and signal generation inside the gas volume. For the results presented here, *advanced* digitization scheme has been used.

- **Clustering and HitFinder:** Digits are grouped into *clusters* using a suitable clustering algorithm. Based on the particle multiplicity and associated cluster overlap, the clusters are either broken into several sub-clusters which have been treated as hits (advanced hit finder) or each cluster is treated as one hit (simple hit finder). The centroids of the sub-clusters in case of advanced hit finding or of the main cluster in case of simple hit finder is assigned to be the location of a MUCH-hits which are then taken as candidates for track propagation.

- **Track propagation:** Tracks reconstructed in STS are propagated using the Kalman Filter technique to pass through the MUCH layers. MUCH hits located around the propagation

point are taken as the candidates of the propagated track. For final analysis, χ^2 of track fitting, number of STS and MUCH layers associated to the propagated tracks are taken as track validation parameters.

2.3.1 Detector segmentation, digitization, clustering and hit formation

The muon tracking chambers will be under the conditions of high hit density and large event rates (10 MHz). The aim of the segmentation study is to get a realistic and optimized detector layout with respect to the physics measurements. In order to take into account the variation of hit density with the radial distance from the beam pipe (density falls approximately as $1/r$), the muon chamber readout planes are segmented in different annular regions with pads of appropriate shapes and sizes required to achieve the desired pad occupancy. Apart from the hit-occupancy, another constraint is the spatial resolution that limits the maximal pad size.
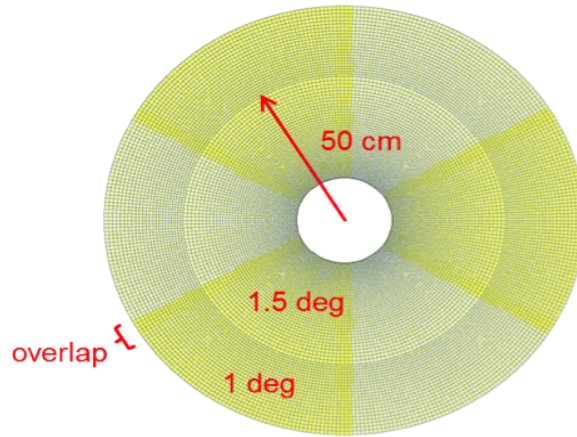
Figure 2.13: Schematic views of the segmentations of a layer, entire area has been divided into projective pads of 1 degree annular regions and with two rings of different annular dimensions

In case of sector geometry, projective pads of radially increasing size are implemented in segmentation as shown in Fig. 2.13. The dimensions of the pads are determined by the angular separation on transverse plane. The entire region could be divided into pads of uniform or varying angular regions as shown in the figure. For our present implementation, pads are based on $1°$ separation in azimuthal angle. We have performed a study in which segmentation-angle was varied from $0.3°$ to $1.2°$. Final reconstructed background spectra were studied at different segmentations. As shown in Fig. 2.14, the normalized background is optimum at $1°$ uniform segmentation without significant reduction in signal efficiency. Even though all results shown here are for $1°$ pads, the present segmentation scheme results in relatively large pad size in the outer periphery of layers. As a part of future optimization of the segmentation, if required, we have the option to divide the pads at larger radii into smaller than $1°$ intervals. Simulation of GEM detector response (digitization), which is schematically shown in Fig. 2.15 is based on a simple assumption that a GEM active gas volume can be split into the drift and avalanche regions. This means that the triple-GEM structure is ignored in the simulation at the moment. The digitization algorithm can be logically split into several steps:

- Determination of the number of primary electrons emitted in the drift volume for each Monte-Carlo point is based on the Landau distribution for an argon-based gas mixture, track length in the drift volume, particle type and energy. Primary electrons are generated
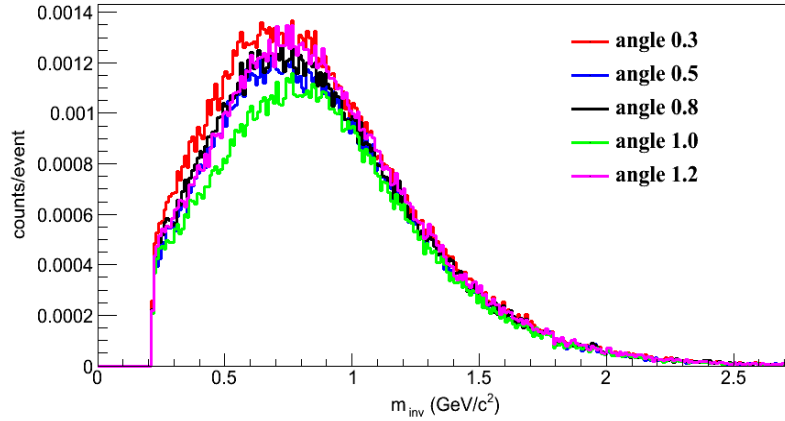
Figure 2.14:   Normalized background for different segmentation angles. We have chosen 1-degree uniform segmentation as our baseline option.
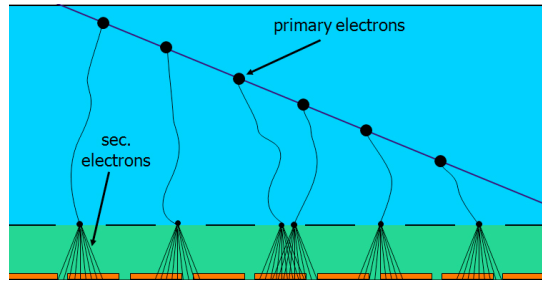

Figure 2.15:   Schematic representation of the signal generation process in GEM

randomly along the track. Parameters of the Landau distribution are determined with the HEED [5] package.

- Determination of the number of secondary electrons emitted in the avalanche region for each primary electron. Exponential gas gain distribution with a default mean gas gain of 10^4 is used in this step.

- Intersection of secondary electron spots with the pad structure of a module and determination of the charge arrived at each pad. The default spot radius is set to 0.6 mm as measured for the triple-GEM detectors during beam tests. Charge arrival time is calculated from the Monte-Carlo point time plus the primary electron drift time: t = d/v (d -distance travelled by the primary electron towards the avalanche region, v - drift velocity, v = 100 micro-m/ns by default).

- Time-dependent summation have been performed for charges from all Monte-Carlo points pad-by-pad and conversion of the charge-vs-time distribution has been done to get the timing response of the foreseen MUCH readout electronics. Timing response on a delta-function-like charge from secondary electrons is simulated by the linear peaking period of 20 ns and the falling edge described as an exponential decrease with 40 ns slope. Response to several delta-function-like charge signals is described as a convolution in time of responses from several delta-functions. Random noise of the readout electronics is also added at this step.

- Application of the threshold to the readout response and determination of the time stamp (a moment when the response exceeds the threshold value): The charge information is

converted into ADC channels with one of the three methods: amplitude with the flash discriminator, Wilkinson integration or time-over-threshold approach.

- The time stamp and the ADC information is decoded into 32-bit word and stored in the array of CbmMuchDigi objects together with the 32-bit channel Id for subsequent processing.

Fig. 2.16 illustrates the results from the digitization algorithm showing the reconstructed charge on pads corresponding to Monte-Carlo track projections. In addition to the visual control of the fired pad to MC track correspondence, the quality assurance algorithm has been developed. One of the quality criteria is the distribution of the full charge from the track as function of energy and particle type. An example of the charge vs. energy logarithm distributions is shown on Fig. 2.17. The obtained distributions agree well with the Bethe-Bloch dependence of the most-probable value of the input Landau shape corrected for the mean gas gain (see black line). Fig. 2.18 shows the distributions of deposited charges by the minimum ionizing particles. The charge deposition spectrum follows the Landau distribution as expected. The detector parameters are
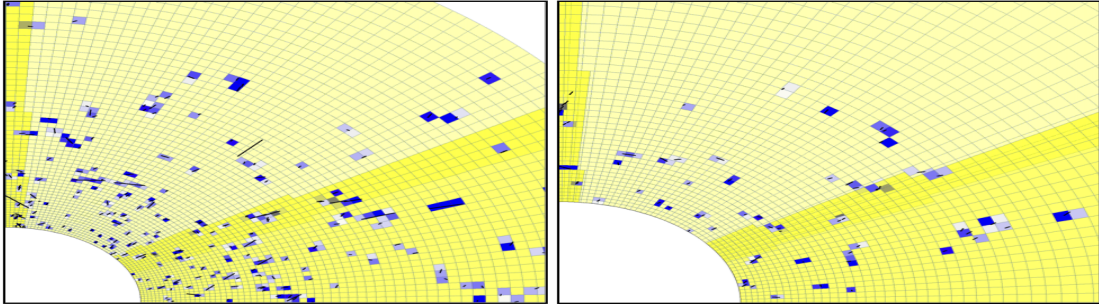
Figure 2.16: Illustration of digitization scheme for station 1 and 2
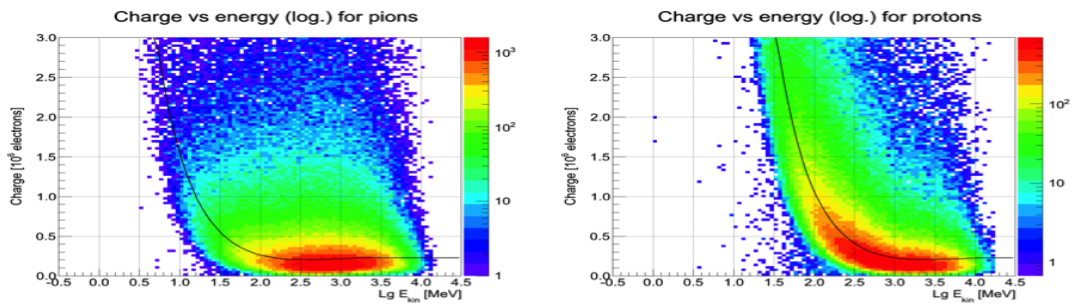
Figure 2.17: Deposited charge versus particle energy for pions and protons

tunable and could take values depending on the exact micro-pattern detector technology. The spot radius is chosen to represent the existing experimental data. The avalanche spot for each primary electron is projected to the pad plane and the sum of charges at each pad is calculated. Apart from the spot radius one can also tune the parameters like ADC resolution, the maximum charge that can be collected by a pad and the threshold charge. The maximum charge defines the dynamic range of the readout ASIC. If for a particular channel, the corresponding energy deposition goes beyond the specified dynamic range, the channel gets saturated. The threshold charge is set above the expected noise level. In the current study, we set following values to the above parameters: (i) Number of ADC Channels: 256 (ii) Q_{max} : 80 fc (iii) Q_{th} : 1 fc (iv) GEM spot radius: 600 micron.
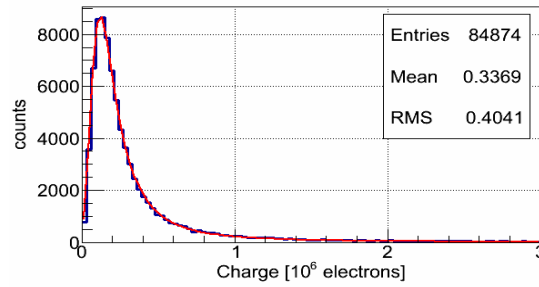
Figure 2.18:   Charge deposition by a minimum ionization particle (MIP) in the gas volume

The *digits* formed by the procedure discussed above are clubbed together to form clusters, which are then deconvoluted to form hits. The following algorithms have been implemented for the cluster deconvolution and hit finding:

- **one hit per pad:** A trivial algorithm when a hit is created for each fired pad. The hit positions correspond to pad centers, while the hit uncertainties are taken as pad dimensions divided by $\sqrt{12}$. Main advantages of this algorithm are the simplicity of implementation and low CPU-time consumption. The main disadvantage is that too many hits are created, many of them appear to be far away from real track positions. Many additional hits lead also to enhanced combinatorial background and inefficiency at the track finding level.

- **one hit per cluster:** One hit per cluster is created. Hit coordinates are determined by the center-of-gravity averaging with weights equal to charges induced on pads. This algorithm is also quite simple and fast. In the case of small pads, this algorithm allows to define track position more precisely than in the previous case. In the case of large clusters, this algorithm may cause too large difference between the reconstructed hit positions and real track coordinates (see Fig. 2.19, center, for example).

- **search for local maxima** A search for local maxima in the charge distribution is performed cluster-by-cluster. Hit coordinates are assigned to centers of pads, corresponding to local maxima. If cluster dimensions are less than 2 x 2 pads, *one hit per cluster* algorithm is used to determine hit coordinates for small clusters with better precision. The main advantage of the local-maxima method is that it works for large clusters, it allows to find several single track hits that contributed to one cluster (see Fig. 2.19, right for example). Nevertheless, in the case of long clusters (usually produced by single but very inclined low-energy electrons) local maxima may originate from random fluctuations of charge on pads. Therefore search for local maxima may lead to creation of fake hits, which do not correspond to real tracks. Moreover, one should keep in mind that some tracks still could remain unresolved by this algorithm.

The **search for local maxima** is used as a default algorithm in the MUCH simulations. The developed algorithms for the cluster and hit finding can be used not only for simulation purposes but also for the reconstruction of real data. Fig. 2.20 represents the results for the central region of the first MUCH layer in a central Au + Au collisions at 25AGeV where one expects highest occupancy. Fig. 2.20 illustrates that track positions are correctly reconstructed in majority of cases.
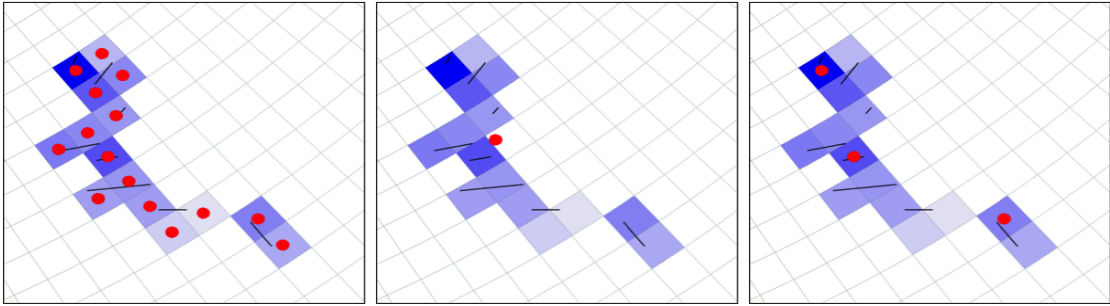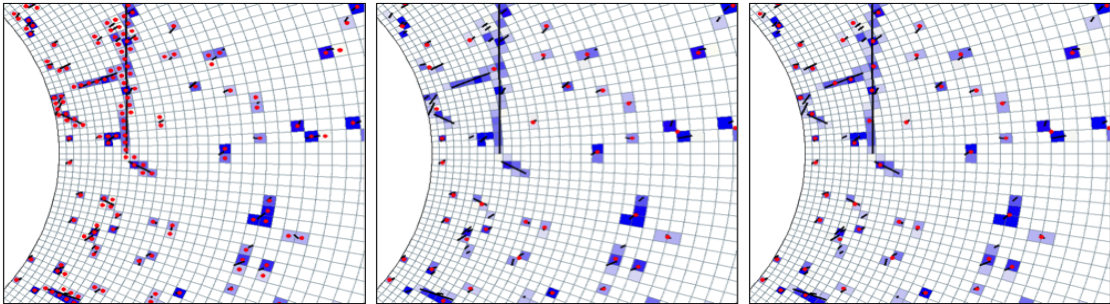
Figure 2.19: Illustration of three types of hit finder scheme

Figure 2.20: Illustration of hit-finding in a central Au+Au event at 25 AGeV collisions in case of central region of the first station: (left) *one hit per cluster*, (middle) *one hit per cluster* and (right) *search for local maxima*

2.3.2 MUCH Track Reconstruction

The main challenge of the track recognition in the CBM-MUCH detector results from the large multiplicity in heavy-ion collisions. About 1000 charged particles are produced in central Au + Au collisions at top CBM energies. This high charged particles multiplicity leads to a high track and hit density in the MUCH detector, especially on the first detector planes (see Fig. 2.21).

The developed track reconstruction algorithm in MUCH is based on track following using reconstructed tracks in the STS as seeds. The STS track reconstruction is based on the cellular automaton method [6] and STS track parameters are used as starting point for the subsequent track prolongation. This track following is based on the standard Kalman filter technique [7] and is used for the estimation of track parameters [8] and trajectory recognition. Main logical components are track propagation, track finding, track fitting and finally selection of good tracks. Each of the steps will be described in the following in some more detail.

2.3.2.1 Track propagation

The track propagation algorithm estimates the trajectory and its errors in a covariance matrix while taking into account three physics processes that influence the trajectory, i.e. energy loss, multiple scattering and the influence of the magnetic field. The influence of the material on the track momentum is taken into account by calculating the expected average energy loss due to ionization (Bethe-Bloch formula) and bremsstrahlung (Bethe-Heitler formula) [9]. Adding process noise in the track propagation includes the influence on the error, i.e. the covariance matrix due to multiple scattering. Here, a Gaussian approximation using the Highland formula [9] is used
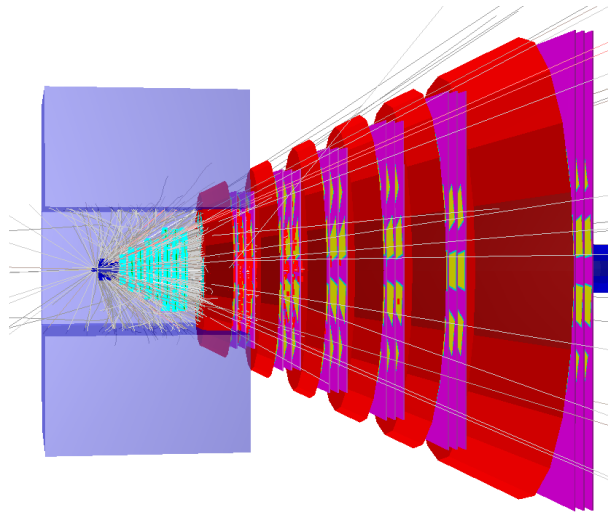
Figure 2.21: Visualization of one simulated central Au - Au collision at 25 AGeV.

to estimate the average scattering angle. The propagation of the trajectory is done according to the equation of motion. If the track passes a magnetic field, the equation of motion for a charged particle is solved applying the 4th order Runge-Kutta method [10]. For passing a field free region, a straight line is used for propagation and the transport matrix calculation. The transport matrix is calculated by integrating the derivatives along the so-called zero trajectory [11]. A detailed description of the developed track propagation can be found in [12].

2.3.2.2   Track finding and fitting

In the track finding algorithm hits are attached to the propagated track at each detector station using two different methods. Either just the nearest hit is attached to the track, or all hits within a certain environment are included. For the first method, only one track is further propagated, the branching method allows several track branches to be followed, one for each attached hit. Common techniques to these methods are the above described track following, the Kalman Filter and the calculation of the validation region for hits.

Assignment of new hits is done step by step at each detector station. After the track propagation to the next station, possible hits are attached and track parameters are updated by the Kalman Filter. For the attachment of hits a validation gate is calculated to allow a high degree of confidence in the hit-to-track assignment. The validation gate is defined based on the residual vector r (distance between the fitted track and the hit) and the residual covariance matrix R. In the context of Kalman-based tracking filters, a validation gate can be expressed as $v = rR^{-1}r^T < d$. The cut value d is chosen such that a defined probability of rejecting the correct hit is achieved. Here this probability is chosen to be 0.001. Values for d can be taken from χ^2 tables as a function of the on the number of effective degrees of freedom. Here the effective degree of freedom is 1 for a straw tube detector hits and 2 for pixel hits from pads in a GEM detector. The algorithm takes into account provision of missing hits due to detector inefficiencies, dead zones in the detector, inefficiency of hit finder algorithm among others.

Two methods which can be chosen for hit assignment to tracks differ in the way how a situation is dealt with in which several hits lie within the validation gate. In case of the branching method,

a new track branch is created for each hit lying within the validation gate. Since the number of branches can grow exponentially, the χ^2 value is calculated for each track branch and unlikely ones are rejected. Also for each input track seeds, number of created branches is calculated and if it exceeds the limit then the tracking continues using nearest neighbor approach. For the second method no track branches are created. The nearest neighbor method attaches the hit with the smallest v, if lying in the validation region at all.

2.3.2.3 MUCH Reconstruction Performance

After track finding, the so called clone tracks (consisting of a very similar set of hits) and ghost tracks (consisting of a random set of hits) have to be rejected while keeping correctly found tracks with high efficiency. The selection algorithm works in two steps. First, tracks are sorted by their quality which is defined by the track length and χ^2. Then, starting from the highest quality tracks all hits belonging to a track are checked. In particular, the number of hits shared with other tracks is calculated and the track is rejected if more than 15% of the hits are shared. The results presented here are based on studies performed with standard simulations for central Au + Au collisions at 25 AGeV beam energy. Events were generated with the UrQMD event generator [2]. In order to enhance statistics and investigate the MUCH response to primary muons, the J/ψ particles decaying into $\mu+$ $\mu-$ pair were embedded into each UrQMD event. The SIS300 detector setup has been used for simulations.

The performance of the algorithms was obtained by using information from the Monte Carlo input. During the efficiency calculation, the level of correspondence between the found and simulated tracks is estimated. A track is defined as correctly found if it has more than 70% of hits from one Monte-Carlo track, otherwise a track is defined as ghost track. The track reconstruction efficiency is defined as $Efficiency = N_{reconstructed}/N_{accepted}$. $N_{reconstructed}$ is the number of correctly found tracks after reconstruction, $N_{accepted}$ is the number of reconstructable tracks in the MUCH acceptance, i.e. tracks that have at least 6 detected hits in the MUCH. Results shown here are for muon tracks since these are the most important for the muon simulations.

Fig. 2.22 shows the track reconstruction efficiency as a function of the momentum for MUCH (taking only the segment in MUCH for selecting the tracks) and global tracking efficiency for STS-MUCH (where the tracks are selected based on criteria on both the STS and MUCH segments) for 25 AGeV beam energy. The MUCH track reconstruction efficiency integrated over the momentum range 0-10 GeV/c is 95.9% for nearest neighbor method and 95.8% for branching method. The mean efficiency for tracking in STS-MUCH is 95.1% for nearest neighbor and 94.9% for branching method. Both methods show the same efficiency but the nearest neighbor approach has some advantages: it is easier to implement and it is faster. This method was used by default in event reconstruction.

2.3.3 Muon identification and analysis

From the global reconstructed tracks, we apply a set of cuts at the analysis level to identify muons. The aim is to reduce background due to non-muonic tracks and muons from weak decays of pions and kaons. The cuts which have been used on reconstructed tracks for selection of muon candidates are (a) from STS: number of hits in STS and χ^2 of the STS segment of the track and (b) from MUCH segment of the track: number of much layers, χ^2 of the MUCH segment of the track. Additionally, a cut on χ^2_{vertex} is also applied. In Fig 2.23 the distributions of these
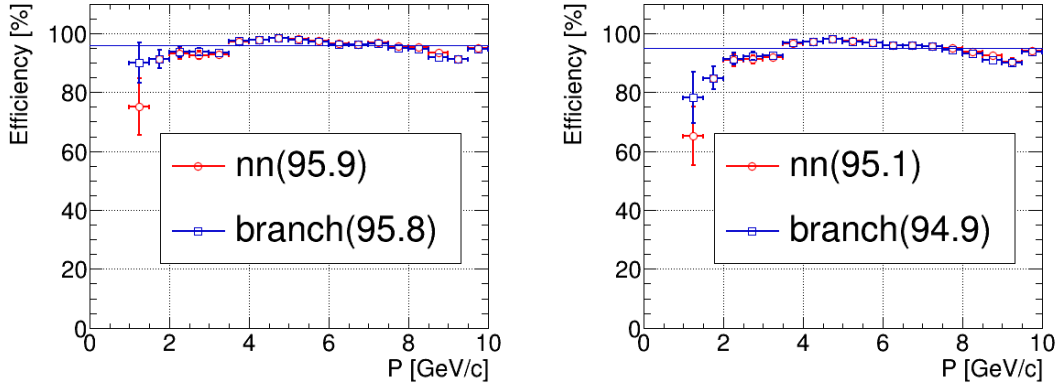
Figure 2.22: Track reconstruction efficiency for primary muon tracks from J/ψ as a function of momentum for two tracking algorithms: nearest neighbor (red) and branching (blue). Left plot shows MUCH tracking efficiency, right plot shows STS-MUCH tracking efficiency. Horizontal lines represent numbers integrated over momentum.

parameters for signal (ω) and background are shown as simulated for Pluto and UrQMD events respectively at 25 AGeV collisions. The left-panel of Fig 2.23 illustrates the distribution of the number of STS layers, and in the right panel the distributions of the "number of MUCH layers" are shown for signal and background. Based on the separation power of these cuts between signal and background, we obtain a set of final cuts that have been used in this analysis for selection of muon candidates. It should be noted that for selection of muons from low-mass vector mesons and charmonia, the numbers of MUCH hits in a track are taken to be different. For example, while for low-mass vector mesons the number of much layers can be up to 15, however, for charmonium it should have more than 15 MUCH hits in order to ensure that the corresponding track has traversed the thick absorber.
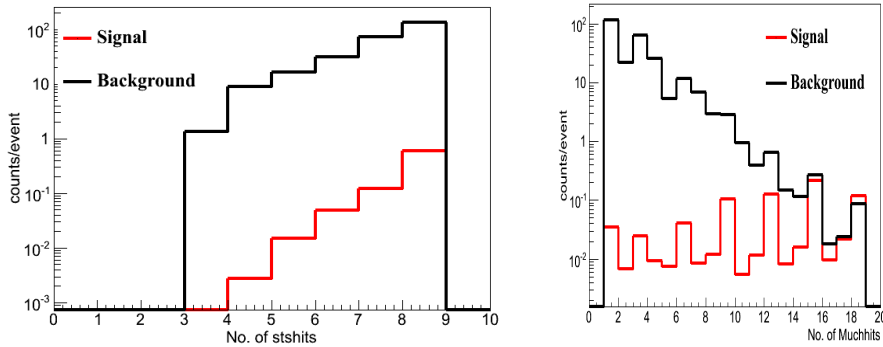
Figure 2.23: Distributions of various parameter extracted for signal (ω) and background (central Au+Au collisions at 25 AGeV) . Left panel: number of STS hits (layers), right panel: number of MUCH hits (layers).

2.3.3.1 Optimization of cuts

We have performed various tests using the MC data to evaluate the performance of MUCH. One of the first tests performed was to test the survival of different types of primary and secondary

particles with the variation of cut values. As there is no muon from UrQMD output, decay muons are present only in the secondary samples. It is seen that, for a fixed reasonable cut on MUCH hits, the use of cuts using 6 STS hits and χ^2 less than 2.0 remove most of the pions and other particles without removing muons significantly. In the top panel of Fig. 2.24 the reconstructed di-muon invariant mass spectra of UrQMD background events (25 AGeV Au+Au collisions) are shown for different cuts on number of STS stations and on χ^2. The cuts of 6 STS hits and χ^2 less than 2.0 reduce the background considerably. The use of stricter cuts (like 7 sts hits and $\chi^2 <$ 1) reduces both background and signal, and does not help to improve the signal to background ratio. The bottom panel of Fig. 2.24 illustrates the effect of requiring different number of MUCH hits to reduce the background, while keeping the cuts on STS same. It should be mentioned that, for the following discussions, final efficiency results are obtained after the use of final cuts that is aimed at reducing the background in addition to increase of efficiency. The efficiency results obtained in subsequent discussions should be viewed in that context when compared with the results shown in previous section while describing tracking efficiency.
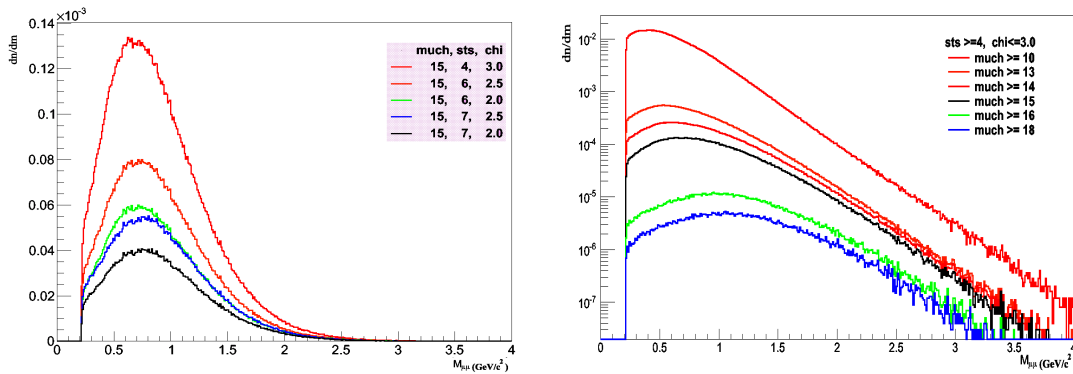
Figure 2.24: Di-muon invariant mass background distributions reconstructed for central Au+Au collisions at 25 AGeV. Left panel: Background after varying number of STS hits and χ^2 values while keeping the cut of MUCH hits constant. Right panel: background for different numbers of MUCH stations keeping cuts on STS constant.

2.4 Physics performance studies

2.4.1 Input

Simulations for the optimization of the detector design in the di-muon measurement setup have been performed within the *cbmroot* framework that allows full event simulation and reconstruction. Apart from cbmroot, the event generators PLUTO [13] and UrQMD3.3 [2] have been used for generating signals and background events, respectively. PLUTO generates the phase space distributions and the decay of the vector mesons taking multiplicities from the transport model Hadron String Dynamics (HSD) [14]. HSD has been found to match the data at AGS and SPS energies quite well. The parameters of the PLUTO signal generator are tuned to correspond to the FAIR energy regime. It should be mentioned that the self-triggered readout system in which CBM will take data requires data processing in 4-dimension (x,y,z and time). The generation of events from this 4D data is a procedure that will be discussed in a document describing detailed data collection and analysis procedure. In this chapter, the results have been shown using the conventional event based simulation. For simulating the performance in CBM we have taken

two types of inputs: dimuon decays from low-mass vector mesons and from charmonium. In the low mass region we considered channels like $\omega \rightarrow \pi^0 \mu^+ \mu^-$, $\omega \rightarrow \mu^+ \mu^-$, $\eta \rightarrow \mu^+ \mu^-$, $\eta \rightarrow \gamma \mu^+ \mu^-$, $\rho^0 \rightarrow \mu^+ \mu^-$, $\phi \rightarrow \mu^+ \mu^-$. In Fig. 2.25 the invariant mass distribution of the cocktail is shown which was taken as input for the simulation of 25 AGeV central Au+Au collisions.
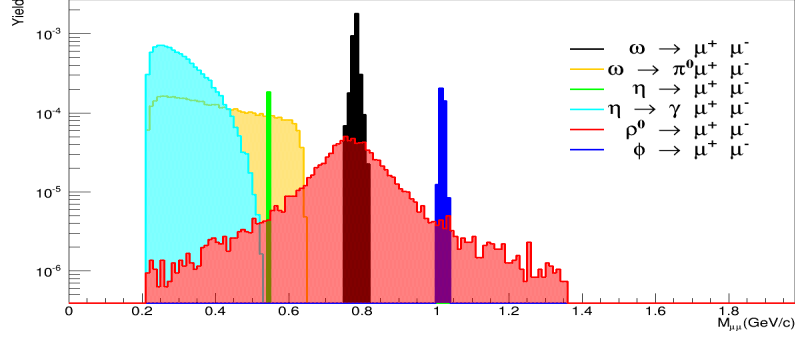
Figure 2.25: Cocktail of different dimuon sources at the low mass region of the invariant mass spectra as used in the simulation of central Au + Au collisions at 25 AGeV.

The cocktail does not contain any spectral modifications of low-mass vector mesons, only Breit-Wigner shape of the resonances was assumed. In the simulation, different multiplicities and branching ratios have been taken into account. Fig. 2.26 depicts the y-p_T acceptance of ρ^0 at 25 AGeV and 8 AGeV beam energies, respectively. In Fig. 2.27 the y-p_T acceptance for J/ψ at
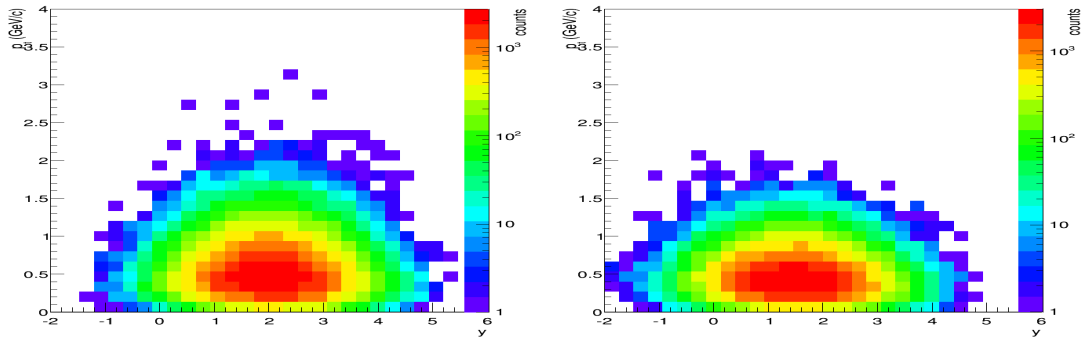
Figure 2.26: 4π phase-space distribution of ρ mesons in the plane of transverse momentum versus rapidity calculated for central Au+Au collisions at 25 AGeV (left) and 8 AGeV (right) by the PLUTO event generator

25 AGeV and 10 AGeV input energies are shown. In Fig. 2.28 the momentum distributions of the decay muons from ρ mesons (left) and J/ψ mesons (right) as simulated in central Au+Au collisions at 25 AGeV are shown. It can be seen that muons from ρ^0 meson decays exhibit a much softer momentum spectrum than those from J/ψ decays. The momentum distribution is decisive for the efficiency of the muon detection behind the hadron absorber.
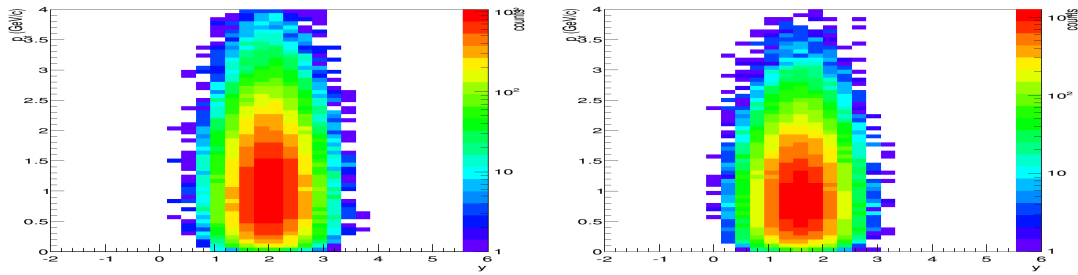
Figure 2.27: 4π phase-space distribution of J/ψ mesons in the plane of transverse momentum versus rapidity calculated for central Au+Au collisions at 25 AGeV (left) and 10 AGeV (right) by the PLUTO event generator
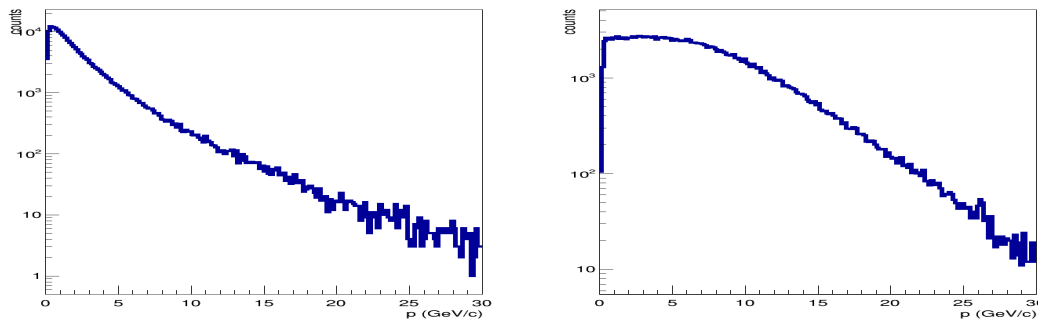
Figure 2.28: Momentum distributions of muons from ρ^0 (left) and J/Ψ (right) at 25 AGeV central Au+Au collisions

2.4.2 Results of performance simulation in SIS-100 and SIS-300 configurations

In the study of the physics performance based on the inputs discussed earlier in both LMVM and charmonia sectors, we have used GEM as the detector technology in all layers. Even though only first two chambers will be made of GEM, however, it turned out that with proper optimization of cut parameters, we can obtain results similar to a configuration with GEMs only.

For background estimation, we have calculated the invariant mass spectra from the reconstructed muons using the UrQMD event generator. In order to increase the statistics in the background calculation we have applied the superevent technique, where reconstructed tracks from the central UrQMD events where mixed, and then used to calculate the combinatorial background. In this way we enhanced quadratically the number of reconstructed background pairs. The signal efficiency was determined by reconstructing signal particles (e.g. ρ^0, J/ψ) which were embedded into the UrQMD events. For the determination of the signal-to-background (S/B) ratio, the signal multiplicity and branching ratio where taken into account together with the proper normalization of the background.

2.4.2.1 Results for SIS-100 collisions

We have performed a simulation of low-mass vector mesons for central Au + Au collisions at 4 AGeV using the SIS100-A setup which is shown in Fig. 2.7. It comprises 3 absorbers, 9 detector

layers, and the TOF detector. The resulting invariant mass spectrum and the S/B ratio for central Au + Au collisions at 4 AGeV is shown in the left and the right panel of Fig. 2.29, respectively. In Fig. 2.30 the corresponding phase-space distribution for reconstructed ρ^0 mesons is shown.
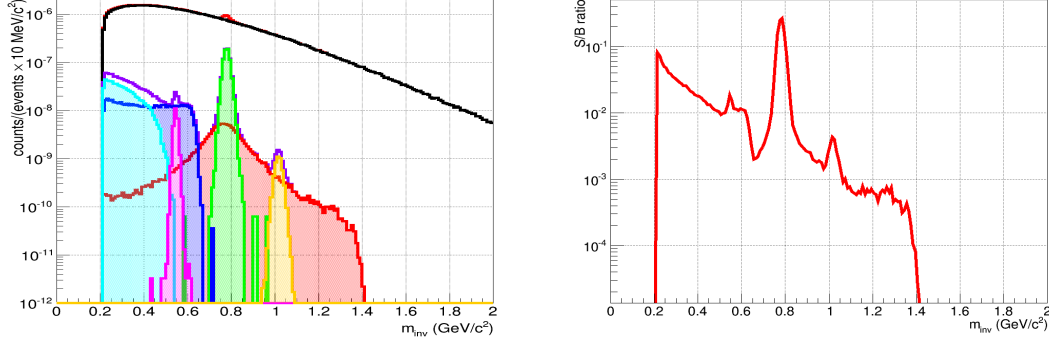
Figure 2.29: Invariant mass distribution of reconstructed muon pairs from decaying low-mass vector mesons together with the combinatorial background (black histogram) simulated for central Au + Au collisions at 4 AGeV using the SIS100-A setup (left panel). The signal spectrum contains ϕ (yellow), ρ (magenta), omega (green), η (red), ω-Dalitz (dark blue) and η-Dalitz (light blue). The corresponding signal/background ratio is shown in the right panel.
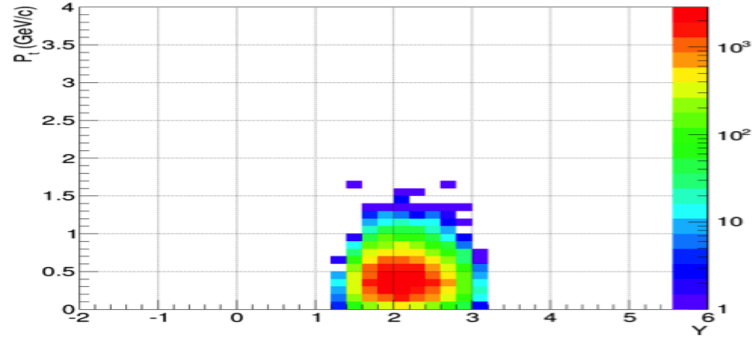
Figure 2.30: Phase-space distribution for reconstructed ρ-mesons as a function of the transverse momentum and rapidity simulated for central Au+Au collisions at 4 AGeV. Midrapidity is around $Y = 1.2$

For the measurement of low-mass vector mesons at Au + Au collisions at 8-14 AGeV, we use the SIS100-B setup with 4 MUCH stations and 4 absorber layers. In addition the TOF wall is used for background rejection. Fig 2.31 (left) depicts the low-mass dimuon invariant mass spectrum simulated for central Au+Au collisions at 8 AGeV. The corresponding signal to background ratio is shown in Fig. 2.31 (right). This ratio is very similar to the one for central Au+Au collisions at 25 AGeV with full MUCH configuration as shown in later section. In Fig. 2.32 the y-p_T acceptance of the reconstructed ρ^0 mesons is shown demonstrating that the forward rapidity region is covered (midrapidity is around y=1.4).

Figure 2.33 (left) depicts the invariant mass distributions for J/ψ mesons in the SIS100-C configuration for p+Au collisions at 30 GeV beam energy. The J/ψ reconstruction efficiency was found to be 30%. Even after processing of 5 million UrQMD events without embedded signal, the background below the J/ψ peak region has been found to be extremely small. Therefore, the
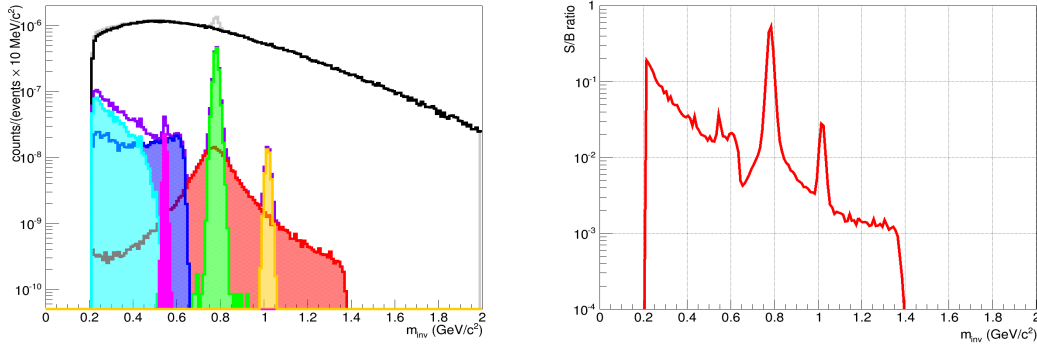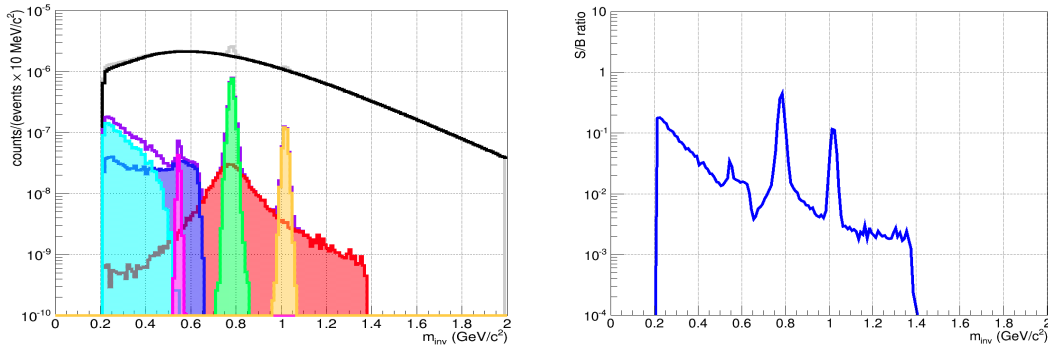
Figure 2.31: Invariant mass distribution of the reconstructed muon pairs from decaying low-mass vector mesons together with the combinatorial background (black histogram) simulated for central Au + Au collisions at 8 AGeV using the SIS100-B setup (left panel). The corresponding signal/background ratio is shown in the right panel.
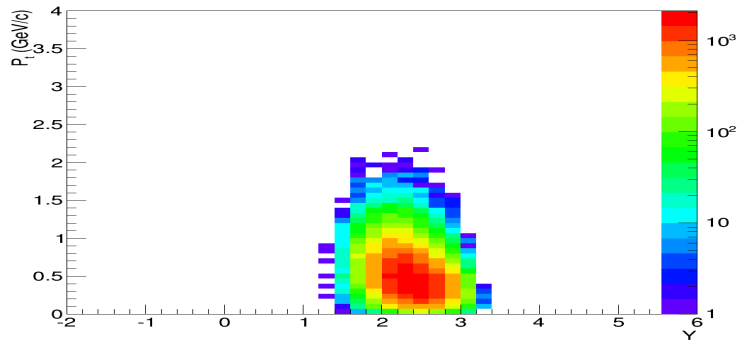
Figure 2.32: Phase-space distribution for reconstructed ρ-mesons as function of transverse momentum and rapidity simulated for central Au+Au collisions at 8 AGeV. Midrapidity is around $Y = 1.5$.

shape of the background shown in Fig. 2.33(left) has been estimated from a superevent analysis and then fitted with an exponential function to a few background events obtained with an event-by-event analysis. In spite of the uncertainties in the estimation of background, the identification of J/ψ mesons in proton-nucleus collisions at top SIS100 energy seems to be easily feasible. It remains to be demonstrated how far one can go down in energy before losing the signal.

For the simulation of J/ψ measurements in Au + Au collisions at SIS100 beam energies the same MUCH configuration has been used as for p+Au collisions (Fig. 2.9). In Fig 2.33 (right) the dimuon invariant mass distribution around 3 GeV/c^2 is shown as simulated for Au+Au collisions at 10 AGeV energy. Please note that the threshold energy for J/ψ production in elementary (nucleon-nucleon) collisions is about 12 GeV. The J/ψ multiplicity has been taken from HSD calculations. Although the J/ψ peak is not very prominent above the background, the yield can be determined accurately with a proper measurement of the background. The systematic error on the signal due to background subtraction is $\Delta S/S = \Delta B/B$ x B/S with B/S being the background-to-signal ratio. The background can be measured to an accuracy of about $\Delta B/B = 0.002$. From Fig 2.33 (right), we extract a value of $B/S=17$, resulting in an error on the signal of $\Delta S/S=0.034$. The overall J/ψ reconstruction efficiency is 0.6%. Fig 2.34 shows the acceptance plots for the input (PLUTO) and reconstructed J/ψ at 10 AGeV Au+Au collisions.
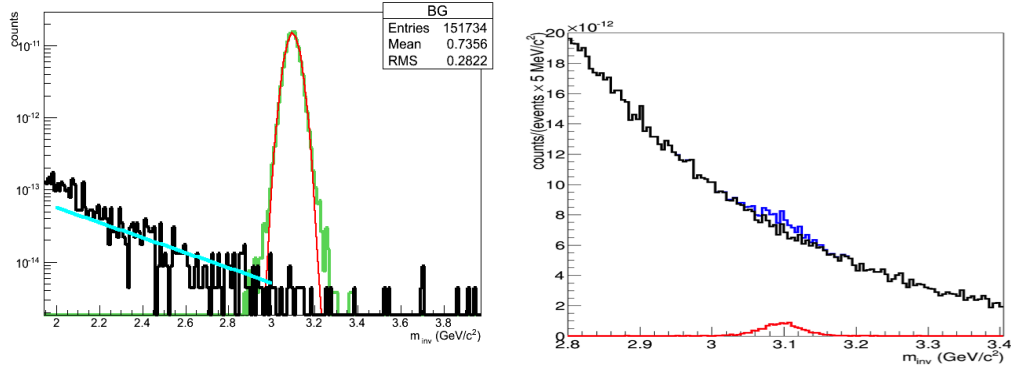
Figure 2.33:   Di-muon invariant mass spectra around 3 GeV/c^2 as simulated for 30 GeV p + Au collisions superposed on a scaled background (left, see text). Dimuon invariant mass spectra around 3 GeV/c^2 as simulated for central Au + Au collisions at 10 AGeV (right).
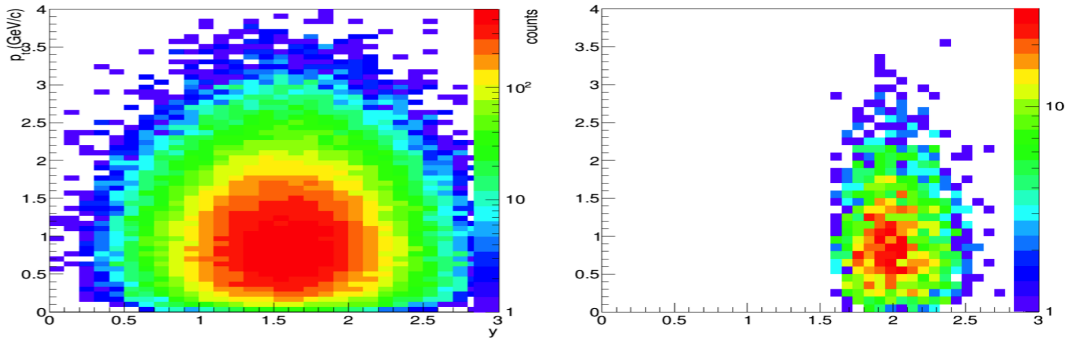
Figure 2.34:   Phase-space distributions for J/ψ-mesons as function of transverse momentum and rapidity simulated for central Au+Au collisions at 8 AGeV with the PLUTO event generator before (left) and after reconstruction (right).

2.4.2.2   Results for SIS-300 collisions

For the simulations of the low-mass vector mesons and charmonium at SIS300 energies we use the MUCH configurations SIS300-A and SIS300-B, respectively. In Fig. 2.35 (left), the invariant mass distribution of the reconstructed muon pairs from the low-mass vector mesons is shown together with the combinatorial background. Fig. 2.35 (right) depicts the signal-to-background ratio S/B as extracted from Fig. 2.35 (left). This value is of crucial importance for the accuracy of the signal extraction. The systematic error on the signal due to background subtraction is $\Delta S/S = \Delta B/B$ x B/S with B/S being the background-to-signal ratio. The background can be measured to an accuracy of about $\Delta B/B = 0.002$. Therefore, in order to obtain an error on the signal of at least $\Delta S/S = 0.1$ one needs values of B/S=50 or smaller. This is clearly fulfilled for the resonances ω and ϕ, and also for invariant masses below 0.6 GeV/c^2. The overall efficiencies (including overall geometrical detector acceptance) are 0.6% for the ω, 0.2% for the ω Dalitz decay, 1% for the ϕ, 0.6% for the ρ, 0.4% for the η, and 0.2% for the η Dalitz decay.

The composition of the reconstructed background tracks per event for low-mass vector mesons from central Au+Au collisions at 25 AGeV is shown in Fig. 2.36. The dominant contributions are muons from weak decays of pions and kaons. At higher momenta, the yield of punch-through kaons is also significant. The overall multiplicity of reconstructed tracks is about one in 10

Figure 2.35: (left) Invariant mass distributions of reconstructed muon pairs from decaying low-mass vector mesons together with the combinatorial background simulated for central Au+Au collisions at 25 AGeV. and (right) signal to background ratio of the low mass dimuon invariant mass spectra for central Au+Au collisions at 25 AGeV.

collisions. This number would be reduced further in minimum bias collisions by about a factor of 4. The resulting background pair multiplicity would then be $0.025^2 \approx 0.0006$ which would allow for a trigger on low-mass vector mesons. Figure 2.37 shows the y-p_T acceptance of the
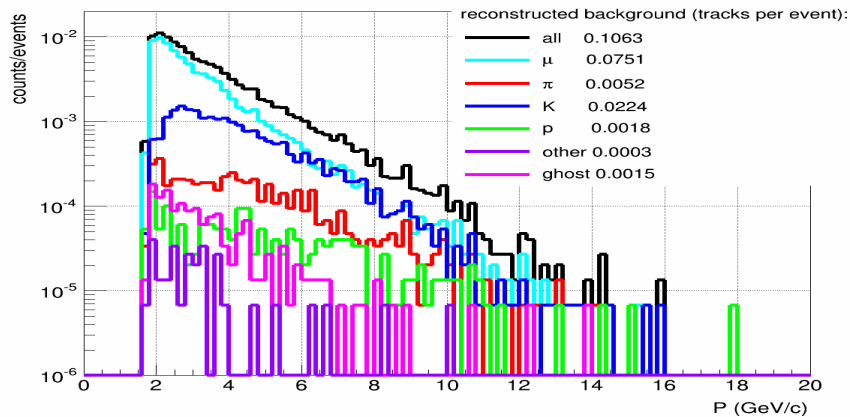
Figure 2.36: Composition of the reconstructed background tracks per event for low-mass vector mesons from central Au+Au collisions at 25 AGeV.

reconstructed ρ mesons. It is observed that only the region from mid-rapidity towards forward rapidity is covered by the detected particles as an effect of the absorber. Nevertheless, the rapidity coverage is sufficient to reconstruct almost the full phase space.

The measurement of J/ψ mesons is favored by the absorber technique as the decay muons from charmonium exhibit harder momentum spectra as compared to those from ρ^0 or ω mesons, and, hence, are much less absorbed. The left panel of Fig 2.38 depicts the invariant mass spectra after the application of J/ψ related cuts and superposed on the background for central Au+Au collisions at 25 AGeV. The J/ψ peak is clearly visible. The corresponding acceptance plot is shown the right panel of Fig 2.38 illustrating that the majority of the phase-space is covered. The composition of the reconstructed background tracks per event for J/ψ mesons from central Au+Au collisions at 25 AGeV is shown in Fig. 2.39. The background is completely dominated by muons from weak decays of pions and kaons. The overall multiplicity of reconstructed tracks is about 0.02 per event. This number would be reduced further in minimum bias collisions by
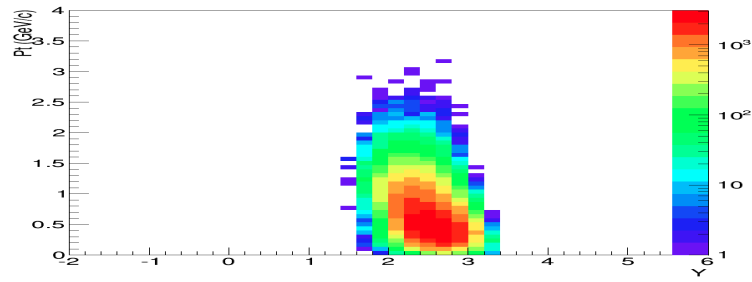
Figure 2.37: y-p_T acceptance of ρ^0 mesons for central Au+Au collisions at 25 AGeV.
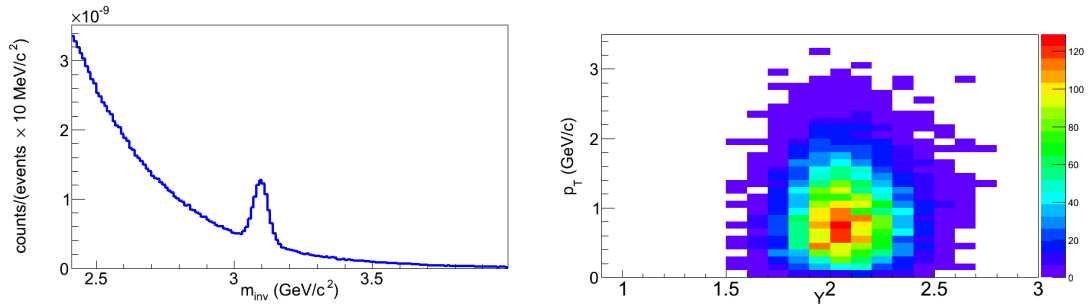
Figure 2.38: Simulation of J/ψ identification in 25 AGeV central Au+Au collisions. Left: Reconstructed invariant dimuon mass distribution around 3 GeV/c^2. Right: Acceptance for J/ψ mesons as function of transverse momentum and rapidity.

about a factor of 4. The resulting background pair multiplicity would then be $0.005^2 \approx 2.5 \times 10^{-5}$ which makes it possible to run at reaction rates of 10 MHz using a trigger on 2 tracks in the last detector station.
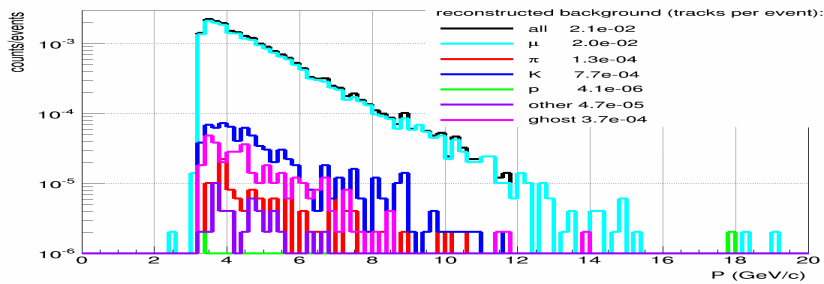
Figure 2.39: Composition of the reconstructed background tracks per event for J/ψ mesons from central Au+Au collisions at 25 AGeV.

2.5   Data rate on chambers

The CBM experiment is designed to measure rare diagnostic probes of the fireball, and hence, will be operated at reaction rates up to 10MHz. This poses challenges with respect to the rate capability and radiation hardness on the muon chambers. We have studied two parameters related to the rate capability in detail i.e., particle density and detector occupancy. The density of the Monte Carlo (MC) points on the much detectors i.e. the number of MUCH points per unit area per event on the chamber planes gives an estimate of the rate of incident particles on the chamber planes. The particle density is maximum at the first station and reduces for the chambers downstream. In Fig. 2.6 we have plotted the radial distribution of MUCH points in the first station (represented by plots for 60cm carbon). As input we have used 1k central Au + Au collisions at 25 AGeV. For minimum bias collisions, the numbers will be roughly around 25 % of the central values.

As expected, the density is maximum near the beam pipe and falls off as we go to the edges. For 1 cm^2 pads, the peak data rate for 10MHz collision rate will be approximately 10 MHz (beam rate) x 0.07 x 0.25 = 0.2MHz on the first station. After digitization, the ionization process (primary and avalanche) adds to the profile of much points and thereby increases the data volume accordingly. The data rate shown for 1 cm^2 pad reduces according to the pad size. The occupancy, i.e. the fraction of total number of pads fired per event gives an estimate of the data rate. In Fig. 2.40, we have shown the radial distributions of occupancy for the trapezoidal modules, at the first two stations of the SIS300 geometry, for 25 AGeV central Au+Au collisions. It should however be mentioned that for the self-triggered system, more useful quantity from the data rate requirement will be the occupancy by minimum bias events, which is roughly 2% at a region of the first station near the beam pipe. These quantities have been used extensively in designing the layout of the readout boards in the detector plane as discussed in chapter 4.
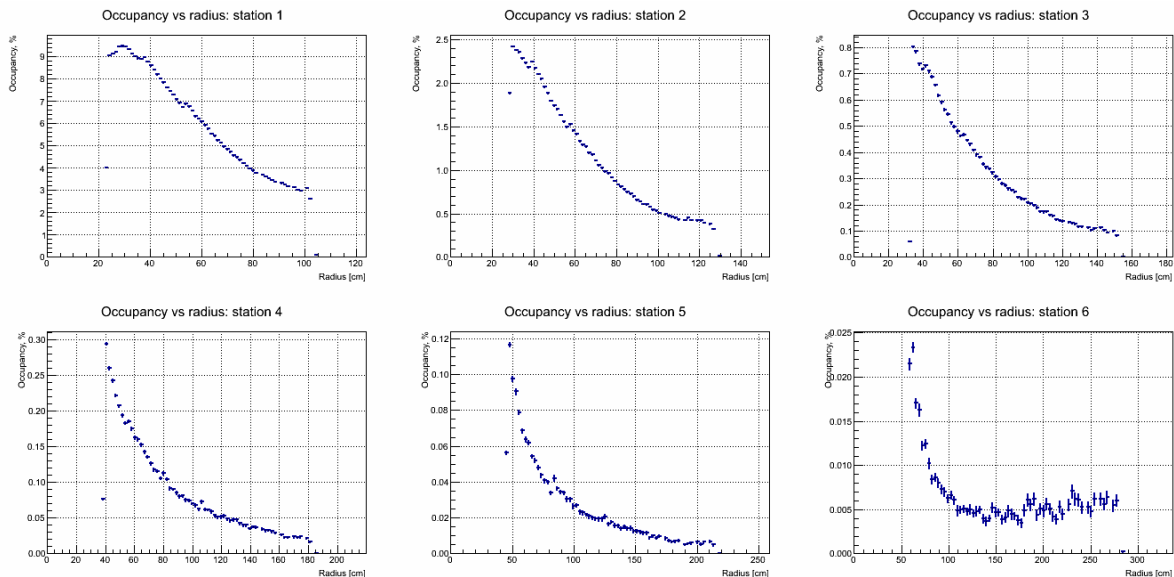
Figure 2.40: Radial distribution of occupancy for six stations of SIS300 MUCH geometry with trapezoidal modules. The plot is generated for central Au + Au collisions at 25 AGeV beam energy

The number of pads fired in the first station is maximum due to the highest particle density. Ideally for a projective segmentation, if the pad area is projected according to the hit rate, then

the occupancy should remain constant over the entire radial distance. In our case, we have taken pads corresponding to 1 degree in azimuth. This resulting occupancy is shown in Fig. 2.40. The falling trend is the result of faster than 1/r dependencies of the partice density. However, for beam energy of 25 AGeV the maximum occupancy at the first station is 8% and falling rapidly. The segmentation therefore results in close to the desired value of 5% occupancy. In case of trapezoidal modules, where radially increasing pads of angular width 1 degree in azimuth is used, the maximum occupancy for minimum bias collisions is observed in the first station gives a data rate of 0.2 MHz.

2.6   Comparison with FLUKA

In simulations using the cbmroot framework we have used the GEANT3 code for particle transport. As our study involves mostly hadronic interaction inside the absorber, we have done additional simulations using the FLUKA transport code.

The FLUKA code also provides estimates of the total dose of different particle species, i.e., hadrons, neutrons, non-ionising-particles among others at the locations of different MUCH stations. Each of these species has different effect on the chamber and electronics and need to be dealt with separately. In Chapter-3, we discuss in detail the test of the prototype chambers in the environments of some of these species. We show in Fig. 2.41 to Fig. 2.44 the calculated doses and intensities of different types of radiations for station-1 for a running period of 2 months. Simulations have been performed at two different beam energies i.e. 35 AGeV (left plots) and 10 AGeV (right plots). For station-1, the average maximum dose is about 500 Grey in 2 months, but FLUKA shows a hot region with an order of magnitude increase in dose due to highly energetic delta-electrons produced from the target. This observation from FLUKA about enhanced δ-electrons might require a revisit. This hot region is not seen for the more downstream stations. The corresponding dose reduces drastically when going from 1st to 5th station as shown in Fig. 2.45 to Fig. 2.47. The dose to be expected at SIS100 collisions is about a factor of 2 to 3 smaller as compared to 35 AGeV Au + Au collisions.
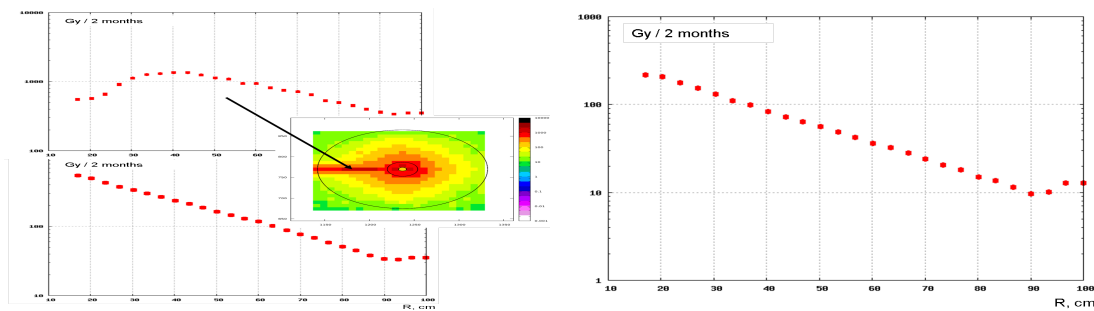
Figure 2.41: Radial distribution of total dose in the 1st station of MUCH for minimum bias Au + Au collisions at 35 AGeV (left) and 10 AGeV (right).
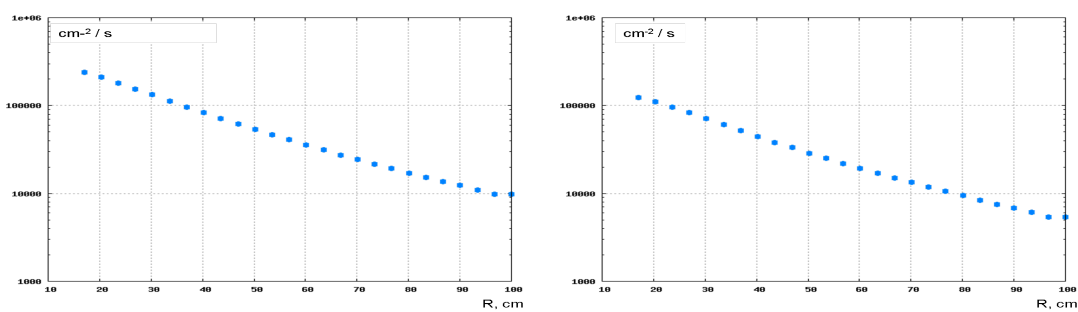
Figure 2.42: Radial distribution of hadrons incident on the 1st station of MUCH for minimum bias Au + Au collisions at 35 AGeV (left) and 10 AGeV (right).
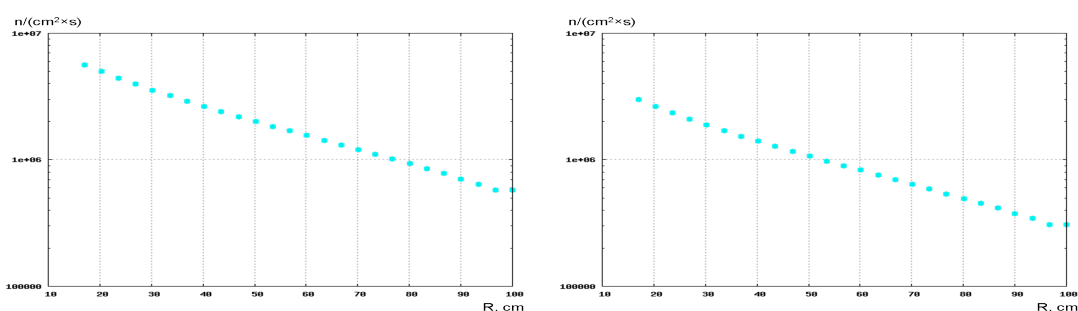
Figure 2.43: Radial distribution of neutrons incident on the 1st station of MUCH for minimum bias Au + Au collisions at 35 AGeV (left) and 10 AGeV (right).
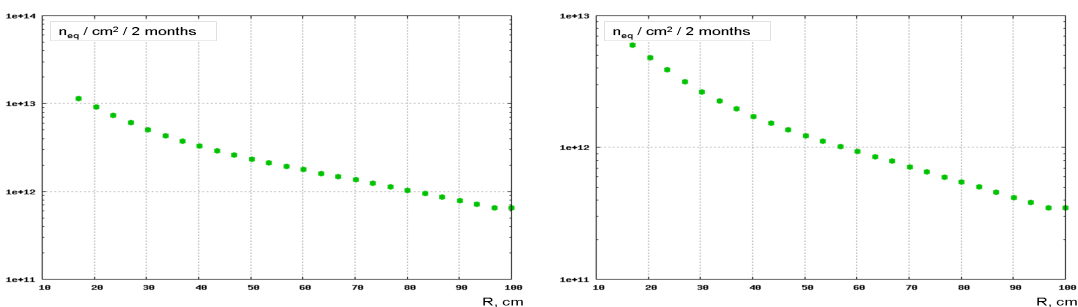
Figure 2.44: Radial distribution of NIEL on the 1st MUCH station for minimum bias Au + Au collisions at 35 AGeV (left) and 10 AGeV (right).
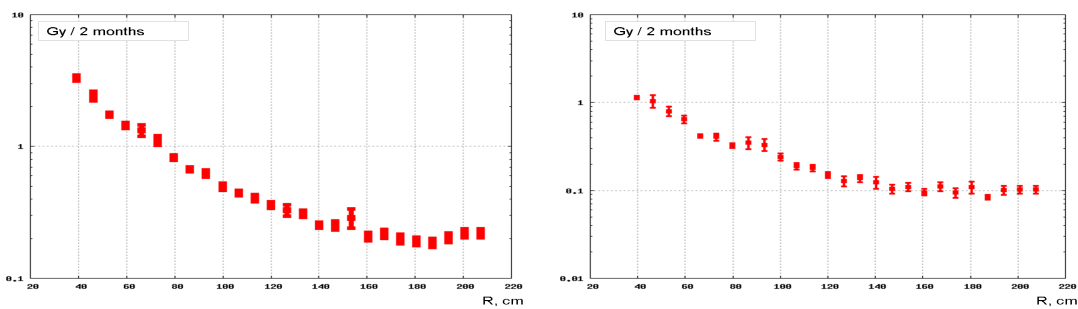
Figure 2.45: Radial distribution of total dose in the 5th station of MUCH for minimum bias Au + Au collisions at 35 AGeV (left) and 10 AGeV (right).
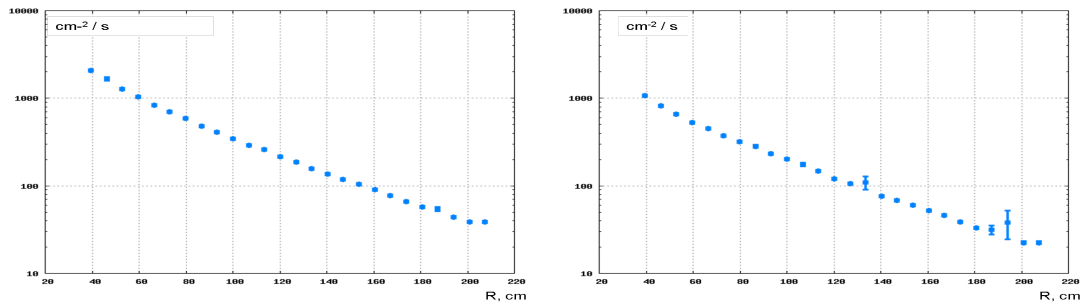
Figure 2.46: Radial distribution of hadrons incident on the 5th station of MUCH for minimum bias Au + Au collisions at 35 AGeV (left) and 10 AGeV (right).
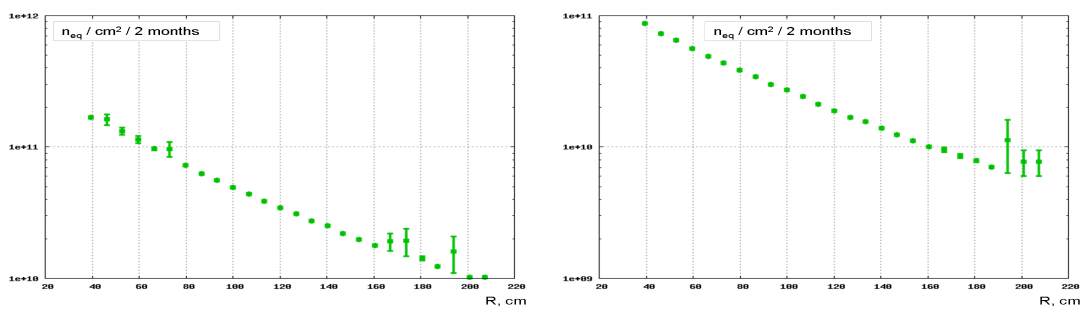
Figure 2.47: Radial distribution of NIEL on the 5th MUCH station for minimum bias Au+Au collisions at 35 AGeV (left) and 10 AGeV (right).

2.6.1 Dynamic range simulation

We have made simulations to study the effect of available dynamic range of MUCH readout ASIC. If the charge deposition is larger than the available dynamic range, the signals will saturate. Fig. 2.48 shows the invariant mass spectra for different dynamic ranges, which shows that it remains almost unaffected to the change in dynamic range.
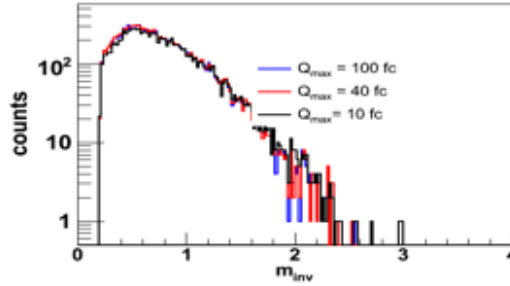
Figure 2.48: Effect of dynamic range implementation: Invariant mass distributions for different dynamic range implementation have been superposed with each other. The spectra do not show any significant variation

2.7 Trigger simulation with MUCH

An algorithm has been developed to trigger the events rich in J/ψ online. It is envisaged that this algorithm could be applied on data using the First-level Event Selection (FLES) algorithms running on the computer farm. The scheme of the trigger logic is depicted in Fig. 2.49. The aim is to select events online which contain muon pairs coming from charmonium decay. The algorithm has been run both in SIS300 and SIS100 MUCH geometries. For faster selection, hits from the 3 layers of the last station positioned after the 1 m thick iron absorber, which we call trigger station have been used. Since our muon detection system is placed outside the magnetic field, high momentum muons coming from the decay of J/ψ mesons will go approximately straight up to the last station. The present algorithm is based on following steps:

(a) Events with 3 hits from the trigger station with one from each of the 3 layers are taken as trigger candidates. The selected hits are then fitted with straight lines both in X-Z & Y-Z plane and passing through the origin (0, 0) i.e. $X = m_0 \times Z$; $Y = m_1 \times Z$

(b) All possible combinations are made of the available hits

(c) Cuts are applied on both χ_X^2 and χ_Y^2 of fits

(d) Hit combinations satisfying the cuts are called triplets

(e) Hit once used for formation of a valid triplet was not used further

(f) The slope parameters, m_0 and m_1 of the fitted straight lines are extracted

(g) A new parameter $\alpha = \sqrt{(m_0^2 + m_1^2)}$ has been defined

(h) Cut is applied on α .

The cuts are applied in a sequential manner.
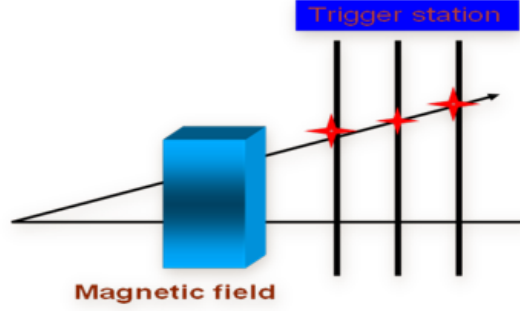
Figure 2.49: Schematic of the trigger logic for charmonium in MUCH

Cut	$eff_{overall}(\%)$	Suppression factor
No cut	29.3	-
1	29.2	30
2	24.5	314
3	24.2	879
4	15.3	1430

Table 2.2: Efficiency and suppression factors with different cuts in trigger algorithm

For estimating the performance of the proposed algorithm, we have simulated 80 K minimum bias UrQMD events for 25 AGeV Au + Au collisions for simulating the background and 1 K Pluto events for signals from J/ψ decayed into muons. The results for background suppression factors (BSF) and the J/ψ efficiency are shown in Table 2.2. In the table the specification of the cuts are as follows. Cut-1 demands that an event should have at least one triplet, whereas those events having two triplets satisfy Cut-2. Cut-3 specifies that at least one of the two triplets satisfies the α cut, whereas Cut-4 signifies that both the triplets satisfy the α cut. The J/ψ reconstruction efficiency is obtained after full reconstruction of tracks and measurement of area under the invariant mass peak. It is found from the study that there is no significant change in the phase space coverage of the accepted J/ψ for the events accepted after application of trigger cuts. It has also been shown that a similar algorithm can be employed to select J/ψ enriched events at SIS100 energy range.

Bibliography

[1] http://www.fair-center.eu/for-users/experiments/cbm.html

[2] S. A. Bass et. al., Prog. Part and Nucl. Phys 41 (1998) 225

[3] R. Brun et. al., GEANT3, CERN/DD/EE/84-1, 1986, long writeup W5013, 1993

[4] see chapter-3 for details

[5] I. Smirnov, HEED simulation program for energy loss, St. Petersburg

[6] I. Kisel, Nucl. Instr. and Meth. A 566 (2006) 85

[7] R. Kalman Transactions of the ASME, Journal of Basic Engineering Series D 82 (1960) 35

[8] R. Fruhwirth, Nucl. Instr. and Meth. A 262 (1987) 444

[9] C. Amstel, The Review of Particle Physics, Phys. Lette B 667 (2008

[10] W. Press, Numerical Recipes: The Art of Scientific Computing , Cambridge Unv Press (2007)

[11] R. Fruhwirth et. al. , Data analysis techniques in high energy physics, Cambridge Univ Press (2000)

[12] A. Lebedev and G. Ososkov, LIT track propagation for CBM , CBM Note (2008)

[13] www-hades.gsi.de/pluto

[14] E.Bratkovskaya,http://fias.uni-frankfurt.de/ brat/hsd.html

Chapter 3

Detector development for CBM-MUCH

3.1   Introduction and technology options

The MUCH concept as discussed in detail in Chapter 2, requires up to six detector stations, each station consisting of 3 layers. Each layer can therefore be considered as one tracking layer consisting of detectors built using specific detector technology. Unlike other subsystems at CBM, MUCH therefore could consist of different types of detectors each using specific technology. The choice of the detector technology is governed by following criteria apart from the requirements of high resolution and high efficiency.

- **Particle density**: Depending on the location of the station and of the layer, density of incident detectable particles may vary from 1 cm^{-2} to 10^{-4} cm^{-2}. The particle density is governed by the profile of incident particles coupled to the total absorber thickness it passes through. The particle density determines the profile and segmentation of the detectors.

- **Particle rate**: CBM is to operate at 10 MHz collision rate. The interaction rate and the particle density together determine the particle rate a detector needs to handle. It has been found by simulation as discussed in Chapter-2, that for an Caron-Iron-absorber setup, maximum required rate is 0.4 MHz/cm^2 at the innermost part of the layer located immediately after the carbon absorber.

- **Detector area**: The layers located at the end of MUCH setup need to be considerably larger in size compared to the stations located close to the magnet. The ability to build large area detectors using a particular technology governs the selection of technology at those locations.

- **Radiation hardness**: One specific challenge that the MUCH detectors face is the large number of secondaries produced inside the absorber which reach the detector stations unabsorbed. Neutrons are the biggest contributors. It has been estimated that 1st station is to face about 10^7 neutrons $\text{cm}^{-2} \text{ sec}^{-1}$. The detector must not produce hits due to these neutrons, otherwise they will add to the hit density. In addition to that the detector materials must be resistant to the huge neutron flux both in long and short duration.

  Even though the detectors face mostly minimum ionizing particles, however, at CBM energy range, slow-moving ionizing particles might deposit relatively larger amount of energy and the detector must be able to withstand this large energy deposition. As discussed in

Chapter-2, In MUCH configuration, the criticality of radiation hardness is applicable to the detectors in the first few stations only. The detectors located in most downstream stations, even though need to be of large size, handle very low particle density.

- **Cost**: Like in all high energy physics experiments, cost of detectors and electronics must be optimized properly, as it forms a major fraction of the total cost. It is therefore extremely important that proper selection in detector technology is made to optimize the cost. The total area to be handled by 18 layers of MUCH is about 200 m^2, out of which the area of first three stations taken together is 50 m^2. This large detector area must be segmented with optimum number of pads to keep the number of electronics channels under control.

Keeping the above factors in mind, detailed simulations have been performed for optimization of MUCH geometry as discussed in Chapter-2. The decision on detector technology has been taken by looking at the requirements at different stations separately. First few stations face harsh radiation environment and require specialized technology and the later stations can use conventional detector technology that can be built in large area. We have studied the options of using different technologies at different radial distances of a layer. However, mostly due to complexity in implementation, it has been decided that the three layers of a station will use one particular technology.

In Table.2.1, we have summarized the baseline technology options of MUCH versions. In this chapter, we discuss in details the R&D performed on two technology options i.e., GEM and Straw tube detector. The tracking chambers for the Transition radiation detectors (TRD) will be located at the end of RICH or MUCH setup of CBM. Therefore, TRD has been taken as the baseline option for the last MUCH station both for SIS100 and SIS300 configurations. The number of TRD layers to be actually implemented will depend on the requirement of number of layers for muon tracking. The details of TRD will be available in a separate technical design report for that subsystem. However, some details on TRD R&D will be available in [1, 2, 3, 4].

For the first few stations, which face high particle rate and harsh radiation environment, we considered gaseous detector options based on GEM, MICROMEGAS and MWPC. So far, MWPC is the most widely used type of gaseous detector for HEP experiments. However, the use of MWPC in MUCH is constrained by its rate handling capability. The rate handling capability is limited by space charge constraint. Fig. 3.1 shows the relative gain of a typical MWPC as a function of rate [5]. The gain starts falling sharply after about 10^4 Hz/mm^2 of incident particle rate. The qualifying parameters of these three detector technologies as per literature survey are compared in Table 3.1. It is clear that MWPC will not be able to cope with the required rate at the first stations of MUCH. Out of the two other options, GEM has been taken as the baseline option for the first two stations of both SIS100 and SIS300 after performing detailed R&D on GEM in the CBM-like environment.

Several GEM detectors have been built in various sizes within the dimension ranges of 10 cm×10 cm to 31 cm×31 cm and their characteristics have been studied using both conventional and self-triggered electronics. While sub-system specific self-triggered ASICs are still under development, for detector tests the CBM collaboration is using the nXYTER ASIC developed by the DETNI Collaboration [6]. We also describe the planned procedure to be adopted for building the large size GEM detectors as will be used in the MUCH stations. Detectors using straw tubes built by
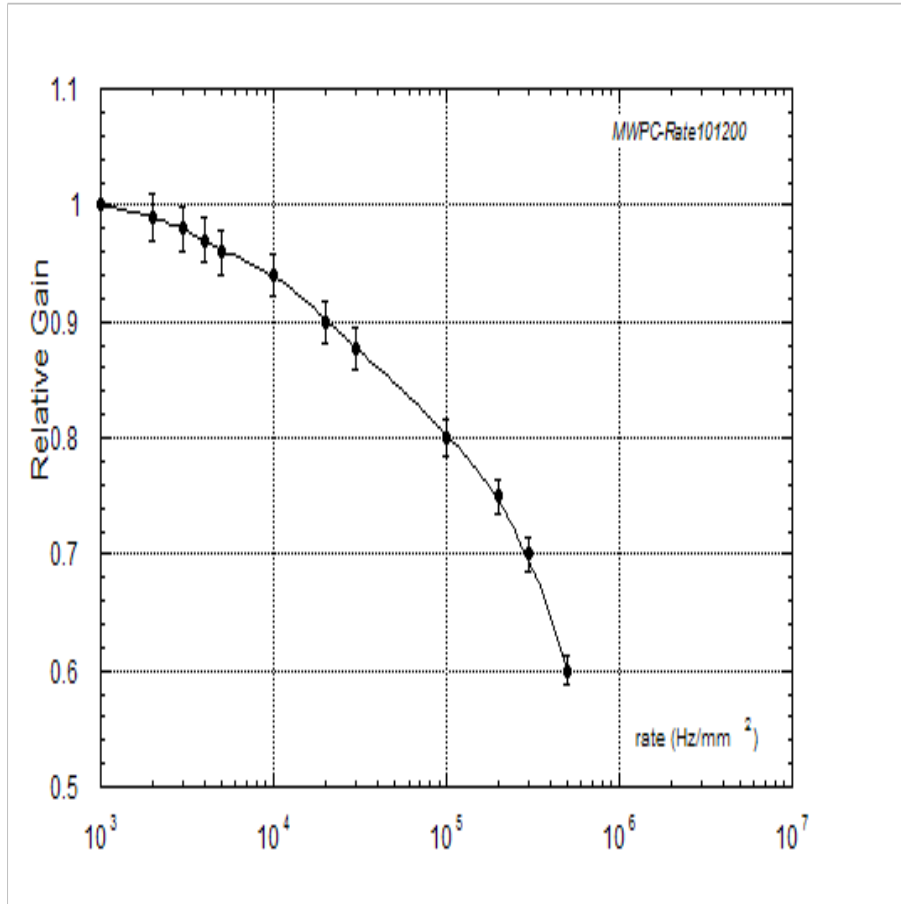
Figure 3.1: Relative gain of a MWPC as a function of rate.

the Dubna group are being successfully used in ATLAS [35] and COMPASS [33] experiments. The same group has been participating in CBM straw activities. We here discuss the R&D on straw tube detectors using triggered electronics. The group at PNPI-Russia has been performing R&D on the development of different detector types like thickGEM and hybrid of GEM+Micromegas. We report the progress in Appendix-I.

3.2   Gas Electron Multiplier (GEM)

3.2.1   Introduction to GEM

GEM, the idea of which was developed first at CERN [9, 10], is conceptually a simple gas detector and its advantage lies in the structure of GEM foil. Each GEM foil consists of a large density ($\sim 50/mm^2$) of holes, each of diameter 70 μm with 140 μm pitch on a 50 μm thick polyimide foil metalized with 5 μm thick copper on both surfaces. Relatively low voltage ($\sim$400V) applied across the foil produces very high (100 kV/cm) electric field inside the holes, making GEM an amplifier of electrons when placed inside a suitable gas volume.

The technology for the production of GEM foils has evolved over the years. Earlier the foil was made by the so-called double-mask (DM) technology where two masks are used on top and bottom layers of the foil before etching. While this technology produced foils of sizes from

Table 3.1: Comparison of rate handling capacity of various micro-pattern gas detectors

Parameter	MWPC	GEM	Micromegas
Rate capability (Hz/mm^2)	10^4	5.10^5	10^6
Gain	High (10^6)	Low 10^3 single 10^5 Multi-GEM	high 10^5
Position resolution	$<200\mu m$	$50\mu m$	$<50\mu m$
Time resolution	$\sim100ns$	$50ns$	$50ns$
Effect of mag. field	high	low	low
Cost	Expensive,	Expensive,	Cheap, robust but sparks can be catastrophic to FEE.

10cm×10cm to 30cm×30cm with good quality and yield, the cost was high and most importantly, larger size foils were not possible using this technology.

Over the last few years efforts have been made by the RD51 collaboration at CERN to produce foils using what is now called the single-mask (SM) [12] technology where only one mask is used at the top for etching holes in the foil [13]. The yield of large size good quality foils is significantly lower in case of double-mask technology, but the same improves significantly in the case of single-mask technology thereby reducing the cost. The basic raw material for GEM, the copper-clad polyimide sheets of 50 μm thickness, is readily available in rolls of 0.5 m width. Thus using single mask technology it has now become possible to produce GEM foils of maximum width 0.5 m and length of 1 m or more.

The electron multiplication and hence the gain obtained using a single GEM foil is considerably low. Hence for practical applications one uses cascading of several GEM foils. For building a detector, one or more GEM foils separated by spacers of suitable thicknesses are placed inside a gas tight enclosure filled with suitable gas mixture. The enclosure usually consists of two PCBs. The gap between the top PCB and first GEM foil forms the drift gap. Incoming radiation produces primary ionization in this region. This is followed by subsequent drift of the electrons through the GEM holes which act as amplifying elements. The gap between the last GEM foil and bottom PCB forms the induction or collection gap. Signals due to electrons are collected by the readout electrodes placed on the inner copper layer of the PCB at the bottom of the induction gap.

Suitable voltages are applied in all the gap segments. Depending on the application one can apply same voltage across all the GEM foils in a detector or a different set of voltages can be applied. These are usually applied using a set of resistor chains but during developmental stage it is possible that separate HV units are used to provide voltage to each GEM layer. Typical values of the voltage across the GEM foils are in the range of 300V to 400V.

Most of the cases, GEM detectors use a gas mixture of Ar and CO_2 in the ratio of 70:30. This gas mixture makes the detector insensitive to neutrons.

A comparison of the gain obtained for a GEM detector as a function of voltage shows that the gain increases exponentially as expected for a gaseous detector. The triple GEM version

provides a good working solution for practical applications in high energy physics. A gain $>10^4$ is achieved using triple GEM assemblies for applied voltages of 400 V across the GEM foils with very small (10^{-11}) discharge probability in a gas mixture of $Ar:CO_2$ in 70:30 ratio [15]. It should be mentioned that GEM has the advantage of eliminating the ion tails by opposing electric field thereby generating fast induced signal due to electrons. The arrangement of thin assemblies resulting in very small ion tails helps to operate the detectors at a high rate close to 1 MHz/mm^2 without any gain loss. It has been shown in the literature that the gain remains constant even at the incident particle rate of 2×10^5 Hz/mm^2.

Over the years, GEM detector technology has gone through a series of improvements towards optimizing its parameters. GEM detectors have found uses in several large experiments as tracking and readout devices. Notable examples are TOTEM@LHC [17], STAR@RHIC, PHENIX@RHIC [18], COMPASS@CERN, LHCB@CERN, LEGS@BNL and BONUS@JLAB. CMS has taken up the development of large GEM detectors as a project in the upgrade of their tracking system [19].

3.2.2   GEM Prototypes

The mechanical assembly of the triple GEM detector requires components shown schematically in Fig. 3.2. It is in the form of a gas tight enclosure where the top lid consists of a PCB for the drift plane. The bottom part has a gas tight housing with a groove for O-ring seals. A set of
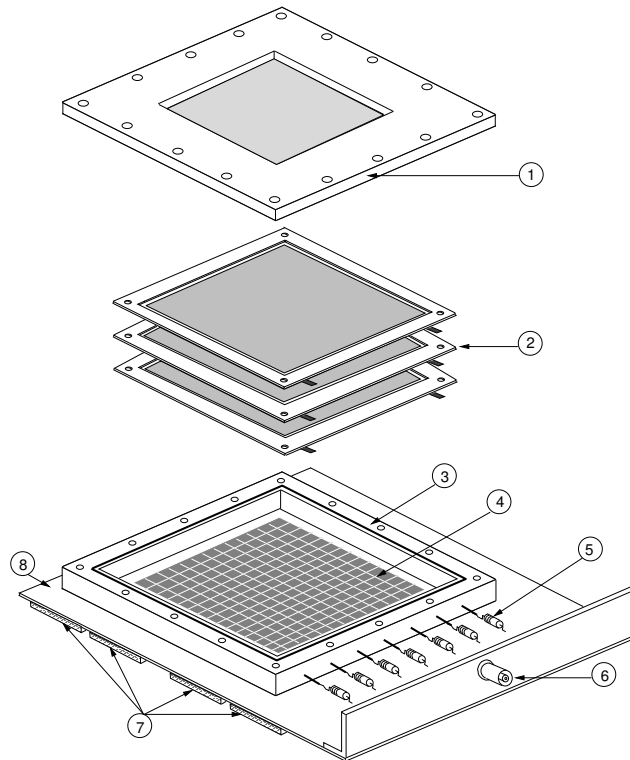
Figure 3.2: Schematic of assembly of a triple GEM detector (1) top chamber lid with drift plane (2) triple GEM foils stretched in FR4 frames (3) gas tight housing frame with 'O' ring seal (4)readout plane (5) GEM series resistors (6) SHV connectors for individual GEM foil bias (7) input connectors to FEB (8) readout PCB.

connectors are provided at the sides for connecting to HV resistors that provides the voltage to

the different segments. It is integrated with the readout PCB at the bottommost plane. A set of multipin connectors are provided at the bottom for connecting the Front-end Boards (FEBs) and SHV connectors are provided at the side for HV input. Three GEM foils, each of size 10cm×10cm and made from single mask technology were placed inside the gas tight housing after suitable stretching and fixing to a frame. The three foils were separated by suitable spacers to provide the necessary gap widths.

In the detectors fabricated at VECC Kolkata, the drift plane at the top was made of copper-clad FR4 board of 10cm x 10cm area. A set of holes, covered by mylar foils from inside the chamber were made on the FR4 board to allow X-rays from ^{55}Fe source to enter the gas volume and the holes are sealed using 100 micron polypropylene. This arrangement facilitated testing the detector using ^{55}Fe source and study their characteristics. Fig. 3.3 (left) shows the photograph of a chamber built at VECC.

The readout PCB was segmented into 512 pads each of 3mm×3mm size. The pad dimensions of the prototype detector correspond to the optimized smallest allowed pad size in the first GEM station at CBM as obtained by detailed simulation in the CBM framework (See Chapter 2). The readout plane was a 4-layer PCB, in which traces were guided into 4 groups each connected to one FEB using two 68-pin connectors affixed on the side of the detector. Out of the four layers in the readout PCB, one was used exclusively for ground connections. Fig. 3.3 (right) shows the outer side of the readout PCB with traces from the pads are shown to be going to connectors. A similar triple-GEM detector has also been fabricated at GSI. This detector was also made up of three CERN-made single mask GEM foils each of dimension 10 cm×10 cm. The widths of the drift gap, first and second transfer gaps and induction gaps were 3mm, 2mm, 2mm, and 2mm respectively. The readout plane of this detector had 256 pads each of size 6mm×6mm, traces of which were divided into four connectors. Fig. 3.4 shows the photograph of the detector fabricated at GSI. Table 3.2 gives a comparison of parameters of two prototypes.
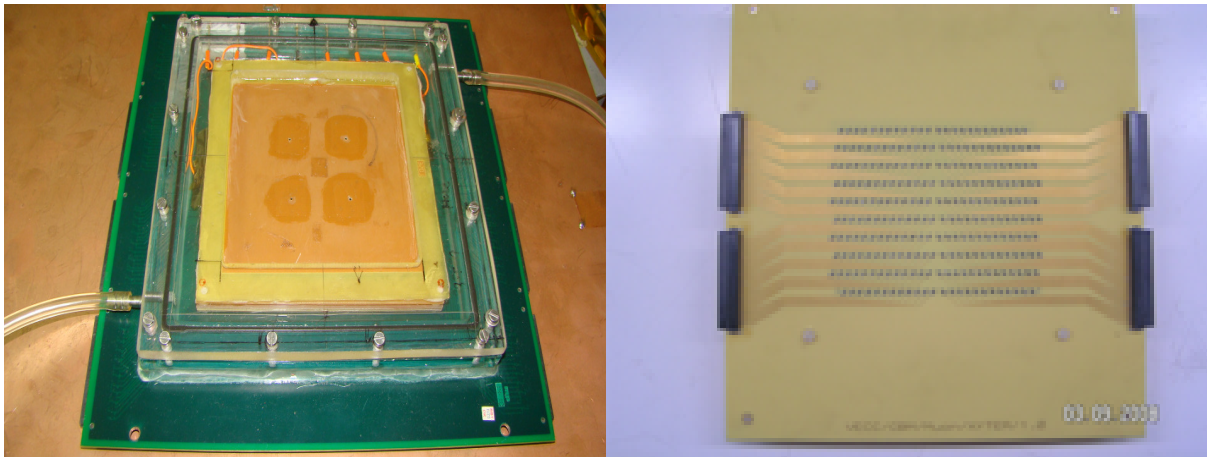
Figure 3.3: (left) Photograph a triple GEM detector fabricated at VECC, (right) outer-side of the bottom PCB for one of the prototype chambers. Connectors are soldered on tracks each of which has a resistance (10 Ω) to protect the electronics from spark.

Parameter	GEM-1	GEM-2
Drift gap	3mm	3mm
Transfer gap-1	1mm	2mm
Transfer gap-2	1mm	2mm
Induction gap	1.5 mm	2mm
segmentation	3mm×3mm	6mm×6mm
Number of pads	512	256

Table 3.2: Parameters of two chambers tested at CERN SPS using pion beams
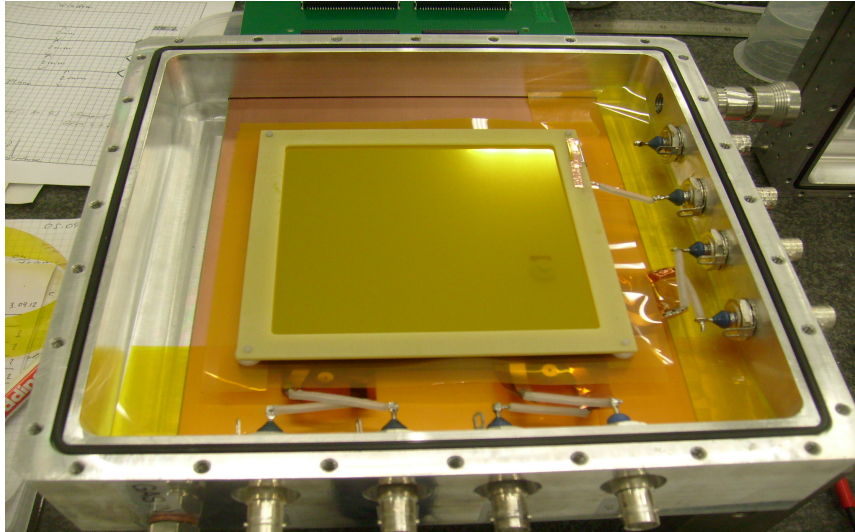
Figure 3.4: Photograph of a triple-GEM detector fabricated at GSI

3.2.3   Laboratory tests

3.2.3.1   Tests with conventional NIM electronics

3.2.3.1.1   Tests using ^{55}Fe X-ray source :   The triple GEM detector made at VECC Kolkata was tested with X-rays from ^{55}Fe sources using conventional NIM electronics of a preamplifier, an amplifier and a MCA setup [20]. A typical pulse height spectrum of this triple-GEM detector for ^{55}Fe source is shown in the left panel of Fig. 3.5. We observe clearly defined peaks with the higher one corresponding to 5.9 keV X-rays. positions were found to shift to higher channels with increasing HV. Variation of gain with HV as calculated from the calibrated charge deposition spectra are shown in the right panel Fig. 3.5. As expected, the gain increases with the applied HV reaching 80,00 at the top HV studied corresponding to ΔV_{GEM} of 420V.

3.2.3.1.2   Tests using cosmic muons: The detector was also tested using cosmic muons. The test setup for cosmic muons consisted of two large and one small (finger) scintillators in coincidence to obtain the trigger. The readout setup used here was similar to the one used for the source test. Although the detector readout plane was finely segmented, for the present tests all pads were connected in parallel as a single input to the preamplifier followed by amplifier and MCA. The efficiency of the detector was determined by taking the ratio of counts at a particular
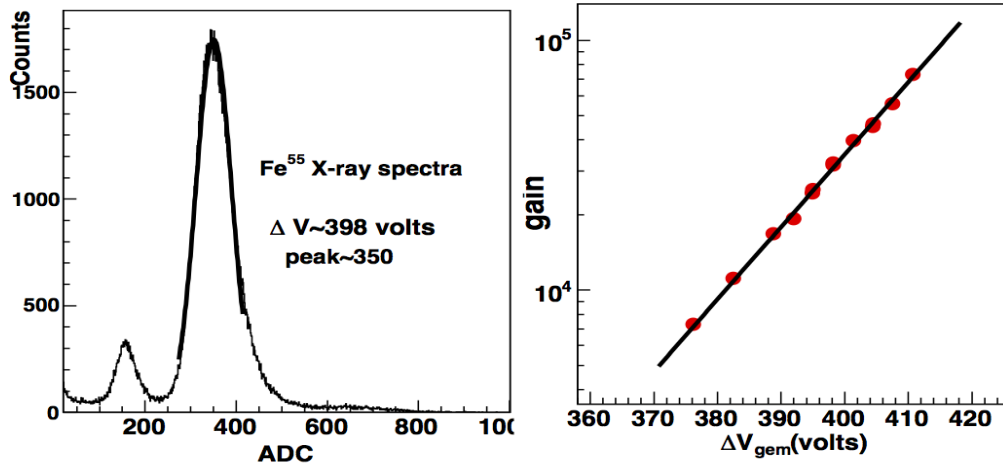
Figure 3.5: (left) ^{55}Fe spectra with triple-GEM assembly and (right) variation of gain with the voltage applied across each GEM foil.

duration of 4-fold (3-scintillators and GEM detector) coincidence and 3-fold (3 scintillators) coincidence counts respectively. Special care was taken to adjust the coverage to make sure that all particles passing through the trigger detectors (defined by the finger scintillator) also passed through the GEM detector. Fig. 3.6 shows the energy deposition spectra for cosmic muons at different voltages applied across GEM foils. As seen in Fig. 3.6, the ADC spectra for cosmic muons at different HVs show well-defined Landau-shapes characterising the MIP spectra. The increase in gain with ΔV_{GEM} is demonstrated by shifting of the MIP peak at higher applied voltages. Fig. 3.7 shows the variation of efficiency of this detector with applied HV for the
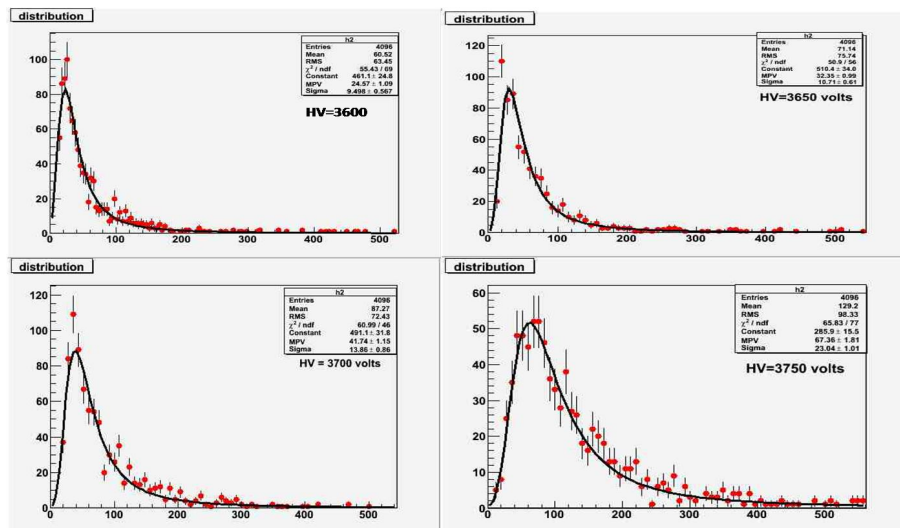
Figure 3.6: MIP spectra from cosmic ray test at increasing HV. Typical Landau-shape is observed.

detection of cosmic muons . The efficiency increases with HV reaching a plateau >95% at ΔV_{GEM} ~420V. Further increase in HV increases the spark probability and therefore no data could be taken at higher voltages.
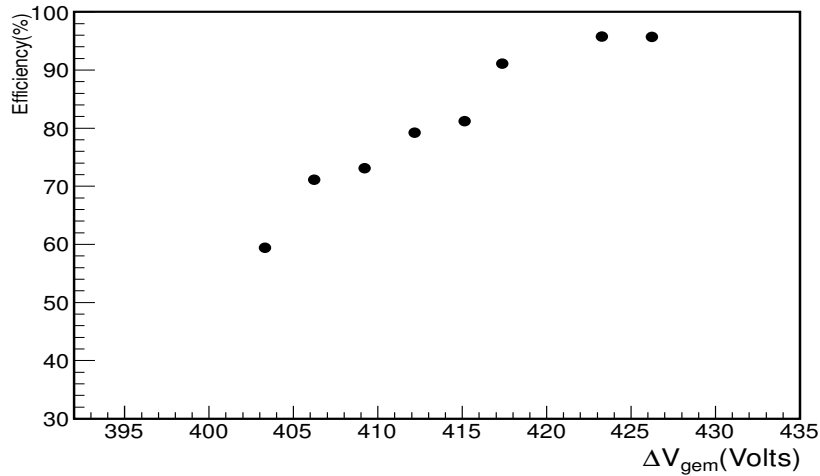
Figure 3.7:   Variation of efficiency with applied voltages as readout by the conventional system for the detection of cosmic muons.

3.2.3.2   Test with self-triggered nXYTER ASIC

For the operation of CBM-MUCH at high interaction rate (10MHz), it requires the use of self-triggered readout electronics. This requirement is guided by the fact that in heavy ion collisions we donot have easy single particle trigger primitives, as our triggers are tracking triggers and requires a large fraction of the data for the trigger. In the self-triggered readout system, no external event trigger is applied and all hits above a predefined threshold are recorded along with their corresponding arrival times as time-stamps. It has been decided that nXYTER, a 128-channel self-triggered ASIC used earlier by the DETNI collaboration [6], will be used in all detector testing experiments during the R&D phase in CBM before the final ASICs are ready for respective detector systems. The response of the triple GEM detector to ^{55}Fe X-ray source has been studied using the self-triggered ASIC nXYTER. The baseline in the nXYTER is shifted to around 2000 ADC and for negative signals, higher signal corresponds to lower ADCs and lowe signals corresponds to higher ADC values, contrary to the conventional method where the signal increase is directly related to an increase in ADC. The ADCs obtained from nXYTER are therefore subtracted channel by channel from corresponding baseline ADC values, resulting in converted ADCs matching the conventional trend with signal strength. Fig. 3.8(left) shows the raw pulse height spectra where the major peak corresponds to the 5.9 keV X-rays. Such peak values were noted for a range of GEM voltages and then after a dedicated baseline run which determines the baseline channel by channel, the peak values of the subtracted ADCs are plotted with respect to GEM voltage as shown in Fig. 3.8(right). The increase in ADC, which reflects increase of gain, is seen to vary exponentially with ΔV_{GEM}, as expected.

3.2.4   Beam tests

The detectors fabricated at VECC and GSI have been tested with proton beams at GSI and COSY-Juelich and with pion and muon beams from the SPS-CERN [21]. The momentum of the beam particles were such that they correspond to MIPs. Most of the results presented below are from the CERN beam tests. Only one result from COSY test is presented where tracking capability was studied using a set of fibre hodoscopes.
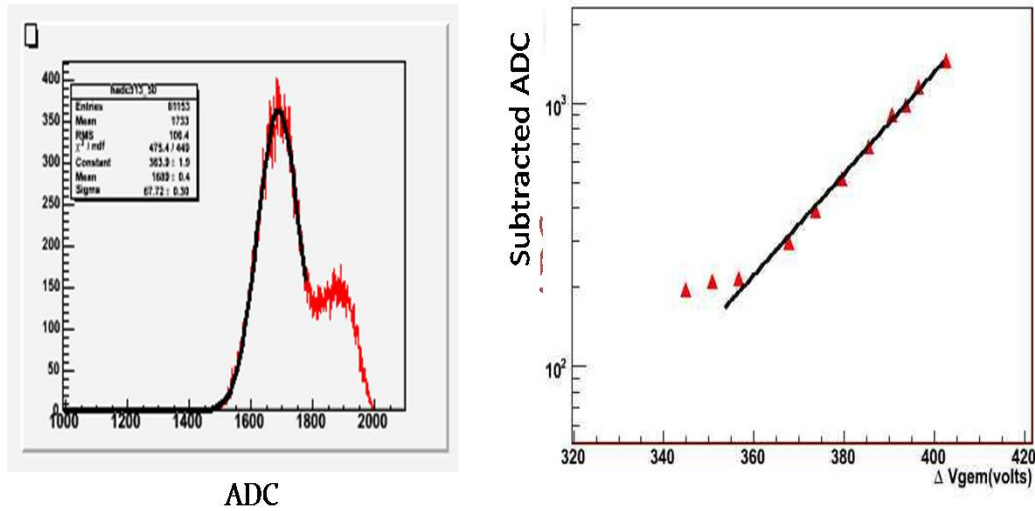
Figure 3.8: (left) ^{55}Fe X-ray spectrum from a triple GEM detector using nXYTER electronics, the X-axis represents raw nXYTER ADC as explained in the text (right) ADC value of the X-ray peak as a function of voltage across GEM foils.

During these tests, the detector fabricated at VECC was operated with equal voltage across the three GEM foils. However, for the results presented here, the GSI detector was operated in a manner such that the voltages across three GEM foils were 370V, 336V and 362V. For both the detectors a gas mixture of Argon and CO_2 was used at a ratio of 70:30 with a flow rate of 50 ml/min.

3.2.4.1   Test setup at CERN

The layout of the setup used at CERN H4 beam line in October 2012 is shown schematically in Fig. 3.9. GEM1 and GEM2 refer to the detectors fabricated at VECC and GSI respectively. For triggering, two cross-scintillators of 2cm×2cm overlap area placed at the beginning of the setup were put in coincidence with two scintillators of similar dimensions at the end of the setup.

In this test, pion beams of 100 GeV momentum were used. The beam intensity was varied by adjusting the collimator openings in the range ±2mm to ±3mm. This provided particle rates varying between 400 Hz and 2.5 KHz.

Fig. 3.10 shows the scheme for signal processing and data acquisition. The nXYTER-based readout discussed earlier was used in this test run. The information of the coincidence signal was distributed to the ROC auxiliary channels to record the reference time-stamps.

GEM1 had 512 pads each of 3mm×3mm size read by 4 FEBs connected to 2 ROCs. GEM2 had 256 pads each of 6mm×6mm size and was read by two FEBs and one ROC. A correlation needs to be obtained between the time-stamps of the coincidence signal and detector hits as recorded by the same readout system.

Here results are presented in detail for GEM1, and only some specific results are presented for GEM2. A threshold on nXYTER corresponding to 1fC was used.
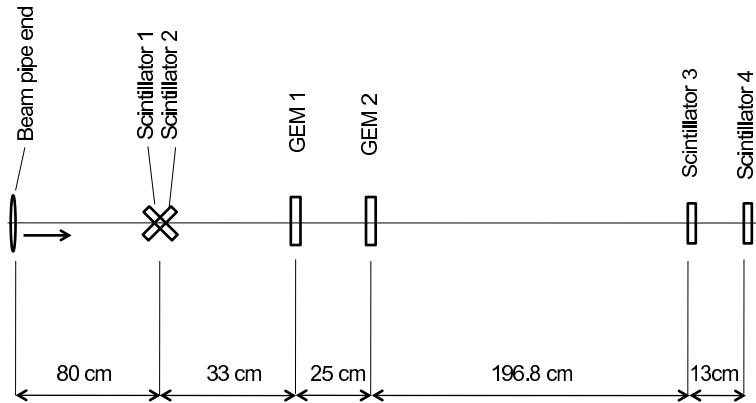
Figure 3.9: Test beam setup at H4 beam line at CERN.
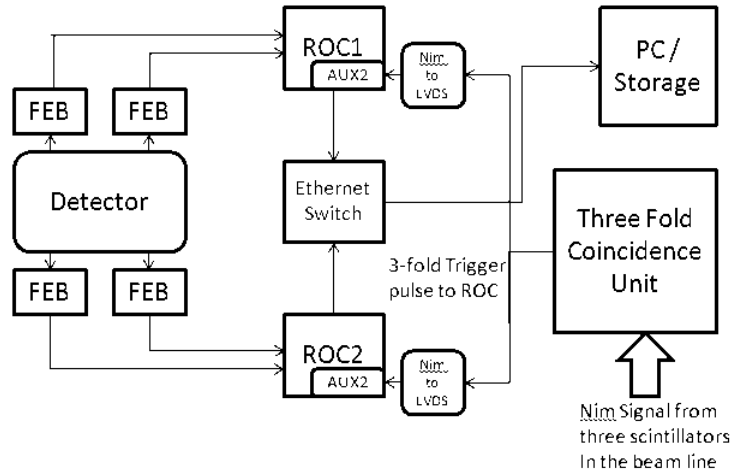
Figure 3.10: Schematic of the data readout setup for tests at CERN.

3.2.4.2   Time correlation and beam spot

In a self-triggered electronics system, all hits above a predetermined threshold read by nXYTER are digitized and stored. In tests involving beam particles, only the hits produced by beam particles should be time-correlated with the coincidence signals.

First step of understanding data taken by a self-triggered readout system is therefore to obtain

the distribution of time-difference between the time-stamps of the GEM-hits and those of the coincidence signals. Such a distribution will be referred to as the time-correlation distribution. Fig. 3.11 shows the time-correlation distribution for a pion run of GEM1 at ΔV_{GEM} of 320V. The position of the peak depends on the delay introduced by the delay settings and cable delay. The distribution shows a well-defined Gaussian shape. The fitted-width (σ) of the time-difference spectra varies with the applied voltage as shown in Fig. 3.12. The fitted width (σ) is related to the time resolution of the detector which improves with the applied voltage reaching a saturation of $\approx$13 nano-seconds at ΔV_{GEM} of 335V. This result is comparable to the time resolution reported elsewhere [15, 22] by triple-GEM detectors of similar configuration. It should be noted that the actual time resolution would be somewhat better after the subtraction of the time-jitter due to the trigger scintillators. Almost complete absence of entries on both sides of the time-correlation peak shows that in the current run the fraction of uncorrelated hits is very small.
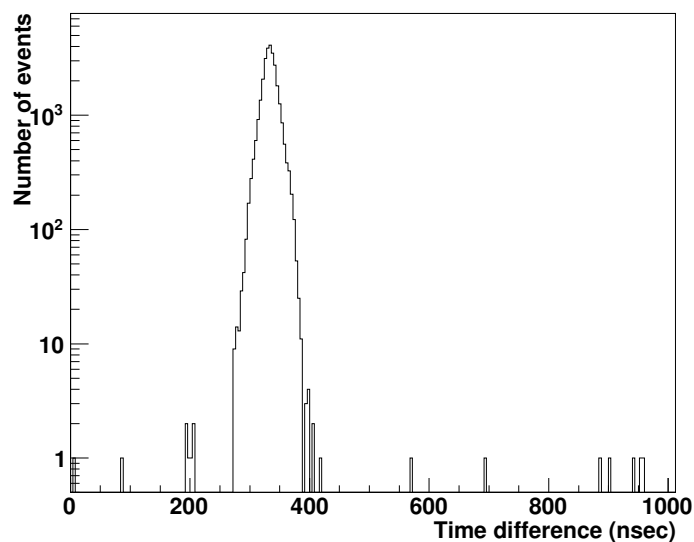
Figure 3.11: The spectra of the time correlation between GEM hits and the coincidence time-stamp. Almost no entries outside the peak shows very good noise performance with negligible fraction of uncorrelated hits. The Gaussian shape of the correlation peak shows good transfer of charge in the detector.

The GEM-hits inside the time-correlation peaks are considered to be beam-related and the detector co-ordinates of such hits for GEM1 are plotted in the left panel of Fig. 3.13 to show the beam spot at ΔV_{GEM} of 335 V. The spread of the spot depends both on the beam-spread and the size of the electron cluster detected by GEM. The beam spot seen by the detector corresponds to the triggered overlap area of 2cm×2cm of trigger scintillators. However, due to narrow profile of GEM avalanche spot coupled to the Gaussian shaped beam profile, the beam spot seen on GEM1 is peaked around a few pads only. The beam seems to be narrowly focused and the low lying pedestal corresponds to the overlap region of the trigger scintillators. Right panel of Fig. 3.13 shows the beam spot for GEM2. This detector had 6mm×6mm pads as opposed to 3mm×3mm pads in GEM1.
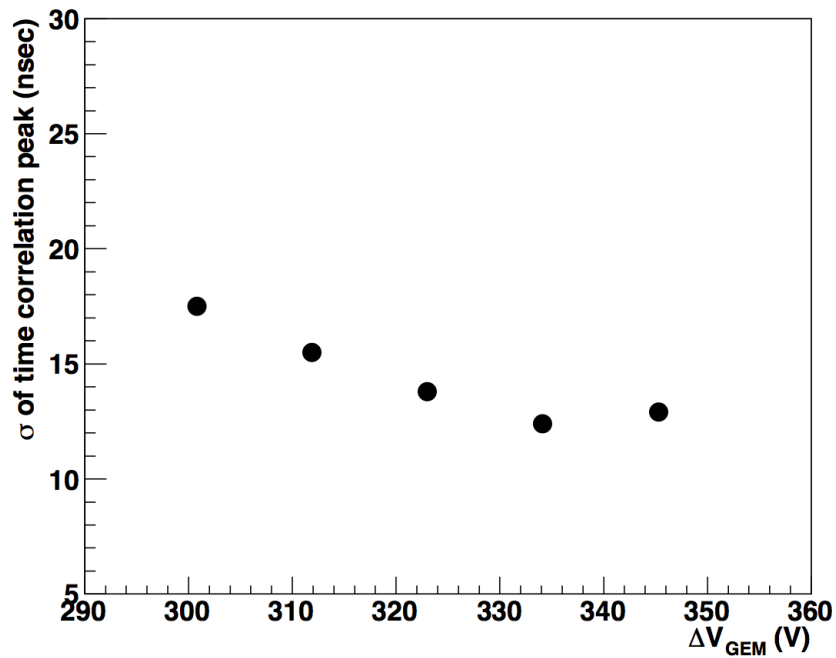
Figure 3.12:　Variation of σ of the time correlation peak with ΔV_{GEM}. The time resolution of the detector can be extracted after subtracting the effect of spread introduced by trigger scintillators and the readout electronics. As expected, the time resolution improves with HV.
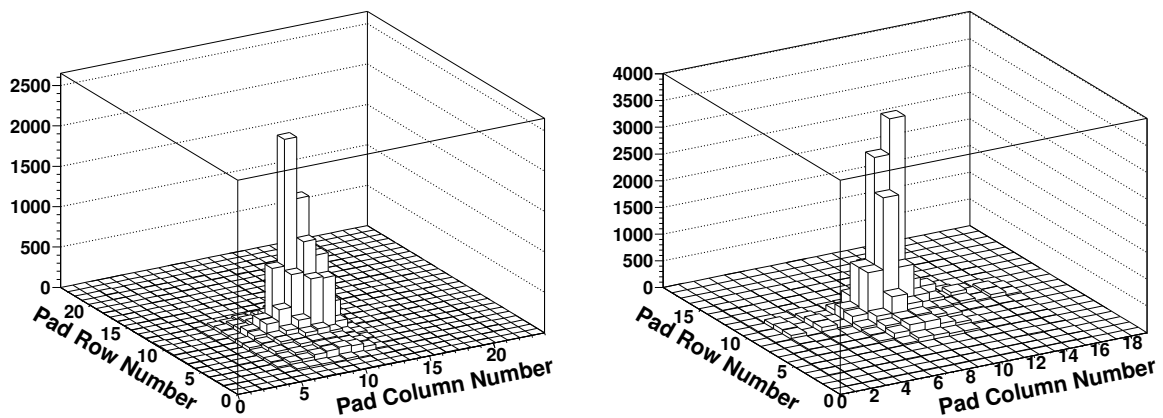
Figure 3.13:　Pion beam spot on GEM1 having 3mm×3mm pads (left) and GEM2 having 6mm×6mm pads (right)

3.2.4.3 Efficiency

For the operation of CBM-MUCH, attaining an efficiency >95% for MIP is a prerequisite for efficient detection of muons. Additionally, it is required that the efficiency remains stable over the operating range of HV, particle rate and other operating conditions. We have seen earlier [20] that an efficiency of >95% is attained with cosmic rays using conventional electronics with a detector of somewhat larger gap widths. In the test beam experiment the coincidence signal was applied as an input to the auxiliary channel of ROC and the particles were taken to be detected in an event if there was at least one hit in the time-correlation window. The efficiency is therefore defined as,

$$\text{Efficiency} = \frac{N_{\text{GEM}}|_{within200nano-seconds}}{N_{trigger}}$$

where, N_{GEM} = Number of events having at least one GEM hit in the time-correlation window and $N_{trigger}$=Total number of coincidence events. We have not made any correction for background as the number of entries outside the peak region is small. This approach might have an overestimation of efficiency by 0.5%.
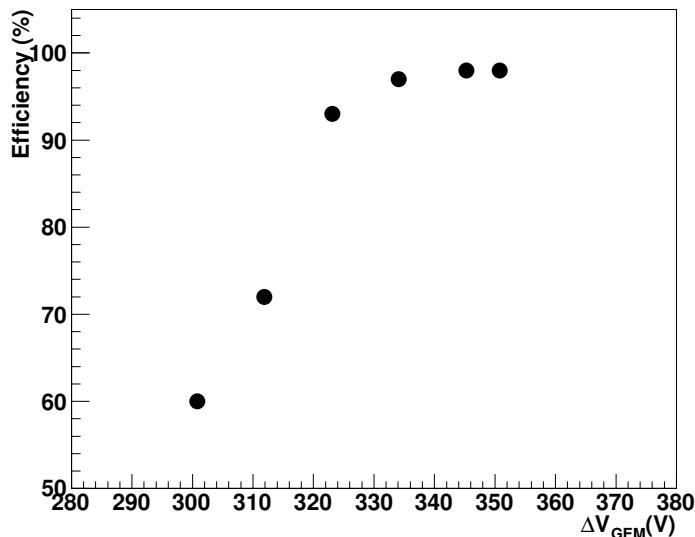
Figure 3.14: Variation of efficiency with ΔV_{GEM}. The efficiency increases sharply and reaches a saturation above 95% around ΔV_{GEM} of 335 V

Fig. 3.14 shows the variation of efficiency of GEM1 with ΔV_{GEM} for pion data taken in this run. The efficiency depends on the signal to background ratio of the detector and has dependence on the applied threshold on nXYTER. From the results shown here, we can conclude that the detector may be operated at ΔV_{GEM} of 340 V with close to 98% efficiency i.e., clearly above the required 95% for efficient muon detection.

3.2.4.4 Pad Multiplicity

As per literature, the profile of electrons in GEM detector for comparable detector configuration is expected to cover on an average about 3 strips of 600 micron strip pitch [23]. For a pad-size

of 3mm×3mm, it is therefore expected that for the beam particle incident at the middle of the pad, the profile should be confined inside one pad.

For projecting tracks on GEM plane of CBM-MUCH, the cluster size requires detailed study as it determines the particle position. Fig. 3.15 (left) shows the distribution of pad-multiplicity of GEM1 for a pion run at ΔV_{GEM} of 335 V. It is seen from Fig. 3.15(left) that the hits are confined mostly to one pad. Fig. 3.15(right) shows that the average pad multiplicity increases slowly from ≈ 1.1 at ΔV_{GEM} of 300 V to ≈ 1.6 at ΔV_{GEM} of 350 V. Increase in gain results in larger transverse size of the GEM profile which is the likely reason of increase in pad multiplicity with voltage.
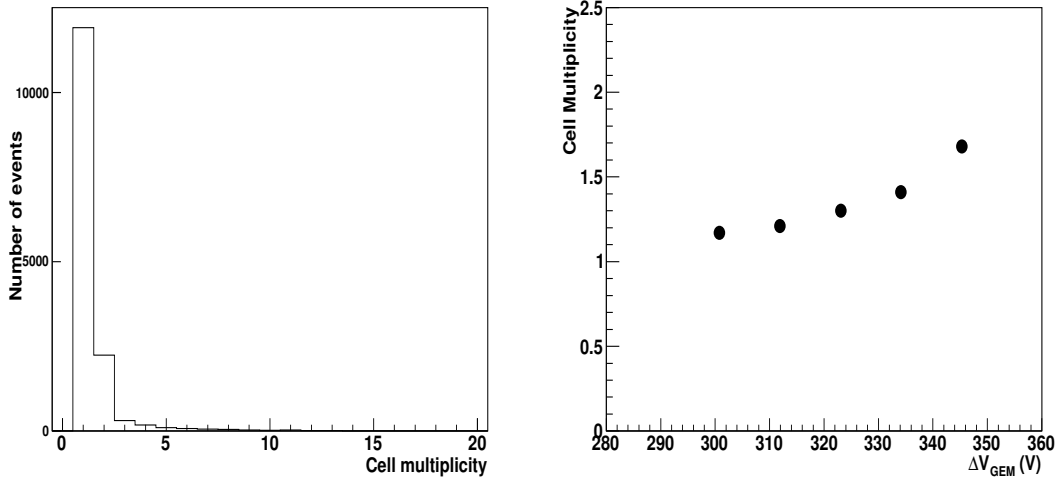
Figure 3.15:   (left)Distribution of event by event pad multiplicity at $\Delta V_{GEM} = 335V$. For this detector of 3mm×3mm pad size, the cluster is confined mostly within one pad. (right)Variation of average pad multiplicity with ΔV_{GEM}

3.2.4.5   Gain

The pedestal subtracted event-wise highest ADCs are plotted in Fig. 3.16 for GEM1 at ΔV_{GEM} = 323V. A well-defined Landau-shaped distribution characterizing the MIP spectra is seen in the figure. The MIP spectra at different ΔV_{GEM} have been fitted with Landau function to extract the MPVs of the distributions. At higher ΔV_{GEM}, ADCs show saturation due to limited dynamic range of nXYTER. In Fig. 3.16, we have superposed the corresponding ADC distributions for GEM2 where ΔV_{GEM} across three GEM foils were 370 V, 336 V and 362 V. This had considerably larger fraction of saturated ADC.

The detector-gain has been extracted by adding ADCs of all pads around the peak in an event. Gains have been extracted only upto $\Delta V_{GEM} = 350V$ beyond which ADC saturates almost completely. Fig. 3.17 shows the variation of extracted gain of GEM1 with ΔV_{GEM}. The errors due to uncertainty in the nXYTER range will be 20%. The gain increases slowly at the beginning rising linearly afterwards as shown in Fig. 3.17. At 350 V, the detector achieves a gain of ≈ 4000 which is comparable to the gain obtained in [20].
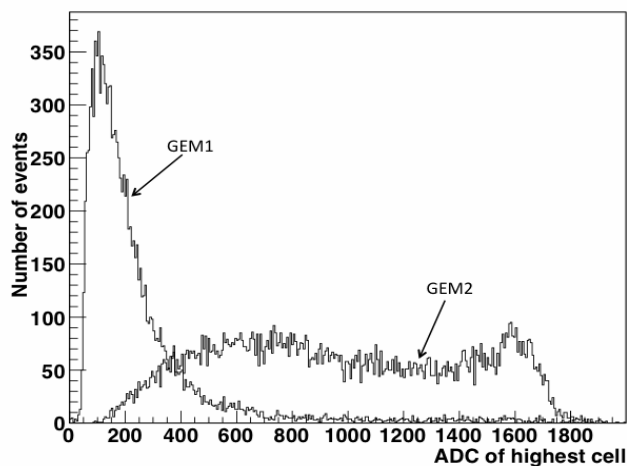
Figure 3.16: Spectra of pads with event-wise highest ADC for GEM1 at $\Delta V_{GEM} = 323$ V and of GEM2 at corresponding voltages across GEM foils i.e., ΔV_{GEM} for 3 gaps of 370 V, 336 V and 362 V respectively. As expected, a larger fraction of ADC spectra get saturated for GEM2 at this voltage.
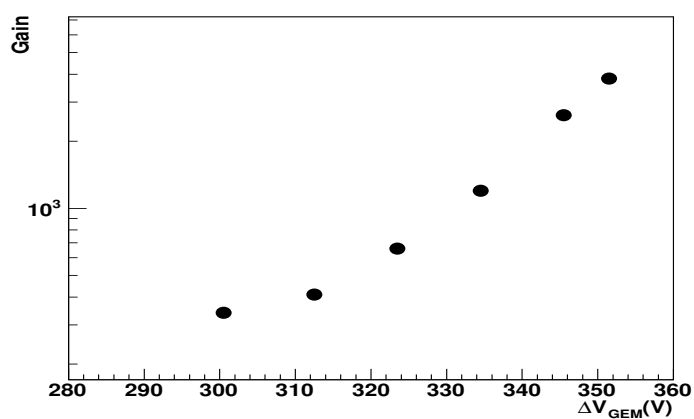
Figure 3.17: Variation of gain for GEM1 with ΔV_{GEM}. The gain varies linearly when seen in a log plot

3.2.5 Tracking with the GEM detectors

Two attempts have been made so far to test the capability of GEM detectors for tracking in CBM-MUCH.

3.2.5.1 Results of COSY tests

We have made first attempt in using GEM spots for tracking in COSY test beam along with the beam spots from hodoscopes. The track-fitting was performed in 1-dimensions using X and Y directions separately. In COSY test beam setup, two fibre hodoscopes each consisting of 0.5mm diameter fibres were placed at the two ends of the beam line. The clusters of the hodoscope hits were fitted to obtain the beam position. The mean X-and Y positions from two hodoscopes were fitted using straight line functions on Y-Z and X-Z planes and the projected positions at the GEM location on both planes were obtained. The results are shown in Fig. 3.18. The GEM spot matches well with the projected position from fitting.
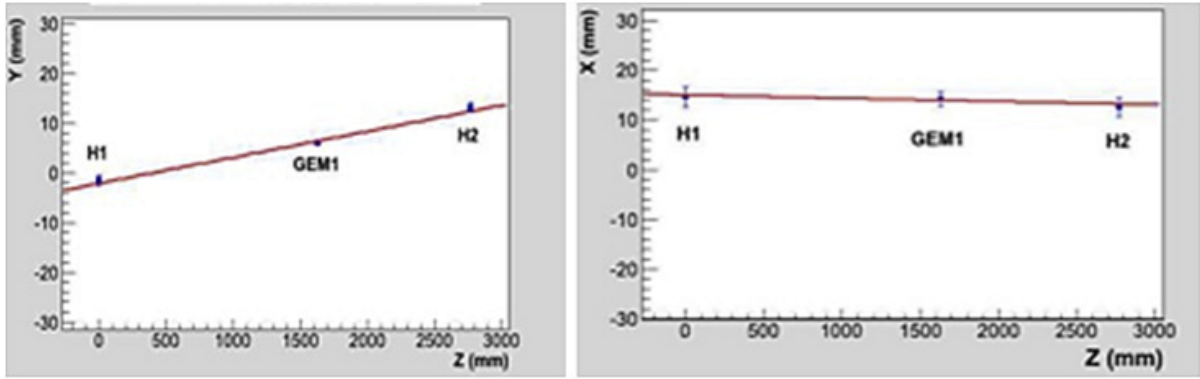
Figure 3.18: GEM hits on projected Y-Z (left) and X-Z plane (right)

3.2.5.2 Mini-MUCH at CERN

In the 2012 test beam run at CERN, we made a setup called mini-MUCH that mimicked the MUCH setup in CBM to an extent. The layout is shown in Fig. 3.19. The name mini-MUCH suggests that the setup has GEM layer and absorbers placed alternately. The total length and the width of absorbers are less than the actual MUCH setup. In addition to that, MUCH system will have 3 GEM layers in each station, while in the case of test beam run, one MUCH chamber was placed in between absorbers. IN our analysis, ADC weighted mean X, Y positions are determined from the distribution of the hits from a large numbers of events for VEC-GEM, GEM1 and GEM2 as per the labels shown in Fig. 3.19,

Mean values are subtracted event wise from each hit for respective GEMs. Event wise centroids are obtained on each chamber. The events having hits on the triggered pad of VECC GEM are used for tracking by finding the corresponding hits in GEM-1(GSI) and GEM-2(GSI). A fitting by straight line is performed by connecting the event wise centroids at VECC GEM and GEM-2 in X and Y directions separately. Corresponding X, Y positions are then calculated from the fit parameters on GEM-1. The residuals between the measured and the projected positions

on GEM-2 are plotted for all events (Fig. 3.20). The mean and width of the distributions give the mis-alignment and projection resolution of GEM-1. Our result shown in Fig. 3.20 demonstrates that the mean value of mis-alignment is negligible compared to the pad size of the GSI GEM(6mm×6mm). As per Fig. 3.20 and considering the nominal resolution of the pads, the position resolution is ≈ 0.16cm.
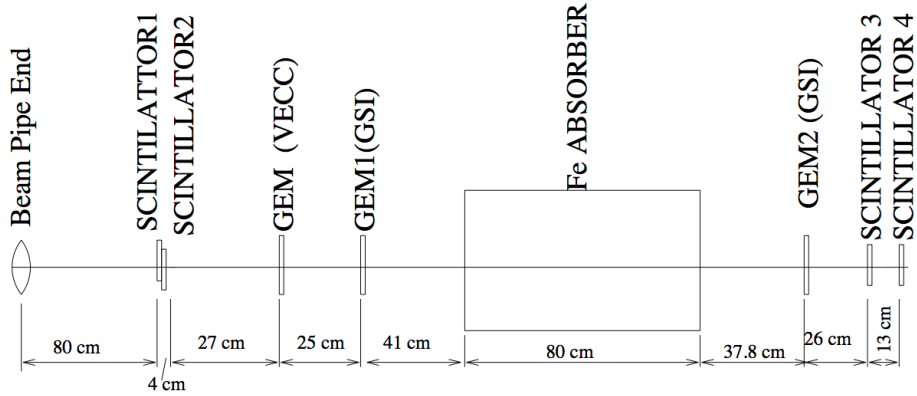
Figure 3.19: MiniMUCH configuration
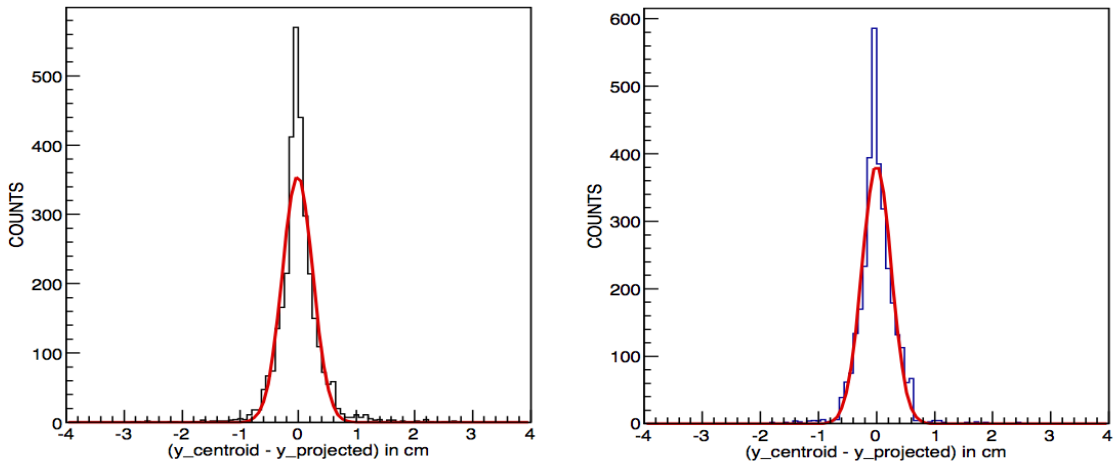
Figure 3.20: Distributions of the residuals along X and Y direction

3.2.6 Rate study

The highest density of the incident particles including secondaries on the first MUCH station is higher than 1MHz/cm^2 for central Au+Au collisions at 35 AGeV. For the smallest usable pad size (3mm×3mm), the hit density per pad is about an order of magnitude lower. In SIS100 configuration, however, the hit density reduces by a factor of four making the highest hit density requirement much below 100 KHz/pad if it operates at same rate as in SIS300 setup. The hit density requirement at larger radial distances and for stations located further downstream reduces significantly.

As shown in earlier sections, as per literature, GEM detectors have been shown to operate with

stable gain up to a beam rate of 0.1MHz/mm^2 [24], considerably higher than our maximum requirement. Earlier studies with GEMs for COMPASS and LHCb prototypes have also shown that the efficiency does not decrease appreciably up to particle rate of 10^5 Hz/mm^2 [25, 26].

In our R&D effort, the testing of the detectors at different rates is a subject of detailed future study. We present here some preliminary results of the studies undertaken so far.

3.2.6.1   Study with X-ray generator

We have performed a systematic study of the rate handing capability of the detector first using X-rays from a Cu X-ray generator and conventional electronics. The intensity of copper X-rays was varied by changing the filament current. The tests were performed in the RD51 laboratory at CERN.

For this test all the zones on the readout plane was shorted using 8 different connectors and the signal was read out from one such zone where the detector was illuminated. The detector was tested at ΔV_{GEM} across each GEM of 358V. The detector was operated at a gain of $\sim 7.10^3$.

In Fig. 3.21 the pulse height spectra acquired at similar time intervals at different rates of input X-rays are superposed with each other. The highest rate as measured by the anode current in this study corresponds to 1.4 MHz/cm^2. It is observed that with increasing intensity, integral of the curve increases, but the peak position remains reasonably stable. Observed changes in the gain of the detector, based on anode current measurement, was found to be around 10%. This demonstrates that the detector gain remains stable upto a detected particle rate of 1.4 MHz/cm^2.
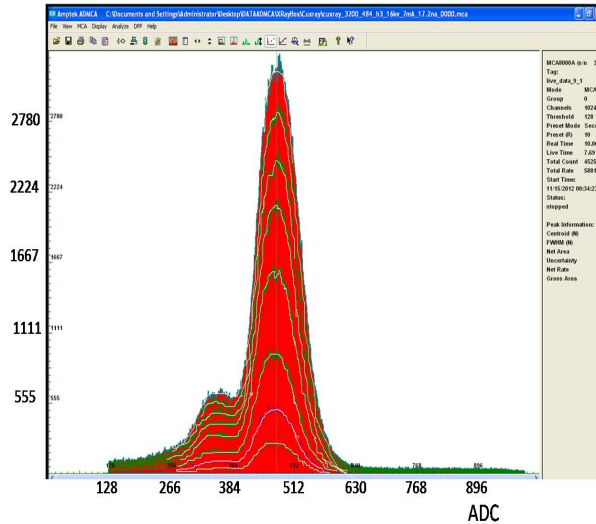
Figure 3.21: Measured pulse-height Spectra using Cu-X-ray generator (8.9 keV) of different intensities

3.2.6.2   Rate study using particle beams

The GEM detector was subjected to varyings rates of particle flux in test beams. The rate had strong variations within the spills in all the test runs. In addition to that, the rates of muons were considerably smaller compared to pion beam at SPS and proton beams at COSY. The rates at

which the detector has been operated so far showing >90% efficiency are from ∼1 KHz/cm² for muon beam to ∼200 KHz/cm² for pions and protons. The gain remains stable for this range of beam rate. In all the test runs using particle beams, we used self-triggered nXYTER electronics.

Fig. 3.22 shows the 2D histogram of the pad response of the detector, readout via nXYTER electronics at low and high beam rates of 600Hz (left panel) and 30 KHz (right panel) respectively as obtained in 2012 CERN test beam run. It is observed that, for the low intensity runs, a well-defined beam spot is seen at the centre, but the beam-spot is not clearly visible in high intensity runs. For high intensity run, a large number of pads outside the central region are seen to be affected. Additionally, the efficiency of the low intensity run was 98%, while at higher beam intensities upto 100 KHz, the efficiency dropped to as low as 50%, if only pads around the beam position were taken into account. This effect was found to be more prominent at higher gain of the detector.

Since the detector has already been operated at high rates using X-rays from the generator, it is unlikely that the behaviour observed in test beam runs is due to malfunctioning of the detector. The only difference between high intensity X-ray runs and those of the beam runs is in the use of electronics. For X-ray studies we used conventional NIM electronics but for beam tests it was the self-triggered nXYTER ASIC. If one were to focus on nXYTER, saturation of preamplifier could be one reason for the abnormal observation seen above.

This observation led us to investigate the operation of nXYTER and study its parameters that could affect the behavior at high rates. This study is described in next section.
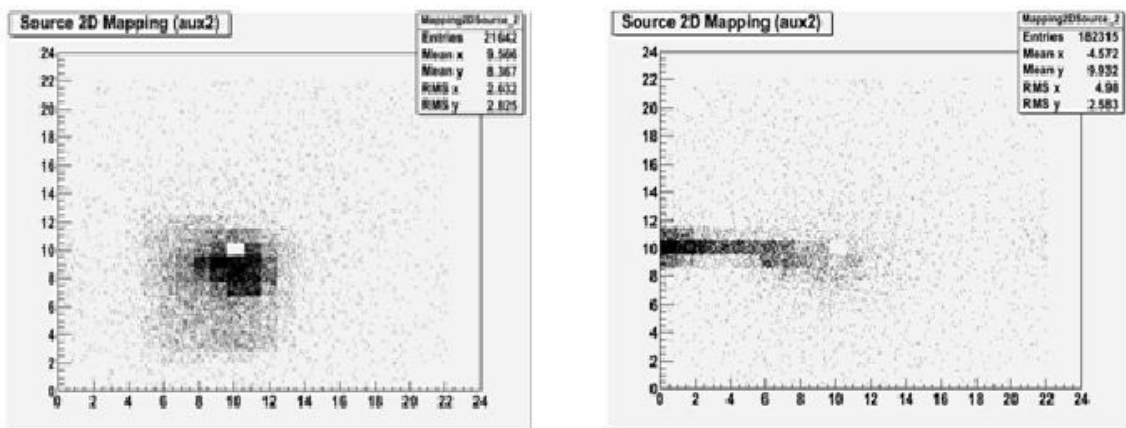
Figure 3.22: 2D beam spot for (left) low rate pion beam and (right) high rate pion beam

3.2.6.3   Study of frequency response of nXYTER

Within nXYTER ASIC a parameter v_bf_b controls the feedback resistance setting which determines the time constant of pre-amplifier discharge stage. A low value of v_bf_b is equivalent to a high feedback resistance and consequently slow time constant. For the test beam runs described before we had used v_bf_b=25 all along.

To test the frequency response of an nXYTER channel, input pulses with a charge injector was applied to the preamplifier using a 1pf injection capacitance as shown schematically in Fig. 3.23. Our first attempt at using a tail pulse as input to the pre-amplifier of nXYTER proved inconclusive [27].
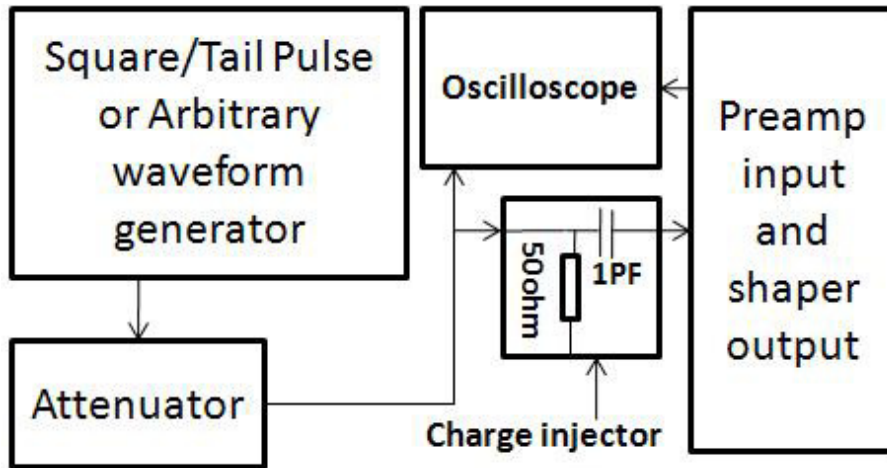
Figure 3.23: Block diagram of the testing setup for the study of frequency response of nXYTER.

Because of the falling edges that discharge the preamplifier, the effect of preamplifier saturation cannot be seen with tail pulses. Real detector pulses inject finite charge on preamplifier, which is analogous to either rising or the falling edge of the pulse, unlike the case of pulses from generators where the tail pulses have both the edges. Therefore a special type of waveform was used to simulate the detector pulse at high intensity. A ladder waveform was designed using an arbitrary waveform generator.

The ladder waveform was taken as input to the charge injector, which in turn is fed to the preamplifier on nXYTER test channel. The screenshots shown in Fig. 3.24 have three waveforms each, topmost is input ladder waveform, middle is the fast shaper output and the slow shaper output is at the bottom.

In the left part of Fig. 3.24 we see a drop in amplitude with consecutive step pulses showing the preamplifier saturation. The feedback resistance of the preamplifier is then reduced by increasing the $v_b f_b$ register setting to 80. This results in restoring the preamplifier output pulses and all output pulse heights become equal as can be seen in the oscilloscope waveform in the right part of Fig. 3.24. The output waveforms in this figure suggest that with decreasing feedback resistance, the saturation of preamplifier is avoided.

A detailed study has been carried out for the optimum value of $v_b f_b$ to be set at each frequency of operation in order to operate the nXYTER without saturation of the preamplifier. The study has been done for several values of input frequency ranging from low values of a few hundred Hz to 1 MHz and for two values of input charges, which correspond to two different gains of the GEM detector in operation.

The results are summarized in Fig. 3.25. It is observed that for higher input charge the value of $v_b f_b$ need to be still higher (equivalent to further reduction in feedback resistance) for the proper operation of preamplifier without going into saturation.

3.2.6.4   Study using X-ray source and nXYTER

To verify the results obtained from the new setup using ladder waveform as discussed previously, we have performed the testing of the triple GEM detector read out by nXYTER based readout
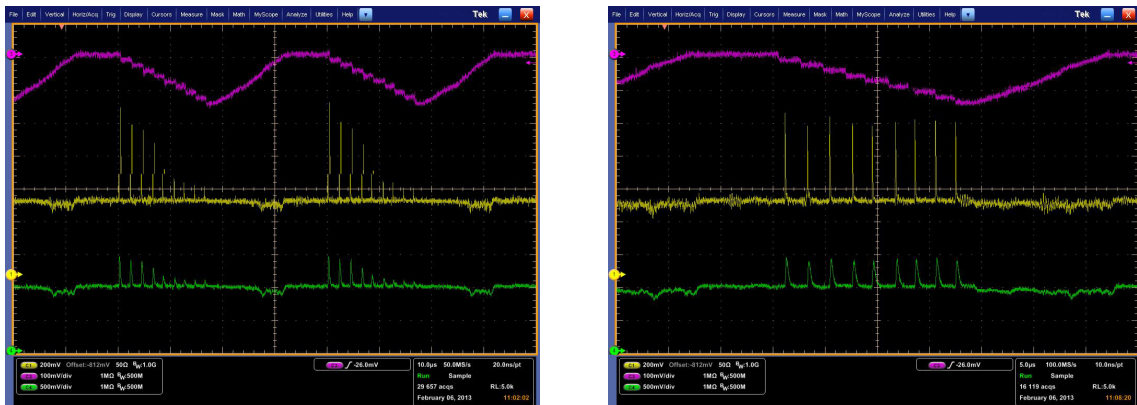
Figure 3.24: (left) Pulse shapes with 15fC input charge and v_bf_b=25 (high feedback resistance of preamplifier). The output is reducing continuously with steps. (right) pulse shapes for the same case with v_bf_b=80 (lower feedback resistance). The pulses are now are of same heights. Input frequency in both cases is 500 kHz.
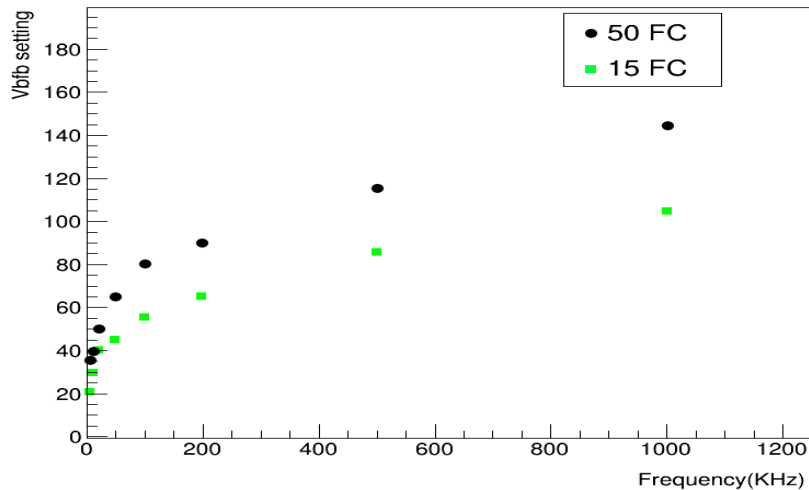
Figure 3.25: Minimum values of v_bf_b as a function of input frequency for two different setting of input charge.

system. X-rays from ^{55}Fe source was used as input. The rate of X-rays from ^{55}Fe source as measured by the detected particles could go upto 4KHz for a collimator of 2mm diameter opening on GEM detector PCB. The source was placed at constant position over the diameter opening throughout the study.

Two runs with high and low v_bf_b of 120 and 6 respectively were taken for same interval of time to get similar statistics. Fig. 3.26(left) shows the beam spot and Fig. 3.26(right) shows the amplitude spectra of the center pad for ^{55}Fe source at $v_bf_b = 6$. One can notice that there are very few entries at the centre for the case with $v_bf_b = 6$ and the amplitude reduces drastically almost merging completely with the pedestal near ADC=0 for the central pad. The beam spot also shows a hole at the centre indicating a loss in efficiency. This is due to preamplifier saturation as concluded from the ladder waveform test results. Fig. 3.27 shows the results for a higher value of $v_bf_b = 120$. It can be seen from the figures that both the pulse height spectra and beam spot of the centre pad are restored to the expected shape.
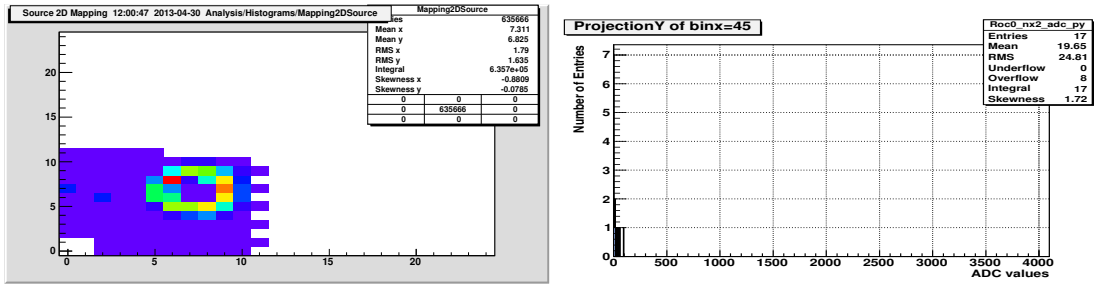
Figure 3.26: X-ray beam spot (left) and the energy deposition spectrum for the peak channel (right) at vbfb=6. With low vbfb, the energy spectrum merges with the pedestal and beam spot shows a hole in the middle.
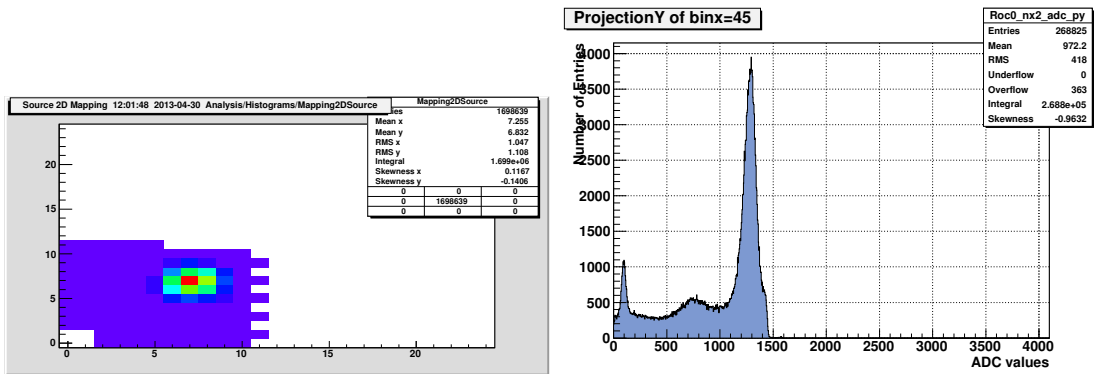
Figure 3.27: X-ray beam spot and energy deposition spectra at higher vbfb. The beam spot and energy spectra are restored.

3.2.7   Neutron irradiation

3.2.7.1   Introduction

GEM detectors installed in the first station are expected to receive substantial dose of neutrons. The neutron flux on the innermost part of the first station, as simulated using FLUKA will be $\sim 6.10^6$ cm^{-2}sec^{-1}. Although Ar + CO$_2$ gas is insensitive to neutrons, construction material of GEM, in particular the Cu layers on PCBs and GEM foils, may get activated and produce ionising signals which will act as background for the hits used in tracking of muons. We have therefore performed neutron irradiation test on the chambers. The aim of the neutron tests is two fold: to measure how many neutron hits is seen by the detector so as to have an idea of the number of background hits per event on the GEM detector and also to study the response of the detector before and after neutron irradiation, in terms of relative change in gain, or in terms of any physical damage due to irradiation.

3.2.7.2   Experimental arrangement

Neutron irradiation test was carried out at VECC K=130 cyclotron. The setup is schematically shown in the left part of Fig. 3.28 and a photograph of the experimental arrangement is shown in the right part of Fig. 3.28. Beams of 40 MeV α-particles of varying intensity were incident on a 0.5 cm thick Tantalum target for the production of neutrons. The thick target also stopped

the beam and generated a large flux of γ-rays. To screen away the γ-rays, a Pb shield of 10cm was placed in front of this target thus allowing only the neutrons. The triple GEM chamber was placed at about 80 cm away from the tantalum target and was operated at $\Delta V_{GEM} \sim 340$ Volts across each GEM layer. The gas mixture consisted of Ar/CO_2 mixed in the ratio (70/30). The GEM signal collected by the readout pads was connected to standard NIM electronics and the amplified signal was fed to an MCA from where it was recorded onto a PC. Data corresponding to different beam currents (which corresponded to different neutron intensities) were taken and the response of the detector studied. The neutron flux reaches $10^5/cm^2/sec$ at the maximum beam current of $4\mu A$.
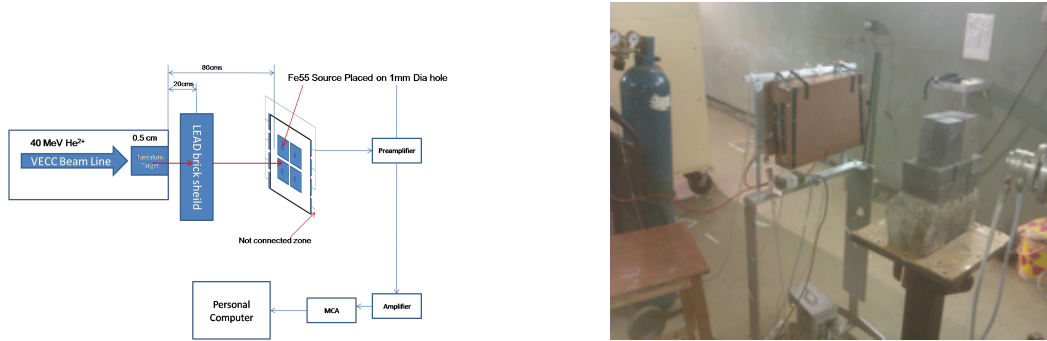
Figure 3.28: (left) Schematic of neutron irradiation at VECC cyclotron, (right) photograph of the setup. A set of lead bricks are placed in between the detector and target to stop the photon flux generated on the target.

3.2.7.3   Results

Neutrons flux was estimated by measuring the flux with BF_3 counters for current ranges from 50 nA to 500 nA. The BF_3 counter saturates above 300 nA current, the calibration curve is therefore taken from the linear fit of the non-saturated region of the curve. A calibration relation thus obtained was extrapolated to obtain the neutron flux for higher beam currents. The BF_3 counter was then replaced by the GEM detector at the same location.

Fig. 3.29 (left) shows the pulse height spectra from the detector for four different beam currents(neutron intensities) without Pb shielding. Counts have been normalized to number of GEM hits per 100 seconds per 100 cm^2. The highest neutron flux corresponding to a beam current of $4\mu A$, as derived from the calibrated fit was about 10^5 neutrons/cm^2/s. For every current setting, three sets of data were taken and the number of GEM hits for each of these sets was estimated. Fig. 3.29 (right) shows the measurement of average number of hits vs. the beam current. From the results of hit count for various neutron intensities, we find that about 350 hits/cm^2/s was seen corresponding to a maximum neutron flux of $\approx 10^5/cm^2$/s.

From the integrated count of the ADC spectra, the detector hit produced per neutron at highest neutron flux is $3.5 \times 10^{-3}/cm^2$/neutron which results in a tiny fraction of the hits produced by ionizing particles in an event. It can therefore be concluded that neutrons will not add to the background significantly.

A calculation has been performed using FLUKA in which the test setup was implemented including the target and α-beams of varying intensity. The flux obtained for the highest beam intensity was comparable to the highest flux expected on the first MUCH station in 35 GeV AuAu collisions. The total dose received by the detector was found to be about an order of
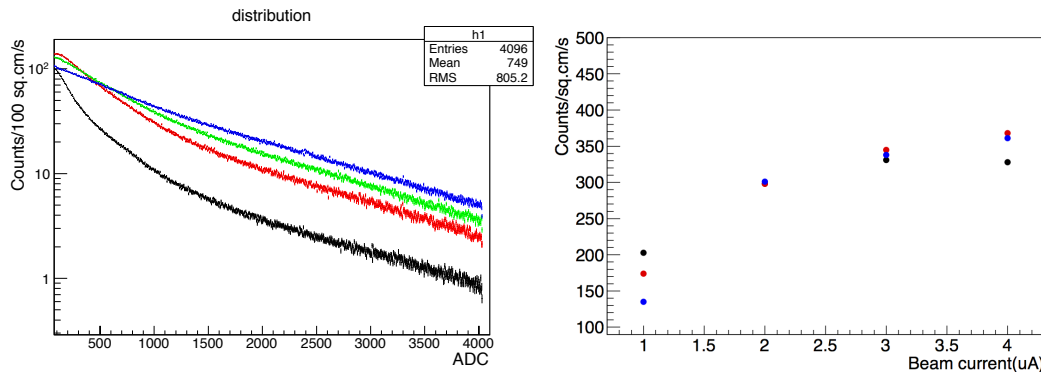
Figure 3.29: ADC spectra of GEM (left) and average hit due to neutron (right) at different beam intensities

magnitude lower compared to the expected dose in SIS300 operation of a year. The received dose in this case however can be compared to the dose likely to be received at SIS100 MUCH configuration.

3.2.8   Long term study of GEM

The GEM detectors will operate in CBM MUCH for ten years. We have undertaken a program to study the long-term behaviour of operation of GEM detectors. This study has been pursued at GSI. Preliminary results are described below.

3.2.8.1   Effect of environmental parameters

Gaseous detectors are known to be affected by environmental parameters, in particular fluctuations in the ambient temperature and pressure causes detector gain to fluctuate [28]. In order to study this effect, one triple GEM detector made from single mask technology has been tested for 15 days continuously at GEM voltages of 400-395-390 V. The ^{55}Fe spectra have been taken at 10-minute interval. The mean position of 5.9 keV ^{55}Fe X-ray peak has been recorded with time. The variation of mean as a function of time is shown in Fig. 3.30 (red lines). The ambient temperature and pressure was also recorded continuously and the T/p as a function of time is shown in the same figure as blue lines. Looking at the two curves, it is clear that there exists a definite correlation between mean and T/p which is well known for any gas detector. The correlation plot is shown in Fig. 3.31. It is found [28] that the effective gain G has an exponential dependence on the ratio T/p :

$$G(T/p) = A.e^{BT/p} \tag{3.1}$$

The T/p is the ratio of temperature and pressure. A and B are fit parameters, determined by fitting the exponential function. The corrected and normalized gain g, expected to be independent of environmental parameters, is computed from the effective gain G according to

$$g = \frac{G}{Ae^{BT/p}} \tag{3.2}$$

An exponential fit to the correlation plot is also shown in Fig. 3.31. The variation of normalized gain with time as obtained by Eq. 3.2 is plotted in Fig. 3.32. There is about 10% peak to peak variation of gain with time even after normalization. This variation comes from the variation of
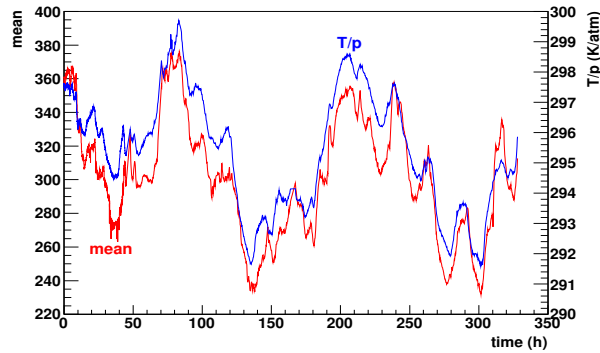
Figure 3.30: Mean position of ^{55}Fe peak as a function of time (in red, left axis) and T/p as function of time (blue, right axis). There is a definite relationship between mean and T/p.
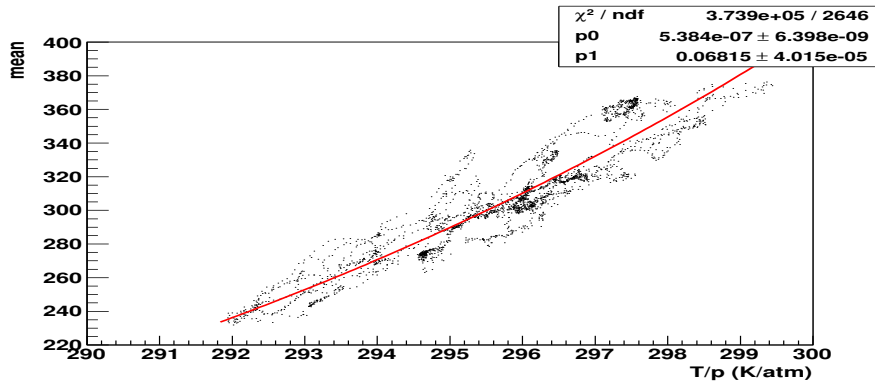
Figure 3.31: Correlation between detector gain and ratio of temperature and pressure. Exponential fit is also shown.

O_2 concentration in the gas and variation of gas ratio due to change in characteristics of mass flow controller with temperature. The variation of energy resolution with time for the detector is shown in Fig. 3.33. The resolution is seen to vary between 17-20% in the whole period of operation.

3.2.8.2 Ageing study

An infrastructure has been set up at the GSI detector laboratory to study the ageing properties of gas filled detectors such as multi wire proportional chambers (MWPC), gas electron multipliers (GEM) among others[29, 30]. It has been found earlier that GEM can withstand a cumulative dose of 7mC/mm^2[31]. An accuracy in the relative gain measurement better than 1% has been achieved by monitoring environmental conditions and by systematic improvements of the measuring equipment [30]. The ageing study of one GEM module is performed in the same ageing measurement set-up by using an 8 keV Cu X-ray generator to verify the stability and integrity of the GEM detectors over a period of time. The setup is schematically shown in Fig. 3.34.

The GEM has been operated at 395-390-385 V with drift, induction and transfer fields at 2.5 kV/cm, 2 kV/cm and 3 kV/cm respectively. The centre of the upper part of the GEM (region A) was exposed to high rate Cu X-rays for 10 minutes. Subsequently the ^{55}Fe spectra have been collected for 1 minute each from upper and lower part (region B) of the GEM. The
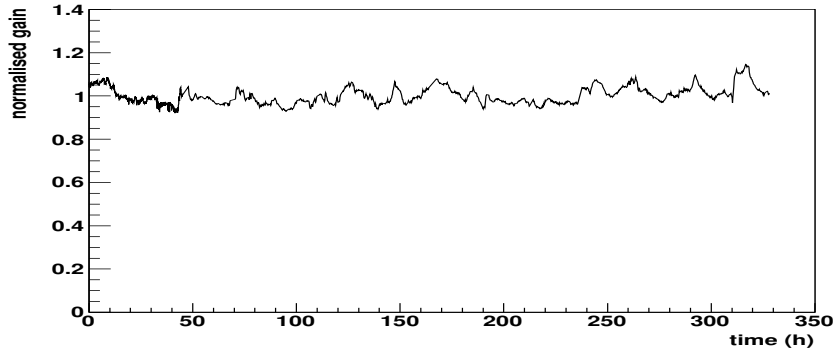
Figure 3.32: Normalized gain vs time
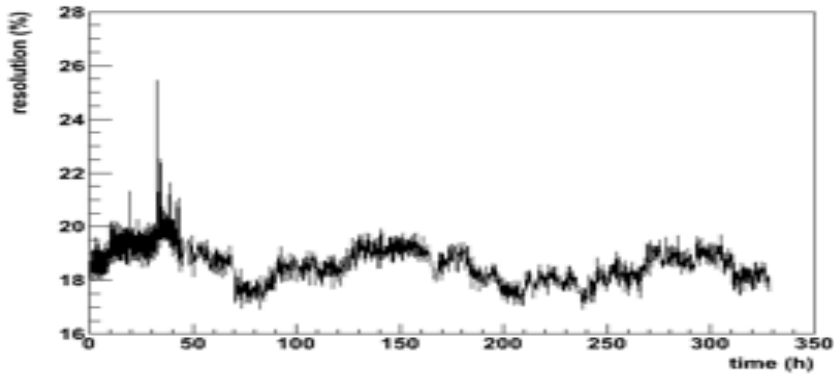
Figure 3.33: Energy resolution vs. time. The energy resolution varies between 17-20% during the period of data taking

^{55}Fe source has been placed in such a way that the X-rays direct toward the upper part of the GEM in the same spot, which was exposed by Cu X-ray. The ratio of the mean positions of 5.9 keV ^{55}Fe X-ray peak from upper side and lower side of GEM is the normalized gain and corrects the effect of pressure and temperature variations. The whole measurement is performed for about 70 hours. The rate of the Cu X-ray was about 240 kHz. The rate of X-ray on two sides of the detector as a function of time is shown in Figure 3.35 which are nearly constant at 60 and 240 KHz respectively. The lower part of the detector was only illuminated with ^{55}Fe X-ray source. It should be noted that the highest rate is comparable to the rate expected at SIS100 MUCH environment.

The mean position of the ^{55}Fe peak for the two zones as a function of time is also shown in Fig. 3.35. The mean varies with time due to change of pressure and temperature. The gains from the two regions are slightly different due to the difference in gain of the pre-amplifiers. The gains from two parts are shown to vary upto a maximum of 10%. It should be noted that at this gain, efficiency does not change significantly as shown in the plateau earlier. The accumulated charge on the detector is calculated from the rate of the X-ray and average gain of the detector. The normalized gain studied as function of accumulated charge per unit area shows no sign of ageing after accumulation of more than 0.04 mC/mm^2. The resolution from both parts varies between 16% to 19% in the period of operation. However, there is no significant variation with increase in beam rate.
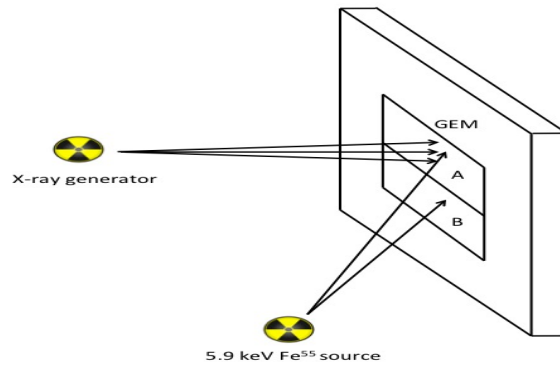
Figure 3.34: Schematic of the setup to study ageing of GEM.
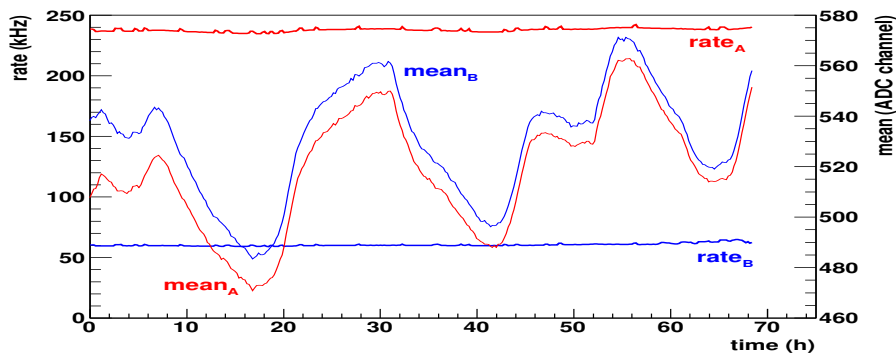
Figure 3.35: (left axis) : Rates of X-rays falling on regions A and B of GEM as a function of time, (right axis) : Mean position of ^{55}Fe peak vs. time in the two zones A and B.

3.2.9 Intermediate size GEM detector

So far all our R&D activities towards building GEM detectors and studying its characteristics have been carried out using standard 10cm×10cm GEMs. However, the actual layout option of the CBM detector consists of large (1 m x 0.5 m) sector shaped chambers. Hence, as a next step towards approaching the actual design of the tracking chamber modules, it is required to build and investigate the performance of a detector with large size GEMs.

As next step towards building large sector-shaped detector as required for MUCH, we have built a triple-GEM detector of intermediate size (30cm×30cm). One major feature of this detector is that the readout plane is sector-shaped with projective geometry of 1 degree angular separation. For the ease of fabrication, pads are rectangular with dR=R$\Delta\Phi$.

GEM foils being 50 microns thin need to be stretched, which is followed by gluing on a FR4 based boundary frame. Stretching and gluing of GEMs are delicate operations and the technicalities involved in handling 10cm×10cm standard GEMs, cannot be just scaled to large pieces. Large area increases the chances of mechanical sagging of GEMs. This has to be prevented by ensuring that there is no under-stretch and also by using edge frames with thin supporting cross ribs which have a minimum of dead area. The edge frames bare 1 mm thick and typically 1.5 cm wide. Care has to be taken that there is no overstretch, otherwise it causes the opposite corners to bend. The foil clamped in a suitable jig can be stretched either mechanically or by using thermal techniques. Each of these procedures has their own advantages and disadvantages. The

conventional mechanical stretching, though fast, may lead to problems of membrane-creeps. This foil creep can be avoided if one follows the thermal stretching technique. Such a technique has been followed by several groups in the world. At VECC, we apply the the thermal stretching technique as our first attempt to stretch and frame large size GEMs. The goal is to arrive at an efficient production procedure for making such large GEM modules. We have discussed in chapter-4, while discussing the fabrication plan of large chambers, other options of stretching techniques which could be employed. GEM foils of 30cm×30cm were procured from CERN

Figure 3.36: One single layer 30cm×30cm GEM detector

along with the edge frames. The thickness of these frames is equal to the gaps between the two consecutive GEMs. Fig. 3.36 shows the picture of a raw GEM foil. The top surface of the foil is segmented into 12 strips. This reduces the overall capacitance of the foil, so that no severe discharge takes place. This foil was sandwiched between perspex frames of appropriate dimension as shown in Fig. 3.37. The Perspex jig was then heated using lamps as shown in the
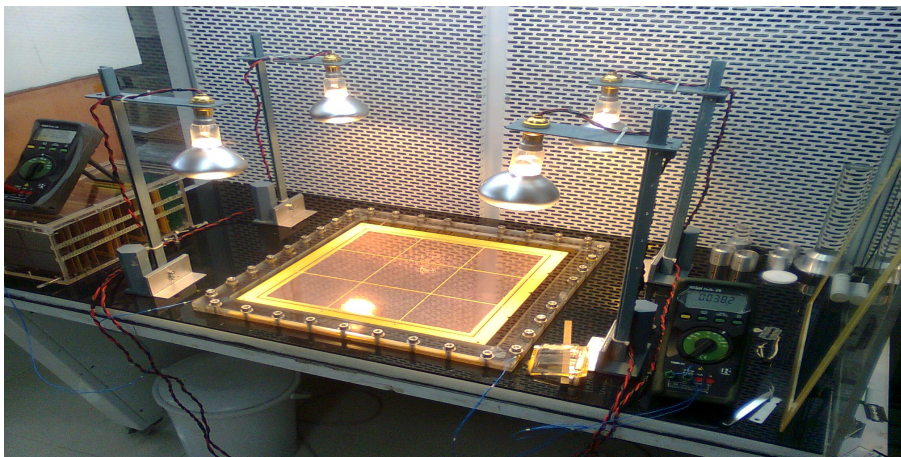
Figure 3.37: Jig for thermal stretching of GEM foils

Fig. 3.37. Once the membrane became tight at optimum heating, a thin layer of glue was then applied on the surface of the edge frame and the frame was then gently placed over the stretched foil. The entire assembly is then left undisturbed for at least 20 hours for the glue to settle and fix. It is very important to control the temperature of the frames to prevent overstretching. We built appropriate temperature controllers for this purpose which maintained the temperatures to about 45°C with a permissible deviation of 1°C.

The framed single-GEM put in a chamber was tested in $Ar/CO_2(70/30)$ gas mixture at ΔV_{GEM} of about 520 V. The GEM was placed on a readout plane having three strips and together with the drift plane, the assembly was placed in a specially built chamber as shown in the Fig. 3.38. Appropriate provisions were made to allow ^{55}Fe X-rays to pass through. Data were collected using
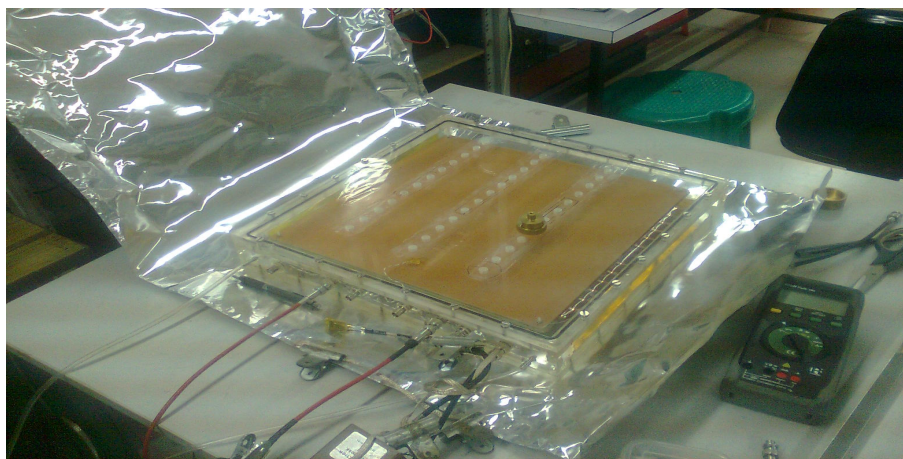
Figure 3.38: Single 30cm×30cm GEM foil under test with ^{55}Fe source at VECC.

conventional NIM electronics and with source placed at several places on the chamber in order to estimate the gain variation. Fig. 3.39 shows the distribution of the relative gain determined for 16 different positions. A variation of ~6% is seen from the RMS of this distribution, which implies a reasonably low gain variation that might be attributed to the variation of hole dimensions in the foil. Three single GEM foils thus stretched are then mounted on a chamber. Resistive chain
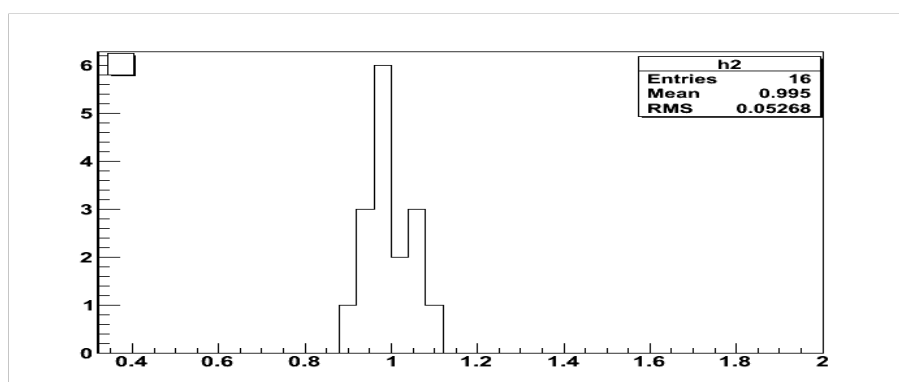
Figure 3.39: Relative gain distribution for the first indigenously stretched 30cm×30cm GEM foil.

has been used for application of voltage. The readout plane is segmented in a way similar to the final segmentation plane (Fig. 3.40). Fig. 3.41 shows the Fe-55 spectra at two different voltages showing clearly defined peaks. The uniformity for triple-GEM chamber was about 10%.

This chamber has been tested in December-2013 at COSY-Juelich using high intensity proton beams. Preliminary results as discussed below showed that the chamber could be operated at higher rate without any degradation of efficiency.
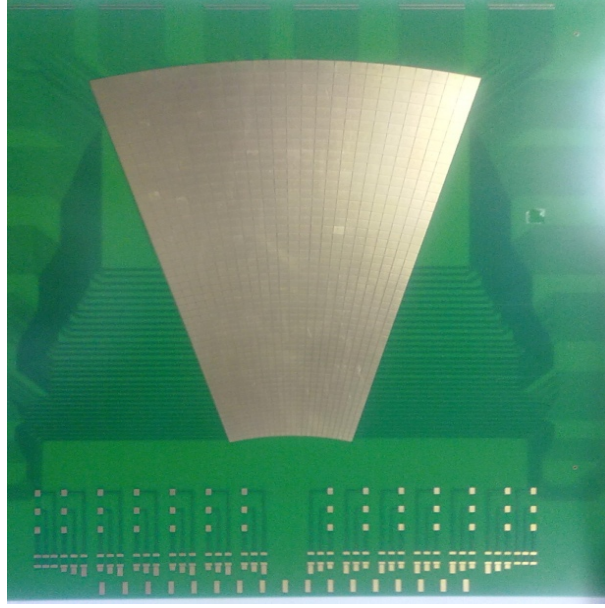
Figure 3.40: Sector-shaped readout PCB
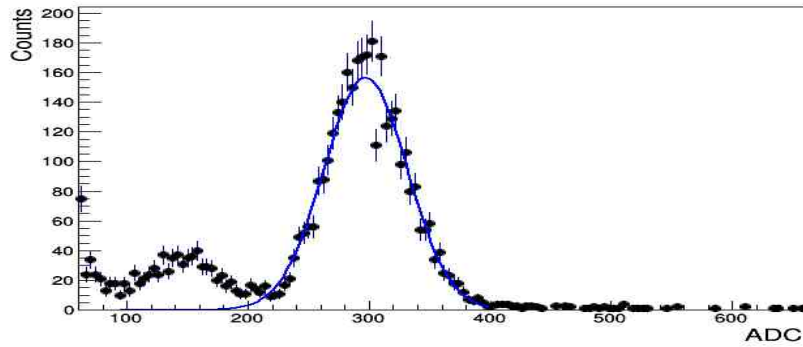
Figure 3.41: Spectra of X-rays from Fe-55 source measured by triple-GEM chamber of 30cm×30cm size GEM

3.2.9.1   Testing of the intermediate size GEM chamber

The schematic layout of the experimental setup used at COSY beam line in December 2013 is shown in Fig. 3.42, GEM1 and GEM2 represent two small (10 cm × 10 cm) size chambers of 512 readout pads each of $3\ mm \times 3\ mm$ in size and 256 readout pads each of $6\ mm \times 6\ mm$ size respectively. The drift, transfer gap-1, transfer gap-2 and induction gap of GEM1 and GEM2 are $(3\ mm, 1\ mm, 1\ mm, 1.5\ mm)$ and $(3\ mm, 2\ mm, 2\ mm, 2\ mm)$ respectively. GEM3 is a $31cm \times 31cm$ detector with trapezoidal readout geometry. The readout pads are increasing in size from $2.97\ mm \times 2.97\ mm$ to $11.21\ mm \times 11.21\ mm$. The drift gap, transfer gap and induction gap of GEM3 are same as of GEM1. In this test setup, 3 GEM detectors along with 3 STS detectors were tested using proton beam of momentum 2.36 GeV/c.

As the readout system, nXYTER based ASIC readout system has been used. A special grounding scheme was in place to reduce the noise considerably as measured by very low hits in no beam condition. The coincidence signal, generated by coincidence of upstream scintillators was distributed to the ROC auxiliary channels to record the coincidence time-stamps. GEM1 was
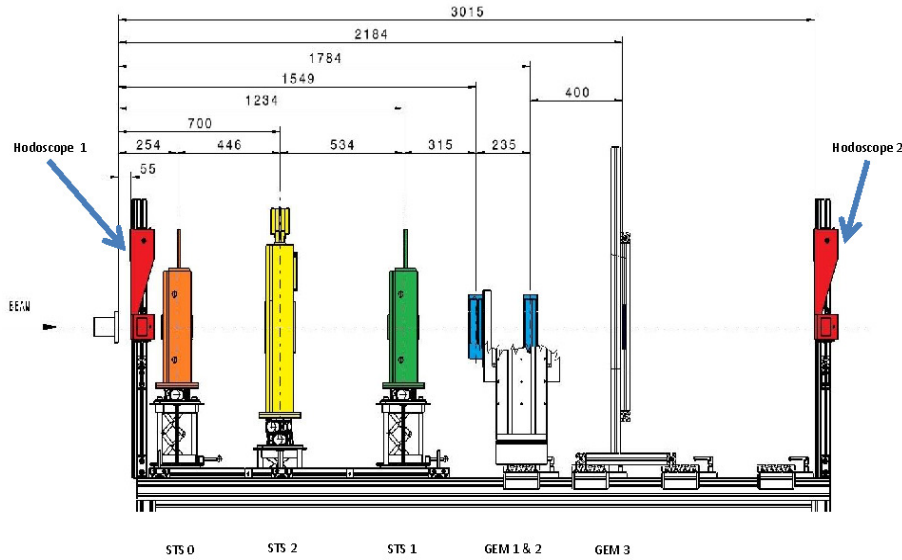
Figure 3.42: Experimental Setup at COSY in December 2013, the 31 cm × 31 cm size chamber was tested in this setup.

readout by 4 FEBs connected to 2 ROCs and GEM2 was readout by 2 FEBs connected to one ROC. GEM3 was readout by 8 FEBs connected to 4 ROCs. Here mainly the results of the GEM3 are reported.

The first step of analysis of data is to obtain the distribution of time difference between the time stamps of the hits and that of the coincidence signal. The time correlation spectra is shown in Fig.3.43 for GEM3 at $\Delta V_{GEM} = 366.30\ V$.
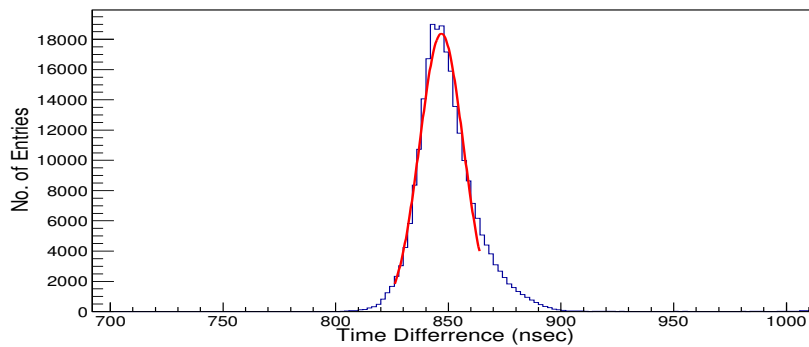
Figure 3.43: Spectra of the time correlation between GEM hits and the hodoscope coincidence signal.

The position of the peak depends on the nXYTER parameters and the cable delay. The spectra is a well defined Gaussian distribution. The fitted width (σ) varies with ΔV_{GEM} as shown in Fig. 3.44. The width is related to the time resolution of the detector which improves with ΔV_{GEM} reaching a minimum value of 11.41 nsec at $\Delta V_{GEM} = 366.3\ V$. This value is comparable to the standard value reported for GEM. Only hits within the time correlation peak are taken for analysis.

The hits within the time-correlation peak are considered to be correlated with the coincidence
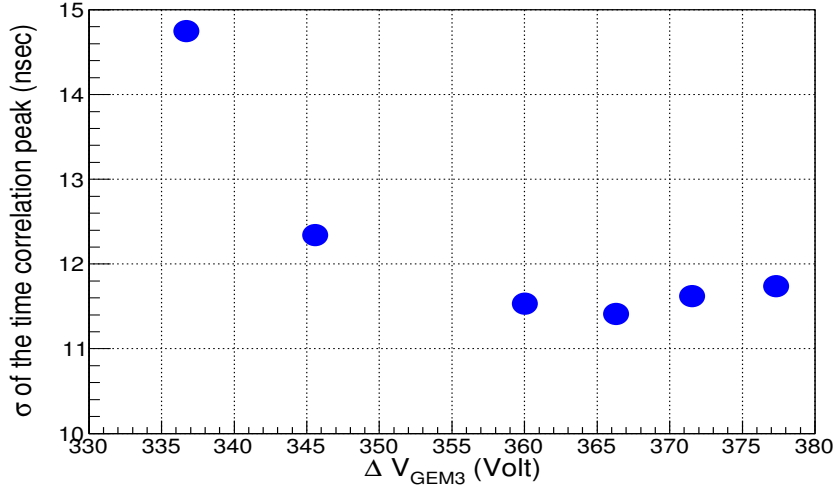
Figure 3.44:   Variation of the σ of the time-difference distribution with ΔV_{GEM} for GEM3
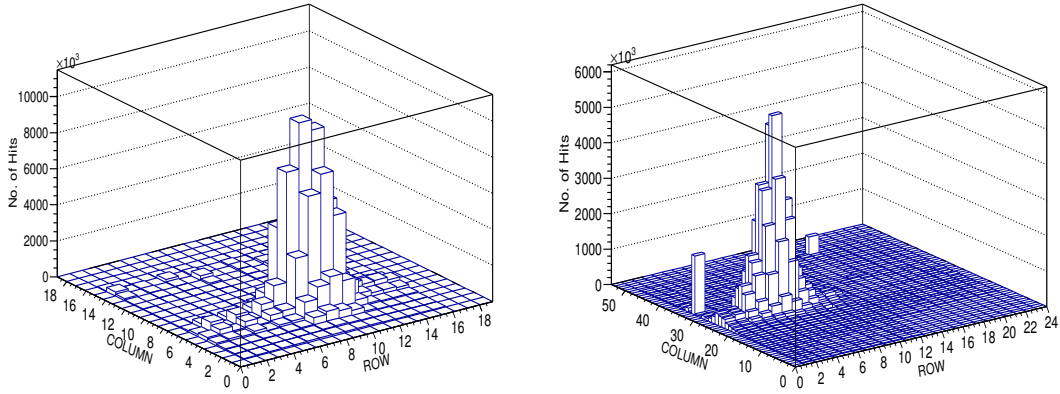
Figure 3.45: Proton beam profile of GEM2 (up) and GEM3 (down) for $\Delta V_{GEM} = 381.64\ V$ at 400 KHz particle rate

signal. The beamspots are drawn with the co-ordinates (row, column) of the hits in the detector. During a beam run, the beam position was not constant during the entire run. The position of the beam was moving from one pad to the adjacent one and again back to the previous pad which was confirmed by the beam hodoscope. The beamspot seen on GEM3 is peaked around few cells only due to narrow profile of avalanche in the GEM foil. Fig. 3.45 shows the beamspot on GEM2 and GEM3 respectively at $\Delta V_{GEM} = 381.64\ V$ and $\Delta V_{GEM} = 374.44\ V$ respectively at 1.2 MHz/cm^2 particle rate. As can been seen from the figure that we do not observe any structure inside the beamspot at higher intensities as was seen earlier before adjusting Vbfb parameter of the nXYTER.

For obtaining the efficiency we have taken the coincidence of signals from the hodoscope with the signals seen on GEM2. The variation of the efficiency with ΔV_{GEM} is shown in Fig. 3.46 for high particle rates. The efficiency reaches 95% at $\Delta V_{GEM} = 360.01\ V$. It is clear from the plot that GEM3 may be operated at $\Delta V_{GEM} = 366.30\ V$ with almost 98% efficiency. This value is above the pre-requisite value ($> 95\%$) for the operation of CBM-MUCH for MIP to detect muons efficiently.

Due to the narrow profile of the electron avalanche in GEM, the beamspot is expected to cover
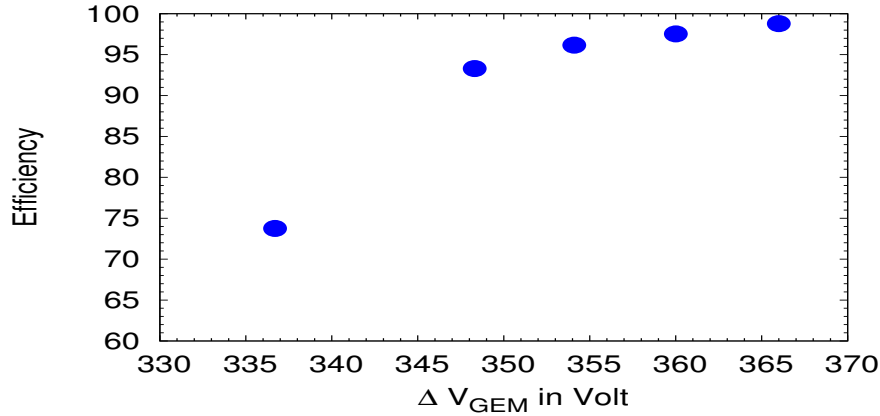
Figure 3.46: Efficiency Vs. ΔV_{GEM} for GEM3 at High Intensity (400 KHz)

about three strips of $600\mu m$ width. So, for the readout pad used in GEM3, the beam profile should be within one pad. Fig. 3.47 shows the cell multiplicity of GEM3 at $\Delta V_{GEM} = 366.30\ V$. The cluster is mostly confined within one cell. In Fig. 3.48, the variation of cell multiplicity is
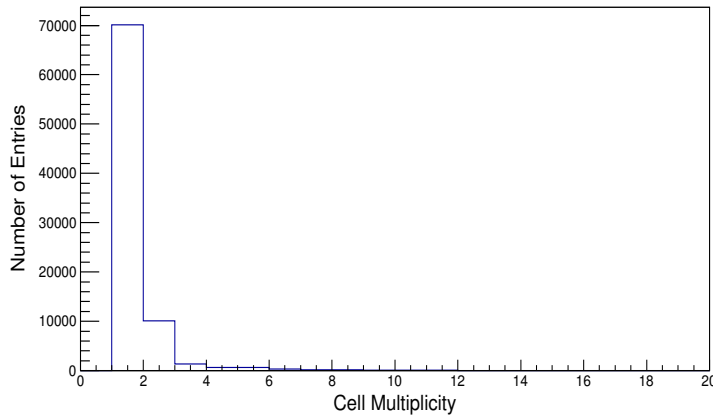
Figure 3.47: Event by event Cell multiplicity distribution for $\Delta V_{GEM} = 366.30\ V$. The pad size at the beamspot is $6.92\ mm \times 6.92\ mm$.

shown with ΔV_{GEM} of GEM3 for the pad of area $5.36\ mm \times 5.36\ mm$. From the plot it is clear that the cell multiplicity increases with ΔV_{GEM} mainly because of the increase in gain resulting in large transverse area on the GEM. The pedestal subtracted event by event ADC distribution for the pads of highest strength and fitted with Landau distribution is shown in Fig. 3.49 for GEM3 for $\Delta V_{GEM} = 366.30\ V$. The MIP spectra at different ΔV_{GEM} have been fitted to find the MPV values of the distribution. As the ΔV_{GEM} increases, the ADC spectra start to saturate due to limited dynamic range of the nXYTER. The variation of the MPV values with ΔV_{GEM} of GEM3 is shown in Fig. 3.50. The MPV values increases exponentially with ΔV_{GEM}. The trend is same in case of high particle rates.

It is evident from the results shown above that the intermediate size chamber has been tested successfully with the high intensity proton beams. The efficiency remains above 95% and the cluster size is mostly limited to one cell. For larger pad size the cluster size reduces. With limited beam time period, we have performed some testing of the uniformity of gains over the
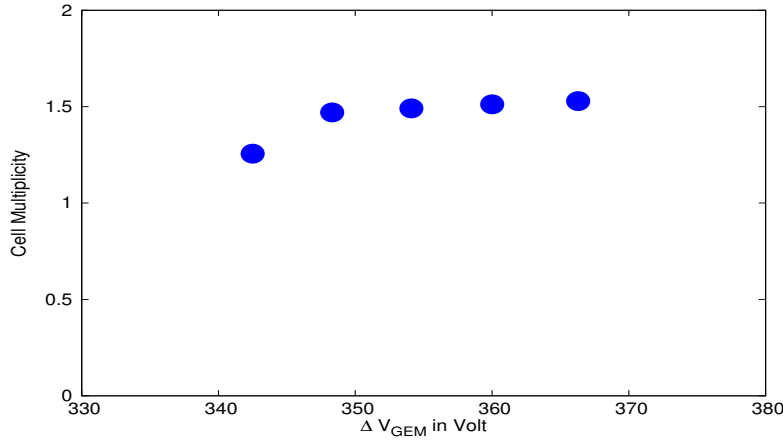
Figure 3.48: Variation of Cell Multiplicity with ΔV_{GEM} for GEM3
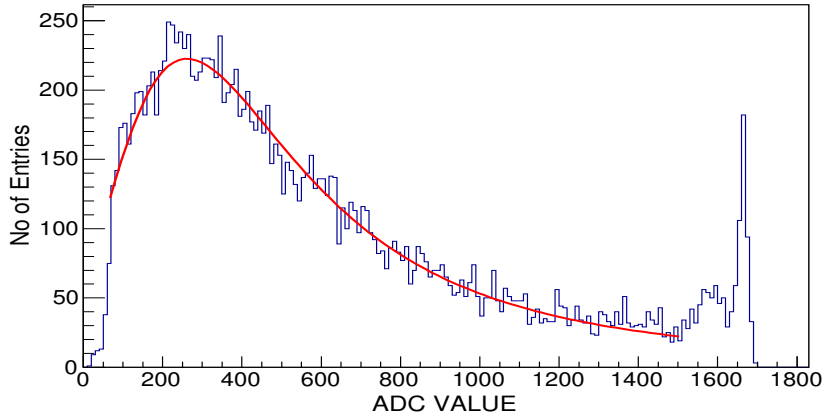
Figure 3.49: ADC spectra on the readout pad with highest strength for GEM3 at $\Delta V_{GEM} = 366.30\ V$

detector area of varying pad size. The gain remains reasonably constant. We would therefore like to stress that the this intermediate size chamber is an important step towards the real size prototype chamber for several features of large chambers have already been implemented in the intermediate size chamber. Some of the features are mentioned below.

- The intermediate size chamber has HV segmentation the size of which is similar to that of the real size chamber

- The intermediate size chamber has semi-projective geometry with the minimum pad size same as that of the real size chamber

- It should be noted that, even though the area of the current chamber (31 cm x 31 cm) is about a factor a three smaller, however the pad sizes are varied to reach to almost the largest size pad of the real chamber

- The chamber has been tested with a self-triggered readout as will be done in case of real size chamber.
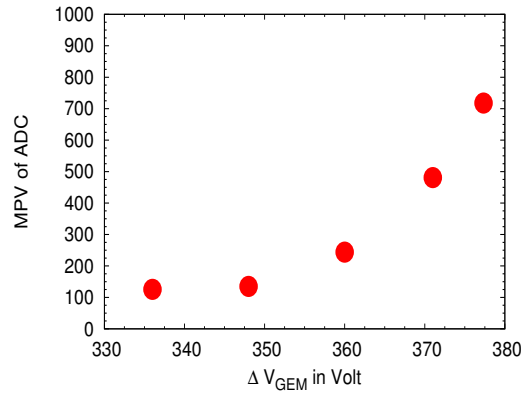
Figure 3.50: variation of MPV values with ΔV_{GEM}

3.2.10 Real size prototype chamber for the first station of MUCH

After successful fabrication and testing of the intermediate size chamber, we have started working on building the real-size prototype which will be suitable for the first station of MUCH. Some of the challenges that require special care for building the real size chamber are : (a) building of a large size chamber PCB (b) fabrication of a large size GEM foil (c) stretching of large size foils and (d) proper layout of the tracks to accommodate the variation in occupancy. We have been working in close contact with the RD51 collaboration at CERN and the CMS upgrade group. For the CMS forward tracker upgrade, triple-GEM chambers of similar sizes are being built. A large amount of R&D have been performed to deal with the issues mentioned above. We were therefore confident that with the available inputs from CERN, we will be able to fabricate the chamber rather quickly. We go over each of the items separately.

- Building of large size chamber PCB: The chamber PCB will have multi-layer configuration with a large number of blind-vias. This makes the fabrication procedure difficult. One option could be to use more than one smaller size PCBs and join them together. This might be the only option for the downstream chambers which are of larger area, however for the first station, we have found a vendor in India who is able to build a large size sector-shaped PCB. The gerber layout of the chamber PCB and the photos of two sides of the fabricated chamber PCB are shown in Fig. 3.51 and Fig. 3.52 and Fig. 3.53 respectively.
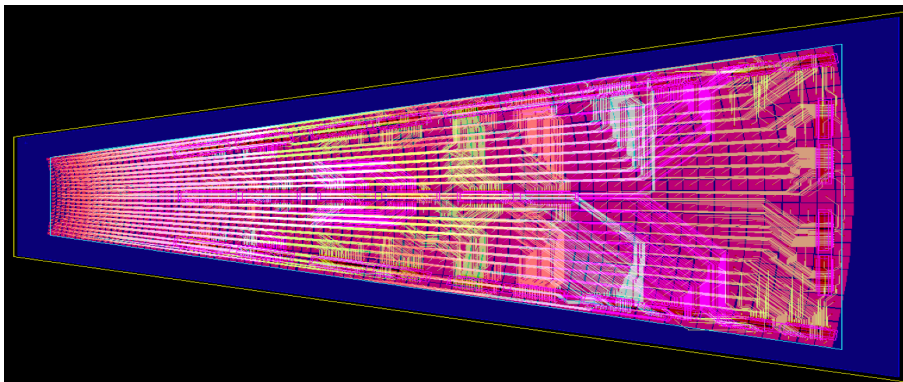
Figure 3.51: Gerber layout of the chamber PCB of the real size prototype chamber
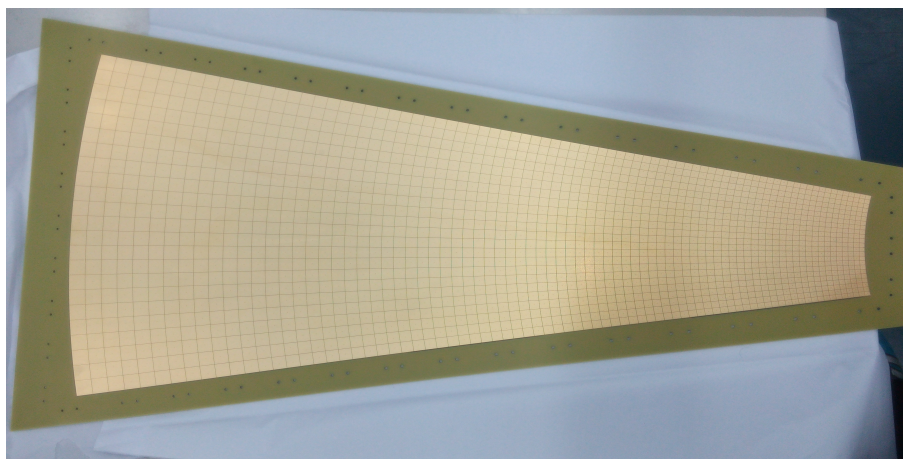
Figure 3.52: Photo of the fabricated chamber PCB of the real size prototype chamber (inner side)
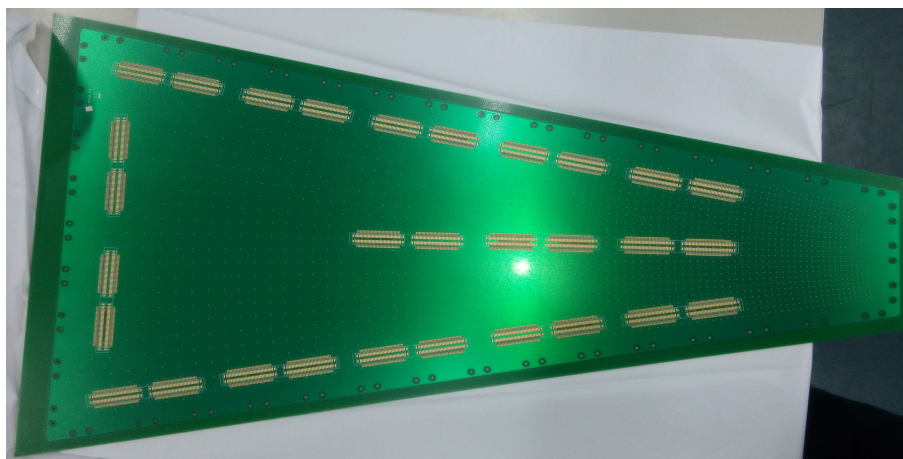
Figure 3.53: Photo of the fabricated chamber PCB of the real size prototype chamber (outer side)

- Fabrication of large size GEM foils: The GEM foil for the prototype chamber is being built at the PCB lab-CERN. The GEM foils being fabricated will have provision of stretching by NS-2 technique. We had several rounds of discussions and a final layout has been arrived at including the positioning of the connectors for signals and HV divider. The layout of the HV segmentation is shown in Fig. 3.54. The segmentation is made based on the occupancy of the chambers in Au+Au collisions at SIS-300 energy. It is therefore expected that the chamber will be able to handle particle rate at SIS100 quite comfortably. We have also shown the HV divider connections on the drift plane in Fig. 3.55.

- We have decided to use the NS2 technique developed at CERN which has the advantanges that (i) foils can be easily replaced (ii) no permanent gluing is done and the foil could be reused, if required. We show the basic principle of NS2 technique in Fig. 3.56. The specially designed screws will have provision to connect to the matching holes in the GEM foils and then the screws could be tighten to get the stretching done.

- Track layout: This has been done very carefully by using multi-layer PCB and the connectors are set in such a way that the maximum occupancy could be less than 5%. While
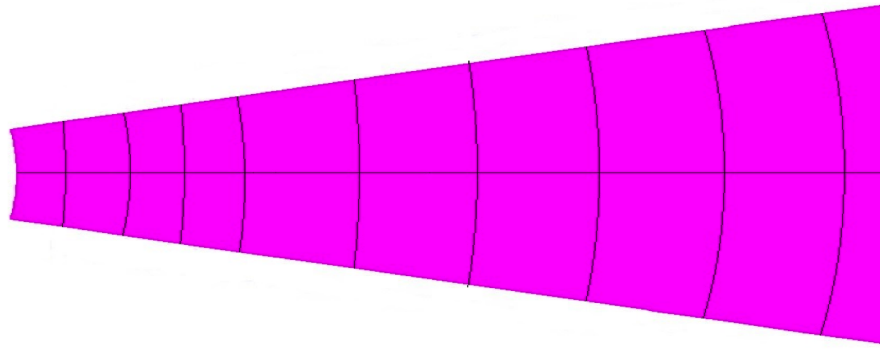
Figure 3.54: Partial layout of the HV segmentation on the GEM foils
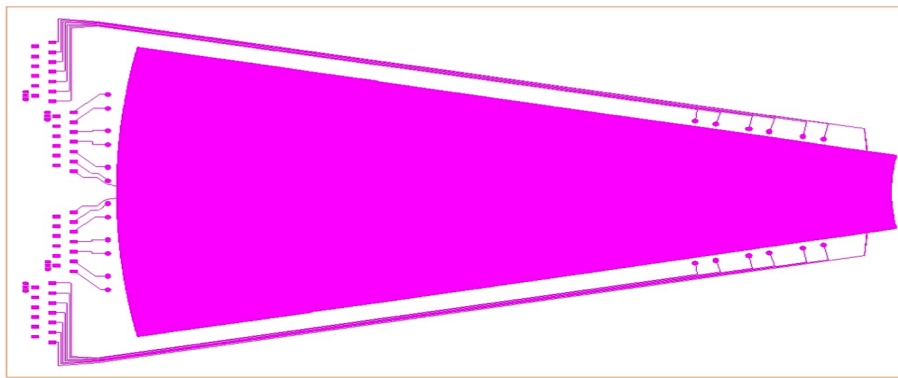
Figure 3.55: Connections of the HV divider on the drift plane

designing the region to be covered by the connectors, it has also been taken care of that the data rate to be handed by the readout ASIC for CBM is within limit of its capability.

The main design criteria of our real-size prototype chamber are: (a) Each GEM foil is segmented into two halves, (b) Each half further segmented into 12 sections, so a total of 24 sections of the foil per layer, (c) HV dividers are facilitated at the Drift plane unlike in our 31 cm x 31 cm case, (d) The active area is divided into 4 zones, each zone is connected to separate HV divider. This is achieved by the drift plane segmented into 4 zones, (e) This way in case the number of FEBs are less than required, still then we can cover one complete zone with both HV and readout electronics, (f) We can as well try to combine all the zones with appropriate jumpers, if required.

Fig. 3.57 shows the schematic layout of the assembly of different layers to build the final chamber. The gap widths are maintained same as that of the intermediate size chamber. The production plan and the required time could be divided into following steps: (1) Physical inspection of the readout plane, and the drift plane. (this involves basically pad/tracks connectivity and the dimension check, 2-3 days), (2) Physical Inspection of the holes of each GEM foils, (3) Leakage current test of the foils - segment by segment (4-5 hours/foil), (4) Inspection of the stretching frames and their alignment (1 hour), (5) Mounting and stretching of the GEMs using NS2 stretching technique sandwiched between drift plane and readout plane (5 hours) , (6) Gas tightness check - the volume will be sealed via O-rings. NS2 technique does not involve any gluing process, (7) Soldering of the connectors on the readout plane: (2 days, 30 connectors), (8) Soldering of protection resistances and resistive chain (4-5 hours), (9) Test of the chambers in lab using either β or cosmic rays, (10) Gain uniformity measurement in lab using X-rays (5
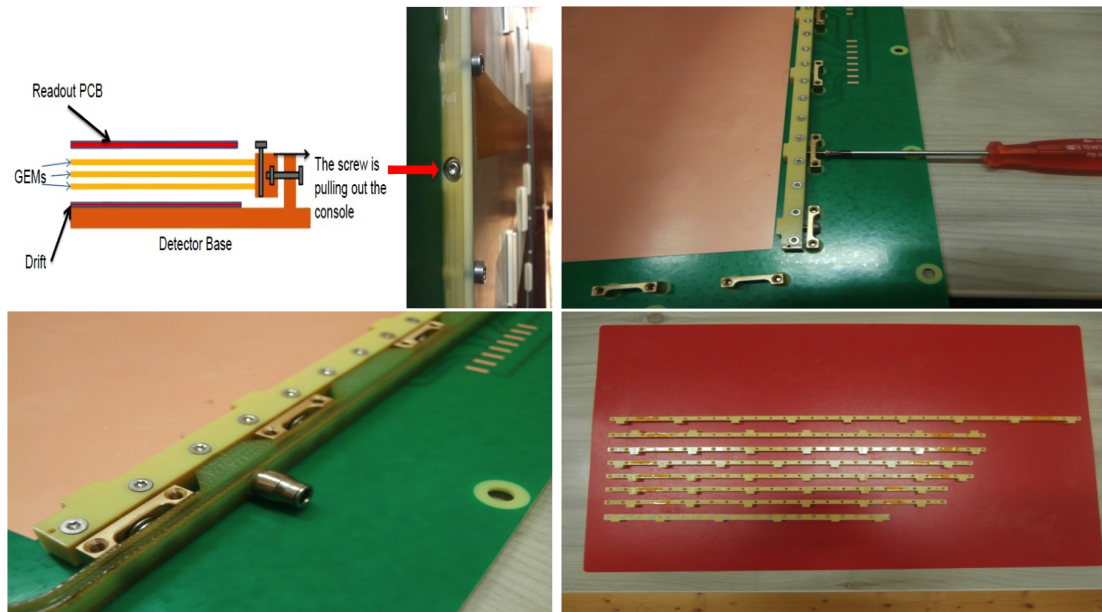
Figure 3.56: GEM foil stretching using NS-2 technique, (top-left) special screws connected to spacers on the edge of the chamber, (top-right) A chamber ready for NS-2 stretching, (bottom-left) a GEM foil stretched and assembled, (bottom-right) view of several layers.
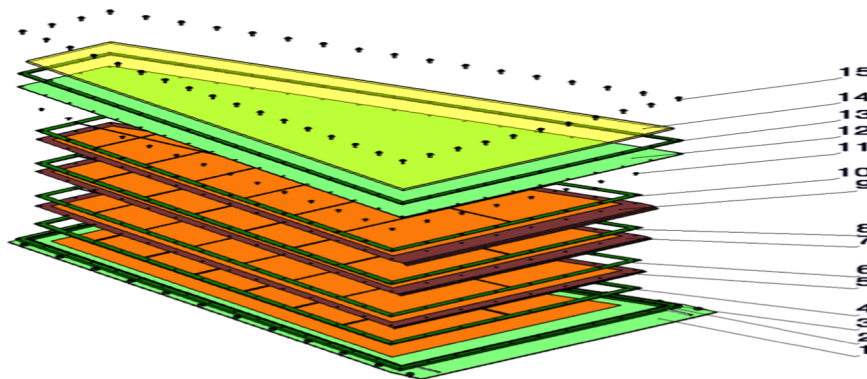
Figure 3.57: Schematic layout of assembly of different layers to build a final chamber

days)

This takes about 10 -12 days for one chamber initially, for subsequent modules, the time required is expected to reduce.

3.2.10.1   Results from CMS-GEM prototype built using NS-2 technique

We would like to discuss about the forward GEM trackers developed at CERN using the technique which we have planned to follow [32]. These results will give an idea about the use of these techniques in building such large chambers. It should be noted that, we also plan to use GEM foils from the CERN PCB lab and the techniques will be similar to the one used by the CMS collaboration for their forward tracker. The CMS collaboration has developed large size prototypes of various sizes (from 99 to 120 cm in length and 22 to 50 cm of width). These chambers have been built using the NS-2 technique and tested with X-rays and with test beams.

Fig. 3.58 shows one such chamber built using the technique mentioned above. The right figure shows the chamber with electronic boards connected to them.
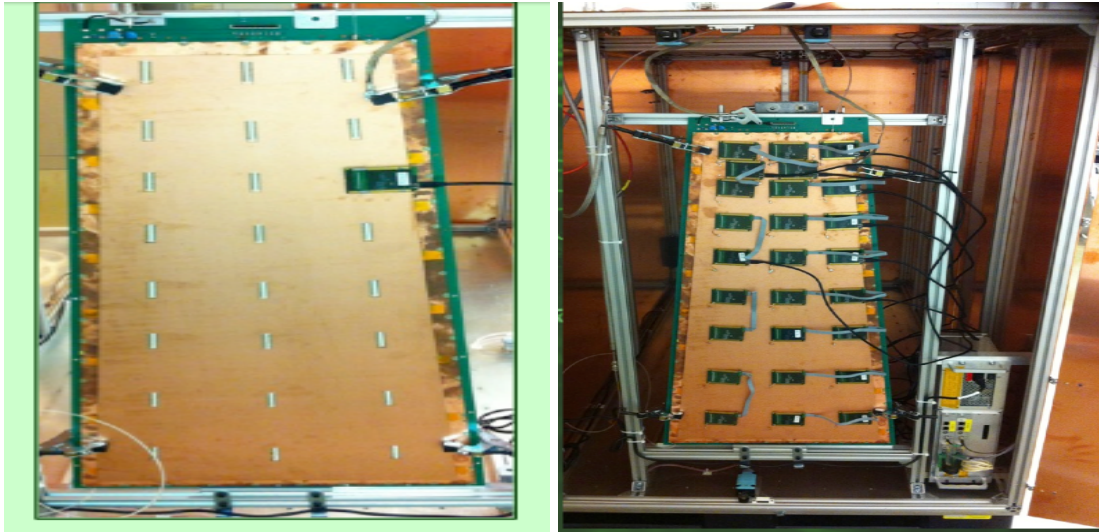
Figure 3.58: CMS forward tracker GEM chamber without (left) and with (right) readout boards connected.

Fig. 3.59 (left) and Fig. 3.59 (right) show the efficiency and time resolution of such a large chamber. The figures clearly show that the performance is similar to the one we obtained for small and intermediate size chambers.
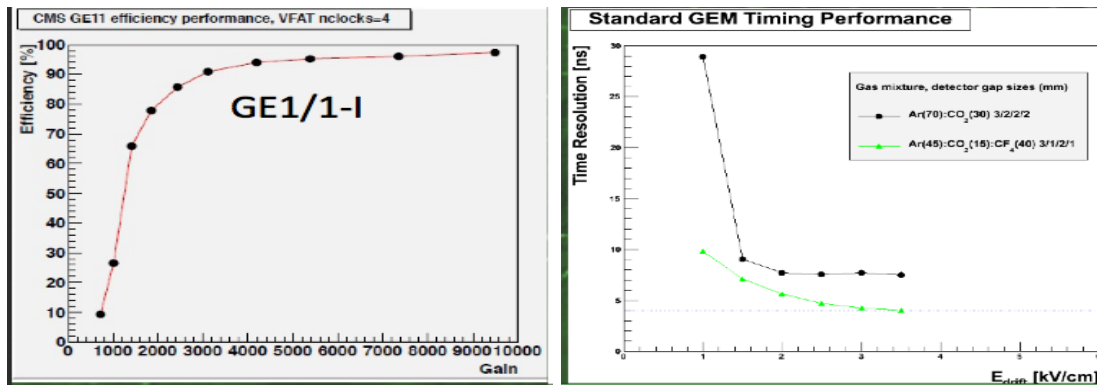
Figure 3.59: Variation of efficiency(left) and time resolution in nsec (right) of a large size CMS forward tracker GEM chamber with the applied voltage.

In view of the results obtained by the large CMS GEM chamber, we can conclude that using the same technique as was used by CMS, it is technically feasible to build and operate with high efficiency the CBM-MUCH chambers which are of similar (or smaller) size in comparison to the CMS GEM chambers.

3.2.10.2 First real size prototype chamber

As per strategy discussed above, we got the first prototype chamber of the size suitable for the first layer of the first station positioned after magnet was assembled at CERN. The PCBs were fabricated by a company in India and were transported to CERN. NS-2 technique was used for

the fabrication of the chamber. The GEM foils were custom built at CERN as per our design. The chamber shown in Fig 3.60 was tested with X-rays at CERN and then with proton beams at COSY-Juelich. The chamber showed > 95% efficiency that was stable till the beam rate of 2.5 MHz/cm^2.
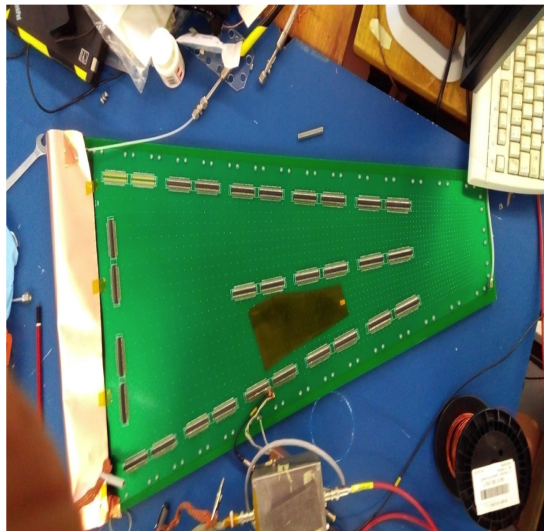
Figure 3.60: First prototype chamber assembled at CERN.

3.3 Straw tube detector

3.3.1 Introduction

A straw detector cell is a drift tube composed of a long plastic straw and a central anode wire. Straws can be assembled in thousands to form large particle tracking devices. Appealing features are moderate cost and independent operation of the individual drift cells. For MUCH use, an assembly of straw stations containing 12 double layers modules, each consisting of about 1184 straws, is in development. Each straw station contains three identical octagonal chambers measuring X and two rotated (+10, -10) coordinates of a passing charged particle. Each chamber consists of two identical modules with some overlap between them to avoid dead regions. The chambers are having inner holes for the beam pipe with a diameter of 43 cm. Fig. 3.61 and Fig. 3.62 show the schematic layout of the straw module and the straw chamber, respectively. The schematic view of the MUCH Straw Station is shown in Fig. 3.63.

Each module contains two layers of straws of length ranging from 84 cm to 190 cm (keeping 5th MUCH station in mind), which are inserted into a carbon frame (for reason of cost, carbon frame elements can be changed to Al). The straws of one layer are glued together to form a plane. Every plane is divided into three sections. The central part, being closer to the beam axis, is exposed to higher particle rates. This part has a central half-hole for the beam pipe. Each layer has 592 straws with 6.0 mm inner diameter. The chosen diameter is a compromise between minimizing the number of channels and the occupancy. A plane of this kind has a much higher mechanical stability compared to individual straws. This improves the ruggedness and reduces the load onto the frame, which would be needed to keep individual straws straight enough by tension. The production technology was developed for the straw subsystem of the COMPASS spectrometer [33] and used for the different size chambers of the setup SVD-2 and OKA of the U-70 accelerator at IHEP (Protvino) [34].
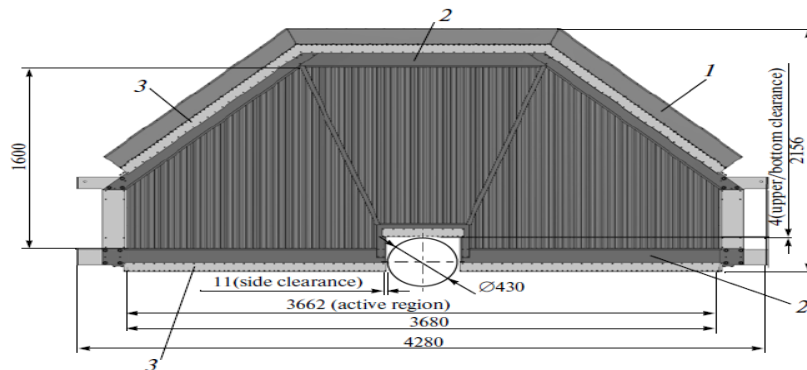
Figure 3.61: Schematic view of MUCH straw module. 1 - mother boards for the readout and high voltage supply of the straw anodes, 2- carbon plastic elements and 3- Al elements of the frame.

Two straw planes are combined into one double layer and mounted on carbon bars of the frame as shown in Fig. 3.61. Utilization of the carbon plastic for these bars is preferable because of relatively large temperature expansion coefficient for Al. The carbon plastic bars may be replaced by metal bars if temperature near the station remains steady ($\pm3°C$). Aluminum bars were used for the other direction and as a support of the motherboards. One layer of the straws is shifted by half a diameter with respect to the other in order to resolve left-right ambiguities. The anode wires of the drift tubes are centered in the straws by two end-plugs and one or two small plastic
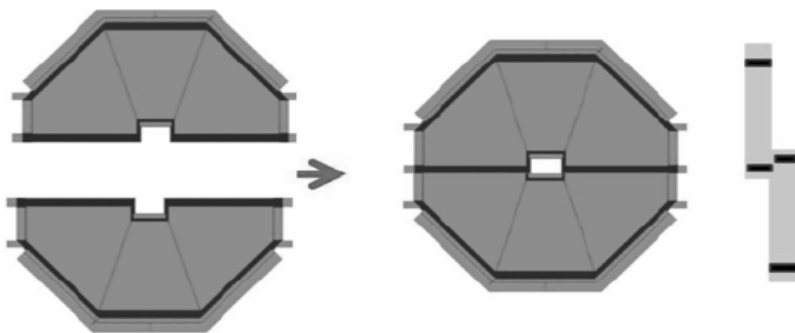
Figure 3.62: Schematic view of the MUCH straw chamber.

spacers. The diameter of these gold-plated tungsten wires is 30 micron. The ends of the straws of a double layer are glued gas tight on each side of the frame, which serves at the same time as a part of the gas manifolds. Gases are supplied through the end-plugs and the gas manifolds. The length of the straw tubes is affected by humidity. In order to keep the straw tubes straight and exclude any possibility of the straw bending, they can be reinforced by carbon wires like it was done for the ATLAS TRT [35, 36] . But the long straws should be installed into the frame under a small pre-tension and kept under low humidity. In order to minimize the effects of humidity the straw planes will be closed by thin Al planes from both module sides to provide the possibility to surround the straws by a dry gas. The additional construction elements will include mother and termination boards, which will be located near outer and inner straw ends, respectively. We discuss in subsequent sections details of some of the elements of this detector and the assembly procedure.
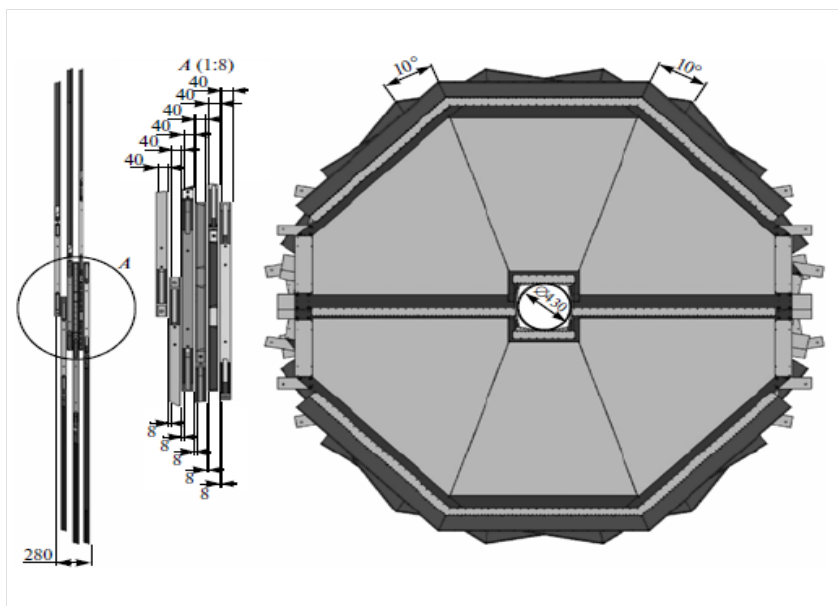
Figure 3.63: Schematic view of the MUCH station with three chambers.

3.3.1.1 Straws

The structure of a straw tube is shown in Fig. 3.64. The straws for the prototype are wound from two kapton film strips. Carbon loaded Kapton film of the 160 XC 370 type from DUPONT and aluminized (500 Angstorm) Kapton film of the NH type will be used as inner and outer strips, respectively. Both films will be covered by a glue layer with a thickness of 7 μm on one side. The inner diameter of the straws will be 6 mm and the tolerance of the diameter was specified to 0,+30 μm. The inner surface of the straw is used as cathode. The straws are manufactured by industrial method. The first step is the preparation of the film, second one is the preparation of the film strips with the width of 8±0.1 mm. Two strips are wound around a mandrel with 4 mm overlap under temperature near 200° C. Table 3.3 presents the straw parameters and material specification.
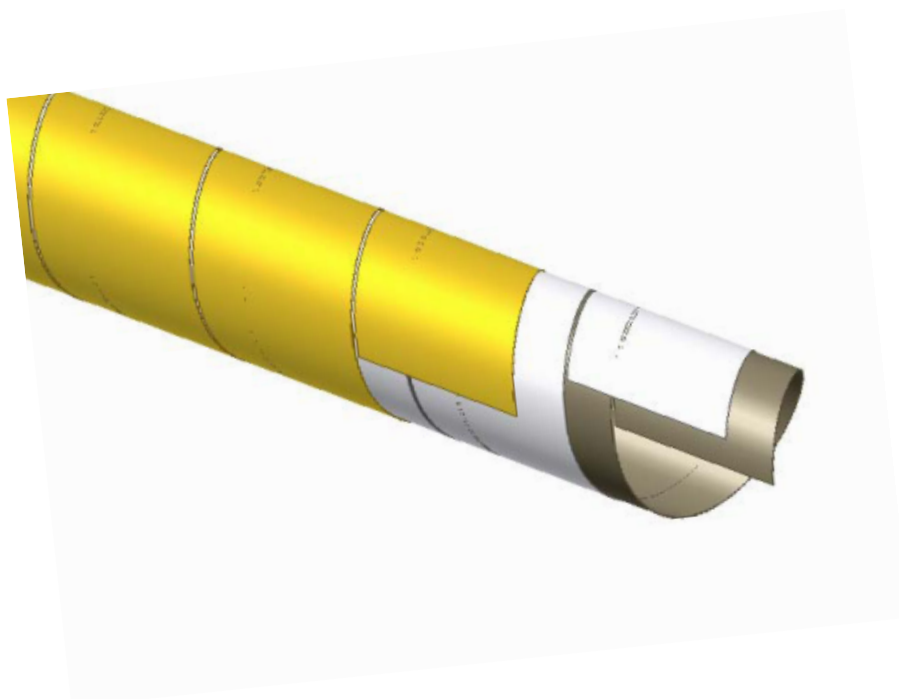
Figure 3.64: straw tube consisting of carbon loaded inner layer with a thickness of 40μm and an aluminized Kapton outer layer with a thickness of 25 μm

3.3.1.2 Anode wire

The anode for the straws is a gold-plate tungsten (with 2% of rhenium) wire with a 30±0.3 micron diameter (type 861, Luma). The anode wires are centered in the straws by two end-plugs and four small plastic spacers. The electrical resistance of this wire is about 60 Ω/m. The wire tension will be set to 70±10 g, close to the elastic limit which is around 1.2 N [33]. The wire should meet following requirements.

- Wire ellipticity should correspond to wire diameter variation of ±2%.

- The base wire must be free of defects, specifically cracks, splits etc.

- Base wire should be electrically polished to provide a smooth surface free from any defects.

Kapton Film	Plyimide type 100 HN of 25 $\pm 2\mu$m thickness, density - 1.42 g/cm^3
Loaded Kapton Film	XC160, 40 μm in thickness, resistivity 370 Ω/square
Al layer	0.2 + 0.1 μm
Polyurethane layer	(5 $\pm$ 2) μm thickness
Straw Inner diameter	6 + 0.03 mm
Straw length	from 84 to 190cm
Impedance	66 - 72 Ω
Straw dimension	Y, incline $\pm$ 10°

Table 3.3: Material specifications for straw tube detector.

- The base wire surface should be also carefully treated (light electrolytic cleaning) to eliminate all traces of oxides and other possible pollutants just before gold plating.

- The base wire is to be plated with pure gold. No nickel additives to the gold, no Ni-flashing of the wire surface before gold plating are allowed.

- The finished, gold plated wire must have a clean surface which is free of any contaminant, e.g. oil, dirt, dust, fibres, chemical residuals etc. No mechanical treatment of the wire surface is allowed after gold plating.

The wire is intended to be used without further cleaning at the production sites. The straw cathode will be grounded and the anode will be under high voltage.

3.3.1.3   Elements of the straw position

A set of equipments are needed to position and fix both the straw into its frame and the anode wire into the straws. An outer insulation end plug and an inner insulation end plug were used to connect the ends of the straws to the outer and inner bars of the frame respectively. The accurate positioning and holding of the ends of the straws in this support frame are provided by matching of its diameters. Moreover the design of fixed anode elements should be matched by connecting the anodes with the end cap board, also called mother board (MB). Connecting elements have to be within a precision of 30 μm. The choice of raw material for the elements was based upon the following criteria:

- mechanical behavior: stiffness, stability among others

- radiation hardness

- low outgassing, low gas permeability

The gas supply has been made through the end-plugs and a gas-manifold, which is integrated into the Al-frame construction. Polycarbonate end-plugs made by the method of pressure moulding are used to fix the wires at the straw ends. The diameter of the end-plugs is 6.0(+ 0, - 0.02) mm. There are grooves on the outer surface of the end-plugs to connect the internal straw volume to the volume common to all the straws. There is also a gutter to install a ring contact spring,

which allows one to connect the cathode to the common *ground* of the chamber. The wire goes through the Cu pins inserted in the end-plugs. The top pin is then crimped, a tension of 90 g is applied to the wire, and the bottom pin is finally crimped at the end. The inner diameter of the pins is 130 micron. To decrease a gravitational and electrostatic displacement of the anode wires low mass spacers with central hole 0.12 mm in diameter also made of polycarbonate by the method of moulding are placed at distances more than one meter. The diameter of the spacer is 5.97 (+ 0, - 0.02) mm and the mass of one spacer is 15 mg. The spacers are pasted on the anode wires with Araldite 2013 glue before mounting the wires in the straws.

3.3.1.4 The End-Cap Boards

The active End-Cap Mother Board (MB) is the interface between the straw tubes on one side and the readout electronics and high voltage on the other side. Big straw lengths require use of termination at the far end from the readout side of the straws. A simplified schematic circuit of one detector channel is shown in Fig. 3.65. The signal readout will be organized from one end of the tube. A series resistor at the amplifier input together with the input resistance of the amplifier should provide the right impedance for the termination on the readout side of a straw. The other ends will be connected to the termination boards (TB), where 100 pF capacitors will be used between anodes and termination resistors of 330 Ω. The MBs will feed the anode voltage to and read the information from the straws on both module planes, and will be mounted on Al elements of the frame, while TBs for the straw anode termination will be mounted on the opposite side. The octagonal shape of the chamber requires several different types of MBs.
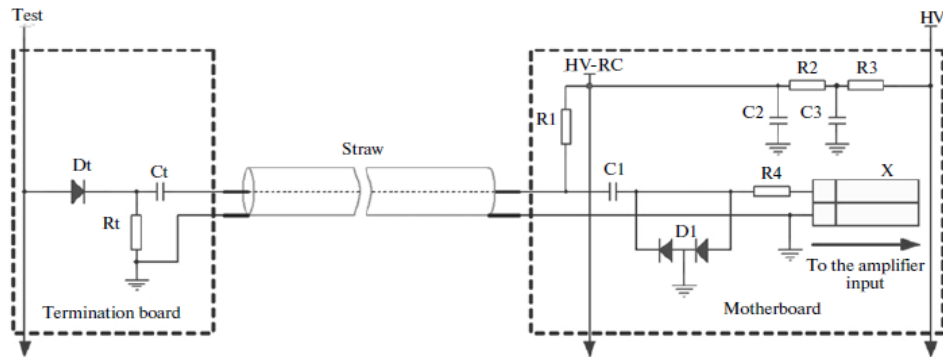
Figure 3.65: A simplified TB and MB circuit for one channel.

3.3.1.5 Assembly procedure

The assembly procedure of a similar detector has been previously described in [33]. Assembly tools and the procedures of assembly of the chambers demands special knowledge and experience. New tools should be developed and produced and some existing one should be corrected for other size. To determine the necessary changes the full-scale prototype has been designed and built. Deviations of the anode wires from their nominal positions, as defined by equal spacing, should be in the range of 100 μm. For a plastic-and-glue structure of 6 m^2 one has to accept some loss in mechanical precision. Stringent requirement to high mechanical precision demands the high precision tools. The calibration positions of each the individual anode wires are required after assembly of modules.

3.3.1.6 Testing after assembly

The assembly site will all be equipped with the test station for validation of the assembled modules before they will be sent to GSI. The test helps to check the operating efficiency of each straw, the high voltage distribution and any possible connectivity problems in the electronics signal read-out for each straw. Uniform gas gain along the straw tube is important for the safety of the detector and for optimal performance. The main reason for gas gain non-uniformity is some geometric deformation of the straw such as non-straightness or non-circularity or wire offset from the axis of the straw that leads to a distortion of the electric field. For a wire offset of more than 400 micron, the local increase of electric field substantially increases the gas gain. In this case, the rate of discharge and large amplitude signals increase significantly, making the straw very unstable. The specification for the maximum wire offset is 300 micron. A short term high voltage stability test should be carried out during the assembly of the modules to check the anode wires. After assembly, the produced modules will be checked against tightness and functioning all electronics channels. The chamber channels will be tested with the help of a ^{55}Fe source by a test amplifier. The goal of the X-Ray tests will be to detect leakage currents, to measure the gas gain uniformity (better than 10%) along the length of each straw at a fixed anode voltage, signal attenuation along the straws, and a level of own noises. An X-ray CCD apparatus can be used for the off-lines scanning of straw double layer modules.

3.3.2 Building of a prototype and testing the performance

A prototype chamber has been built as shown in Fig. 3.66 using the assembly procedure discussed earlier. The dimension of the chamber corresponds to the 3rd station of MUCH. We show the distribution of the tension applied on the straws in Fig. 3.67. We have tested the chamber using Fe-55 source. The current at different motherboards have been shown in Fig. 3.68. The amplitude distribution along the straws for two peak MBs (16 and 32) are shown in Fig. 3.69. The chamber has been tested using different gas compositions as discussed below. The variation and stability of gain has also been studied. It is seen that the chambers could have stable operation at a gain of 10^4. The cross-talk distribution is shown in Fig. 3.70 which is of the order of 1%.
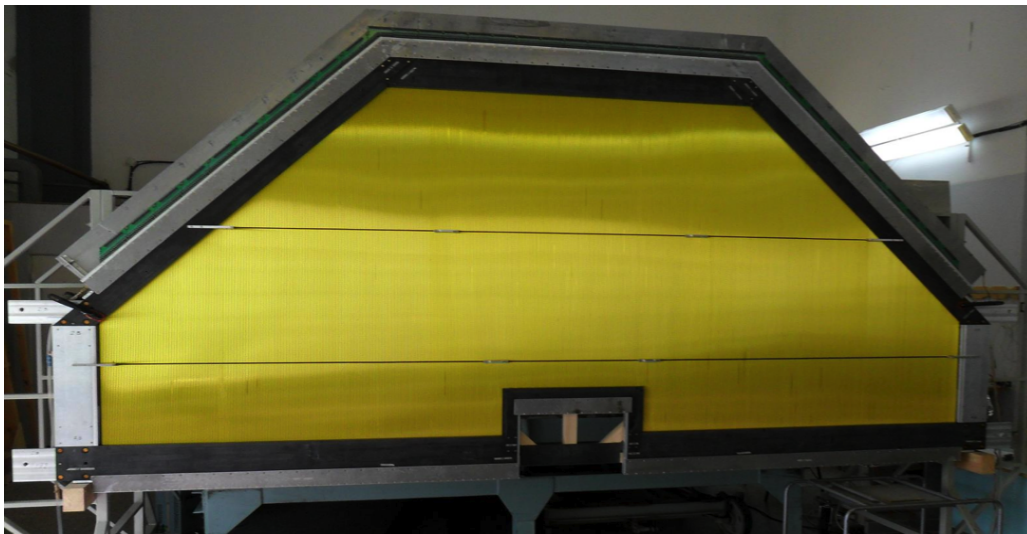
Figure 3.66: A straw tube chamber prototype.
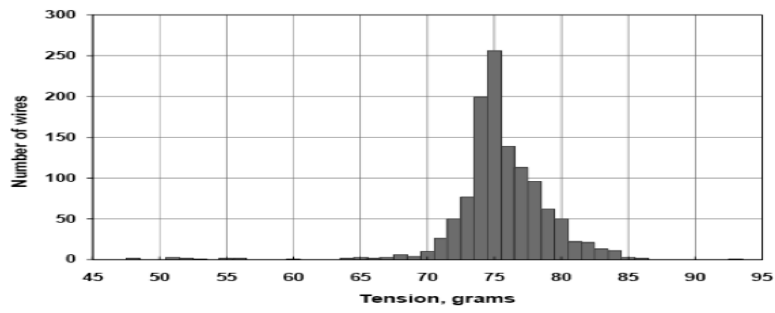
Figure 3.67: Distribution of tension (gm) applied on straws.
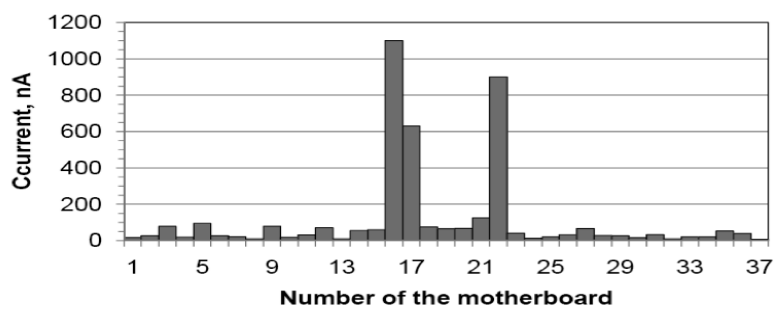
Figure 3.68: Current on different MBs.
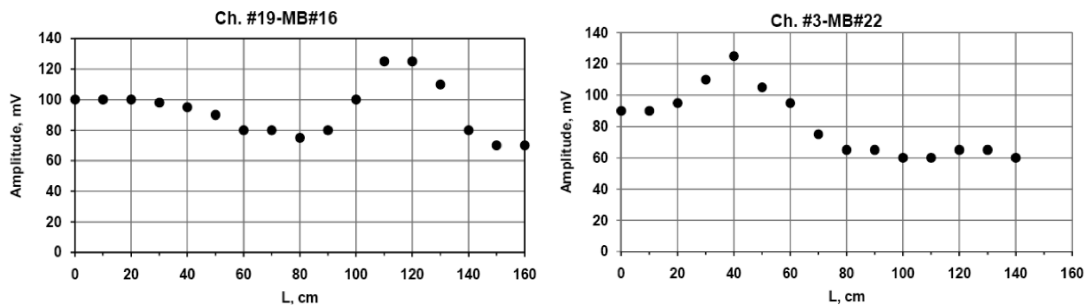
Figure 3.69: Signal amplitudes on two MBs (16 and 32).
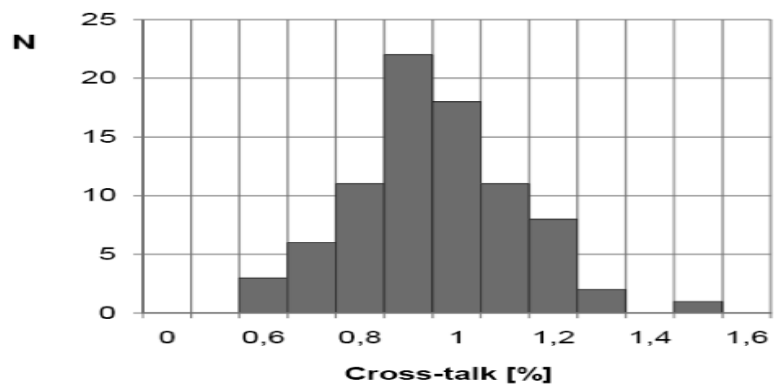
Figure 3.70: Cross-talk distribution.

Gas mixture	Percentage	t_{max}, ns	dE/E, %
Ar/CO_2	70/30	68.4	18.08
$Ar/CO_2/CF_4$	63/32/5	66.7	22.5
$Ar/CO_2/CF_4$	63/27/10	60	26.4
$Ar/CO_2/CF_4$	63/17/20	45	33.5
Ar/CO_2O_2	(70/30)/0.8	64.1	18.8
$Ar/CO_2/O_2$	(70/30)/1	63.2	19
$Ar/CO_2/O_2$	(70/30)/1.5	59.5	28
$Ar/CO_2/O_2$	(70/30)/3	56.2	-

Table 3.4: Energy resolution and electron drift time t_{max} of the straws with the diameter 4 mm for detection of 5.9 keV X-rays with gain G = 1.4×10^4.

3.3.2.1   Gas composition

The gas used in the chamber must guarantee stable operation of the straws for a large integrated charge and for high flux of particles crossing straw tubes. Ar/CO_2 mixtures provide stable operation without streamer discharges up to high gas gain. The study of the time spectra of the straw signals shows that the charge collection will be faster if CF_4 is added to the gas mixture. An addition of O_2 by $\leq 3\%$ causes the reduction of the collection time less than 5% [40]. Fig
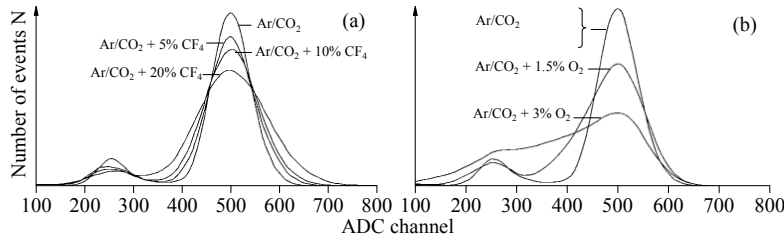
Figure 3.71: Amplitude spectrum of the straw with a diameter of 6 mm for X-rays from ^{55}Fe source. Gas mixture $ArCO_2$ with (a) CF_4 and (b) O_2 additives; G = 1.4×10^4

3.71 shows the amplitude spectra of the X-rays from ^{55}Fe source for the straws with diameters of 6 mm passing through with the gas mixture $ArCO_2$ with CF_4 and O_2 additives. If the partial pressure of CF4 in the gas mixture is increased by 1%, the energy resolution worsens by about 0.7% (Table 3.4). CF4 additives with particular partial pressure practically does not influence the energy resolution of the straws with a diameter 6 mm, while in the case of $ArCO_2$ mixture without CF4, the energy resolution does not change for the straws with a diameter of up to 10 mm. CF4 additive does not influence the efficiency of detection of both X-rays and β particles. The straw gas mixture was finally chosen to be 80% Ar + 20% CO2. The CF4 can be used as additional component of the gas mixture for cleaning of the detector during special cleaning runs.

3.3.2.2   Gas Gain and stability of operation

Figure 3.72 shows how the gas gain depends on the high voltage based on the X-rays from Fe-55 source. From this figure the extracted gas gain is in the range 4 - 8×10^4.

Fluctuation of the atmospheric pressure and temperature can lead to large variations of the
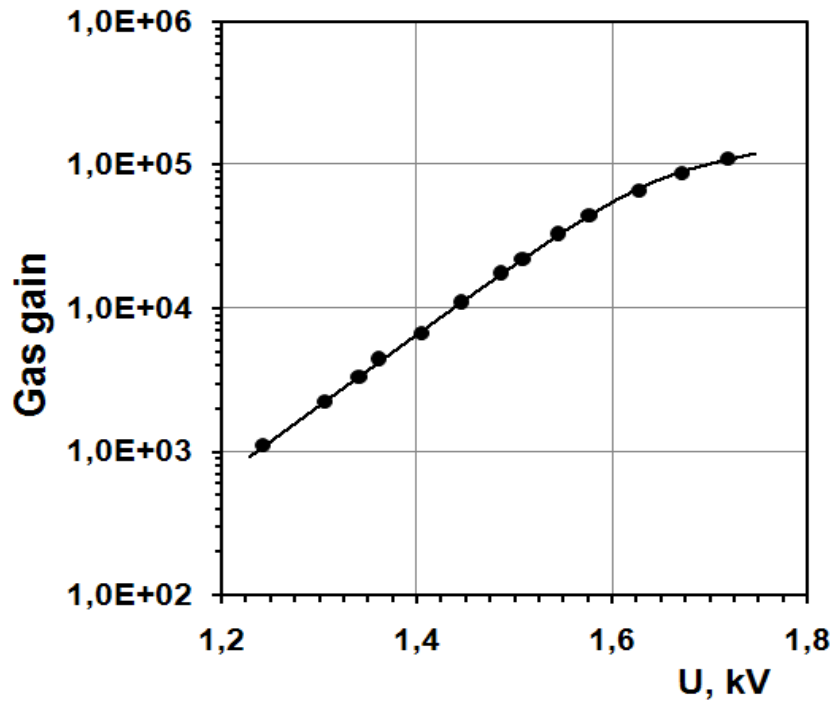
Figure 3.72: Variation of the gas gain with applied high voltage

gas gain and the high voltage should be adjusted constantly to follow them. The temperature dependence of the gas gain has been measured and found to be 1.7% per degree. The required operational high voltage range corresponding to a straw gain in the range $4\text{-}8\times10^4$ is ~1.57 - 1.65 kV. The gain uniformity in the chamber is of the order of 4%.

We mention some of the points below that are relevant to the assembly and performance of the straw tube detectors.

- The group at JINR has been involved in several straw tube tracker projects like COMPASS spectrometer. The present chamber in CBM will be somewhat larger in dimension compard to the COMPASS chamber. One of the aims of building the full size engineering prototype was to go through all the procedures of building of the components, mechanical inspection and testing with Fe-55 source. The could be concluded that the CBM-MUCH chamber, could be built even with existing equipments however as a limiting case of application. If required, new equipment will be used.

- small changes in design will be made whenever required, one example is the region near the beam-hole which required strengthening.

- straw length is dependent on humidity which might lead to change in the measurement of the local co-ordinate. In the present case, it has been excluded by using the technique discussed in [39].

3.3.3 Measurement of the radial coordinates

The straws with inner diameters of 4 and 9.53 mm have been tested in the SPS test beam at CERN, with the same gas mixture of Ar/CO_2 (80/20) and the gas gain $\sim 7 \times 10^4$ in both cases. The efficiency was about $\sim 98\%$ and 99% for the 4 mm and 9.53 mm straws, respectively. Figure 3.73 shows the typical distribution of the deviations of the measured particle coordinates from those corresponding to the tracks reconstructed using the data from silicon pad detectors [37]. The typical values of the intrinsic resolution of single straw for the Ar-CO_2 gas mixture is in range of 180 - 200 μm.
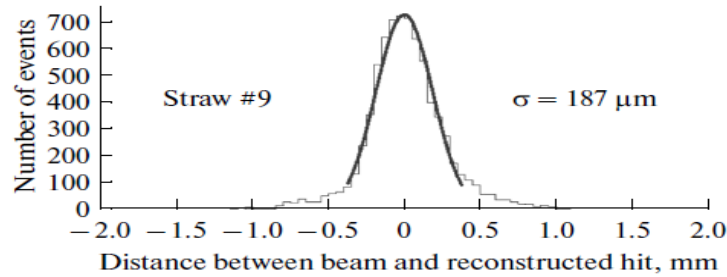
Figure 3.73: Difference of coordinates measured in the 4 mm straw tube and predicted at the tube position using the track reconstructed in silicon detectors

The spatial resolution for the 9.53 mm and 4 mm straws as a function of the scaled distance to the anode (normalized to the tube inner radius) is shown in Fig. 3.74 [38]. In both cases these dependencies can be well described by a single curve. The observed universality of the dependence makes it possible to predict the coordinate resolution for the straws with different diameters given the operation parameters are similar (gas composition and gas gain). It also simplifies the task of track fitting by providing the error parametrization curve. The spatial resolution changes from ≈ 400 micron to ≈ 80 micron near the anode and cathode, respectively.
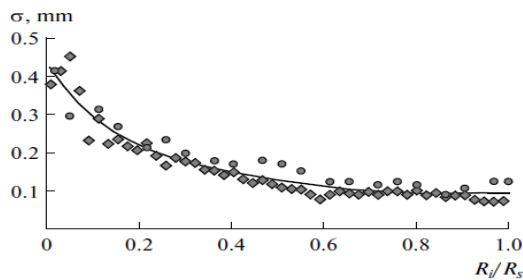
Figure 3.74: Spatial resolution as a function of the scaled distance to the anode for the straws with 4 mm (circles) and 9.53 mm (diamonds) inner diameter. The straws were blown with the gas mixture Ar/CO_2 (80/20), and the gas gain was about 7×10^4 in both cases

Each chamber of MUCH has two straw layers, and one layer is shifted by half a diameter with respect to the other in order to resolve left-right ambiguities and to obtain single track efficiency for a double layer above 99%. The double layer arrangement also helps to improve efficiency and radial resolution measurements. It is possible to use for the drift-time measurements the data from one half of the straw which is located near the cathode. A simple estimate shows that in this case the averaged spatial resolution of a two layer chamber will be in the range of 90 to 120 μm.

Bibliography

[1] M. Petri et.al., Nucl. Instrum. and Meth. A, A 732 (2013), 375 - 379, DOI:10.1016/j.nima.2013.07.087

[2] M. Petri et.al., Nucl. Instrum. and Meth. A, 714 (2013) 17

[3] M. Petrovici et.al., Rom. Journ. Phys. 56:654-663, 2011

[4] M. Petrovici et.al., Nucl. Instrum. and Meth. A 579(2007), 961-966 2007

[5] S.S. Al. Dargazelli et.al., NIM 156 (1978)63

[6] A.S. Brogna et al., Nucl. Instr. and Meth. A 568 (2006) 301

[7] E. Abat ert al., JINST 3: P10003, 2008.

[8] V.N. Bytchkov et al., Nucl. Instr.& Meth. In Phys. Res. A556 (2006) 66-79.

[9] F. Sauli et al., Nucl. Instr. and Meth. A 386 (1997)531.

[10] M. Alfonsi et al., Nucl. Instr and Meth. A 581 (2007)283

[11] M. Alfonsi et al., Nucl. Instr and Meth. A 518 (2004)106

[12] M. Villa, et al., Nucl. Instr. and Meth. A(2010),

[13] M. Villa et al., doi:10.1016/j.nima.2010.06.312

[14] S.Bachmann et.al., Nucl. Instr. and Meth. A 479 (2002)294

[15] M. Zeigler et. al., arxiv: hep-ex/0007007v1

[16] A.Bressan etl.al, CERN-PPE-TA1-GD (2/10/98) (CERN-EP/98-163), R. Bouclier et.al. Nucl. Inst. and Meth. A 396 (1997) 50

[17] V. Avati et. al., Nucl.Inst. Meth., A 490 (2002) 117-203

[18] A. Kozlov et.al. Nucl. Inst. and Meth. A 523 (2004) 345

[19] D.Abbaneo et.al., arxiv:1012.3675,D.Abbaneo et.al., Nucl. Inst. and Meth. A 718 (2013)383, P. E. Karchin et.al., Nucl. Inst. and Meth. A 37 (2012)561

[20] A. K. Dubey, et al., Nucl. Instr. and Meth. A(2012), doi:10.1016/ j.nima.2012.10.043

[21] A.K. Dubey et al., Submitted to Nucl. Instr. and Meth.

[22] A. Bressan et. al., Nucl. Instr. and Meth. A 425 (1999)262

[23] M. Tytgat et. al., Nucl. Instr. and Meth. arXiv:1111.7249v1, F. Simon et. al, arxiv:0711.3751v1

[24] G. Bencivenni et al., Nucl. Instr. and Meth. A 494 (2002)156

[25] M.Alfonsi et.al., Nucl. Inst. and Meth. A 581 (2007)283

[26] B.Ketzer et.al., Nucl. Phys B (Proc. suppl) 125 (2003) 368,C. Altumbas et.al. Nucl. Inst. and Mth. 490 (2002) 197

[27] J. Saini, A.K. Dubey, S. Chattopadhyay, R.N. Singaraju, Intl. Nucl. Phys. Symp. Mumbai (2013).

[28] M.C. Altunbas et al., NIM A 515 (2003) 249.

[29] A. Abuhoza, et al., *Physics Procedia* **37** (2012) 442.

[30] A. Abuhoza, et al., *Nuclear Instruments and Methods in Physics Research Section A* **718** (2013) 400.

[31] M. C. Altunbas et. al., Nucl. Inst and Methods A 551 (2003) 249

[32] http://indico.cern.ch/event/323839/session/4/contribution/47/material/slides/1.pdf

[33] V.N. Bytchkov et al., Nucl. Instr.& Meth. In Phys. Res. A556 (2006) 66-79.

[34] SVD-2 and OKA of the U-70 accelerator at IHEP (Protvino

[35] E. Abat ert al., JINST 3: P10003, 2008.

[36] Yu. V. Gusakov et al. , Phys.Part.Nucl.41:1-26,2010.

[37] S.N. Bazylev et al. Nucl. Instrum. and Meth. In Phys.Res.A 6321 (2011) 75.

[38] N. D. Dikusar et al., Phys. Part. and Nucl. Lett., 2012, Vol. 9, No. 2, pp. 172.

[39] K. I. Davkov et al., Instruments and Experimental Techniques, 56 (2013) No. 5, pp 525

[40] V.M.Lucenko et al, Phys. Part. and Nucl. Lett., 2006, Vol. No.5(134),p.273.

[41] V. Peshekhonov et al, Phys. of Part. and Nucl. Lett., 2012, Vol. 9, No. 2, pp. 172.

Chapter 4

Integration of muon detector system at CBM

4.1 Introduction

In this chapter we will discuss details of integration of MUCH in CBM. As CBM will be working in two operating modes, so it is extremely important that details of integration aspects as itemized below are considered.

- Mechanical integration: The CBM cave will have different floors in the building to house different services like electronics, gas, power converters among others. In the main hall, CBM setup will be installed immediately after the HADES setup mainly in SIS100 running scenario. In SIS300 scenario, when the setup will be somewhat longer, the length of the hall required to install the entire CBM-MUCH system is 7.3 metre starting from the target position. At the heart of the CBM system is the dipole magnet which extends upto a distance of 160cm before others systems are installed. Inside the magnet, the main tracking system i.e., Silicon Tracking Station (STS) housed in an enclosure will occupy the space upto 120cm. In the di-electron mode of operation, RICH detector will be installed just outside the magnet as has been discussed in detail in RICH TDR. Muon chambers (MUCH) , in the di-muon mode of operation, needs to be as closely located to the target as possible to avoid the pions decaying to muons enhancing the dimuon background. As has been discussed in detail in chapter-2, the face of the first absorber is at 120 cm from the target that is inside the magnet. The total thickness of the absorber, in SIS300 setup is 265 cm, is to be installed in 6 segments with the first one made of carbon and others of iron. The detector stations, 3 layers of each station, and housed in a 30 cm space in between two successive absorbers are to be installed with a provision of movements in transverse directions. All the services are to be mounted with the main platform. The system of absorber segments and detector stations together are to be mounted on a platform that can have a possibility of movement to a parking position for operation in di-electron mode. Mechanical integration of the entire muon system poses several challenges to be discussed in the concerned section.

- Electronics Integration: The readout electronics for the MUCH begins with the Front End Board (FEB) that is to be mounted with the chambers directly. One or more dedicated ASIC(s) housed in the FEB(s) will process the analogue signals from the chambers. The

digitized signals from a group of FEBs will be transported to GBTx data concentrator ASICs which forward the data over optical links to FPGA based data processing boards (DPBs) outside of the CBM cave. A board called Readout Board (ROB) is to be used to hold the GBTx and associated optics components. The data are then transported to the first level event selector (FLES) of CBM. The electronics hardware at each of these tiers will face different levels of radiation dose and therefore need to be radiation resistant accordingly. The most hostile radiation environment will be handled by the FEBs and therefore need to be placed at a proper position to reduce the effect. In addition to the high radiation environment, the FLES has to be properly designed to be mechanically and electrically compatible with the entire CBM environment. The supply of high and low voltages to the detectors and cooling need to be designed properly.

- Safety: Both the mechanical system due to its weight coupled to the movement requirement and electronic readout system must be designed to deal with safety aspects of the system. This is to be done in accordance with the procedures to be followed by CBM as a whole.

- Gas handling system: All the detectors being used in CBM-MUCH use gases of different compositions. It is therefore necessary that suitable gas handling system is to be integrated to the system.

4.2   Mechanical Integration

MUCH system has two major mechanical assembly components i.e. (a) assembly of MUCH absorbers in the CBM setup and (b) assembly of individual chambers. It should be noted that following points are to be taken into consideration while designing the system,

- MUCH will take data only in the muon setup, so there should be provision that detectors of the electron setup could be placed in a short interval and with minimum intervention as and when required.

- There will be two setups, i.e. SIS100 and SIS300 for MUCH with varying number of stations at different locations. Care should be taken so that repetitions are minimized in building different components. In general, absorbers will be built only once to be used both in SIS100 and SIS300 setups.

- Proper care to be taken for assembly of the first MUCH absorber that is likely to be placed inside the magnet.

- Provisions of mounting and dismounting of other detectors in the setup should be made.

- The choice of materials should take care of the magnetic field whenever present in the setup.

The discussions to follow are divided into two subsections, while the first one deals with the assembly of MUCH platform, absorber and movement mechanism, in the other subsection, we discuss the assembly procedure of chambers, mainly the larger GEM chambers. Some details of the assembly of straw tube detector have been discussed in chapter-3.

Part	Z-start	Z-extent	Z-end
STS-box			1200
Clearance	1200	50	1250
C Absorber 1	1250	600	1850
Detector stations 1	1850	300	2150
Fe Absorber 2	2150	700	2850
Detector station 2	2850	300	3150
Fe Absorber 3	3150	1350	4500
Clearance	4500	100	4600
TRD 1-4 layers	4600	1800	6400

Table 4.1: Z-positions(mm) of different components in SIS100 configuration

Part	Z-start	Z-extent	Z-end
STS-box			1200
Clearance	1200	50	1250
C Absorber 1	1250	600	1850
Detector stations 1	1850	300	2150
Fe Absorber 2	2150	200	2350
Detector station 2	2350	300	2650
Fe Absorber 3	2650	200	2850
Detector Station 3	2850	300	3150
Fe Absorber 4	3150	300	3450
Detector station 4	3450	300	3750
Fe Absorber 5	3750	350	4100
Detector station 5	4100	300	4400
Fe Absorber 6	4400	1000	5400
Clearance	5400	100	5500
TRD 1-4 layers	5500	1800	7300

Table 4.2: Z-positions (mm) of different configurations in SIS300 configuration

4.2.1 Integration of absorbers and assembly of MUCH subsystem

Two configurations of MUCH, are considered for mechanical integration in this discussion. The positions of the elements of the spectrometer along the beam (Z-direction) are presented in Table 4.1 and Table 4.2 for SIS100 and SIS300 configurations respectively. Both versions have same first absorber (600 mm of carbon with lead insert covering an angular range of 3° to 5.7°), but different number of subsequent tracking stations and absorbers.

The absorbers starting from number 2 till the last one are made of iron. As and when the magnetic forces acting on the MUCH locations are known, decision need to be taken on using non-ferromagnetic materials. Even though such details are to be worked out only after all conditions are worked out, however, it is known that a weight of more than 300 Ton will need to be handled in CBM-MUCH. For this a monolithic basement must be built. The block design discussed here allows reuse of the pieces in different versions of the setup as shown in Fig. 4.1 as has been worked out for an old version of MUCH. Similar exercise will be done for current configuration of the absorbers. This approach is most technologically effective. Most likely the

absorbers (starting from number 2) will be made of parallelepiped pieces (blocks) of iron. The weight of a block is limited by CBM crane (30T maximum). The transverse (XY) size of the blocks in millimeters for absorber number **i** should exceed the value as per the formula given below.

$$X_i = 300 + Z_{endi}\ tan25°$$

where values of Z_{end} are taken from Tables 4.1 and 4.2 , angle 25° is the acceptance of MUCH and 300 mm is added to avoid edge effects in chamber hit density.
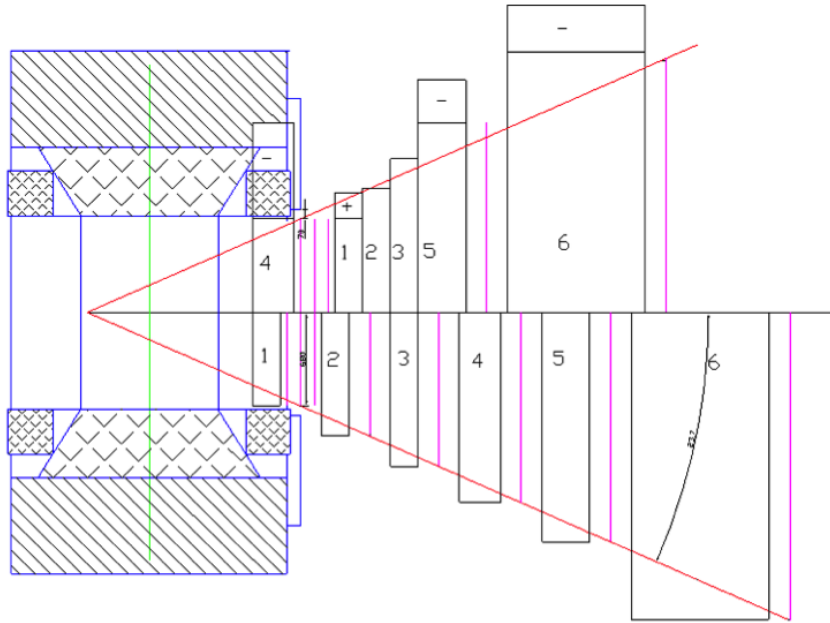
Figure 4.1: An old (2011) design showing the set of the absorbers illustrating possible reusability of the metal pieces. Absorber 1, its interface with Dipole and STS is shown.

4.2.1.1   Installation of First absorber

The first absorber is 60 cm thick piece of carbon covering angular range from 5.7° till 25° with lead insert from 3 ° till 5.7°. As both materials, carbon and lead are not self-supporting, they will be inserted in non-magnetic metallic shell similar to shown in Figure 4.2. To ensure stiffness, the reinforcement plates divide the conical shell. There is also reinforcement collar foreseen around the cone.

The absorber will be fixed on the front surface of the Dipole yoke with *Mercedes star* mounting as shown in Fig. 4.3. We assume that the required tolerance of the absorber position with respect to the beam axis could be estimated as ±0.2° which translates in ±4.5 mm at the entrance and ±6.5 mm at the end of absorber-1. The weight of the completely assembled absorber is estimated to be of about 2.5 to 3.0 Tons. This is too heavy to perform its fine positioning from the scratch. It is proposed to put the lead insert into the hole and perform the positioning
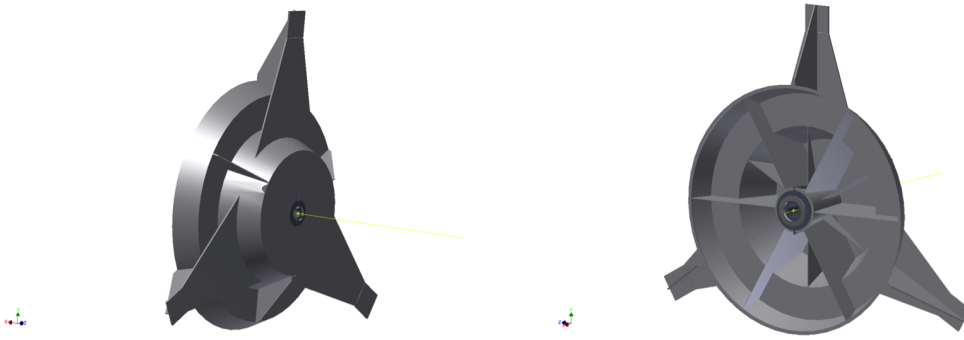
Figure 4.2: The shell of the absorber 1 with inserted lead shield and its support legs

without carbon. A special tooling is required for this procedure. When the shell is correctly positioned with respect to the STS beampipe, one can drill the holes for positioning pins (one pin per leg) and fix the legs with screws in relatively loose holes. At the last stage, the absorber will be dismounted, the machined pieces of graphite will be inserted in open compartments of the shell, and the cover is welded together with shell. At this point the absorber is ready for reinstallation. The deformations due to additional weight should be estimated, they should not exceed the tolerances.
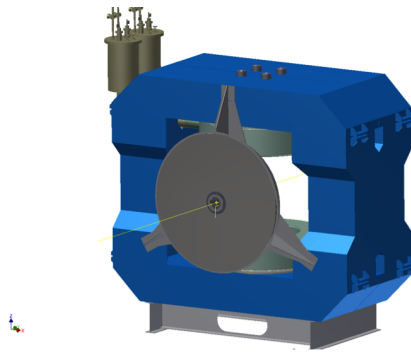
Figure 4.3: The Absorber 1 fixed on the yoke of the dipole magnet

The lead insert will have an inox steel conical tube inside its opening. This tube is required to keep the shape of lead and can be used as beampipe. The tube may extend out of absorber in order to be used for connection with the STS vacuum system. The length of the tube (from 0 to 50 mm) will be defined by the designers of the STS beampipe. If this pipe is fixed in lead insert, the designers can also use the front side of the lead insert for the connection. It is important that to avoid damage during the absorber installation the STS vacuum system could stay a few centimeter away from the parts of the absorber.

4.2.1.2   The subsequent absorbers and interface with TRD

All absorbers other than the first one are made of parallelepiped blocks of iron. The *Izhorskie Zavody OMZ group* company can produce the rolled iron pieces with thickness from 100 to 700 mm. These pieces can be grouped in required blocks, each with weight below 30 Ton.

The absorbers will be installed on dedicated supports. The design of the support and the absorber fixation at the top will be developed only after the magnetic forces are estimated. Most
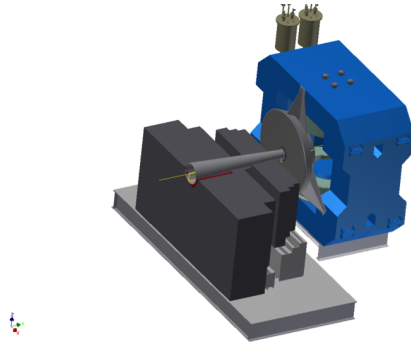
Figure 4.4: Partly assembled MUCH SIS100 configuration. Lower halves of the absorbers are put on their supports. MUCH beampipe is also connected.

probably the down support will be made of iron beams, the fixation of the upper parts of the absorber could be located in upper central zone, between the moving system of right and left half-chambers.

4.2.1.3   Beampipe

As it has been mentioned in discussion on the absorber 1, the first chunk of the MUCH beampipe is integrated in its lead insert. After the absorber 1, the beampipe keeps the opening angle of 3 Degrees, but starts with slightly larger diameter, keeping completely in the shadow of the beam shield. The flange connection allows the adjustment of the beampipe direction. The beampipe passes through the inserts in the absorber openings. The geometry of the inserts reflects different positions of the absorbers in SIS100 and SIS300 configurations. The 3-screw fixator at the exit of MUCH can adjust the position of the beampipe. The flange for connection with TRD beampipe will be located behind it.

4.2.1.4   Superstructure

The half-chambers will hang on the individual rails attached to the transverse beam. These beams are attached to the superstructure. A preliminary version of the superstructure for MUCH in version SIS100 is shown in Fig. 4.5.

How the superstructure is fixed on the basement or MUCH platform is not defined, because the magnetic forces are not estimated. Most likely reinforcements will be required. The length of the transverse beams should be sufficient to have an access to the half-chambers in service positions (see Fig. 4.6). Also it is likely that the distance between the pillars should be maximized in order to reduce magnetic forces.

4.2.1.5   Chamber suspension and positioning

Details on suspension, fixation and movements from working to service positions are being worked out, some preliminary versions have been discussed in next sections. One option is that each half-chamber is assembled on its local transport platform. This platform guarantees safe storage of the detectors when they are not mounted on MUCH superstructure and provides a convenient
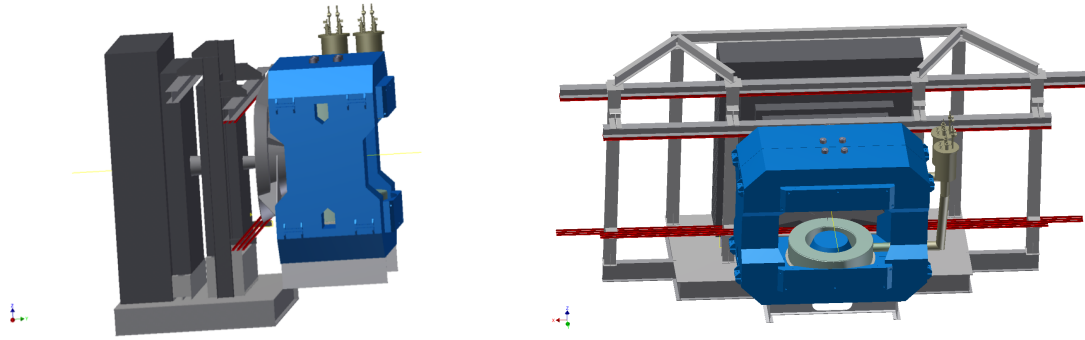
Figure 4.5: Two views of MUCH mechanics in SIS100 configuration. Chambers and their suspension/translation/positioning systems and the cable holding system (should be below the low chamber guides) are not shown.
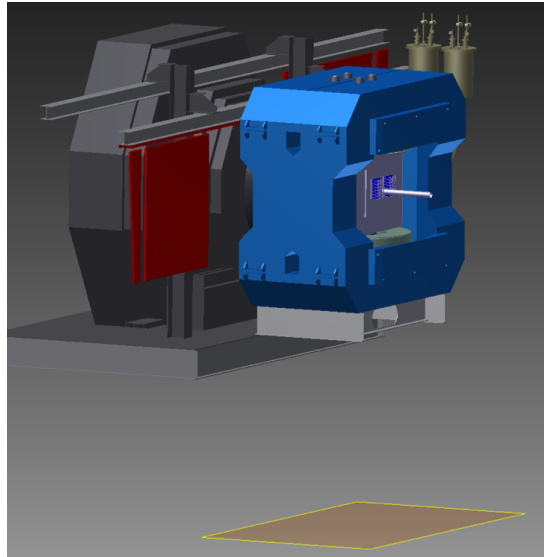
Figure 4.6: The setup of MUCH, version SIS100, a half-chamber of the first station is shown in service position. The diamond below represents the floor of the CBM cave. The beam level height is 5.7 m. The shape of absorbers is obsolete.

way of their transportation and hanging. For that option, dedicated tooling for half-chamber transfer from transfer panel to hanging should be developed.

4.2.1.6 Chamber alignment

Each tracking chamber is composed of two half-chambers that might be mechanically independent with their own frames. Each half-chamber includes several detection elements (trapezium-shaped GEM chambers) fixed on the frame. The absolute position (in CBM frame) of each pad in the detection element should be known with precision of about few millimeters As there are thick absorbers in between the tracking stations, it is impossible to make an alignment of all chambers with particles. The chambers should be aligned optically before the run. If necessary, a simple position monitoring system could be used. In order to perform the optical alignment, the chamber frame will be equipped with precision holes used to install survey tools (prisms or reflecting balls). The fixed survey marks (light-reflecting stickers) are also glued. The 3D coordinates of these holes

are known with respect of the GEM pad pattern. The theodolite or photogrammetry technique will enable to measure the coordinates of the survey marks relatively to the CBM reference marks on the walls of the cave. The photogrammetry technique is widely used at CERN. In this method the object of interest is equipped by light-reflecting survey marks and several dozens of photos from arbitrary positions are taken. The analysis of these photos can result in the coordinates values with precision of better than few hundreds of micron. The analysis time is few minutes. The frame of each half-chamber is fixed in separate rail along X direction. In the data-taking position (chambers are in closed positions) the detection elements overlap in the middle. Each rail is fixed to the transverse beams of the superstructure. The displacement along X of the half-chamber will be manually driven, a system to lock the half-chambers in the middle is foreseen.

During the final positioning the following adjustments of each half-chamber are foreseen:

1. Vertical position (Y).

2. An angle between horizontal axis of the chamber and axis X of CBM frame.

3. An angle between chamber plane and vertical axis Y.

4. Position along the beam (Z).

In order to achieve this, each half-chamber will have a fine positioning mechanisms on its top to adjust independently the vertical positions of its corners with precision of 1 mm in a range of ± 10 mm (adjustments 1 and 2). One should foresee the possibility to make adjustments 1 and 2 when the chambers are in running position. The verticality (adjustment 3) is achieved by Z-movement of the guides below the chamber. The absolute position in Z will be measured optically. Fine adjustments in beam direction (Z, adjustment 4) on top of the chamber should be foreseen in order to avoid touching between the chambers. The adjustment scenario could be as follows:

- The half-chamber is pulled out from running position to the service one.

- The removable survey marks are installed on their places.

- The 3D position of each mark (removable and fixed) is determined with respect of the CBM survey marks. This procedure enables to measure the relative positions of each detection elements.

- The required corrections are determined and applied.

- The chamber pulls in at its place in running position.

- The procedure repeats for all half-chambers.

- The Dipole magnet turns on and the superstructure deformations are measured.

- If necessary, the corrections are applied.

4.2.1.7 Services

One needs to distinguish between the external connections to the detector and the distribution inside the detector. Here we estimate the number of external connections. This discussion is based on SIS100 cinfiguration only, SIS300 could be extended accordingly.

Each half-chamber will require following services:

- Gas: inlet and outlet pipes. The connectors for instant connection in one click are available.

- High voltage : The High Voltage system requires precise voltage settings , current control, ramp up/down settings and trip detection. A typical case for the use of resistive chain requires current measurement with a resolution of 100nA.

  Station 1: each sector is subdivided in 15 HV segments; 8 sectors per half-plane results in 120 HV channels. Commercially available multi-wire connectors reduce the number of required cables to 5.

  Station 2: each sector is subdivided in 20 HV segments; 10 (12 for SIS300 option) sectors per half-plane, results in 200 (240 for SIS300) HV channels. Requires 10 connectors.

  The number of external channels could be reduced if remotely controlled local HV switch could be installed. One switch per sector i.e. 1 connector per half plane could be sufficient. The drawback of such kind of solution is that no information about the currents in each segment will be available.

- Low Voltage system for the FEB and ROB boards: As the readout system including the ASIC are still in developmental stage, so we can give estimates based on the available preliminary information. A FEB consisting of 128 channels might draw current in the range of 300mA to 500mA. The number of channels could be of the order of half a million and number of FEBs will be decided accordingly. The options available could be DC-DC converter (48V to 5V and further from 5V to 3.3V or 1.8V) that has been reported to be operating in other systems in presence of magnetic field. However, details need to be worked out with final electronics and chambers.

- Ethernet cables might be requires for remote control of the detector. One external cable is sufficient. Local ROB at each half plane will distribute required signals.

- Optical fibers: 68 fibers per half-plane, i.e. 2 multi-fiber connectors externally

- Water-cooling option is being discussed which requires 2 connectors per half-plane.

Each half plane therefore will be connected with the external world with

- 5 (10) HV connectors

- 1 LV connector in case of DC-DC convertor or from 3 to 10 LV multi-wire connectors (dependent on the assumptions)

- 1 ETHERNET connector

- 2 optical fiber connectors

- 2 gas connectors

- 2 water connectors

One can estimate that it takes for one person less than an hour to plug or unplug the half-chamber. The weight of the services attached to a half-chamber is estimated to be of about 250 kg. In order to minimize the external (especially dynamical) loads at half-chamber we propose to use dedicated service poles. All external service connections will be fixed on this pole, the distribution of services with flexible cables to the half-chambers are to be organized.

4.2.1.8   Half-chambers: access and maintenance

The half chamber in service position is shown in Fig. 4.6. Note, that the beam axis is located at 5.7 m above the level of the floor of the cave. As the full height of the chamber could be more than 4 m there must be a possibility to work at a height of about 7 m. The lifting platforms as depicted in Fig. 4.7 could be used for this purpose. The width of the platform should be about 2 m, so that two people in it can access the extreme ends of the tracking module.

Figure 4.7: Example of lifting platform that could be used. Photo taken in ALICE building.

The plan view of the CBM cave taken from the drawing by W. Neiebur, CBM Integration co-ordinator is shown in Fig. 4.8. The SIS100 version of MUCH in working position at the beam line is shown. The SIS300 is expected not to be significantly different.

In order to be accessible, the chambers in service positions should not overlap in transverse direction (X) with other elements of the detector (Magnet, TRD). This means that the half-chambers should have provision to slide out to the distance of about 5 m (size of the TRD frame), so the length of the transverse beam must be more than ± 7m as shown by red rectangles. As the serviceable parts are located at both sides of half-chambers, four lifting platforms is required to guarantee the full access of the half-chambers.

Direct consequence from this is that there might be no room to keep RICH in parking position as it is shown in Fig. 4.8, one might therefore need to find some other places to store RICH when it is not in use.

In case of movable MUCH, if we put it in parking position (directly close to the wall of the cave with detached transverse beams) its transverse beams at the other side will extend by 9 m. As the width of RICH is about ± 3.25 m, the free space from RICH to wall would be 10.375-
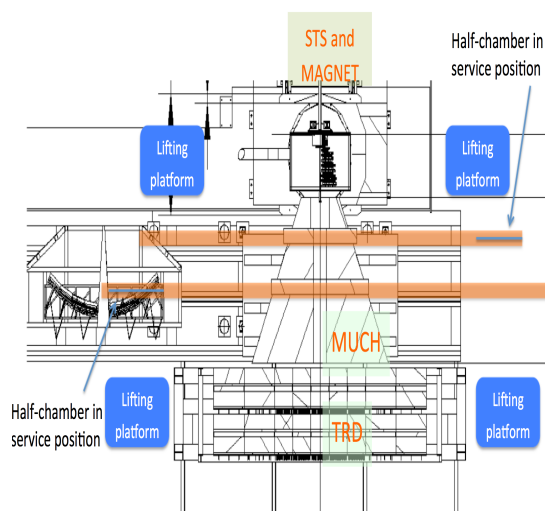
Figure 4.8: Plan view of MUCH in working position (courtesy W. Neibur). The transverse beams (red) and lifting platforms (blue) are also shown

3.25=7.125m. If MUCH is moved close to the wall, the transverse beams from another side should be cut by of about 2 m. This problem in mechanism of chamber movement and accessing of the chambers need to be solved.

4.2.1.9 MUCH platform movements and coexistence with RICH

It was planned from the very beginning that MUCH and RICH will occupy the same place on the beam on alternative basis. As RICH is relatively lightweight device, the CBM 30-Ton crane can easily handle it. The weight of MUCH is estimated to be more than 300-Ton, therefore it could be handled by crane only in pieces. Initially it was proposed that MUCH will sit on its platform and this platform will be movable. The solution of similar task in PHENIX experiment is illustrated in Fig. 4.9. The PHENIX carriage, a 200T weight unit, containing the drift chambers, pad chambers, RICH, TEC, electromagnetic calorimeter is moved along special rails using Hillman roller wheels (see Fig. 4.9 (top,left) and Fig. 4.9(top,right)), guiding wheel (Fig. 4.9(bottom,left)). Two hydraulic actuators (one as shown in Fig. 4.9(bottom,right)) are used for displacements. In should be mentioned that in this case there exists a very stable concrete basement of large size and massive rails.

In case of MUCH there are factors that produce risk for safety and reliability of movements:

- Geometry of the device
    - Length (X) ≈ 7 m
    - Height (Y) ≈ 7 m
    - Width (Z) ≈ 4 m

- Weight of the absorbers
    - Version SIS100: 335T fully assembled, $\approx$170T ready for movement
    - Version SIS300: 365T fully assembled, $\approx$180T ready for movement
    - Center of mass is displaced from geometrical center to large Z causing stability problem.
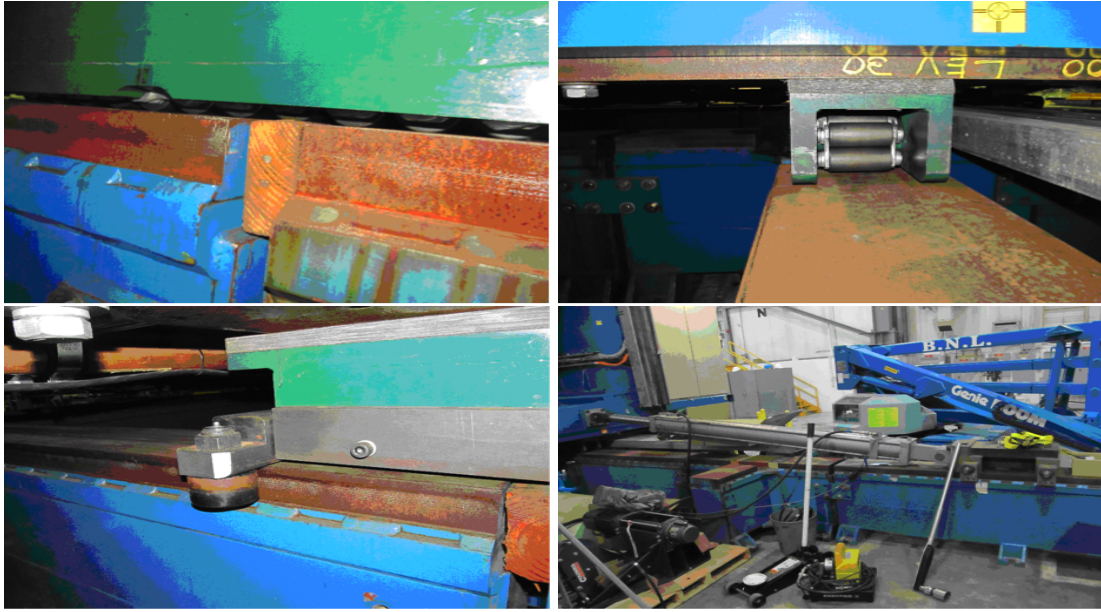
Figure 4.9: The movement system of PHENIX carriage. It is 200-ton installation of the detectors: drift chambers, pad chambers, RICH, TEC, electromagnetic calorimeter.

Based on the above-mentioned issues, the feasibility of MUCH displacement should be looked into more detail. Additionally, the reproducibility of the platform position in X and angle with respect to the beam direction is expected to be poor. Taking in account the above mentioned arguments, a proposal to disassemble MUCH completely on an 'as-it-is' basis for the di-electron mode of operation is being discussed. The pros and cons of such an option will be evaluated in detail including the issue of radiation, reproducibility of the chamber operation and the time required for such an operation. An intermediate solution might be to emove only absorbers and keep the chambers parked.

4.2.2 CBM surface facilities and required area

The plan of CBM ground facilities is shown in Fig. 4.10. It is foreseen that there is a working hall (347 m^2) and a preparation room (179 m^2) to be used by all CBM subdetectors.

MUCH will require dedicated areas for following jobs,

- To keep the pieces (parts of absorbers and superstructure) prior to the assembly in the cave. The requested area is needed at installation period only (3-6 month). If possible there should be place for unpacking and pre-assembling. These operations could be also done in working hall, but the hall in this case will be occupied for relatively long period. If MUCH is disassembled during di-electron mode of operation, irradiated pieces should be stored somewhere in CBM cave.

- Storage of assembled half-chambers fixed at their transport platforms. It should be noted that the chambers could be irradiated!

- A (clean) room for tests/assembly/repairing of the chambers. The required services and test DAQ should be there. If possible, 3 rooms are needed in order to manage the detectors of different type by members of different teams.
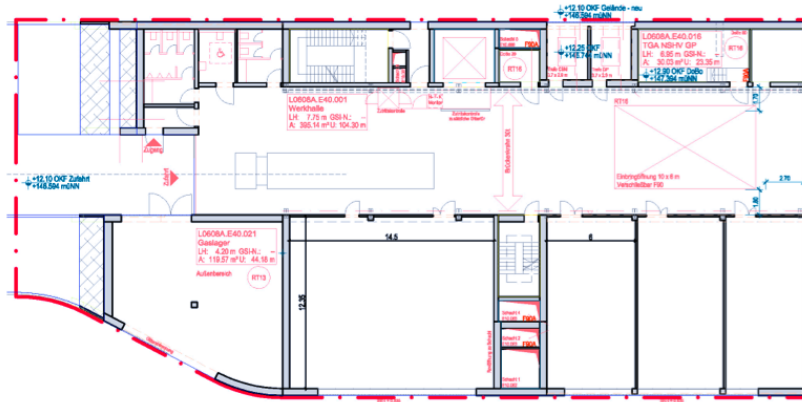
Figure 4.10: The plan of the CBM building: ground floor (courtesy W. Neiebur)

All the listed areas except #1 are required on permanent basis. The rooms 1 and 2 are to be preferably equipped with cranes. We also need a good access for crane to handle the half chambers attached to transport panels.

4.2.3 Integration and assembly of the MUCH mechanics

The assembly sequence can be imagined as follows:

- The absorber basement preparation.

- The first absorber is adjusted and fixed in its place as described earlier

- The absorber supports are installed

- The lower part of the absorbers is fixed in their positions with required precision tolerances.

- The beampipe position is adjusted (see Fig.4.4)

- The upper part of absorbers and their fixation system are put in their place

- The superstructure with attached half-chamber rails installed

The required tolerances of the chamber position in XY plane is about ± 2 mm and about ± 5 mm along Z. Optical fiducial marks will be used to position the chambers. The final positioning of the chambers should be done in magnet ON position, because the magnetic forces will cause deformations in superstructure.

4.2.4 Assembly and installation schedule

To be estimated as soon as quasi-final design will be ready.

4.2.5   Safety aspects

General safety rules used at FAIR are applied. The inflammable gas mixture is used. Gas detectors for severe gas leak are required when tested in relatively small room. The high voltage (HV) to be used is less than 5 kV.

4.2.6   Fabrication and installation of chambers

In this discussion, we have taken only GEM chambers for design study. For inclusion of detectors of other technologies in the setup, some modifications might be necessary.

In the actual MUCH layer design, the annular region of each layer is achieved by overlapping alternately, back -to-back trapezoidal shaped GEM chambers so that the active region of each GEM chamber seamlessly covers the required annular area. Though the GEM foils required can be made with large ($\approx$1-1.5m) length, the width has a limitation of around 600mm due to the available maximum roll width of the copper clad polyimide foil. Thus the outer side of each trapezoidal chamber should not be more than say, around 500mm active width. With this design constraint the number of trapezoidal sectors needed for the annular coverage has to be optimized. The construction concept of large GEM chambers has evolved over the years. We have considered three possible ways of building these chambers. They are:

4.2.6.1   Glue-all layers approach

In this method trapezoidal GEM foils are first stretched over spacer grid-frames using thermal or mechanical stretching means. A thicker (2-2.5mm) drift plane PCB serves as a rigid base, over which all layers are assembled and glued together. The width of the GEM and spacer frames thus becomes the outer wall of the gas tight chamber. The HV tails for GEM foils come out of the chamber walls, so that HV dividers can be mounted outside. Alternately HV dividers can also be placed inside if required. Provision for gas in/out feeds are also made in the frame wall by appropriate machining. Early prototypes of CMS high-eta upgrade chambers followed this procedure. The schematic is shown in Fig. 4.11.
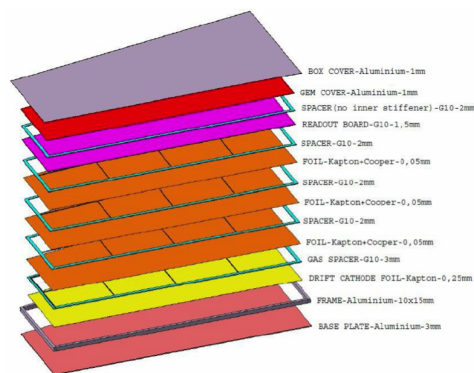
Figure 4.11: sector aeemsbly by glueing all planes in the sector

Though this procedure works for test prototypes, for bulk production and maintenance it has several drawbacks as itemized below.

- Thermal stretching is time consuming and severely limits the production rate of chambers

- Gluing all frames together and oven curing is also a long procedure.

- Gem foils cannot be replaced if defective. Thus the entire chamber has to be rejected (cost burden).

4.2.6.2 O-ring sealed chamber

The modified construction method by introducing an additional O-ring sealed chamber frame is shown in Fig. 4.12.
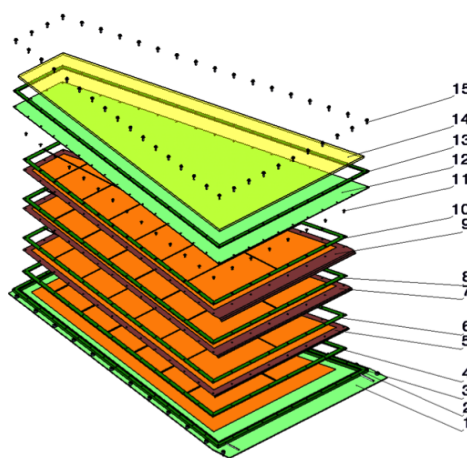
Figure 4.12: Exploded view of the O-ring sealed chamber. 1) drift PCB 2) gas tight outer frame 3) O-ring seal 4) drift gap spacer 5) bottom Gem foil 6) bottom spacer grid frame 7) middle GEM foil 8) middle spacer grid frame 9) top GEM foil 10) top spacer grid frame 11) GEM frame fasteners 12) readout PCB 13) edge frame 14) top honeycomb board 15) outer frame fasteners.
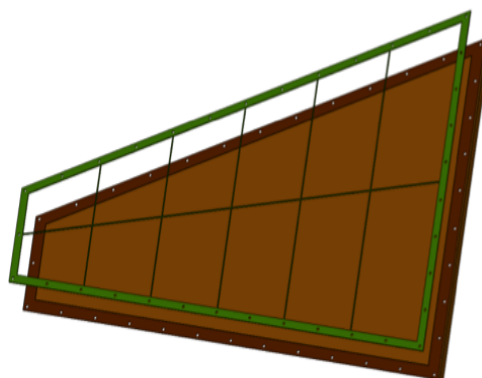
Figure 4.13: GEM foil with gridded spacer frame

The chamber frame is mounted on the rigid drift plane PCB and serves as a gas tight chamber housing. The three GEM foil layers, thermally (or mechanically) stretched over FR4 spacer grid-frames (Fig. 4.13) are assembled over the drift plane with a 3mm drift spacer frame using nylon fasteners. HV segment resistors are soldered at the outer edge of each GEM foil and only the HV tails come out of the chamber through the printed tracks on the drift plane PCB (Fig. 4.14).
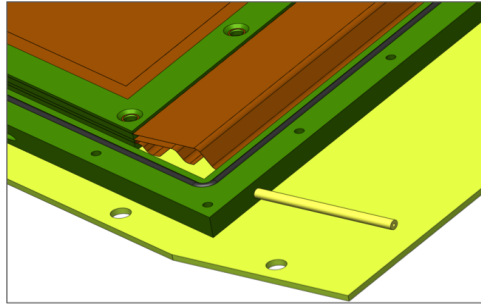
Figure 4.14: HV tails on HEM foils inside the O-ring sealed chamber

The pad plane PCB on top extends over the O-ring outer frame and can be press fitted over the frame by several fasteners. We plan to use O-ring seals both on top and bottom sides of the outer frame, to eliminate time consuming gluing procedure. This method of construction gives access into the chamber interior for service and thus reduces the long term maintenance costs. However the assembly with pre-stretched GEM foils is still a part of this procedure and the associated issues cannot be avoided. The exploded view of the chamber is shown in Fig. 4.14.

4.2.6.3   In-situ stretching method

In order to eliminate the problems associated with thermal stretching and gluing procedures, the CMS high- eta upgrade R&D efforts [7] evolved into an in-situ stretching method (NS2 method). Small to full size prototypes are built at CERN and tested. The size and shape of the chambers tested are similar to the MUCH needs and so the construction technique is actively being considered by us as one of the possible methods for adaptation.

The procedure is briefly described as follows:

- An outer frame with O-ring seals on top and bottom sides is mounted on a rigid drift plane PCB to serve as chamber housing. This eliminates the gluing procedure.

- The bottom GEM foil is placed inside the chamber and specially machined clamp-segments are placed on the edges of the foil. The procedure is repeated with middle and top GEM foils.

- Now all the three layers of each clamp segment are fastened together with screws at select places. While designing the layout of the GEM foil some circular copper patterns are generated at the edges to enhance the grip of the edge clamp segments.

- The clamp segments are provided with an internal groove to accommodate a stainless steel nut. Thus after assembly of the segment a screw can be inserted sideways through the segment which mates with the embedded nut Fig. 4.15.

- The outer chamber frame has provision to insert screws from side walls through a small gas tight O-ring seal and the screw can be coupled to the embedded nut in the corresponding clamp segment.

- After clamping all the foils the screws on the sides of the chamber frame can be tightened to stretch the foils in-situ (Fig. 4.16).The screws are tightened until optimum tension is reached in all the three GEM foils.

Figure 4.15: Closeup view of the clamp segments with the embedded metal nut
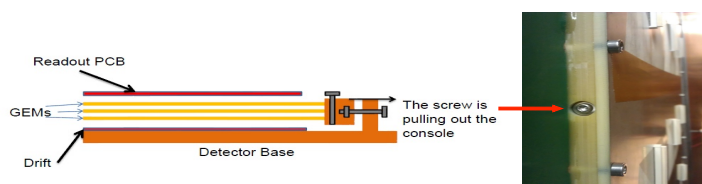
Figure 4.16: Closeup view of the clamp segments with the embedded metal nut

- HV contacts are brought out of the foils through spring contacts. This needs further improvement.

- For large scale production it may be possible to mould the clamp segments with some engineering plastic like PEEK.

- This method completely eliminates the slow gluing procedure and suitable for large volume production of chambers. Also since the grid-spacers are absent in the active zone, sparking probability due to glass filaments on the grid edges is eliminated. The chamber can be opened easily for GEM replacement.

Fig. 4.17 shows the drawing (left) and a fully assembled sector (right). The thickness of the whole chamber will be dependent on the gas thickness of the chamber. At present the space available (30cm) for assembly of 3 layers seem to be sufficient keeping a gap of 3 mm in between layers.

4.2.6.4   mounting of sectors on stand

Fig. 4.18 shows the assembly of the sectors on a frame to build a station consisting of three layers. Each layer has chambers on two sides with overlap along the edges of the chambers to cover the dead areas. The sectors will be assembled on two sides of two support half-plates. Each half plate when joined form a full layer. The half-plates could be moved in transverse
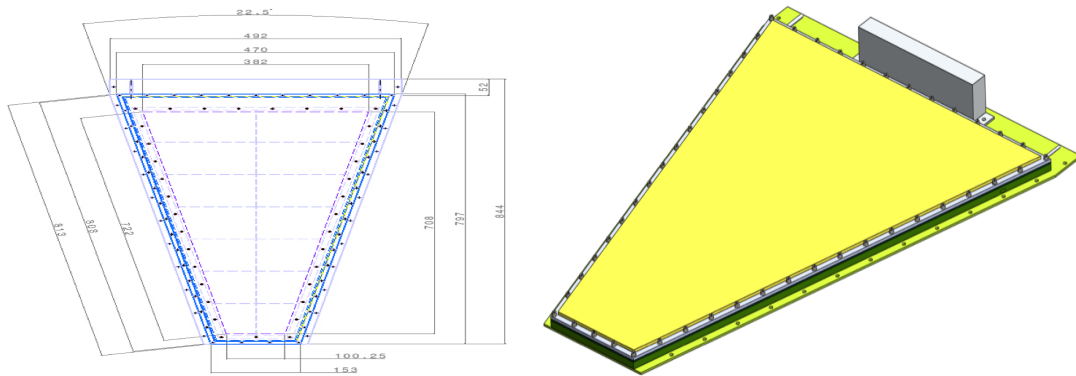
Figure 4.17: Drawing of one sector (left) and after full assembly (right)

direction for service etc. HV, gas and water connections will be taken out from the periphery. The chambers are assembled on the support structure at alternate positions on both sides of the plane. 16-chambers, as obtained for the first station in both the SIS100 and SIS300 setups, eight on each side of the support plane are shown in the figure.
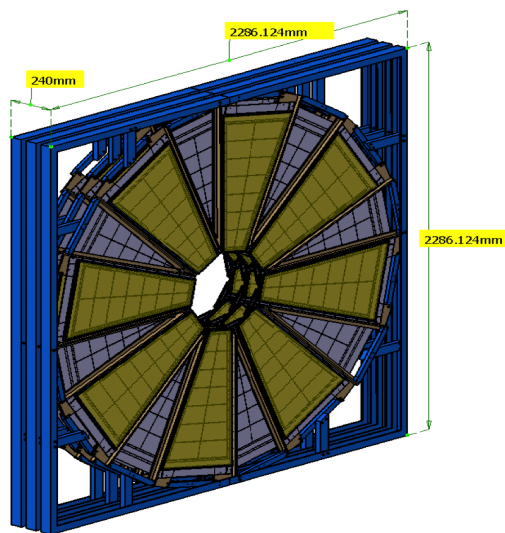
Figure 4.18: A station with 3 layers each of 16-sectors shown after assembly of chambers on one side. For the chambers on other side there will be overlap.

Once the sectors are mounted on the frame to form (half) layers, they need to be assembled on a stand. Fig. 4.19 and Fig. 4.20 show two views of assembled layers. The figure shows the mounted layers when separated in transverse plane. The details of movement mechanism will be installed later, however the guidelines are given in earlier section. For example, Fig. 4.6 shows the half-chambers in hanging positions. In that case, the guiding rail mechanism need to be reevaluated than shown in Figs. 4.19 and 4.20.

We enlist here some of the design notes for layers.

- Water cooled Aluminium plates are part of the support structure. They add rigidity to the structure and also provide a cooled surface for FEB mounting.

- Choice of slide rails to move in/out the two halves of the structure is not yet made and will be decided when the dimensions and weights are fixed.
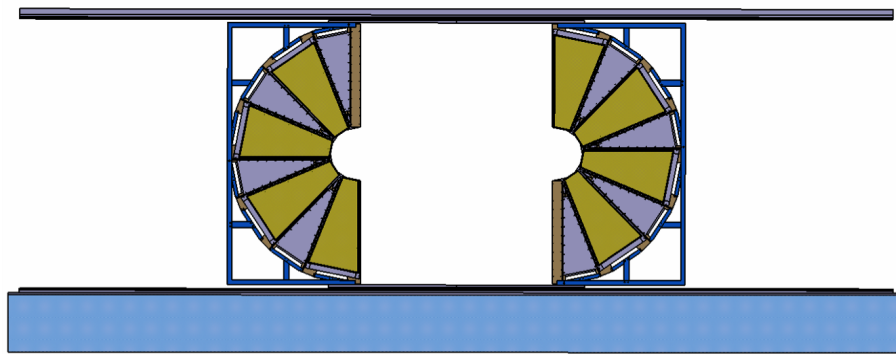
Figure 4.19: One view of the sectors mounted on support plane and on stand. Each half can be serviced separately
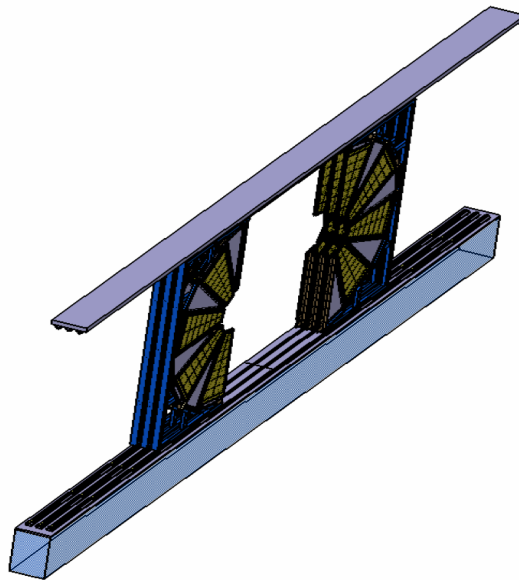
Figure 4.20: Another view of the half-layers mounted on support plane and on stand. Each half can be serviced separately

- Gas and water manifolds run on the periphery of the structure.

- Signal connections are brought out from the readout plane through flexible kapton cables and are connected to FEBs on the side (mounted on the cooling plate)

- All HV, LV , DCS cables run on the periphery on a ladder frame. All services coming out of the sectors will be connected to the service poles to be provided on the platform.

- No component is overly large and can be CNC machined to required precision.

4.3 Readout Electronics

4.3.1 General concept of the CBM readout chain

Many of the signatures pursued by the CBM experiment are based on rare processes. To achieve an adequate sensitivity, the detector systems are designed to operate at interaction rates of up to 10 MHz for A-A collisions and up to several 100 MHz for p-p and p-A collisions. It is the task of the data acquisition and event selection system to identify the candidate events for the physics signals under study and send them to the archival storage. One of the challenging aspects in CBM is the measurement of open and hidden charm in heavy ion collisions down to very low cross sections. The D mesons are identified via the displaced vertices of their decay products, the decision for selecting candidate events thus requires tracking, primary vertex reconstruction, and secondary vertex finding in the STS. In addition, the system has to be configurable to handle a wide range of physics signals, ranging from D and J/ψ in A-A collisions over low-mass dileptons in p-A collisions.

The conventional system design with triggered front-end electronics allows to keep the event information for a limited time, usually a few microseconds, in the front-end electronics while a fast first level trigger decision is determined from a subset of the data. Upon a positive trigger decision, the data acquisition system transports the selected event to higher-level trigger processing or archival storage. A system with such a fixed trigger latency constraint is not well matched to the complex algorithms needed for a D trigger, especially in the case of heavy ion interactions, where the multiplicities and thus the numerical effort needed for a decision varies strongly from event to event.

The concepts adopted for CBM uses self-triggered frontend electronics, where each particle hit is autonomously detected and the measured hit parameters are stored with precise timestamps in large buffer pools. The event building, done by evaluating the time correlation of hits and the selection of interesting events is then performed by processing resources accessing these buffers via a high speed network fabric. The large size of the buffer pool ensures that the essential performance factor is the total computational throughput rather than decision latency. Since we avoid dedicated trigger data-paths, all detectors can contribute to event selection decisions at all levels, yielding the required flexibility to cope with the different operation modes. In this approach there is no physical trigger signal, which prompts a data acquisition system to read a selected event and transport it to further processing or storage. We thus avoid the term *trigger* in this chapter. The role of the data acquisition system is to transport data from the front-end to processing resources and finally to archival storage. The event selection is done in several layers of processing resources, reminiscent of the trigger level hierarchy in conventional systems. One consequence of using self-triggered front-end electronics is a much higher data flow coming from the detector front-ends. For CBM, a data rate of about 1 TByte/sec is expected. However, communication cost is currently improving faster over time than processing cost, an observation sometimes termed Gilder's law, making such a concept not only feasible but also cost effective.

4.3.2 Overall readout architecture

Based on the philosophy discussed earlier, the general layout of CBM subdetector readout system is shown in Fig. 4.21.

The DAQ architecture is divided into 4 layers:

- FEB (Front End Board)

- ROC (Readout Controller) or GbTx based boards.

- DPB (Data processing board)

- FLES (First Level Event Selector) with storage.

In CBM ,the signal from the detector is processed by the analog front end electronics based on sub-detector specific ASIC (nXYTER is being used in all test runs) and the signals are digitised in the Front End Electronics Board (FEB) and then sent to the Read Out Controller (ROC) board (for test beam) or to the boards containing GbTx (for final CBM data taking). The ROC or the GbTx boards collect data from the individual front-end units and aggregate the traffic on a set of high speed links which connect the detector with the area where the data buffers and the data processing is located and named as DPB. A rough estimate for the total data rate is 1 TB/sec that could be finally transported off the detector with about 1000 links with 10 Gbps each. For our case, the Front End Board (FEB) will be specific to MUCH. GbTx for transportation of FEB data to the controller could be general to CBM at least to the STS and MUCH. DPB could have functionality specific to MUCH. GbTx ASIC is taken from CERN which will be used in large LHC experiments. The details of individual systems of different layers specific to MUCH are discussed below. A separate technical design reports will discuss details about the readout systems common to CBM.
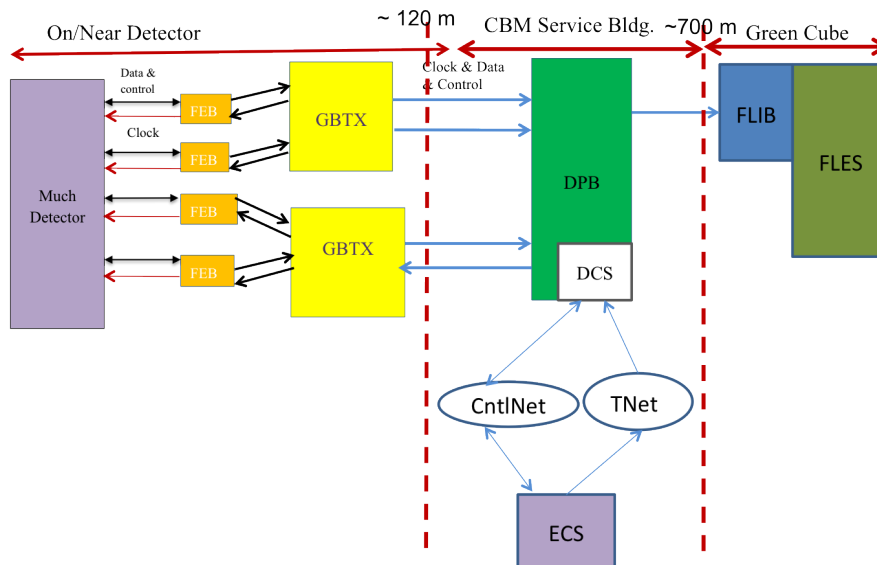
Figure 4.21: Layout of MUCH readout in CBM using GbTx

4.3.3   Front End Electronics Board (FEB) for GEM chambers

Table.4.3 gives a summary of the requirements of two GEM chambers in the first two stations of MUCH. The table gives the chamber and pad dimensions alongwith the total number of pads required in these two chambers. For reading out these pads, as per CBM requirement, we need front end boards. We discuss below the evolution and the decision on the baseline solution of the FEB of GEMs for MUCH.

St No.	Layer No.	Total pads	R1 (cm)	Pad size (mm)	R2 (cm)	Pad size (mm)	Area (sq.mt)
1	1	28800	25	4.35	100.25	17.48	2.95
	2	28800	25	4.35	100.25	17.48	2.95
	3	28800	25	4.35	100.25	17.48	2.95
2	1	30240	29.5	5	123.5	21.3	4.5
	2	30240	29.5	5	123.5	21.3	4.5
	3	30240	29.5	5	123.5	21.3	4.5

Table 4.3: Dimensions and the distribution of pads and optimized number of FEBs on 2 stations of MUCH. Number of FEBs per layer is 240

parameter	value
Dynamic Range	25 fc
Fast Shaper Gain	47 mV/fc
Slow Shaper Gain	24 mV/fc
Power Dissipation	12 mW/channel
Noise	1000 fc
Total Current consumption	406 mA
Minimum time resolution	2 ns
Fast shaper shaping time constant	40 ns
Slow shaper shaping time constant	160 ns

Table 4.4: Specifications of nXYTER

Before the final chain of the readout system of CBM is designed and tested, GEM detectors of MUCH have been taking data using self-triggered nXYTER based readout system where a somewhat modified and reduced version of the proposed CBM readout chain has been used. The specifications of nXYTER is given in Table 4.4. nXYTER based FEE boards being used in the CBM test beam experiments get connected directly to the detector via two 68-pin ERNI connectors. The data are then stored in the ring buffer internal to the nXYTER ASIC to be subsequently fed in synchronization to ADC. The ADC data along with the time stamp from nXYTER ASIC in synchronization are sent to ROC board through 80-pin ERNI connector via twisted pair LVDS cable. In addition to this there is an I2C bus to configure the different parameters of nXYTER. One of such FEE boards (FEB) is shown in Fig. 4.22. The FEB to be used in the final experiment will certainly look different from the current one, however the experience gained from the functionality will be useful in design and building the final FEB. The FEB shown in Fig. 4.22, for example consists of only one ASIC, which might change depending on the placement of the FEBs as per the occupancy of the chamber and the number of channels available in the final FEB. Our final baseline FEB will follow the FEB to be used by STS because of the advantage of using the same backend and subsequent boards in the chain. Some ongoing R&D on the development of a MUCH-specific ASIC has been discussed in the Appendix-C, which if developed and tested successfully might, based on the requirement, find its use in the SIS300 MUCH.
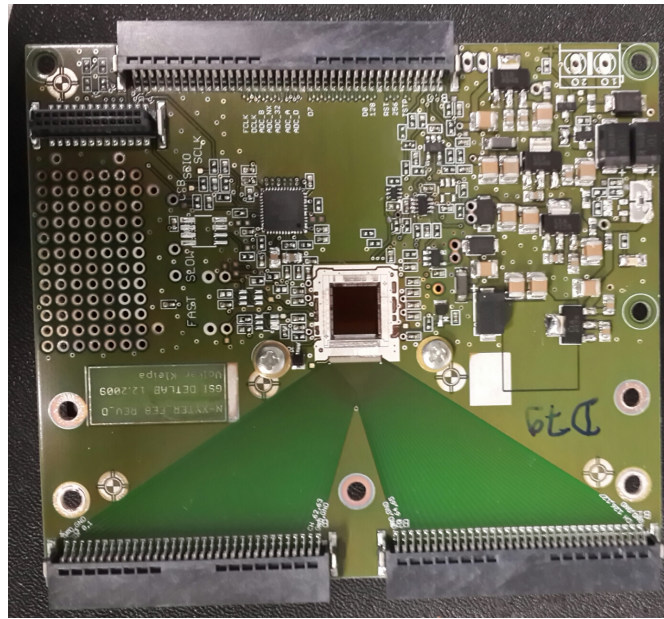
Figure 4.22: A FEB board with nXYTER

4.3.3.1 GEM FEE ASIC

Table 4.5 gives the specification of the MUCH ASIC for the GEM chambers. Even though the specifications to be met by the ASIC for GEM detectors are similar in many respects with those of the ASIC for STS, however, there are several parameters (e.g., dynamic range) that differ from the STS requirements. Even though the components responsible for processing analogue detector pulse might differ from STS-XYTER, however, as per plan the new MUCH ASIC backend will be made similar to the STS-XYTER. The activities related to MUCH ASIC should therefore be viewed as the development of STS-XYTER and the pulse processing system for GEM taken together.

GEM chambers of MUCH will have projective segmentation with the smallest pad size being as small as 4.35 mm X 4.35 mm in the inner region and as large as 2.13 cm X 2.13 cm in the outer region of the chamber. This sets the requirement of a high density ASIC to meet the requirements in the inner region of the detector. Earlier tests show that the nXYTER chip used for STS was also suitable for the MUCH-GEM detector in terms of rate handling capability and density requirements after the use of additional bias settings to meet the detector specific requirements. STS-XYTER is designed on same architecture of self-triggered nXYTER ASIC and it meets the basic requirements of high density and high rate capability.

We discuss below the status of the development of the STS-XYTER for use in the GEM chambers of MUCH.

4.3.3.2 Status of STS-XYTER development for use in MUCH-GEM

The simplified block diagram of the STS-XYTER is shown in Fig. 4.23 The blocks as located on the full chip are depicted in Fig. 4.24. The chip includes 128 channels consisting of a charge sensitive amplifier (CSA), a shaper (SH) and an analogue to digital converter (ADC). The functional diagram of a channel is depicted in Fig. 4.25. An essential new feature compared with the

parameter	value
number of channels	128/64 + 2 test channels (prelim)
input signal polarity	positive and negative
accepted input leakage current	10 nA
input capacitance (detector + cable)	30 pF
ENC @ 30 pF input capacitance	1000e
ADC range	50 fC
ADC channel	1.56 fC
timing resolution	10 ns
power dissipation per channel:	< 10 mW
operating temperature range	$\Delta T < 40C$
technology	UMC 180 nm
Max hit rate per channel	2 MHz
Shaping time constant	40 ns
Spark protection	yes

Table 4.5: Parameters of MUCH-ASIC, as fulfilled by the dual gain version of the of the STS-XYTER.

nXYTER architecture is an effective two level discriminator scheme. The discriminator in the fast signal lane triggers the latch of a time stamp at a high timing resolution. Due to the higher bandwidth of the fast lane, the noise level and thus the noise-related trigger rate is comparatively high in such a self-triggered system if the discrimination level is kept low. In such a situation, noise-related hits would swamp data channels and create dead time, while if the threshold is kept too high, the essential low level hits would remain undetected. The two level trigger scheme employed in the STS-XYTER adds a veto to the transmission of data in case the flash ADC has generated **zero**. The discrimination level of the LSB may be shifted through a control register and effectively serves as a secondary discriminator that is exposed to the low bandwidth, low noise energy signal. This strategy makes the Rice formula applicable to the signal of the energy channel while keeping the high time resolution achieved from triggering on the fast timing channel.
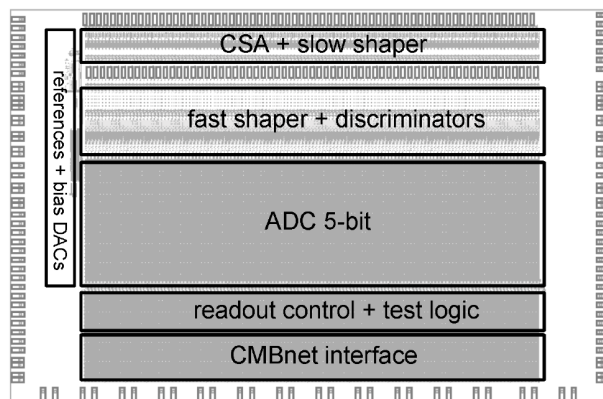
Figure 4.23: Location of the blocks on the STS-XYTER ASIC

The first version of the STS-XYTER has been delivered and tests have been started. MUCH Electronics experts have been participating in these tests, and the required input will be provided for the design of the next version of the ASIC. A new version of STS-XYTER has been designed
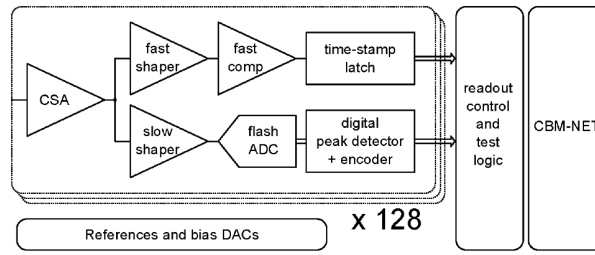
Figure 4.24: block-diagram of STS-XYTER
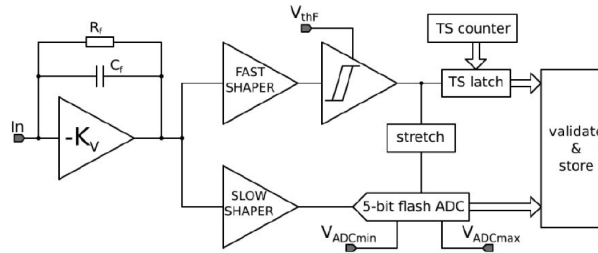
Figure 4.25: Functional diagram of one channel

with the provision of dual-gain which is suitable for use in both STS and MUCH. The first version of the design will be submitted for fabrication in March 2015.

4.3.3.3   Integration of FEBs on GEM chamber

The FEE boards for every sector are planned to be installed on the 8mm aluminum plate as shown schematically in Fig. 4.26. The FEBs corresponding to a sector will be mounted on the backside of the neighboring sector. The heat sink of the FEE board will be at the bottom and connected to these aluminum plates. According to the current plan, these plates are water cooled which serves as coolant for the heat generated by FEE board. These plates also serve as the support structure and gives mechanical strength to the full assembly.

The largest dimension of the FEB will be around 10cm × 3cm which can fit comfortably within the sector geometry. This dimension is for a FEB with two 64-channel ASICs. If 128 channels fit in the same die-size of STS-XYTER, the dimension may be further reduced. The signals from the MUCH chambers will be taken out via Kapton cable as shown in the Fig. 4.26. For this purpose, kapton cables of 3-4 different sizes will be used to meet the requirement of varying pad size to FEE length. Table 4.3 gives the distributions of pads in first 2 chambers and the optimized number of FEBs. The number of sectors are 16 and 20 for the first and second stations respectively and the number of FEBs per layer is upto 240.

4.3.4   Front End Electronics for the Straw tube detectors

As a baseline solution for the Straw tube readout system with 1-D readout, it has been decided to use the readout system of one of the existing CBM sub-detectors for the straw tube detector as well. For our purpose , we will use PADI-GET4 based readout system being developed for the CBM-TOF detector for the straw tube detector as well. The system will have self-triggered system with the capability of reading timing signals with very high resolution. This system
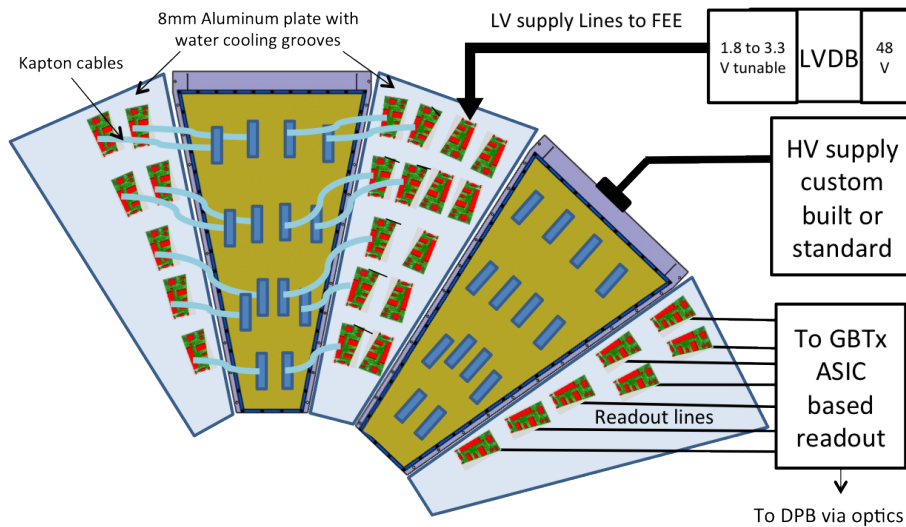
Figure: Show the integration of chamber with the electronics

Figure 4.26: Integration of FEBs on chamber

should therefore be comfortably used for relatively low position resolution use in the straw tube detector. Some other ongoing developments on the straw tube readout have been discussed in Appendix-C, which if required, might be used in SIS300 MUCH. We summarize the baseline solution of the Straw tube readout below, the details of which are available in the technical design report of the CBM-TOF system.

4.3.4.1 Use of TOF readout system for ST detector

The two CBM-Much layers will be realized by multilayer straw-tube systems in each station. These straw-tubes of diameter 6 mm are intended to be read out in a position sensitive manner only in one dimension, namely the signal drift dimension which is the position lateral to the straw and its anode wire. Along the individual straw, no position information will be sought. The reason for this is that with an additional readout of the position information along the anode wire, each straw needs to be equipped with two pre-amplifiers, one on each end of the straw. Also, typically, the resulting resolution that may be achieved by means of a charge division measurement, is at maximum on the order of 1%, resulting a mere 3 cm resolution of position for this system. The Position information along the straw will thus be extracted through coincidence of hits from several straw layers that are rotated with respect to each other as to achieve a stereo angle of at least 60°. Hits on a straw do leave a track of charges within the straw, which will drift towards the anode wire. Typically, the charges allocated closest to the anode will reach the anode first, other clusters may reach the anode with a considerable delay. For the readout of such a straw-device, the time of incidence of drifting charges onto the anode is to be determined. With a start signal at hand, the drift time can be determined and thus the lateral distance of the track from the anode wire may be determined to much higher precision than just the diameter of the straw. For the identification of the track location, only the very first arriving charges and their signals are relevant. Later arriving clusters will create some after-pulsing, which needs to be discarded in digital processing in the DAQ system. Consistent with the entire CBM DAQ system, the straw signals will be read-out in freely streaming data mode. Each Signal, once registered, will be assigned with a timestamp that is coherent and synchronized with the global

time system. With each signal assigned a globally valid timestamp, the overall track position in the straw tracker may be determined by a least squares analysis, even though not even a global start signal might be available. It is expected to improve the position resolution of the straw tracker by more than an order of magnitude over the mere diameter of the straw. Typical drift speeds of signals in an Ar-CO_2 mixture are 6 cm/μs, depending upon the local electric field strength. Drift times as long as about 50 to 100ns are thus to be expected. The electronic readout system for the Straw-Detector needs to: (a) realize the free streaming data generation and readout (b) allow determination of the signal time-stamp with a precision of at least 1ns (c) generate sufficient signal from a MIP generated track that traverses the straw laterally

To this end, a fast, extremely sensitive pre-amplifier and discriminator circuit with very low threshold variation is needed, joined with a means of precise time-stamp generation. Within the CBM detector system, the TOF detector subsystem has been designed to similar but much more challenging specifications. Here, RPC signals are detected as the TOF stop signal. The signals are read-out by a custom made ASIC by the name of PADI, which has continuously been improved to meet the needed specifications and is now in its eighth and final iteration PADI 8. It sends its precisely timed discriminator pulses to a subsequent TDC system that is either realized by the equally custom made TDC ASIC Get4 or, alternatively by an FPGA-based TDC. This system has been shown to perform with a timing resolution of 38 ps (excluding the detector). On top of the mere time of incidence identification, it also allows for time over threshold and thus a pulse height measurement. The CBM-TOF system clearly outperforms the needs of the MUCH-Straw plane readout and is, being fully developed and available, a very good and thus the most economic choice. It fully addresses the free streaming readout concept as it will be implemented in most CBM subsystems and is already fully integrated into the CBM-DAQ concept. The straws can be operated at a gain from 1000 to 10000 through the choice of Anode voltage, which will be adapted to meet the input specifications of the PADI pre amplifier perfectly. The equivalent noise charge of 1145 enc, is transformed to an output noise level of 5.5 mV, with baseline variations of 1 mV (1σ) found far below. Additionally, its input impedance may be matched between 50 and 150 Ohms in order to adapt to the detector needs. Consequently, the first arriving charge clusters of only a few electrons will generate sufficient signal to generate a trigger and thus the time of incidence. PADI-8 performs at a conversion gain of 30mV/fC. PADI with its 8-channel package on a chip is well adapted to the geometry of the straws. Its power generation of 17mW/channel can be handled on the perimeter of the straw station without imposing any challenges.

4.3.5 Environmental condition

The station-1 of MUCH will receive highest dose of 300Gy/2 months (i.e. 30000 Rad at 25 cm, the radial distance of the beginning of active area of layer-1 of 1st station) as was simulated by FLUKA and described in Chapter 2. Total CBM-MUCH operating period in 10 years is expected to be of 20 operational months, and the CBM readout electronics are made to withstand the total dose of 2MRad which is considerably higher than the total dose requirements discussed above. The region beyond 90 cm will be receiving the dose of 30 Gy/2 months.

4.3.6 HV requirements

The estimate of the requirement of HV channels has been done for first two stations only. 15 HV channels per sector for station-1 and a maximum of 20 HV channels per sector for station 2. Taking 16 sectors per layer for station-1, total number of HV channels = 16 X 15 X 3 = 720.

20 sectors per layer for station-2 for SIS300 gives total number of HV channels = 20 X 20 X 3 = 1200.

For HV distribution, one supply cable per sector (for 15/20 HV segmentations per sector) is planned to be taken from HV supply to the detector.

For the above mentioned system, a total heat load of 100W/sector is envisaged. This will add to the requirement of cooling the system.

4.3.7 LV requirements

A load requirement per 128-channel FEE board is 2 W (max). So per layer for 240 FEE boards, load requirements is about 480 W plus overhead of ROB that converts electrical signal to optical and transfers data to data procession board. So maximum load requirement is about 0.6 kW per layer. Two 48 V and 8 A load current capability wires for each half of the layer will be used.

A Low Voltage Distribution Box (LVDB) is being designed to feed power to 8-FEE boards. Each sector will require 2-LVDB with 1-spare channel to fed ROBs for each sector. Since the MUCH detector is movable the obstacle in movement and the cable count should be small. Therefore, a 48 V supply is planned to brought close to the detector, and the 48V is stepped down to 5V which is then reduced to 1.8V - 3.3V using a SMPS DC to DC converter on Low Voltage Distribution Board (LVDB). This LVDB has additional feature of over current protection, Voltage and current monitoring and control, individual channel ON/OFF through the slow control system. Each LVDB is designed to feed power to eight FEE boards. A 2-channel prototype is designed and tested at VECC with over-current protection, voltage regulation and voltage monitoring tested with RS-232 and Ethernet communication. Preliminary results of voltage regulation and load regulation are shown in Fig. 4.27
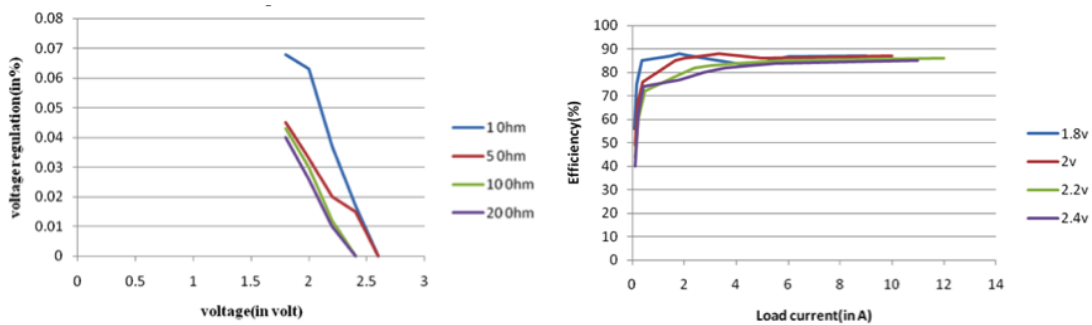
Figure 4.27:   Voltage regulation performance

4.3.8 Cabling

- For sectors of station-1 and station-2, 15 and 20 HV channels respectively are required. So for each sector, one option is to use 30-pin HV connector along with 24 conductor cables with insulation per core of the order of 6 kV. Probable supply solution could be A1535 of CAEN with 3.5 kV/3 mA with 12/24 channel input with 30 pin connector.

- For LV, per layer we need 2/4 multi conductor cables of 6 mm^2 to feed 500 W/250 W per cable to the detector.

- Control cables will be required to control and monitoring of LV distribution boards. These cables are around one cable for 6-FEE boards so on an average 30 control cables per layer will be required.

- GBTx ASIC can handle around 6-FEE boards which correspond to one fiber cable. So on an average 28 fiber cables per layer will be required.

To meet the cable requirements and at the same time maintaining the space constraint, LV cables and fiber cable which has the origin very near to the detector will be routed within the empty space between two chambers.

4.3.9 Data Processing Board (DPB)

Data Processing board provides the generic DAQ and Control interface. It encapsulates subsystem specific formats and protocols and provides the data container stream to FLIB/FLES. The data processing on DPB is detector specific. For MUCH, following features may be implemented in DPB before sending the data to FLES.

- Mapping, i.e. the real X-Y co-ordinate from the channel information may be implemented and encapsulate in the data.

- Threshold: channel-by-channel threshold may be calculated and stored in a buffer and may be used for producing pedestal subtracted data in the subsequent runs.

- Electronic calibration: individual channels can be calibrated using a mechanism like look-up table.

4.3.10 FLES

The description of FLES is to be integrated as a part of main CBM document, for MUCH the data from DPB will be transmitted to the FLES and might be used for generation of trigger. The trigger algorithms discussed in chapter 2 (simulation) have been found to be implementable in GPU, and the use of CUDA helps in improving the performance significantly.

4.3.11 Detector control system

For the detector control system of CBM, *Experimental Physics and Industrial Control System (EPICS)* will be used. EPICS is a set of software tools and applications which provide a software infrastructure for use in building distributed control systems to operate devices such as Particle Accelerators, Large Experiments and major Telescopes. Such distributed control systems typically comprise tens or even hundreds of computers, networked together to allow communication between them and to provide control and feedback of the various parts of the device from a central control room or even remotely over the internet. It uses Client/Server and Publish/Subscribe techniques to communicate between various computers. Most servers (called Input/output Controllers or IOCs) perform real-world I/O and local control tasks, and publish this information to clients using the Channel Access (CA) network protocol. CA is specially designed for the kind of high bandwidth, soft real-time networking applications that EPICS is used for, and is one

reason why it will be used to build a control system for CBM experiment. For MUCH, following sub-systems will use the detector control system.

- *High Voltage System HV:* The whole detector system shall be segmented into approximately 2000 HV channels.

  For each channel following information should be written into the high voltage power supply : channel name, voltage set, maximum current allowed, RAMPup, RAMPdown, trip parameter, enable/disable POWER ON option, switch ON/OFF.

  For each channel we should read: channel name, set voltage, output voltage, output current, maximum current, RAMPup, RAMPdown, trip parameter, enable/disable POWER ON option, status. High voltage is supposed to stay constant during data taking, while the current may vary.

- *Low Voltage System LV:* The detector system shall require a larger number of Front End Boards and each FEB requires active control system.

  For each channel the following information should be written into the low voltage power supply: output voltage set, current limit, ramp up time.

  For each channel we should read: sense voltage, channel voltage, current.

- *Gas Handling System:* The Gas handling system is defined in the next section. All the active as well as passive parameters shall be incorporated in the central control system for the Muon detector system. An interlock with the HV and LV system shall be provided to protect the detector in case of failure of the Gas system.

- *Cooling System:* The temperature and circulation of the chilled water needs to be monitored and an interlock shall be provided between the cooling system and the LV.

- *Temperature Monitoring:* The control system shall be incorporating temperature sensors distributed all over the detector system and shall generate suitable alarms in case of abnormal increase in temperature in any region of the detector.

- *Geometry Monitoring:* A suitable geometry monitoring as well as alignment system is foreseen to make sure that all the absorbers as well as chambers are properly aligned and none of the mechanical tolerances are being violated.

- *Environment monitoring:* Suitable Sensors shall be incorporated at strategic locations on the whole system to monitor various environment parameters like atmospheric pressure, humidity, temperature, level of radiation among others and interlocked with subsystems like HV, LV among others.

4.4   Gas handling system

The gas system for CBM-MUCH will be built in such a way that different gas mixtures could be delivered for different sub-detectors. If required, more than one systems will be installed to serve the purpose. One such system is shown in Fig. 4.28 where it provides mixture of provide $Ar+20\%CO_2+5\%$ i-Butane. The system operates nominally as a closed circuit gas system with the majority of mixture recirculation through the detector [1, 2, 3, 4]. The re-circulation flow can be adjusted in the range of 60-80 SLPM. During normal operation a fresh mixture is added with the mass flow controllers FM1, FM2 and FM3 in the range of 0.1-10 SLPM. FM1 is the master

and FM2, FM3 are the slaves To support the constant differential pressure measured by PT6 sensor in the range of 2±0.1mbar, the control system will change the flow through the detector using the bypass solenoid valve BSV1. If the differential pressure is increasing, the mixture flow through the back pressure control valve BPCV1 will be increased too by the closing of BSV1 and PT6 readings will drop. In case of PT6 differential pressure drop, the flow through BPCV1 will be reduced by closing the BSV1. The pressure indicating switch PIS1 will support the low (0.5mbar) and high (1.5mbar) differential pressure levels upstream of the compressor C1. The gas system can be operated in an open configuration for the purging. A bypass valve BMV1 is manually adjusted to enable the optimum flow rate through the detector.
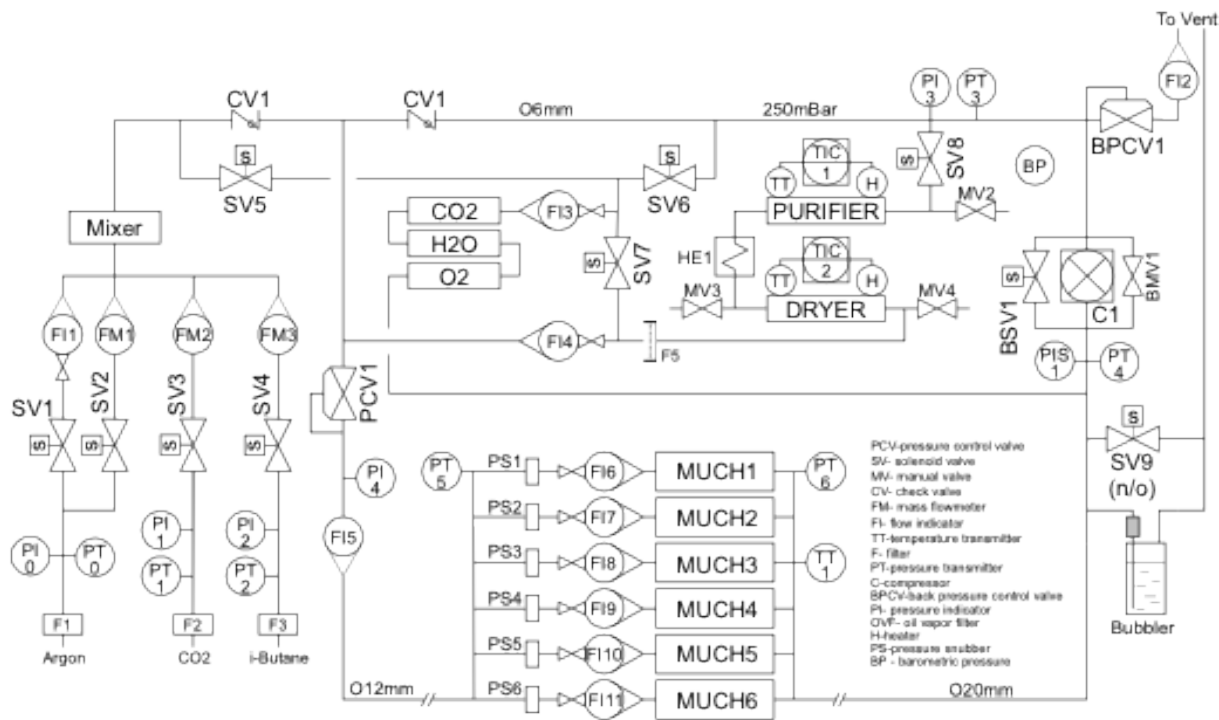
Figure 4.28: Gas handling system of CBM-MUCH

The purity and content of recirculation mixture is monitored using Carbon Dioxide, Oxygen and Humidity analyzers. A fraction (up to 50%) of the recirculation gas can be passed through the Purifier and Dryer to remove Oxygen and Moisture. There is a possibility to check the mixture content and purity with the analyzers after the Purifier and Dryer to determine their saturation. The Purifier is filled with active copper. Its operating and regenerating temperature is 220°C. Oxygen content after the Purifier/Dryer is about 2-3 ppm. The Purifier regeneration is performed with $Ar+5\%H_2$ mixture.

Dryer is filled with KA(3A) molecular sieves. Its normal operating temperature is 22°C. Water content is 1-2 ppm in the Dry output flow at this temperature. The regeneration of the Dryer is performed at 350-400°C.

A computer driven data acquisition/control system [5, 6] monitors all of the process variables including MUCH differential pressure stabilization. The computer system flags quantities which fall outside of predefined limits and initiates corrective action.

Bibliography

[1] L. Kotchenda et. al, STAR TPC Gas System.NIM A499 (2003) 703-712.

[2] L. Kotchenda et.al, PHENIX TEC-TRD Detector Gas System. Preprint PNPI-2712, Gatchina (2007).

[3] PHENIX Muon Tracking Detector Gas System. Nucl. Inst. and Meth. A 578 (2007) 172.

[4] L. Kochenda et al., CBM Progress report, Darmstadt (2010), p. 31.

[5] P.Kravtsov and V.Trofimov. Multi-Channel Measuring Instrument for Slow Control Systems. Preprint PNPI-2723, Gatchina (2007).

[6] P. Kravtsov et al., CBM Progress report, Darmstadt (2010), p. 32.

[7] Construction and test of CMS NS2 GEMs (GE1/1): RD51 collaboration meeting, Stony Brook, October 2012

Chapter 5

Project planning and Cost

5.1   Introduction

5.2   Project coordination structure and planning

Table 5.1 gives the list of the institutions involved at present in works related to MUCH. The development, installation and operation of the system will be primarily handled by the collaborators from India and Russia. The collaborators from GSI will be involved in systems which are connected to the main CBM system like mechanical integration, electronics readout system among others.

Table 5.2 gives the layout of the sharing of various jobs among the collaborating institutions. In general, the planning has been made in such a way that specific subsystems especially in the production phase are to be handled independently by an institute or by a consortium. For example, production of electronics will be handled by the Indian collaborators, the mechanical and gas handling system will be the responsibility of the PNPI group. On the detector front, VECC will build the GEM stations and JINR will built Straw tube chambers. The simulation, analysis details, software-related works including those for readout will be handled jointly.

We give below brief descriptions of the jobs involved and the planned roadmap of execution.

- **Detector R&D:** Ongoing detector R&D will be completed after fabrication of real-size prototype chambers of each type i.e., one of GEM and another of Straw tube as required in the first phase. Presently, a GEM chamber of intermediate size (30cm $\times$ 30cm) has been successfully built and tested with source and proton beam. The layout of readout pads of this intermediate chamber is similar to that of the final chamber. The job of building a 1m $\times$ 0.5m prototype has started and it is expected to be completed by 2015, which will then be tested extensively with source and beam. During this period, all the procedure for building large size chamber will be established, which will be followed during production. Similarly, building and testing of full-size prototype of the Straw tube detector will be performed. The chambers will be tested for efficiency, uniformity of gain, stability and rate handling capability among others. As the timeline for complete readout electronics is somewhat delayed compared to that of chamber prototype, so the chambers will be tested with the latest available electronics. The aim will however be to test the chambers using

Sr. No	Name of the Institution	Address
1.	Aligarh Muslim University	Aligarh, India
2.	Banaras Hindu University	Varanasi, India
3.	Bose Institute	Kolkata,India
4.	Calcutta University	Kolkata, India
5.	Indian Institute of Technology	Kharagpur, India
6.	Institute of Physics	Bhubaneswar,India
7.	Jammu University	Jammu, India
8.	JINR	Dubna, Russia
9.	Kashmir University	Srinagar, India
10.	MEPHI	Moscow, Russia
11.	North Bengal University	Siliguri, India
12.	Panjab University	Chandigarh, India
13.	PNPI	Gatchina, Russia
14.	Rajashthan University	Jaipur, India
15.	Variable Energy Cyclotron Centre	Kolkata, India

Table 5.1: Institutions participating in CBM-MUCH project

Task	Responsibilities
Detector R&D	VECC, JINR,PNPI
Production of GEM chambers	VECC, BHU,BI
Production of Straw Tube Chambers	JINR
Mechanical system of MUCH	PNPI, VECC, GSI
R&D on MUCH ASIC	MEPHI, GSI, VECC
R&D on readout boards	VECC, GSI
Production and testing of Readout boards	VECC, GSI, BI, JU
Production of Gas system	PNPI
Development of offline software	Indian team, PNPI, GSI, JINR
Development of Online software	Indian team, GSI
Pre-installation assembly and testing	Full CBM-MUCH team
Installation	Full CBM-MUCH team
Commissioning	Full CBM-MUCH team

Table 5.2: Work load sharing among CBM-MUCH collaborators

close-to-the-final electronics. This phase of work will be performed mostly at VECC and Dubna respectively. R&D will also continue in the hybrid detector development at PNPI.

- **Production of GEM chambers:** The procedures established during the R&D phase will be followed at the time of production of final chambers. Each and every step will be followed by the validation procedures. Dedicated labs are planned to be built at three places (VECC-Kolkata, BI-Kolkata, BHU-Varanasi) for this work. One of the most challenging steps is to stretch the foil and mount them on the frame. Even though several options exist, the final procedure has not yet been established. depending on the complexity of the procedure, we might perform this procedure at one place (VECC) and then transport the framed GEMs to other places where they will be mounted and tested. A set of personnel will be trained for all the procedures.

- **Production of Straw Tube Chambers:** JINR-Dubna has already established detailed procedure of building the Straw tube detector. The same lab will undertake the job. As per plan, the chambers will be tested with CBM compatible electronics at the prototype level itself.

- **Mechanical system of MUCH & Design, prototyping and production of the system:** PNPI group has been working on the design of the mechanical system of MUCH which includes mounting of MUCH, movement mechanism and other procedures during di-electron mode of data taking. As the system is very heavy, proper care must be taken for handling the system. The detector groups are responsible for mechanical assembly of the respective chambers/sectors and their movement mechanism. The final integration of the system will be done in collaboration with the *integration team of CBM* stationed at GSI. Once the design is completed, prototypes will be built and tested.

- **R&D on MUCH ASIC and on readout boards:** Currently, the collaborators involved in the development of MUCH-ASIC are from MEPHI, Russia and Kracow, Poland. The Kracow group is involved in the development of STS-XYTER ASIC. Collaborators from VECC and GSI are involved in testing the prototype ASICs. Once the MUCH-compatible STS-XYTER is produced and boards are made, they will be tested extensively by coupling them with the chambers. Similar R&D will be performed on Front End Boards (FEB) and other boards placed downstream the chain.

- **Production and testing of Readout Boards:** Final production of boards are likely to take place in India by the Indian industries.

- **Production of Gas handling system:** This job will be performed by colleagues from PNPI. PNPI is also involved in building gas distribution system for RICH, so similar systems including their control will be built for MUCH. One or more system(s) will be built to supply gas mixtures of different compositions.

- **Development of offline and online software:** CBM is mainly a computing driven experiment and will require dedicated teams handling softwares both online and offline. Members from almost all the collaborating institutes will take part in development and testing of the software for MUCH.

- **Installation and commissioning:** Based on the scheduling of CBM, MUCH chambers will be assembled in the assembly area and will be tested thoroughly with source and cosmic rays. Once certified, they will be transported to the experimental hall for installation and commissioning.

5.3 Cost

The cost of the project has been evaluated as per today's cost estimate. Cost for the major items like, GEM foil, HV, LV systems, readout boards among others have been estimated based on today's market survey. The cost estimate for the full MUCH version is given in the Table. 5.3. The cost for the start version SIS100-C is estimated to be about 80% of the cost of the full-version SIS300-B.

Items	Total cost (kEuro)
GEM detectors (including mechanical assembly)	1000
Straw tube detector (including mechanical assembly)	600
HV system	600
LV system	300
Cooling	100
Gas supply system including controls	600
Absorbers including support	800
Detector mechanics (mainframe)	800
Readout Electronics (FEE, DPB and other boards + slow control)	2500
Safety	100
Spare parts	500
Alignment	200
Transport	300
Installation and commissioning	500
Onsite infrastructure, cables, crates	500
Total	9400

Table 5.3: Cost table for MUCH project (full version)

5.3.1   Planning and timeline

The timeline of the project till the commissioning in SIS-100 phase is given in Fig. 5.1. This is in accordance to the FAIR timeline as of now.

	2014	2015	2016	2017	2018	2019
Micropattern chambers						
Full size prototypes	▓▓					
Preseries production		▓				
Production and testing			▓▓	▓		
Transport, installation					▓	
Commissionning						▓
Electronics						
ASIC design + prototyping	▓▓	▓				
ASIC production			▓			
FEB prototype design	▓▓	▓				
FEB production and tests			▓	▓		
Straw tube detectors						
Full size prototypes	▓▓					
Production and testing		▓	▓	▓		
Transport, installation					▓	
Commissionning						▓
Hadron absorbers						
Design	▓▓	▓				
Coordination with industry		▓	▓			
Production				▓		
Transport, installation					▓	
Mechanics						
Design	▓▓	▓				
Coordination with industry		▓	▓			
Production				▓		
Transport, installation					▓	
Gas systems						
Design	▓	▓				
Production			▓	▓		
Transport, installation					▓	

Figure 5.1: Timeline for various MUCH subsystems

List of Figures

List of Tables

Appendix A

The CBM collaboration

T. Ablyazimov[1], A. Abuhoza[2,60,3], R. Adak[4], M. Adamczyk[5], M.M. Aggarwal[6], Z. Ahammed[7], F. Ahmad[8], N. Ahmad[9], S. Ahmad[8], A. Akindinov[10], P. Akishin[1], E. Akishina[1], T. Akishina[1], V. Akishina[11,1,2], M. Al-Turany[2], E. Alexandrov[1], I. Alexandrov[1], S. Amar-Youcef[3], M. Anđelić[12], O. Andreeva[13], C. Andrei[14], A. Andronic[2], Yu. Anisimov[15], H. Appelshäuser[3], A. Arend[3], D. Argintaru[16], E. Atkin[17], S. Avdeev[15], R. Averbeck[2], M.D. Azmi[9], V. Baban[16], M. Bach[11], E. Badura[2], S. Bähr[18], T. Balle[3], T. Balog[2], M. Balzer[18], S. Bandyopadhyay[19], P. Banerjee[20], N. Baranova[21], T. Barczyk[5], D. Bartoş[14], S. Bashir[8], M. Baszczyk[22], O. Batenkov[23], V. Baublis[24], M. Baznat[15], J. Becker[18], K.-H. Becker[25], S. Belogurov[10], J. Bendarouach[26], I. Berceanu[14], A. Bercuci[14], A. Berdnikov[27], Y. Berdnikov[27], R. Berendes[28], C. Bergmann[28], D. Bertini[2], O. Bertini[2], C. Beşliu[16], O. Bezshyyko[29], P.P. Bhaduri[7], A. Bhasin[30], A.K. Bhati[6], B. Bhattacharjee[31], A. Bhattacharyya[19], T.K. Bhattacharyya[20], T. Blank[18], D. Blau[32], C. Blume[3], Yu. Bocharov[17], M. Borysova[33], T. Breitner[34], U. Brüning[35], J. Brzychczyk[5], A. Bubak[36], H. Büsching[3], A. Bychkov[15], A. Byszuk[37], Xu Cai[38], M. Călin[16], Ping Cao[39], G. Caragheorgheopol[14], I. Carević[12], V. Cătănescu[14], A. Chakrabarti[19], S. Chatterji[2], Sanatan Chattopadhyay[19], Subhasis Chattopadhyay[7], Hongfang Chen[39], Jianping Cheng[40], V. Chepurnov[15], S. Chernenko[15], A. Chernogorov[10], Kyung-Eon Choi[41], M.I. Ciobanu[2,61], G. Claus[42], F. Constantin[14], V. Covlea[16], M. Csanád[43], N. D'Ascenzo[44], S. Das[4], K. Davkov[15], V. Davkov[15], J. de Cuveland[11], B. Debnath[31], D. Dementiev[15], Zhi Deng[40], H. Deppe[2], I. Deppner[45], O. Derenovskaya[1], C.A. Deveaux[26], M. Deveaux[3], K. Dey[31], M. Dey[7], P. Dillenseger[3], V. Dobyrn[24], D. Doering[3], A. Dorokhov[42], M. Dreschmann[18], A. Drozd[22], A.K. Dubey[7], S. Dubnichka[15], A. Dubnichkova[15], M. Dürr[26], L. Dutka[5], M. Dželalija[12], D. Emschermann[2], H. Engel[34], V. Eremin[46], T. Eşanu[16], J. Eschke[47,2], D. Eschweiler[11], Jongsik Eum[41], Huanhuan Fan[39,45], Xingming Fan[48], O. Fateev[15], I. Filozova[1], D. Finogeev[13], P. Fischer[35], H. Flemming[2], U. Frankenfeld[2], V. Friese[2], E. Friske[49], I. Fröhlich[3], J. Frühauf[2], Á. Fülöp[43], J. Gajda[22], T. Galatyuk[50,2], A. Galkin[44], G. Gangopadhyay[19], C. García Chávez[34], J. Gebelein[34], P. Ghosh[3,2], S.K. Ghosh[4], S. Gläßel[3], M. Goffe[42], L. Golinka-Bezshyyko[29], V. Golovatyuk[15], S. Golovnya[51], V. Golovtsov[24], M. Golubeva[13], D. Golubkov[10], A. Gómez Ramírez[34], S. Gorbunov[11], S. Gorokhov[51], D. Gottschalk[45], P. Gryboś[22], A. Grzeszczuk[36], F. Guber[13], K. Gudima[15], A. Gupta[30], Yu. Gusakov[15], A. Haldar[20], S. Haldar[20], H. Hartmann[11], J. Hehner[2], K. Heidel[48], N. Heine[28], A. Herghelegiu[14], N. Herrmann[45], B. Heß[49], J.M. Heuser[2], A. Himmi[42], C. Höhne[26], R. Holzmann[2], Guangming Huang[38], Xinjie Huang[40], D. Hutter[11], E. Iakovleva[11], A. Ierusalimov[15], E.-M. Ilgenfritz[15], M. Irfan[9], M. Ivanov[2], Valery Ivanov[1], Victor Ivanov[1], Vladimir Ivanov[24], A. Ivashkin[13], K. Jaaskelainen[42], H. Jahan[9], V. Jain[7], V. Jakovlev[23], T. Janson[34], A. Jipa[16], I. Kadenko[29], B. Kämpfer[48,62], V. Kalinin[23], K.-H. Kampert[25], Tae Im

Kang[45], E. Kaptur[36], R. Karabowicz[2], O. Karavichev[13], T. Karavicheva[13], D. Karmanov[21],
V. Karnaukhov[15], E. Karpechev[13], K. Kasiński[22], G. Kasprowicz[37], M. Kaur[6], A. Kazantsev[32],
U. Kebschull[34], G. Kekelidze[15], M.M. Khan[9], S.A. Khan[7], A. Khanzadeev[24], F. Khasanov[10],
A. Khvorostukhin[15], V. Kirakosyan[15], M. Kirejczyk[52], A. Kiryakov[51], M. Kiš[2], I. Kisel[11],
P. Kisel[1], S. Kiselev[10], A. Kiss[43], T. Kiss[53], P. Klaus[3], R. Kłeczek[22], Ch. Klein-Bösing[28],
V. Kleipa[2], P. Kmon[22], K. Koch[2], L. Kochenda[24], P. Koczoń[2], W. König[2], M. Kohn[28],
B.W. Kolb[2], A. Kolosova[10], B. Komkov[24], J.M. Kopfer[25], M. Korolev[21], I. Korolko[10],
R. Kotte[48], A. Kovalchuk[33], S. Kowalski[36], M. Koziel[3], G. Kozlov[1], P. Kravtsov[24], E. Krebs[3],
C. Kreidl[35], D. Kresan[2], G. Kretschmar[3], M. Kretz[11], M. Krieger[35], E. Kryshen[24],
W. Kucewicz[22], L. Kudin[24], A. Kugler[54], I. Kulakov[2], J. Kunkel[2], A. Kurepin[13], P. Kurilkin[15],
V. Kushpil[54], V. Kyva[33], V. Ladygin[15], C. Lara[34], P. Larionov[3,2], A. Laso Garcia[48,62],
E. Lavrik[49], I. Lazanu[16], A. Lebedev[2,1], S. Lebedev[26,1], E. Lebedeva[26], J. Lehnert[2],
J. Lehrbach[34], Y. Leifels[2], F. Lemke[35], Cheng Li[39], Jin Li[40], Qiyan Li[3,38], Yuanjing Li[40], Yulan
Li[40], V. Lindenstruth[11,2], B. Linnik[3], Feng Liu[38], I. Lobanov[51], E. Lobanova[51], S. Löchner[2],
P.-A. Loizeau[45], J.A. Lucio Martínez[34], A. Lymanets[49,33], A. Maevskaya[13], S. Mahajan[30],
D.P. Mahapatra[55], T. Mahmoud[26], P. Maj[22], Z. Majka[5], A. Malakhov[15], E. Malankin[17],
D. Malkevich[10], O. Malyatina[17], H. Malygina[3,33,2], S. Mandal[7], V. Manko[32], S. Manz[34],
A.M. Marin Garcia[2], J. Markert[3], S. Masciocchi[2], T. Matulewicz[52], L. Meder[18], M. Merkin[21],
J. Meyer[18], V. Mialkovski[15], J. Michel[3], N. Miftakhov[24], K. Mikhailov[10], V. Mikhaylov[54],
B. Milanović[3], V. Militsija[33], M.F. Mir[8], D. Miskowiec[2], I. Momot[2], T. Morhardt[2],
W.F.J. Müller[47,2], C. Müntz[3], Yu. Murin[15], R. Najman[5], E. Nandy[7], L. Naumann[48],
T. Nayak[7], A. Nedosekin[10], W. Niebur[2], V. Nikulin[24], D. Normanov[17], A. Oancea[34],
Y. Onishchuk[29], D. Osipov[17], G. Ososkov[1], D. Ossetski[44], P. Otfinowski[22], E. Ovcharenko[10],
S. Pal[7], I. Panasenko[33], N.R. Panda[55], S. Parzhitskiy[15], C. Pauly[25], M. Penschuck[3], I. Peric[35],
D. Peshekhonov[15], V. Peshekhonov[15], V. Petráček[56], M. Petriş[14], A. Petrovici[14],
M. Petrovici[14], A. Petrovskiy[17], O. Petukhov[13], K. Piasecki[52], J. Pieper[3], J. Pietraszko[2],
R. Płaneta[5], E. Plekhanov[15], V. Plotnikov[10], V. Plujko[29], J. Pluta[37], A. Pop[14], V. Popov[21],
V. Pospisil[56], B.V.K.S. Potukuchi[30], J. Pouryamout[25], K. Poźniak[37,52], A. Prakash[57],
M. Prokudin[10], I. Pshenichnov[13], M. Pugach[33], V. Pugatch[33], S. Querchfeld[25], L. Radulescu[14],
S. Raha[4], W. Raja[8], F. Rami[42], R. Raniwala[58], S. Raniwala[58], A. Raportirenko[1],
J. Rautenberg[25], J. Rauza[22], R. Ray[4], S. Razin[15], P. Reichelt[3], S. Reinecke[25], A. Reshetin[13],
C. Ristea[16], O. Ristea[16], F. Roether[3], R. Romaniuk[37], A. Rost[50], E. Rostchin[24],
I. Rostovtseva[10], A. Roy[7], J. Rożynek[52], Yu. Ryabov[24], V. Rykalin[51], A. Sadovsky[13],
S. Sadovsky[51], R. Sahoo[59], P.K. Sahu[55], J. Saini[7], S. Samanta[4], S.S. Sambyal[30],
V. Samsonov[24], J. Sánchez Rosado[2], O. Sander[18], S. Sau[19], V. Saveliev[44], S. Schatral[2,35],
C. Schiaua[14], C.J. Schmidt[2], H.R. Schmidt[49], K. Schmidt[36], K. Schweda[2], A. Scurtu[16],
F. Seck[50], S. Seddiki[2], I. Selyuzhenkov[2], A. Semennikov[10], A. Senger[2], P. Senger[2,3],
A. Shabunov[15], Ming Shao[39], M.K. Sharma[30], N. Shumeiko[15], V. Shumikhin[17], B. Sikora[52],
A. Simakov[17], C. Simon[45], C. Simons[2], R.N. Singaraju[7], A.K. Singh[20], B.K. Singh[57],
C.P. Singh[57], V. Singhal[7], M. Singla[2], P. Sitzmann[3], K. Siwek-Wilczyńska[52], L. Škoda[56],
I. Skwira-Chalot[52], I. Som[20], I. Sorokin[2,33], Z. Sosin[5], D. Soyk[2], P. Staszel[5], D. Storozhyk[33],
M. Strikhanov[17], S. Strohauer[3], J. Stroth[3,2], C. Sturm[2], R. Sultanov[10], Yongjie Sun[39],
O. Svoboda[54], R. Szczygieł[22], R. Talukdar[31], Zebo Tang[39], M. Tanha[3], J. Tarasiuk[52],
O. Tarassenkova[24], M.-G. Târzilă[14], T. Tischler[3], P. Tlustý[54], A. Toia[2,3], T. Tolyhi[53],
N. Topil'skaya[13], I. Tsakov[15], Yu. Tsyupa[51], A. Turowiecki[52], F. Uhlig[2], E. Usenko[13], I. Valin[42],
I. Vassiliev[2], E. Verbitskaya[46], W. Verhoeven[28], A. Veshikov[23], R. Visinka[2], Y.P. Viyogi[7],
S. Volkov[24], A. Vorobiev[51], A. Voronin[21], V. Vovchenko[11], E. Vznuzdaev[24], M. Vznuzdaev[24],
Dong Wang[38], Yaping Wang[38], Yi Wang[40], M. Weber[18], C. Wendisch[48], J.P. Wessels[28],
M. Wiebusch[3], J. Wiechula[49], D. Wielanek[37], A. Wieloch[5], N. Winckler[2], M. Winter[42],
K. Wiśniewski[52], D. Wohlfeld[35], Gy. Wolf[53], Sanguk Won[41], J. Wüstenfeld[48], Changzhou

Xiang[38], Nu Xu[38], Jun-Gyu Yi[41], Zhongbao Yin[38], In-Kwon Yoo[41], B. Yuldashev[15],
I. Yushmanov[32], W. Zabołotny[37,52], Yu. Zaitsev[10], Yu. Zanevsky[15], M. Zhalov[24], Ya Peng
Zhang[45], Yifei Zhang[39], Daicui Zhou[38], Xianglei Zhu[40], A. Zinchenko[15], W. Zipper[36],
M. Żoładź[22], P. Zrelov[1], V. Zryuev[15], P. Zumbruch[2], M. Zyzak[2]

[1]Laboratory of Information Technologies, Joint Institute for Nuclear Research (JINR-LIT),
Dubna, Russia
[2]GSI Helmholtzzentrum für Schwerionenforschung GmbH (GSI), Darmstadt, Germany
[3]Institut für Kernphysik, Goethe Universität Frankfurt, Frankfurt, Germany
[4]Department of Physics, Bose Institute, Kolkata, India
[5]Marian Smoluchowski Institute of Physics, Jagiellonian University, Kraków, Poland
[6]Department of Physics, Panjab University, Chandigarh, India
[7]Variable Energy Cyclotron Centre (VECC), Kolkata, India
[8]Department of Physics, University of Kashmir, Srinagar, India
[9]Department of Physics, Aligarh Muslim University, Aligarh, India
[10]Institute for Theoretical and Experimental Physics (ITEP), Moscow, Russia
[11]Frankfurt Institute for Advanced Studies, Goethe Universität Frankfurt (FIAS), Frankfurt,
Germany
[12]University of Split, Split, Croatia
[13]Institute for Nuclear Research (INR), Moscow, Russia
[14]Horia Hulubei National Institute of Physics and Nuclear Engineering (IFIN-HH), Bucharest,
Romania
[15]Veksler and Baldin Laboratory of High Energy Physics, Joint Institute for Nuclear Research
(JINR-VBLHEP), Dubna, Russia
[16]Atomic and Nuclear Physics Department, University of Bucharest, Bucharest, Romania
[17]National Research Nuclear University MEPhI, Moscow, Russia
[18]Karlsruhe Institute of Technology (KIT), Karlsruhe, Germany
[19]Department of Physics and Department of Electronic Science, University of Calcutta,
Kolkata, India
[20]Indian Institute of Technology Kharagpur, Kharagpur, India
[21]Skobeltsyn Institute of Nuclear Phyiscs, Lomonosov Moscow State University (SINP-MSU),
Moscow, Russia
[22]AGH University of Science and Technology (AGH), Kraków, Poland
[23]V.G. Khlopin Radium Institute (KRI), St. Petersburg, Russia
[24]Petersburg Nuclear Physics Institute, NRC Kurchatov Institute (PNPI), Gatchina, Russia
[25]Fachbereich Physik, Bergische Universität Wuppertal, Wuppertal, Germany
[26]Justus-Liebig-Universität Gießen, Gießen, Germany
[27]St. Petersburg State Polytechnic University (SPbSPU), St. Petersburg, Russia
[28]Institut für Kernphysik, Westfälische Wilhelms Universität Münster, Münster, Germany
[29]Department of Nuclear Physics, National Taras Shevchenko University of Kyiv, Kyiv, Ukraine
[30]Department of Physics, University of Jammu, Jammu, India
[31]Department of Physics, Gauhati University, Guwahati, India
[32]National Research Centre "Kurchatov Institute", Moscow, Russia
[33]High Energy Physics Department, Kiev Institute for Nuclear Research (KINR), Kyiv, Ukraine
[34]Institute for Computer Science, Goethe Universität Frankfurt, Frankfurt, Germany
[35]Zentrales Institut für Technische Informatik, Universität Heidelberg, Standort Mannheim,
Heidelberg, Germany
[36]Institute of Physics, University of Silesia, Katowice, Poland
[37]Institute of Electronic Systems, Warsaw University of Technology, Warsaw, Poland
[38]College of Physical Science and Technology, Central China Normal University (CCNU),

Wuhan, China

[39]Department of Modern Physics, University of Science & Technology of China (USTC), Hefei, China

[40]Department of Engineering Physics, Tsinghua University, Beijing, China

[41]Pusan National University (PNU), Pusan, Korea

[42]Institut Pluridisciplinaire Hubert Curien (IPHC), IN2P3-CNRS and Université de Strasbourg, Strasbourg, France

[43]Eötvös Loránd University (ELTE), Budapest, Hungary

[44]National Research Nuclear University, Obninsk, Russia

[45]Physikalisches Institut, Universität Heidelberg, Heidelberg, Germany

[46]Ioffe Physico-Technical Institute, Russian Academy of Sciences, St. Petersburg, Russia

[47]Facility for Antiproton and Ion Research in Europe GmbH (FAIR), Darmstadt, Germany

[48]Institut für Strahlenphysik, Helmholtz-Zentrum Dresden-Rossendorf (HZDR), Dresden, Germany

[49]Physikalisches Institut, Eberhard Karls Universität Tübingen, Tübingen, Germany

[50]Institut für Kernphysik, Technische Universität Darmstadt, Darmstadt, Germany

[51]Institute for High Energy Physics (IHEP), Protvino, Russia

[52]Institute of Experimental Physics, University of Warsaw, Warsaw, Poland

[53]Institute for Particle and Nuclear Physics, Wigner Research Centre for Physics, Hungarian Academy of Sciences, Budapest, Hungary

[54]Nuclear Physics Institute, Academy of Sciences of the Czech Republic, Řež, Czech Republic

[55]Institute of Physics, Bhubaneswar, India

[56]Czech Technical University (CTU), Prag, Czech Republic

[57]Department of Physics, Banaras Hindu University, Varanasi, India

[58]Physics Department, University of Rajasthan, Jaipur, India

[59]Indian Institute of Technology Indore, Indore, India

[60]also: King Abdulaziz City for Science and Technology (KACST), Riyadh, Saudi Arabia

[61]also: Institute of Space Science, Bucharest, Romania

[62]also: Technische Universität Dresden, Dresden, Germany

Appendix B

R&D on hybrid gaseous detectors

B.1   R&D on GEM and Micromegas

As discussed in Chapter-3, R&D on different gaseous detector technologies have been ongoing within the CBM-MUCH collaboration. We have discussed about R&D on GEM and straw tube based detectors in Chapter-3. Another option being worked out extensively by the PNPI group involves R&D on hybrid gaseous (GEM, both thin and thick versions of GEM foils and Micromegas) detectors as discussed below. These detectors, when fully developed could be placed in any one of the stations stating from 3_{rd} to 5_{th}.

Various prototype detectors having two, three or more stages for gas amplification were built in PNPI: double and triple thin GEMs of CERN production (GG and 3G), Double Thick GEMs (DTG), hybrids of thin or thick GEMs with Micromegas (MG and MTG), and some kind of Thick GEM which had four gas amplification stages (called as Monolithic Thick GEM-MoTG). All these prototypes have been tested with radioactive sources (^{55}Fe and ^{90}Sr) at a specially made test stand equipped with gas mixture supply, HV supply, front-end and readout electronics and a set of programs for data analysis. During the work in the lab, we acquired experience in production technology of all types of the detectors mentioned above, measured the variation of gas gain with applied HV, measured the times of charge collection, made estimations of efficiency and discharge probability. We have tried different types of 2 and 3 component gas mixtures with Argon and Helium as the main gases. This first R&D stage resulted in assembling four prototypes (MG, MTG, GG, and DTG), with the sensitive area of 10×10 cm^2 each prepared for beam tests. All prototypes had the same pad structure of the readout electrodes with every pad of 1.5 $\times$ 3.0 mm^2 and the distance of 0.1 mm between the pads.

The chambers built at PNPI were installed at the T-10 facility at CERN (see Fig. B.1,left) to conduct tests with 5 GeV beams mainly of protons and pions. For the tests we used 128 readout channels coupled to rather slow readout electronics. Therefore, it was possible to equip only 5.1×1.2 cm^2 with electronics, all other pads were grounded. We worked with a highest beam rate of 1 kHz. A beam spot was formed (see the beam profile obtained with one of the chambers at the right side of Fig. B.1) by the 4-fold coincidence of signals from four scintillation counters. The coincidence signal served as trigger.

Tests were done at different angles relative to the beam direction ($0°$, $15°$, $30°$ and $45°$) and for two gas mixtures $Ar/CO_2/iC_4H_{10}$ (88/8/4) and $He/CF_4/iC_4H_{10}$ (76/22/2).

Figure B.1: One of the chambers located at the CERN T-10 area (left). An example of the beam profile measured with the chamber is also depicted (right)

Main goals of the tests were to measure:

- amplitude spectra

- gas gains

- detector efficiency

- cluster size (number of the fired pads)

- radius of the charge spot induced on the readout electrode

The efficiency of all the tested detectors, estimated as a ratio of the number of detected events to the number of triggers, are presented in Table B.1. An event is considered to be detected if at least one of the pads after the pedestal subtraction had the amplitude larger than the threshold of $4\,\sigma$, where σ is the width of the electronic noise distribution obtained by fitting by a Gaussian. Due to limited beam time we did not measure the dependence of efficiency with applied high voltage to get the optimal regime, which was later established in the lab with radioactive sources. Table B.1 also contains the estimated values of the gas gains.

To estimate the gas gain, we used following procedure. With the HEED program, the most probable number (MPV-H) of the produced ion pairs in the drift gap of the known dimension was calculated. By fitting the experimental spectra measured by the charge collecting electrode to the Landau distribution, we know the ADC channel corresponding to the MPV-L multiplied by the gas gain, and using the measured calibration coefficient (0.209 fC/ADC channel or $\approx$1250 electrons/ADC channel) we can get the collected charge, or the number of collected electrons corresponding to this MPV-L. The ratio of the measured MPV-L to the calculated MPV-H gives us the value of the gas gain.

Detector	Drift gap	He/CF4/iC$_4$H$_{10}$				Ar/CO$_2$/iC$_4$H$_{10}$			
		MPV-H (electrons)	MPV-L (channels)	GG (x 10^3)	eff (%)	MPV-H (electrons)	MPV-L (channels)	GG (x 10^3)	eff (%)
MG	3.7	7.8	145.6	23.4	98.8	18.2	250.6	17.3	99.9
MTG	4	8.7	96.3	13.9	97.0	20.3	57.4	3.5	99.8
DTG	4	8.7	46.4	6.7	95.0	20.3	73.9	4.5	99.0
GG	4.9	10.8	99.0	11.5	98.2	25.1	41.3	2.1	99.9

Table B.1: Gas gain for two gas combinations He/CF4/iC$_4$H$_{10}$ (76/22/2) and Ar/CO$_2$/iC$_4$H$_{10}$(88/8/4)

The results have shown that for the drift gap of 4 mm, with the type of electronics used and beam intensity of $\approx$1 kHz, we can reach 99 - 100% efficiency of the MIP detection at the gas gain of $\approx$15$\times$10^3 in the He based gas mixture and $\approx$5$\times$10^3 in the Ar based gas mixture for all types of the detectors under test.

The cluster size distribution and the radius of the charge spot induced on the readout electrode caused by a crossing particle are important characteristics that should be taken into account at the stage of the detector design and optimization. A cluster is defined as the number of the neighbouring pads fired above threshold. The cluster size distributions were measured for the He and Ar based gas mixtures at four angles. An example of the cluster size distributions for a MG detector filled with the He based mixture is presented in Fig. B.2.
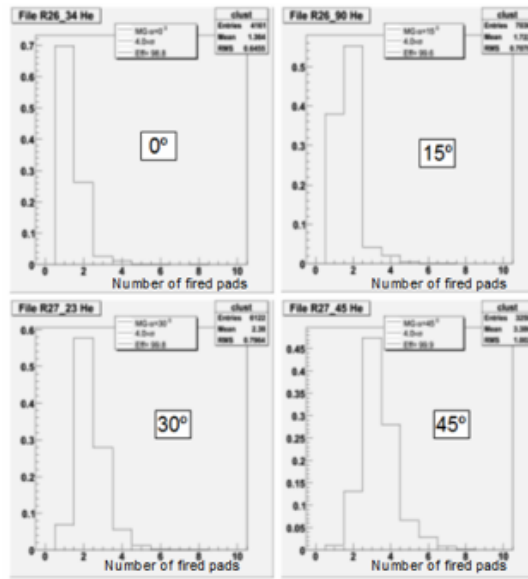
Figure B.2: Cluster size distributions for a MG detector filled with the He based mixture. Horizontal axis: number of fired pads, vertical axis: number of events normalized to 1

It is interesting to compare the cluster sizes for different detectors and gases. Unfortunately, the detectors had different gas gains and different gaps where primary ionization was produced. Following procedure has been applied for normalization:

- fitting the measured amplitude spectra to the Landau distribution we get MPV,

- comparing MPV for different detectors we obtain the coefficients to normalize all MPV to the smallest one that we have for the case of the GG detector with the Ar based gas mixture,

- changing the signal amplitudes by normalization coefficients and applying the thresholds of 4 σ (where σ is the width of the electronics noise distribution fitted to a Gaussian) we find the corrected cluster distributions. The corrected sizes of the clusters for the case of 0° are presented in Table B.2. For a comparison, Table B.2 also shows the efficiency obtained by normalizing the signal amplitudes and applying the threshold at a 4 σ level.

Detector type	He/CF$_4$/iC$_4$H$_{10}$(76/22/2)		Ar/CO$_2$/iC$_4$H$_{10}$ (88/8/4)	
	mean Number of pads	efficiency	Mean number of pads	efficiency
MG	1.24	97.3	1.72	99.5
MTG	1.31	96.8	1.76	99.6
DTG	1.78	94.5	2.14	98.2
GG	1.63	97.9	2.10	99.9

Table B.2: corrected cluster size and efficiency for 0°

The radius r$_{exp}$ of the charge spot induced on the readout electrode was estimated in the case of 0° with a simple model (see Fig. B.3, left side). A class of events with only one or two neighbouring pads fired in the X or Y row were separated. For these events, we built the ratio F = Q1/(Q1+Q2), where Q1 maximal amplitude, and Q2 ≤ Q1 or Q2 = 0 amplitude of the signal from the neighbouring pad. Taking the F distribution (see an example in Fig. B.3, right side) along the X or Y coordinate in assumption of uniform distribution of the beam particles, we can get the charge spot radius.
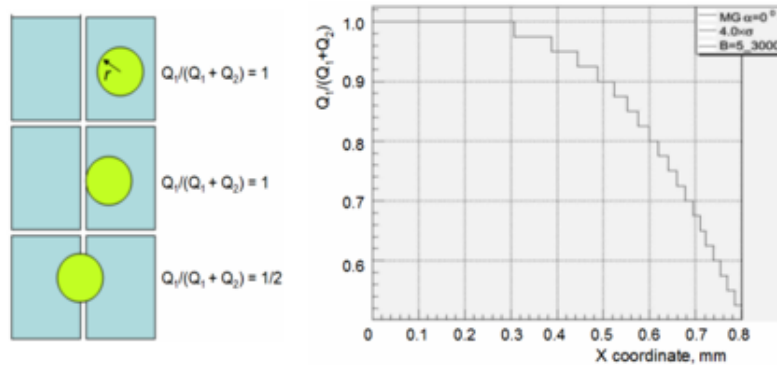
Figure B.3: The model to estimate the charge spot radius r (left side). An example of the distribution of the ratio F = Q_1/(Q_1+Q_2), where Q_1 maximal amplitude, and Q_2 ≤ Q_1 or Q_2 = 0 amplitude of the signal from the neighbouring pad along the X-coordinate for a MG detector filled with the Ar based mixture (right side)

The r$_{MC}$ value could be obtained by Monte-Carlo simulation with the following input data:

- geometry of the detector,

- HEED results for pair production in the He and Ar based mixtures,

- Landau distribution of produced ion pairs in the drift gap,

- experimental gas gain.

In the simulation procedure, we varied the spot radius r$_{MC}$ and checked the cluster size distribution obtained by the same manner as was done for the experimental data. The procedure was stopped when the simulated cluster size distribution coincided with the experimental one. The experimental r values (r$_{exp}$.) and those obtained with the simulation for the case of 0° and X-direction are presented in Table B.3. Practically the same values of *r* were obtained in the consideration of the distribution of the ratio F along the Y-direction.

Detector type	He/CF$_4$/iC$_4$H$_{10}$ (76/22/2)		Ar/CO$_2$/iC$_4$H$_{10}$ (88/8/4)	
	r$_{exp}$ (mm)	r$_{MC}$ (mm)	r$_{exp}$ (mm)	r$_{MC}$ (mm)
MG	0.18	0.19	0.49	0.48
MTG	0.17	0.16	0.45	0.41
DTG	0.42	0.49	0.65	0.73
GG	0.41	0.44	0.58	0.62

Table B.3: spot radii at 0° for two gas combinations

We can see good coincidence of the experimentally obtained and the simulated r values showing the correctness of the detector model used for the simulation procedure and proper understanding of the detector response to charged particles. All prototypes under test showed highly stable working in the beam of low intensity.

Next step of the R&D on detectors for muon tracking system was to make comparison of different prototypes with varying beam intensity. This test was performed using 1 GeV proton beam at PNPI (Gatchina) accelerator. Fig. B.4 shows beam profile at the place of the detectors under test. It was uniformly distributed spot of 25.3 mm in diameter with sharp edges.
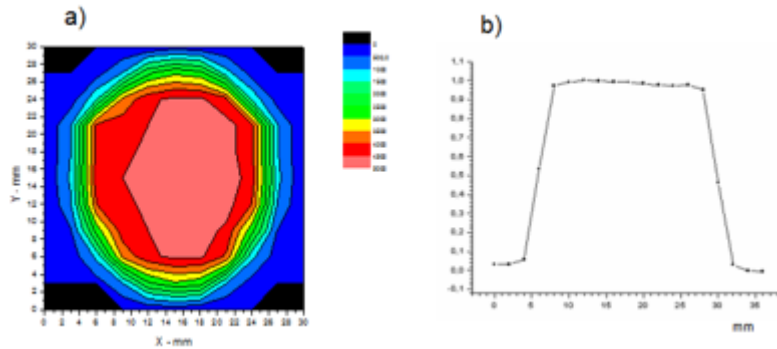
Figure B.4: Test beam profile at the place of the prototype location: a) intensity distribution in the beam spot, b) beam profile.

The experimental setup (schematic view is depicted in Fig. B.5) included:

- differential ionization chamber (DIC) with size of 5 × 5 cm^2 to measure absolute flow of beam particles. DIC is properly working at the rate of 10^5-10^9 Hz/cm^2,

- trigger scintillation counters S1 and S2 with size of 5×5 mm^2 each (coincidence S1.S2 gave a trigger signal),

- monitoring counters S3 and S4 with size of 5 × 5 cm^2 each (coincidence S3.S4 were normalized to trigger signal at low beam intensity),

- polyethylene target of 5 cm thickness,

- detector under test.

Four detectors (see schematic view of the detectors at Fig. B.6), which passed through the lab tests with radioactive sources, were prepared for the beam test. Three of them had two stages of gas amplification:

Figure B.5: Schematic view of the experimental setup: (a) S1, S2, S3 and S4 âĂŞ scintillation counters (b) DIC:ionization chamber (c) GG, MG, DTG and (d) MoTG: detectors under test.

- Micromegas + GEM (MG),

- GEM + GEM (GG),

- Thick GEM + Thick GEM (DTG),

- and fourth one: Monolithic Thick GEM (MoTG) had four stages.

All detectors had same drift gap and similar structure of readout electrodes consisting from readout pad of 4×4 mm^2 and grounded region of 4×4 cm^2 around.
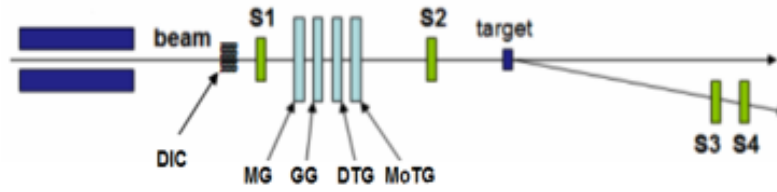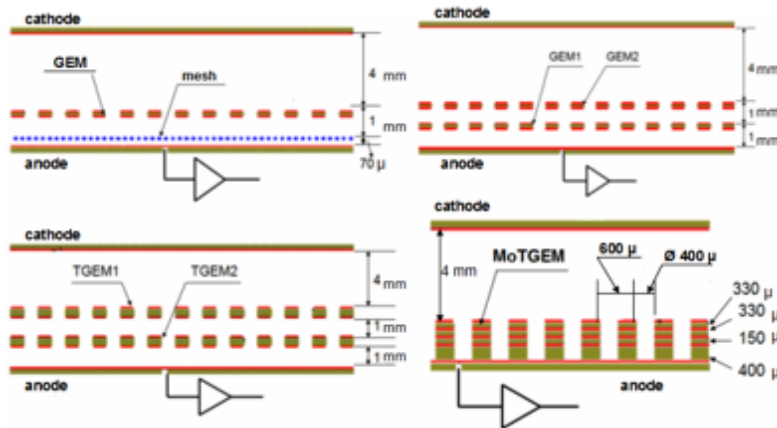

Figure B.6: Schematic view of the detectors prepared for the beam test

Here we have to make some remark about MoTG detector as probable candidate for stations 3 and 4. It was done with simple standard technology that is used for fabrication of multi-layers PCB in electronic industry. It is just four layers (each layer is FR4 covered by Cu) board with drilled holes (see fig. B.6). Last conductive Cu layer has no hole and serves as readout electrode. This detector showed very promising behaviour during the lab test with radioactive sources. Two gas mixtures ($Ar/CO_2/iC_4H_{10}$ (90/8/2) and $He/CF_4/iC_4H_{10}$ (73/25/2)) were used as working gas during the test run.

The charge-sensitive preamplifiers measured the signals formed with CR-RC filter. Two time constants of the preamplifier feed-back chain were used: 15 ns and 30 ns. Equivalent noise charge was less than 1000 electrons for 15 pF input capacitance and 100 ns peaking time. Amplitudes of the signals were measured by 12 bits ADC. Service electronics included coincidence schemes, discriminators, scalars, time delays among others.

At the first step of the test to define the working high voltage regime for each detector, efficiency was measured as a function of the voltage applied to the gaps of gas amplification. For all detec-

tors, the field across the drift gaps were kept the same electric field E=100 V/mm, and in transfer and induction gaps we applied constant field of 200 V/mm. At this step, we worked with low ($\approx 5 \times 10^4$ Hz/cm^2) intensity beam. Efficiency was obtained relative to the trigger (coincidence of S1 and S2 counters) counts. Fig. B.7 and Fig. B.8 present the measured dependences for all detectors working with Ar and He gas mixtures. The working points, shown by arrows, were chosen in the beginning of the plateaus. The values of gas gain are also shown at the pictures.
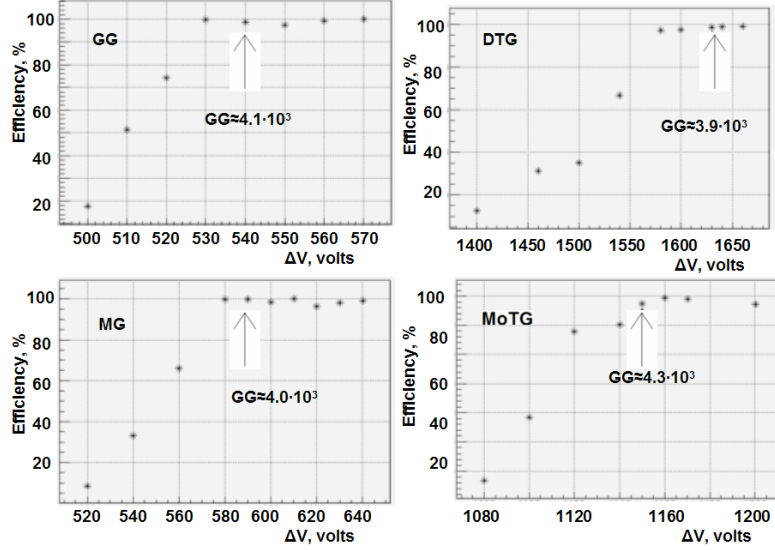

Figure B.7: Dependence of the efficiency from the sum of the potentials ΔV applied to the gas amplification gaps for Ar based gas mixture. Chosen working HV regimes are shown by arrows. Type of the detectors and values of gas gains are also depicted.

Figure B.8: Dependence of the efficiency from the sum of the potentials ΔV applied to the gas amplification gaps for He based gas mixture. Chosen working HV regimes are shown by arrows. Type of the detectors and values of gas gains are also depicted.

At the next step of the test, efficiency was measured as a function of beam intensity. It should be noted that the electronics used in the setup did not allow working with the rate more than 2-3$\times 10^6$ Hz. Due to this the size (4$\times$4 mm^2) of the readout electrode was chosen to have the rate not higher than 2$\times 10^6$ Hz. The same is true for the choice of 5$\times$5 mm^2 for the trigger scintillation counters S1 and S2.

If the counters S$_1$, S$_2$ are ideally aligned to each other and have efficiency of 100% the ratio k of the trigger number N$_{S1.S2}$ to the number of beam particles N$_{DIC}$ measured by ionization chamber should be equal the ratio of the area (5 $\times$ 5 mm^2) occupied by S1,S2 to the size of beam spot (530 mm^2):

k = N$_{S1.S2}$/ N$_{DIC}$ = 25/530 $\approx$ 0.047.

Fig. B.9 shows correlation N$_{S1.S2}$ vs. N$_{DIC}$ fitted to straight line for the case of practically ideal alignment of the S1, S2 (k = 0.0469). Note, from the independent measurements it is known that efficiency of the ionization chamber is equal to 100% for the beam intensity up to 10^9 Hz/cm^2 and deflection from linear dependence would mean an inefficiency of the trigger. It is seen from Fig. B.10 that trigger has 100% of efficiency up to rate of 2.5.10^6 Hz. Finally, if take into account beam duty factor f ($\approx$40%) we can get real intensity I of the beam in the units of Hz/cm^2 using the number of triggers per second:

$I = N_{S1.S2}/(k.f.5.3)$,

where k is obtained from linear fit of the correlation $N_{S1.S2}$ vs. N_{DIC}, f: beam duty factor, 5.3: size of the beam spot in the units of cm^2.
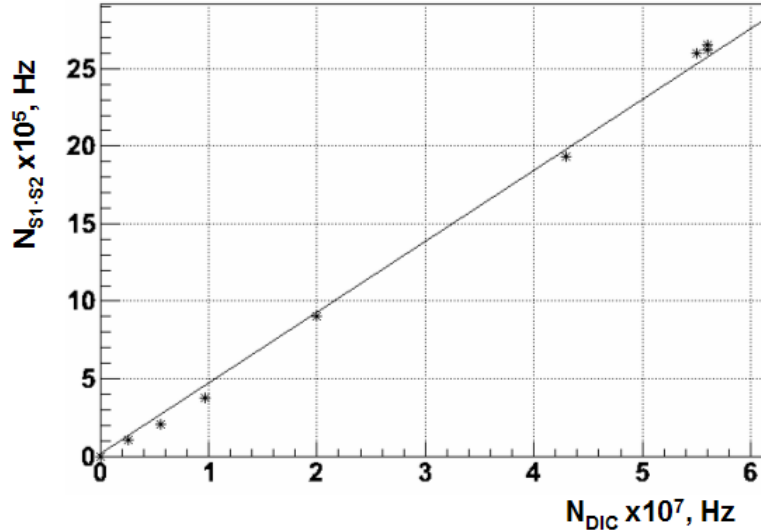

Figure B.9: Example of the dependence NS1.S2 vs. N_{DIC} in case of practically ideal alignment of counters S1, S2 each other. The parameters of the fitting the experimental data to straight line are shown in the frame.

The detector efficiency e was estimated as a ratio of three folds coincidence to two folds one: $e = N_{S1.S2.Ch}/N_{S1.S2}$, where $N_{S1.S2.Ch}$ is the number of coincidences between the trigger signals and the signals of the detector under test. In this approach of efficiency definition a geometry factor should be taken into account. The number $N_{S1.S2}$ is proportional to the size of the spot cut out from the beam by coincidence of the counters S1, S2 (at the ideal alignment of S1, S2 the size of this spot should be 5×5 mm^2). If the readout electrode with size of 4×4 mm^2 is inside the spot of 5×5 mm^2 (case of ideal alignment of the S1, S2) and efficiencies of the detector and trigger are equal to 100% the value of the ratio e should be equal to 0.64, that is if measured detector efficiency is 64% the real efficiency of the detector is 100%. Fig. B.10 demonstrates an example (case of MG detector and Ar based gas mixture) of the dependence $N_{S1.S2.Ch}$ vs $N_{S1.S2}$.

The dependence presented in Fig. B.10 shows linear behaviour at the lower rate that means independence of the detector efficiency with the rate in this region. Deflection from the linear dependence observed at the higher rates means decreasing the detector efficiency. From linear fit of the points at relatively low rates we get slope parameter b which characterizes the quality of alignment of the counters S1, S2 and detector under study. Unfortunately, due to not so precise mechanical fixing of the detector and counters S1, S2 ,every time when we changed detectors during the test run it was necessary to do new alignment and for each case the parameter b had different values laying in the range of 0.48-0.61 (for ideal alignment it should be 0.64). Experimentally obtained values of the parameter b were used for normalization of the detectors efficiencies to 100% in the region of low rate. This normalization looks reasonable because for the same types of the detectors which we tested in the low intensity test beam in CERN we had efficiency on the level of 98-100%.

The dependence of the measured efficiency for all types of detectors under test and Ar and He based gas mixtures from beam intensity is presented in Fig. B.11.
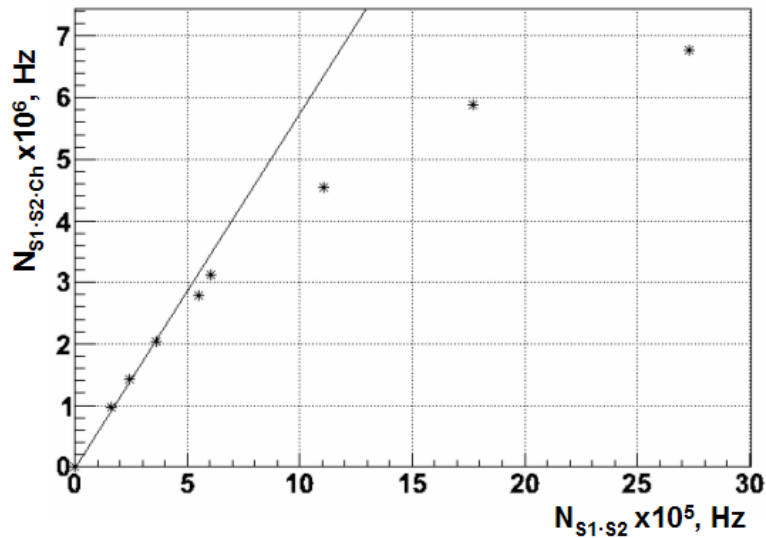
Figure B.10: Example of the dependence $N_{S1.S2.Ch}$ vs. $N_{S1.S2}$ for the case of MG detector and Ar based gas mixture. Also it is shown by strait line the linear fit of the points at low values of $N_{S1.S2}$ and the fit parameters in the frame.

For the hybrid MICROMEGAS+GEM detector, we got the efficiency of 95-100% for the beam intensity up to 3.10^6 Hz/cm^2, and for the beam intensity of $5\text{-}6.10^6$ Hz/cm^2 it was about 90%. For all other detectors decrease of the efficiency started at the intensity of 10^6 Hz/cm^2. We did not see big difference between Ar and He gas mixtures.

In parallel to count information for each detector the amplitude spectra were also measured in terms of ADC. In fig. B.12 an example of such amplitude spectrum is presented. In the spectrum, we can pick out three characteristic regions: noise peak in the region of small amplitudes (less than ≈ 10 ADC channels), Landau peak in the region of more than ≈ 40 ADC channels, and something in the region of 10-40 ADC channels. The data of the region of < 40 were fitted to exponent and Landau distribution and then were extrapolated to the rest part of the spectrum and subtracted. The spectrum obtained after subtraction (see fig. B.13(right)) is well approximated by Landau distribution.

Fig. B.13 shows example of the spectrum modification with the beam intensity. It is clearly seen, the region of low amplitudes is enhanced with increase of the beam intensity.

It could be explained by decrease of gas gain in some cases. Most probably this drop of gas gain should take place at the last gas amplification gap where the produced charge is the largest one. Positive ions require considerable time to be collected and escape amplification gap. So, at higher rate less positive ions will be collected and will be accumulated inside. It can change HV regime causing the decrease of gas gain and, as result, the efficiency.

It is interesting to compare amplitude spectra for different types of the detectors (for example, MG and GG) for similar values of beam intensity and the same gas mixture (see fig. B.14). If we accept the criterion of enriching the region of low amplitudes with increasing the beam intensity (fig. B.14) the MG detector looks preferable.

Also there is an interest to compare the amplitude spectra measured with the same detector (for example, MG detector) for Ar and He gas mixtures (see fig. B.14) taking into account the same criterion. It is seen from fig. B.14 that at the close values of beam intensity the region of low
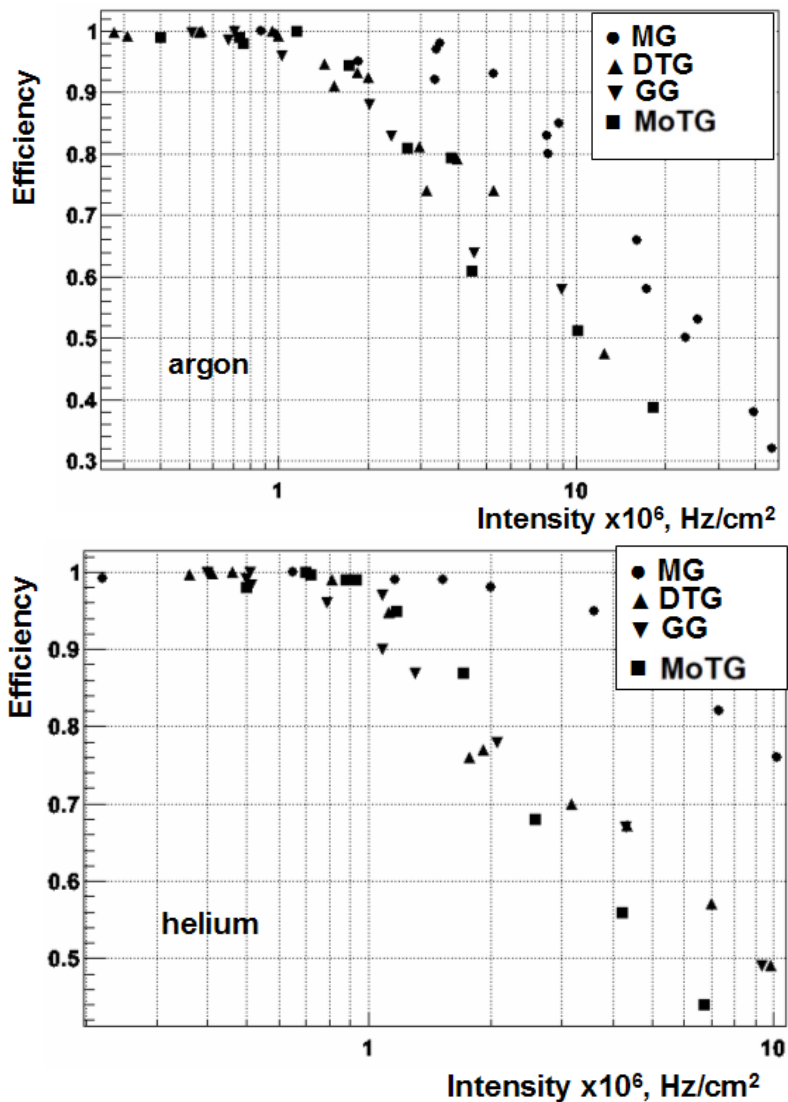
Figure B.11: Dependence of the measured efficiency from beam intensity for Ar and He based mixtures. The types of the detectors are shown in frames.

amplitudes is much more populated for Ar mixture than for He. There is well-known fact that the drift velocity of the positive ions in pure He is much higher than in pure Ar. Our measurements with radioactive sources in the lab have shown that the time of full charge collection, which is mainly defined by a drift of positive ions (for example, in MG detector) is 5-6 times longer in Ar based gas mixture than in He. Therefore, the spectra presented in fig. B.15 illustrate the role of the positive charge collection time at high rates.

In conclusion we can note that comparison of the count and amplitude information received for MG and GG detectors, which are considered as candidates for the first two stations of CBM muon system, gives a preference to the hybrid MG detector and He based gas mixture at very high rates. Serious drawback of hybrid variant is combination of two different technologies that will cause additional difficulties in building the big size detector system. For stations 3 and 4 the DTG or MoTG detectors could be definitely used. Some preference may be given to MoTG detector due to simplicity of production technology.

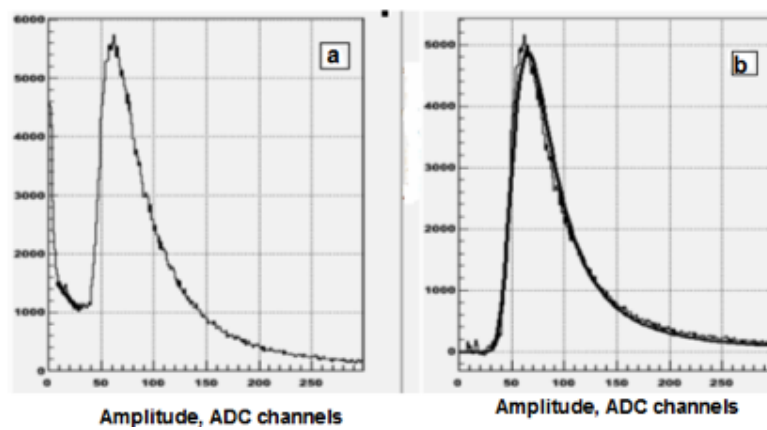Figure B.12: Example of an amplitude spectrum: a) raw spectrum, b) spectrum obtained after subtraction of the portion obtained by extrapolation from the region of amplitudes less than 40 ADC channels. The curve shows the fit of the spectrum to Landau distribution

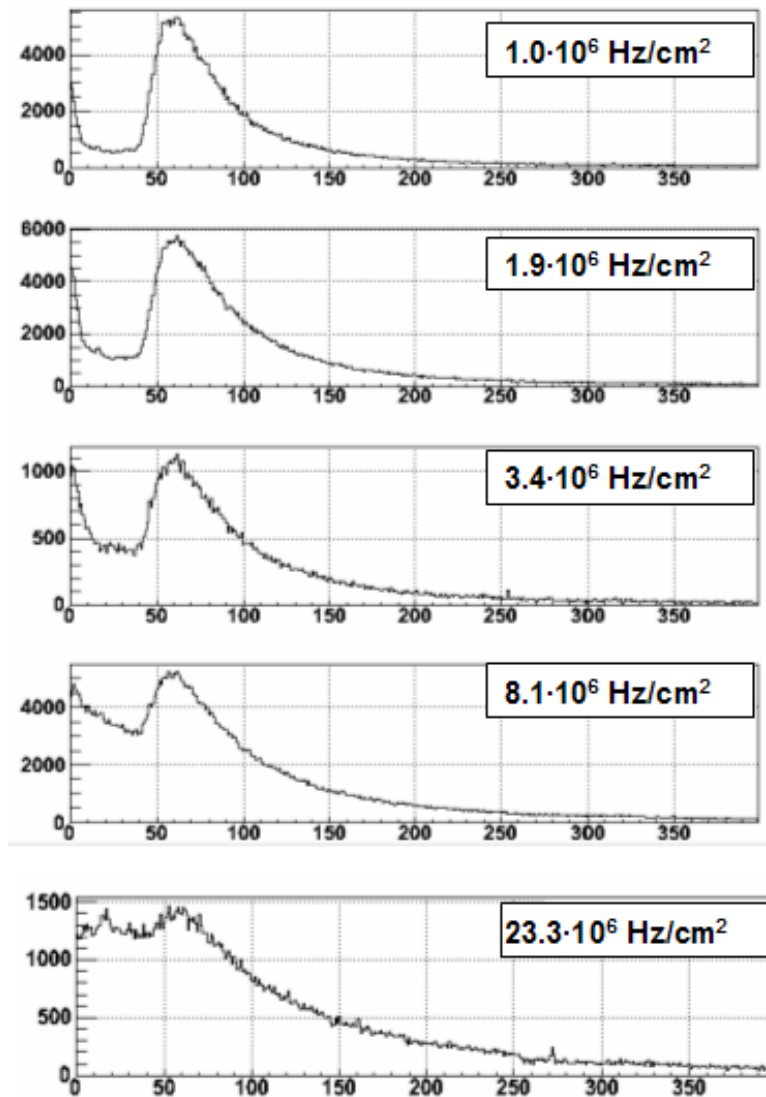Figure B.13: Modification of the spectrum as a function of the beam intensity (shown in the frames) for MG detector with Ar based gas mixture
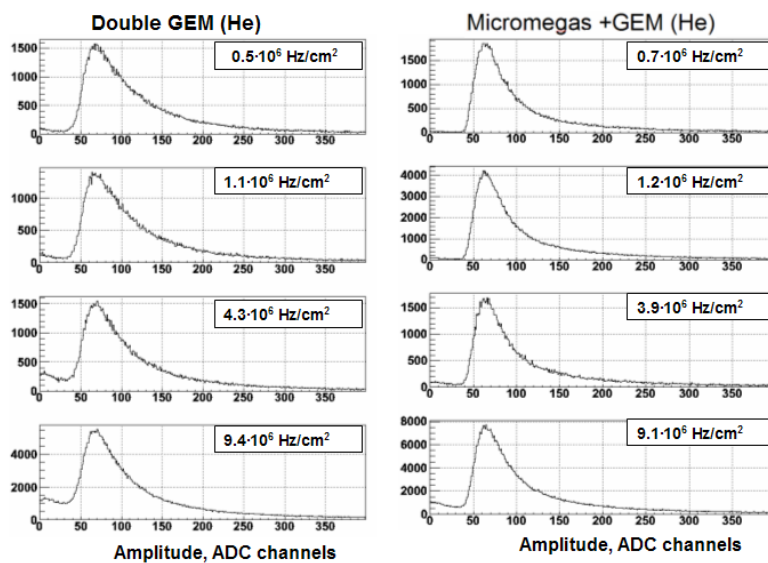
Figure B.14: Comparing the amplitude spectra for MG and GG detectors with He based gas mixture at close beam intensities (shown in the frames)
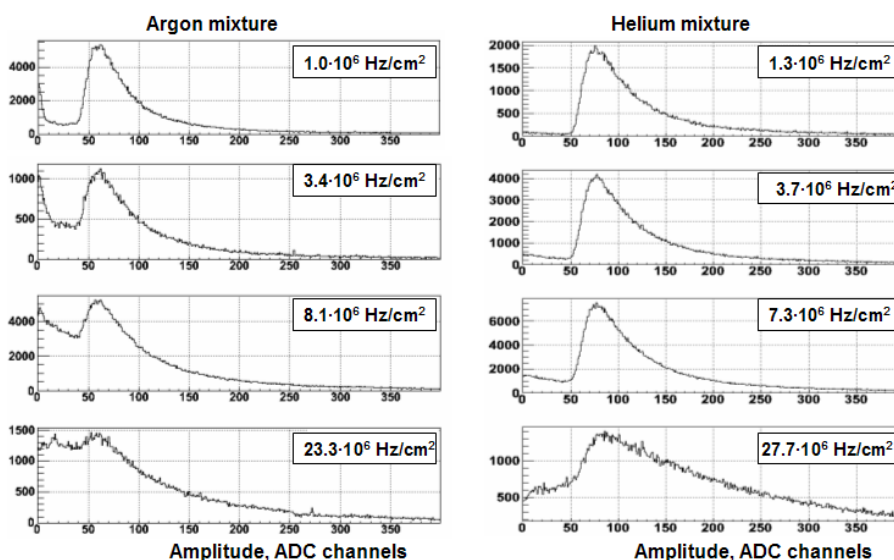

Figure B.15: Amplitude spectra measured by MG detector with Ar and He based gas mixtures at close beam intensities (shown in the frames

Appendix C

Additional R&D on readout of GEM and Straw tube detectors

C.1   Additional R&D on MUCH readout electronics

The requirements of the readout systems of MUCH depends on the subdetectors like GEM, Straw tubes. The R&D and discussions have been going on for quite some time and the baseline solutions are guided by the factor that those FEBs are to be used in other CBM systems (e.g. STS-XYTER for the STS and PADI for TOF) and are therefore fully compatible with the CBM readout system. However, some R&D activities that have been started in these connections towards building dedicated ASICs for GEM and Straw tube detectors are discussed below to give an idea about the activities in these directions. These R&D activties are in preliminary phases and require detailed work before they might be considered to be candidates for use in MUCH. It has therefore been decided to continue with these R&D activities for their possible use in SIS300 phase.

C.1.1   Status of the ASIC development for MUCH

Based on the parameters related to GEM chambers as listed in the integration chapter, the MEPHI group (Moscow) has developed the first version of an ASIC implementing the pulse processing taks. The chip was mounted on a board and tested with generator pulses and with a GEM chamber. A prototype preamplifier chip was developed, the chip structure is shown in Fig. C.1.

The Chip contains:

- 5 CSA + stand alone Shaper channels (Preamp ver. 1)

- 5 CSA channel with built-in shaping (Preamp ver. 2)

- OpAmp block

The specifications of the first prototype are presented in Fig.   C.2. The ASIC prototype has been tested at PNPI with a Fe^{55} source. The test box (GEM detector and its electronics is shown in Fig.   C.3.
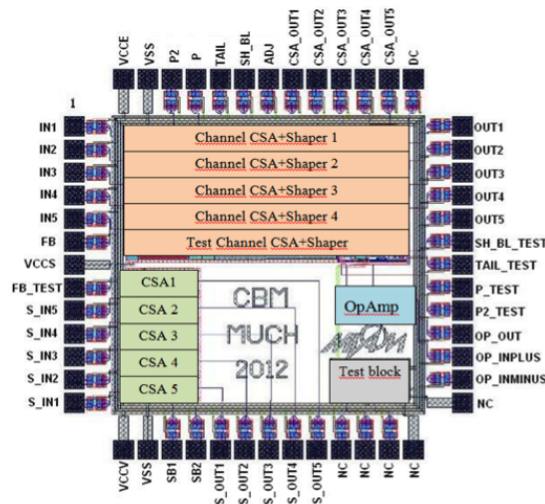
Figure C.1: Chip structure of the preamplifier ASIC (ver.1) developed at MEPHI

The test results demonstrate sufficient amplitude resolution (see Fig. C.4), linearity and dynamic range. The measured noise of 1000 electrons at low input capacitance increases up to 2500 electrons at input capacitance of 100 pF (see Fig. C.5).

Based on the results of prototypes, we have enlisted below the points related to the design of the ASIC.

- The input signals are negative; the charge is distributed according to Landau distribution, the dynamic range is of the order of 50 fC.

- The signal shape is lumpy with a typical charge collection time of 50 ns.

- The detector input capacitances vary from 10 pF for small sectors up to 40 pF for large sectors.

- Though the discharge and breakdown phenomena are greatly reduced comparing to the previous generation of gas detectors, it is still needed to use spark protection circuit at the Front End Electronics input. Namely, one should put the input protection circuit in each channel to save chip from a detector discharge.

- An important feature of MUCH is high rate environment: instant rate in its central part is about 106 counts per second, rapidly decreasing in its peripheral zone. This sets the requirements of a very high ASIC throughput and physical density in the inner region of the detector and it is not important at the chamber ends. The design of MUCH Front End Electronics is based on 180 nm CMOS technology; stand-alone ASIC size is about 7 mm x 7 mm, and power dissipation is below 10 mW/channel. Each channel consists of: charge sensitive preamplifier (input stage), analog shapers with timestamp and pulse height outputs. To achieve this, the signal shaping is split into fast and slow channels: fast channel has a fast shaper, discriminator, and the slow channel has a slow shaper, discriminator and ADC. The total power dissipation is expected to be less than 0.6 W per chip which means that ambient air cooling without radiator can be used. Table **??** presents the main features of the MUCH ASIC. Its block diagram is shown in Fig. C.6.

The front-end part of the chip has an asynchronous data driven architecture in which an analogue
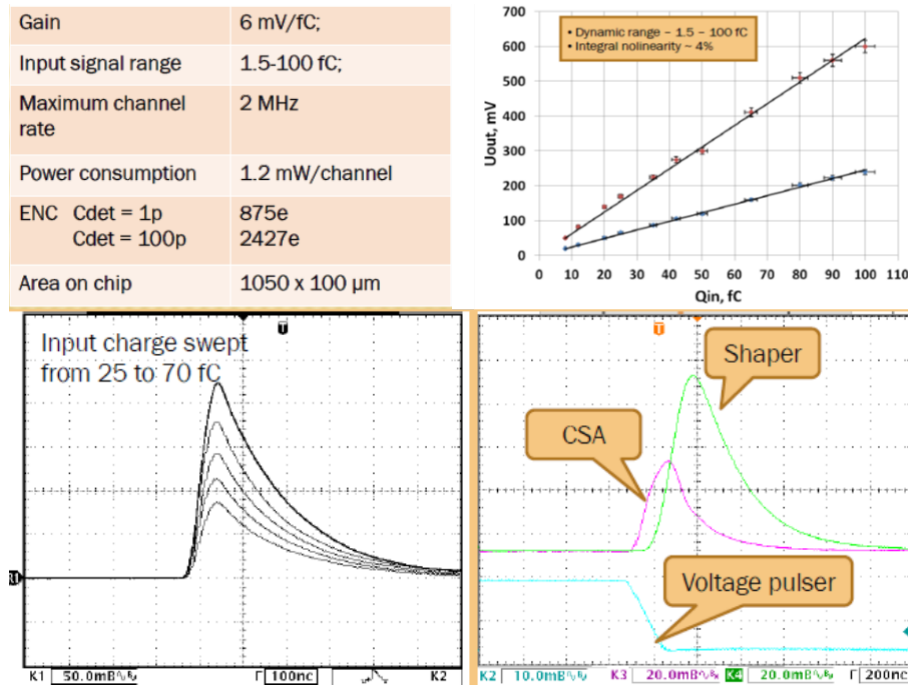
Figure C.2: Specifications (top left), transfer function (top right), and signal shapes of the charge sensitive amplifier (bottom left) and of the shaper (bottom right) of the first version of the ASIC for GEM.

signal triggers the registry of a time stamp and the measurement of the input signal pulse height. In this scheme the time stamp latching is triggered by a simple threshold discriminator in the fast part of the signal shaper corrected by time walk compensation technique. The signal pulse height shaper is different for the central and the peripheral part of the detector. The central part of the detector will experience a high particle rate up to 3×10^5 per second per channel at small pad sizes with detector capacitances of 10-15 pF. Due to time irregularities during beam extraction the instant channel rate can rise to 10^6 per second. In the peripheral zone of the detector the hit density is approximately 60 times lower and the highest detector capacitance is about 40-50 pF. The pulse height data proceeding scheme for the detector periphery is optimized for a maximal signal to noise ratio, while for the central zone the goal is to have maximal throughput. Some details are given in the following:

- Charge sensitive preamplifier (CSA). The CSA is optimized for detector capacitance values up to 100 pF. The p-MOS input transistor provides a smaller noise and has been chosen as the basic version for designing the CSA. To get high dynamic range and high input dynamic capacitance the feedback capacitor value is approximately 0.5 pF.

- Fast signal shaper. The fast filter peaking time is equal to 50 ns. With this value the fraction of collected charge for GEM detector is more than 70%, and time walk is 50 ns. The time walk compensation technique is based on the time over threshold method (TOT). Base line stabilization in fast signal shaper is realized by signal bipolar shaping. The signal to noise ratio for bipolar shaping is typically 40% worse when corresponding unipolar one. On the other side, the bipolar shaping is much more convenient for the use in large systems due to pole-zero adjustment less critical, it also adds suppression of low frequency noise and pile up inspector. It also simplifies schematics. Fast signal shaper gain is 12 mV/fC and the dynamic range is 1.2 V. Fast discriminator threshold is controlled by DAC with
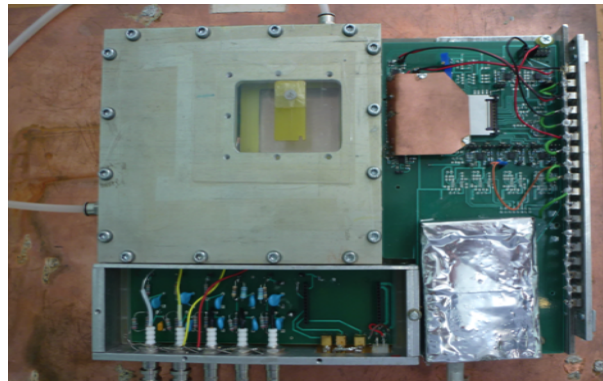
Figure C.3: Setup of testing the ASIC with GEM chamber

5-bit resolution. Threshold range is 64 mV, minimal step is 2 mV.

- Slow signal shaper is realized with CR-RC2 filter with 200 ns peaking time and active base line restorer. At low input count rates,the choice of optimal signal shaping time is connected with detector input capacitance and charge preamplifier input CMOS transistor thermals noise. For a first approximation of 50 pF detector capacitance, a p-MOS transistor with ENC = 1000 e. gives the value of slow shaper peak time equal to 200 ns. Dead time for CR-RC2 shaper with 200 ns is 1 μs. Signal gain is 12 mV/fC and equal to the fast signal shaper one. The fast and slow shaper through-puts are shown on Fig. C.7. The threshold discriminator is also included into slow channel. It is part of the Active Baseline Restorer and self-triggering.

- Two-channel multiplexer under slow control is using the channel to be applied for signal height measurements.

- Peak Detector and ADC. Successive approximation (SAR) ADC is used in each channel of MUCH -XYTER. Its power dissipation is 1.2 mW/ch and conversion time is 150-200 ns per 6 bit at 40 MHz clock.

- Output data format is compatible with the CBM one. Output data: one byte for channel number, one byte for amplitude, and two bytes for front and tail time stamps.

- For the calibration purposes the chip includes an internal calibration generator that allows checking the functionality for each channel. The operation principle is to apply a voltage step pulse to the series capacitor that is connected to the preamplifier input. The amplitude of the voltage step may be changed and thus the injected charge adjusted.

An analog derandomization method [1, 2] could be used as a back-up solution for the ASIC. Four FEE prototype chips, using the 0.18 um mixed mode UMC process have been developed. The chips were manufactured via the Europractice IC-service and tested, showing the functionality of analog derandomization technique.

C.1.2 Additional R&D on the readout of the Straw tube detector

This option requires dedicated R&D, and if required, planned to be implemented in the full version of MUCH. For the start-up version, as we have shown earlier that straw tube detector
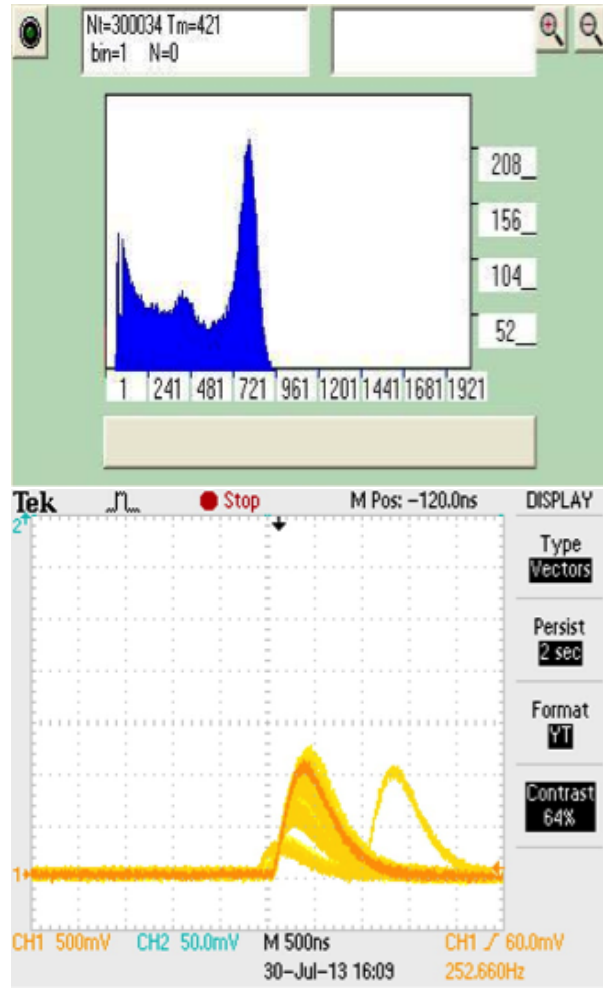
Figure C.4: Spectra from Fe-55 X-ray source (top) and the shaper output pulse (bottom)

with 1-D readout will be able to perform necessary measurements. The discussions below are only to give a flavour of the R&D being performed on this issue.

The longitudinal coordinate in the straw can also be determined by employing the charge-division method when the signals are read out from two ends of the high resistive anode wire. The longitudinal resolution achieved with long straws by this method for the MIP is near to 10 cm (σ). The anode resistivity is from 400 Ω/m to more than 1 kΩ/m, and charge-sensitive amplifiers are used.

A possibility of measuring longitudinal coordinate in straw-tube detectors by using a direct time measurements technique (DTM) was shown earlier [3] and checked now for 2 m long straw tubes [4]. Typical amplifiers for the straw are installed close to the anode ends. The pulses from the outputs of the amplifiers are fed into two channels of the DRS4 Evaluation Board. This board is based on the DRS4 chip, which can sample an input signal with a sampling speed of up to 5 GS/s and stores the analog waveform in a time window of the size determined by the capacitor array [5]. If the avalanche from the registered MIP displaced along the anode wire by δy from its center, the two signals arriving at amplifiers pass the distance L/2 $\pm\delta y$, where L is the anode length. Therefore, the absolute difference $\delta\tau$ is determined as $\delta\tau = 2\delta y/v$ where v is an electromagnetic wave propagation velocity along the anode wire whereas the sign determines the direction of the coordinate displacement with respect to the center of the wire. The difference
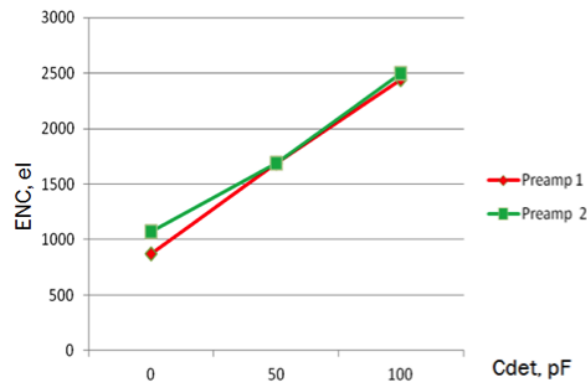
Figure C.5: ENC (Equivalent Noise Charge) as function of the detector capacitance
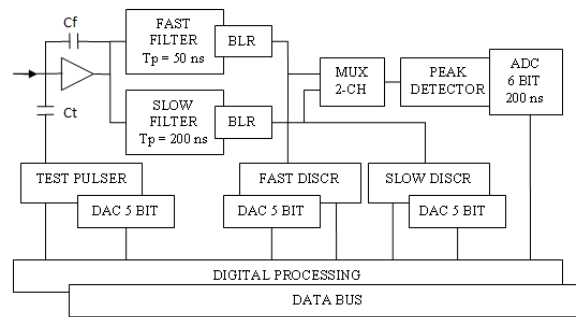

Figure C.6: Block diagram of the ASIC.

between the leading edges of two pulses (t1 and t2) determines the value of the coordinates along the anode. The longitudinal resolution obtained in the case of detection of electrons from the ^{106}Ru is shown in Fig. C.8. The resolution varies from ∼1 cm at the center of the straw to ∼2 cm near the straw end [4].

The DTM allows the use of one amplifier type for the readout of the signals from both coordinates. In that way, this method can be used for the two-dimensional readout.

C.1.2.1 Development of a dedicated ASIC for the Straw tube detector

It has been proposed that an ASIC will be developed for recording signals from the anode drift tubes by measuring the drift time of the electrons from the ionization of the working gas filling tubes. Drift tubes have an inner diameter of 6 mm, with the maximum electron collection time is in the range of ∼60ns. The main parameters of the straw signals are: its peaking time, the time of the rising of the signal from 0 to its maximum, its width on the base line, and its overshoot area - full area of the reverse after impulse. The big overshoot area restrict the operation of the straws at high multiplicity, but we will have occupancy less than 7%. The signal width should be as short as possible to minimize the overlapping of the signals from next particles. The peaking time is the main parameter for high accuracy of the drift-time measurements as well as the threshold of the registration of the MIP. The front-end electronics specifications are set to 6-7ns for the peaking time and ≤4 fC for the threshold.

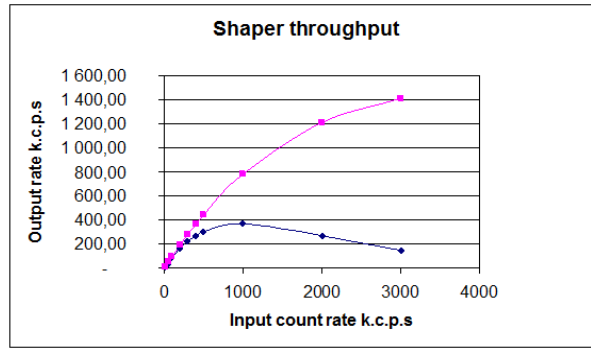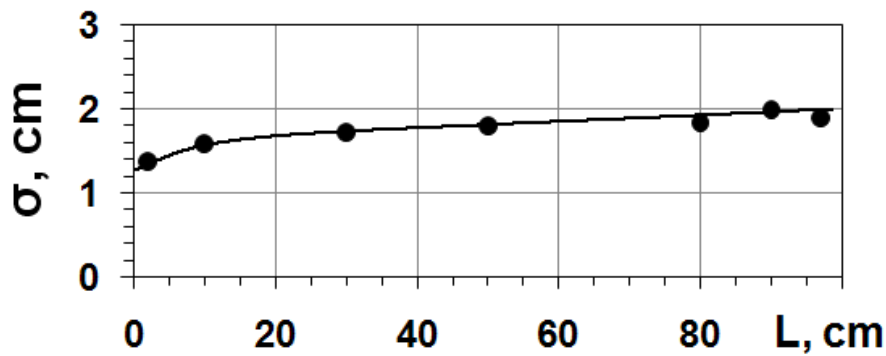The signal processing requirements of the straw tube have led to the design of a full-custom,

Figure C.7: Block diagram of the MUCH-XYTER.

Figure C.8: The longitudinal resolution along the straw as a function of the distance of the ^{106}Ru source from the straw center. The gas mixture is Ar/CO_2 (80/20) and the gas gain is about 8×10^4

analogue, bipolar ASIC. It provides eight channels of amplifier, shaper, discriminator and base line restorer. Some parameters of the amplifier chip are shown in Table C.1.

The main parameters of fast electronics, affecting the accuracy of measurement of electron drift time are: amplifier noise, time delayed output of the discriminator, as well as gain and input impedance. The Table C.2 gives some of the parameters of the fast electronics, the values of which are aimed at ensuring the requirements for FEE.

Number of channels	8
Functions	Preamplifier-shaper + baseline restorer, discriminator
Technology	Bi CMOS
Supply Volgate, V	+3.3 (+5V)
Dissipation power	20mW/channel
Integrated circuit package	QFP (48-80)

Table C.1: Straw tube readout ASIC parameters

Input impedance, Ohm, no more	120-300
Internal noise, ENC (r.m.s.), electrons	1600
Gain uniformity,%	$< \pm 15$
Maximum signal value, fC	300 (200)
Baseline restorer	yes
Peaking time, ns	7-8
transmission coefficient, mV/fC	10/15
Width of signal at the base, ns	<40
Noise counting rate at operating threshold 2fC, kHz	1
Dynamic range for threshold, fC	1.5/20
Intrinsic time resolution,ns	<2
Delay of the output signals, ns	35
Maximum discriminator dead time, ns	10
Power consumption	20mW/channel
Signals	LVDS

Table C.2: Parameters of the ASIC of two chambers tested at CERN SPS using pion beams.

Bibliography

[1] ISSN 00204412, Instruments and Experimental Techniques, 2010, Vol. 53, Issue 4, 524-529.

[2] ISSN 10637397, Russian Microelectronics, March 2013, Vol. 42, Issue 2, 119-126.

[3] R.A. Boie et al., IEEE Trans. Nucl. Sci. NS-28 (1988) 471.

[4] A.M. Makankin et al., arXiv:1301.6018v1 [physics.ins-det].

[5] Paul Scherrer Institut, DRS4, http://drs.web.psi.ch/datasheets.